Thèse n° 9557

Modeling the origins of adhesive wear across scales

Présentée le 23 juin 2022

Faculté de l'environnement naturel, architectural et construit
Laboratoire de simulation en mécanique des solides
Programme doctoral en mécanique

pour l'obtention du grade de Docteur ès Sciences

par

Son-Jonathan PHAM-BA

Acceptée sur proposition du jury

Prof. M. E. S. Violay, présidente du jury
Prof. J.-F. Molinari, directeur de thèse
Prof. R. Aghababaei, rapporteur
Prof. N. Fillot, rapporteur
Prof. W. Curtin, rapporteur

École
polytechnique
fédérale
de Lausanne

2022

ACKNOWLEDGMENTS

The document you are reading could not have come into existence if it wasn't for my academic father (my advisor), Jean-François Molinari. I cannot thank him enough for the ideal environment he provided to me as his Ph.D. student. He cares deeply about the well-being of every member of his team, and he is always enthusiastic, encouraging, and full of ideas. It was a delight to work under his wing.

I am grateful to the jury of my oral exam: Prof. Marie Violay, Prof. Ramin Aghababaei, Prof. William Curtin, and Prof. Nicolas Fillot, who took the time to thoroughly review my work, allowing for an engaging exchange during the defense.

Comparing the day I joined the lab (that was four years ago) to the day I left it, it feels strange to see that almost all the faces have changed. I had the chance to work with Lucas F. and Tobias, and I can now confess that I have always been intimidated by their mastery. It was my great pleasure, and I hope it was mutual, to live with the whole LSMS family: Angelos, Anne-Françoise, Antoine, Birgitte, Enrico, Emma, Emil, Fabian, Fatima, Gianluca, Guillaume, Jacopo, Joaquin, Lucas B., Manon, Martina, Mathias, Mohit, Nicolas, Parissa, Raquel, Roozbeh, Sacha, Thibault G., Thibault R., and Yulin. I gathered a lot of good memories and I hope that I will keep them near me for a long time.

Je remercie Linda, Vannina, Eddy, Christophe, et Cyril, pour les discussions, leur aide, et d'avoir pris le temps de me former pour la partie expérimentale de mes travaux.

Il y a dix ans, je commençai mes études à l'EPFL, et j'ai été très heureux de mener ce parcours jusqu'au bout en compagnie de Paul-Arthur, qui, malgré toutes ses tentatives, n'a pas réussi à faire de moi un danseur accompli. Mes parents auront aussi contribué à ma réussite en gardant mon estomac bien rempli et mes papilles satisfaites.

Et bien sûr, je n'aurais pu me passer de mes escapades musicales, grâce auxquelles j'ai pu faire mes meilleures rencontres. Je remercie Célia et Jonas pour les nombreuses virées loin du travail. Finalement, je remercie chaleureusement Cori, qui fut d'un soutien sans faille durant ma thèse, et sans qui je serais peut-être encore terré dans ma petite chambre d'étudiant.

Lausanne, juin 2022 Son Pham-Ba

ABSTRACT

Friction and wear occur at every interface between solid materials. In the design of mechanical devices, it is desirable to be able to quantify and control the amount of friction and wear, as well as predict their evolution with time. “Tribology” is the science of interacting surfaces in relative motion, which involves many phenomena such as friction, wear, lubrication, and corrosion. Phenomenological models can be used to make predictions on tribological behaviors (the Coulomb’s friction law, for example), but they must be tuned with experimental values, that are not directly available when developing novel materials or surface treatments. From a scientific point of view, these models give little to no insight into the mechanisms involved. This thesis aims to enhance the current understanding of dry friction and wear at a more fundamental level.

All surfaces are rough over a range of length scales, whether they are man-made or natural. When two rough surfaces are put into contact with each other, only a fraction of the total apparent area is actually in contact. To study friction and wear in this context, we must go down at the scale of the smallest asperities of the rough surfaces, where contact happens. The main goal of this thesis is to acquire an understanding of adhesive wear from the nanoscale, and establish a link with the larger scales. To do so, we start by working at the asperity scale, using analytical theories and molecular dynamics simulations to investigate the wear of several interacting micro-contacts. The elastic interactions enable the emergence of a wear regime featuring large wear volumes that are not observed when considering the micro-contacts in an isolated manner, predicting the existence of a severe wear regime. The emergence of severe wear is also found with rough contacts at a larger scale, solved using the boundary element method. To upscale the dynamical nanoscale processes of friction and wear uncovered during this thesis, a coarse-grained discrete element model was formulated. This model is capable of reproducing the adhesive wear mechanisms observed with molecular dynamics, and it can handle more complex situations involving the creation of third-body particles and a third-body layer. The temporal evolution of tribological interfaces is investigated using this model and with the help of physical experiments. We found that the wear process starts with the formation of small wear particles, whose size is dictated by the material properties. The particles grow and merge into a third-body layer, responsible for the macroscopic roughness and providing the sliding resistance. Finally, using some of the knowledge earned along the way, a practical case was investigated. The tribological influence of an oxide layer on silicon samples was assessed using experiments and numerical simulations. We found that the presence of the oxide layer reduces the wear rate of the protected piece, but increases the friction coefficient.

While this thesis was restricted to the study of unlubricated adhesive wear, its founding principles and the developed tools could be used to look at abrasion and lubricated contacts.

Keywords: tribology, asperity, severe wear, rough surface, third-body layer, molecular dynamics, discrete element method, boundary element method, pin-on-disc, silicon

RÉSUMÉ

La friction et l'usure apparaissent dans toutes les interfaces entre matériaux solides. Lors de la conception de systèmes mécaniques, il est souhaitable de pouvoir quantifier et contrôler ces phénomènes, ainsi que de prédire leur évolution dans le temps. La "tribologie" est la science traitant de l'interaction de surfaces en mouvement relatif. De nombreux phénomènes entrent en jeu, tels que la friction, l'usure, la lubrification et la corrosion. Des modèles phénoménologiques peuvent être utilisés pour émettre des prédictions (par exemple, la loi de frottement de Coulomb), mais ils doivent être calibrés sur des mesures expérimentales, indisponibles lorsque l'on développe des matériaux novateurs. D'un point de vue scientifique, ces modèles donnent peu, voire aucun renseignement sur les mécanismes physiques en jeu. Cette thèse a pour but d'enrichir la compréhension actuelle du frottement sec et de l'usure d'un point de vue fondamental.

Toutes les surfaces sont rugueuses à plusieurs échelles de longueur. Lorsque deux surfaces sont mises en contact, seulement une fraction de l'aire totale apparente sera réellement en contact. Pour étudier la friction et l'usure dans ce contexte, il faut se placer à l'échelle des plus petites aspérités présentes sur la rugosité des surfaces, là où le contact se produit. L'objectif principal de cette thèse est d'acquérir une compréhension de l'usure adhésive à partir de l'échelle nano, puis d'établir un lien avec les échelles plus grandes. On commence par étudier l'usure de plusieurs micro-contacts en interaction. Les interactions élastiques permettent l'émergence d'un régime présentant de grands volumes d'usure : un régime d'usure sévère. L'apparition de l'usure sévère s'applique aussi aux contacts entre surfaces rugueuses. Afin de rapporter aux plus grandes échelles les mécanismes nano dynamiques de friction et d'usure découverts dans cette thèse, un modèle d'éléments discrets *coarse-grained* (grains grossiers) est formulé. Ce modèle est capable de reproduire les mécanismes d'usure adhésive observés avec la dynamique moléculaire. Il peut aussi traiter des situations plus complexes, mettant en jeu des particules (voire une couche) de troisième corps. L'évolution temporelle des interfaces tribologiques est étudiée à l'aide de ce modèle ainsi que d'expériences physiques. On observe que le processus d'usure débute par la formation de petites particules d'usure. Les particules grossissent et fusionnent en une tribo-couche, responsable de la rugosité macroscopique et de la résistance au glissement. Pour terminer, en utilisant les connaissances obtenues en chemin, un cas pratique est abordé. L'influence tribologique d'une couche d'oxyde présente sur des pièces en silicium est étudiée à l'aide d'expériences et simulations numériques. On constate que la présence de la couche d'oxyde réduit la vitesse d'usure de la pièce, mais augmente son coefficient de friction.

Bien que cette thèse soit restreinte à l'étude de l'usure adhésive non lubrifiée, les principes sur lesquels elle est fondée et les outils développés pourraient être utilisés pour se pencher sur le phénomène d'abrasion et sur les contacts lubrifiés.

Mot-clés: tribologie, aspérité, usure sévère, surface rugueuse, tribo-couche, dynamique moléculaire, méthode des éléments discrets, méthode des éléments de frontière, *pin-on-disc*, silicium

CONTENTS

ACKNOWLEDGMENTS III

ABSTRACT V

RÉSUMÉ VII

LIST OF FIGURES XI

LIST OF TABLES XVI

NOMENCLATURE XIX

PART I FRAMEWORK

CHAPTER 1 INTRODUCTION 3

1.1 State of the art 3
- 1.1.1 Friction and wear at the macroscopic scale 3
- 1.1.2 Rough surfaces and contact 5
- 1.1.3 Wear at the scale of asperities 10

1.2 Objectives 13

1.3 Approach 14

1.4 Outline 15

CHAPTER 2 NUMERICAL METHODS 17

2.1 Molecular dynamics 17
- 2.1.1 General principles 17
- 2.1.2 Computable quantities 18
- 2.1.3 Silicon and silica 20

2.2 Discrete element method 21
- 2.2.1 Simulation 22
- 2.2.2 Critical time step 23
- 2.2.3 Critical damping 25

2.3 Boundary element method 25
- 2.3.1 Elastic deformation 25
- 2.3.2 Contact 27
- 2.3.3 Contact with friction 28

PART II THEORETICAL AND NUMERICAL ADVANCES

CHAPTER 3 INTERACTION OF MICRO-CONTACTS IN 2D 31

3.1 Theoretical model 32
- 3.1.1 Elastic energy 32

3.1.2 Adhesive energy 36
3.1.3 Energy criterion for debris formation 37
3.2 Validation using simulations 40
3.2.1 Boundary element method 40
3.2.2 Molecular dynamics 41

CHAPTER 4 INTERACTION OF MICRO-CONTACTS IN 3D 45
4.1 Energy balance criterion 46
4.2 Crack initiation criterion 48
4.3 Single sheared micro-contact and critical size 49
4.4 Interaction of two micro-contacts 50
4.5 Wear map 53

CHAPTER 5 FROM MICRO-CONTACTS TO WEAR REGIMES 55
5.1 Numerical model for random rough surfaces 56
5.2 Verification 58
5.3 Wear maps and wear regimes 59
5.4 Roughness parameters 62

CHAPTER 6 BRIDGING SCALES WITH A COARSE-GRAINED DISCRETE ELEMENT MODEL . . . 65
6.1 Method 66
6.1.1 Forces between particles 67
6.1.2 Matching macroscopic material properties 69
6.2 Validation 76
6.2.1 Crystalline lattice 77
6.2.2 Amorphous sample 79
6.2.3 Discretization 81
6.2.4 Calibration 83
6.3 Application: nanoscale adhesive wear 83
6.4 Examples of application 86

CHAPTER 7 FRICTION AND WEAR FROM NANOSCALE UP 89
7.1 Linking local and macroscopic strengths 89
7.1.1 Simulations 89
7.1.2 Model 90
7.2 Wear of rough surfaces at multiple scales 93
7.2.1 Qualitative results 93
7.2.2 Quantitative results 94
7.3 Transition between frictional regimes with wear particles 96

PART III EXPERIMENTAL STUDIES AND MODELING

CHAPTER 8 CREATION AND EVOLUTION OF ROUGHNESS 101
8.1 Experimental setup 102
8.1.1 Sa roughness measurement 104
8.2 Results and discussion 104
8.2.1 Initial wear particle size 104
8.2.2 Roughness formation 108
8.2.3 Roughness evolution 109

CHAPTER 9 ADDING AN OXIDE LAYER 115
9.1 Experimental setup 115
9.2 Results and discussion 116
9.2.1 Friction coefficient 116
9.2.2 Surface roughness 119
9.2.3 Wear 120
9.3 Numerical simulations 123
9.3.1 MD: tangential strength at the atomic scale 123
9.3.2 BEM: modeling experiments 127
9.3.3 Going further with coarse-grained DEM simulations 136

CONCLUSION 139
Outlook 141

APPENDICES

APPENDIX A FRICTIONAL CONTACT WITH THE BOUNDARY ELEMENT METHOD 145
A.1 Formulation 145
A.1.1 Continuous formulation 146
A.1.2 Discrete formulation 147
A.1.3 Minimization 148
A.2 Validation 149
A.3 Computed quantities 151

BIBLIOGRAPHY 153

List of Figures

1.1 Sliding block with friction . . . 4
1.2 Geometrical interpretation of fractal dimension and Hurst exponent . . . 6
1.3 Simplified power spectral density of a rough surface . . . 7
1.4 Measuring the PSD of a rough surface. . . . 8
1.5 Example of computer-generated rough surfaces . . . 9
1.6 Evolution of contact area with normal pressure . . . 9
1.7 MD simulations of colliding asperities under shear . . . 11
1.8 MD simulations of two pairs of colliding asperities under shear . . . 12
1.9 Multiscale view of a macroscopically flat interface . . . 13

2.1 Simple contact in the discrete element method . . . 21
2.2 Elastic half-space with point loads applied at its origin . . . 25
2.3 Different loading condition on an elastic half-space . . . 26
2.4 Normal contact with BEM . . . 27

3.1 Schematics of sheared micro-contacts and possible outcomes . . . 32
3.2 2D semi-infinite solid under a single tangential point load . . . 32
3.3 2D semi-infinite solid under two tangential point loads . . . 34
3.4 2D semi-infinite solid under a uniform tangential load . . . 35
3.5 Formation of a debris particle of size d due to the tangential load q . . . 36
3.6 N equally-spaced uniform loads q of size d and spacing λ . . . 37
3.7 Wear map of the different outcomes for the system of Figure 3.1a . . . 39
3.8 BEM simulations of the elastic energy $E_{\mathrm{el},Nq}$ of N equally-spaced uniform loads q compared to analytical prediction . . . 41
3.9 Distribution of the MD simulations' outcomes on the wear map (Figure 3.7) . . . 42
3.10 Formation of a debris particle from a single micro-contact of size $d = 1.7d^*$ . . . 42
3.11 Three different outcomes from two sheared micro-contacts . . . 43

4.1 Micro-contacts under uniform tangential load on a semi-infinite solid. . . . 45
4.2 Cross section view of the required crack nucleation sites for the formation of a spherical wear particle at a micro-contact. . . . 49
4.3 Two circular contacts under uniform tangential load. . . . 51
4.4 Comparison of the numerical integration and the analytical approximation of the elastic energy stored under two tangentially loaded circular contacts . . . 52
4.5 Different cases of wear particle formation with two micro-contacts . . . 52

4.6 Wear map of the different cases of wear particle formation under tangentially loaded two micro-contacts . . . 54

5.1 Target PSD of generated rough surfaces . . . 56
5.2 BE simulations of the micro-contacts and local contact pressures for increasing normal load . . . 57
5.3 Different cases of wear particle formation with two micro-contacts in the numerical model . . . 58
5.4 Numerical wear maps for two circular micro-contacts . . . 58
5.5 Different cases of wear particle formation in a rough contact . . . 60
5.6 Wear maps of the contact between rough surfaces . . . 60
5.7 Wear curves of the contact between rough surfaces . . . 61
5.8 Effect of the roughness parameters on the wear curves . . . 62

6.1 Two interacting particles . . . 67
6.2 Normal force between two particles as a function of inter-particular distance δ_N . . . 67
6.3 Tangential force between two particles as a function of sliding distance δ_T . . . 68
6.4 Normal force when $r_i + r_j > d_\mathrm{c}$ . . . 72
6.5 Normal force when $r_i + r_j > d_\mathrm{c}$ with corrected δ_f . . . 72
6.6 Matched tensile strength with corrected δ_f . . . 73
6.7 Example of patch test's system and outputs . . . 77
6.8 Effect of target ν on the measured E . . . 78
6.9 Effect of target ν on the measured ν . . . 78
6.10 Effect of d_0, s and target ν on the measured tensile strength $\sigma_\mathrm{m,N}$ . . . 78
6.11 Effect of d_0, s and target ν on the measured shear strength $\sigma_\mathrm{m,T}$ . . . 79
6.12 Effect of d_0 and s on the relaxed volume fraction . . . 80
6.13 Effect of d_0 and s on the measured E . . . 81
6.14 Effect d_0 and s on the measured ν . . . 82
6.15 Effect d_0 and s on the measured tensile strength . . . 82
6.16 Effect d_0 and s on the measured shear strength . . . 82
6.17 Effect of d_0 and s on the measured tensile strength $\sigma_\mathrm{m,T}$ for systems of various sizes and discretizations . . . 82
6.18 Sheared junctions with $d_0 = 1.5\,\mathrm{nm}$ . . . 84
6.19 Sheared junctions with $d_0 = 3\,\mathrm{nm}$ . . . 85
6.20 Sheared junctions with $d_0 = 6\,\mathrm{nm}$ . . . 85
6.21 Scooping experiments on kinetic sand . . . 87
6.22 DEM scooping simulations . . . 87

7.1 DEM model of a junction between two sliding surfaces . . . 90
7.2 Shear resistance of DEM systems with one junction . . . 91
7.3 Predicted shear resistance of systems with one junction . . . 93
7.4 Formation of wear particles from rough surfaces in DEM . . . 94
7.5 Growth of wear particles trapped between sliding rough surfaces . . . 94

7.6 Growth of a shear band 95
7.7 Tangential force measured in both frictional regimes. 95
7.8 Reaching two frictional regimes from trapped wear particles 97
7.9 Evolution of frictional force during a transition of regime 97

8.1 Experimental setup on tribometer 102
8.2 SEM images of wear particles taken from a flat disc after 1 s (8 mm) of sliding 105
8.3 MD simulation of a collision between two amorphous SiO_2 asperities of diameter $d = 7\,\mathrm{nm}$ 106
8.4 MD simulation of a collision between two amorphous SiO_2 asperities of diameter $d = 10\,\mathrm{nm}$ 106
8.5 MD simulation of a collision between two amorphous SiO_2 asperities of diameter $d = 20\,\mathrm{nm}$ 106
8.6 SEM images of wear tracks on flat discs after different amounts of time 108
8.7 Topographic images of discs' initial surfaces and wear tracks after 5 h of sliding . . . 110
8.8 Evolution of friction coefficient and surface roughness from initially smooth and rough SiO_2 surfaces 111
8.9 Example of computation of the Hurst exponent and its evolution from initially smooth and rough SiO_2 surfaces. 111
8.10 Schematics of roughness evolution behaviors 113

9.1 Evolution of friction coefficient for each oxide thickness and averaged curves 117
9.2 Evolution of surface roughness for each oxide thickness 117
9.3 Evolution of friction coefficient and surface roughness from initially flat oxidized Si samples. 118
9.4 Friction coefficient as a function of oxide layer thickness and empirical fits 118
9.5 Wear track on an Si disc after 5 hours.. 118
9.6 Topographies and cross-sections of a worn pin and an oxidized disc at multiple locations after the experiment 119
9.7 Schematic cross-sections of the wear tracks on the different discs 120
9.8 Colored SEM image of a TBL in a portion of the wear track of a worn oxidized Si disc. 121
9.9 SEM image of the cross-section of a groove in the wear track on an oxidized disc. . . 121
9.10 Evolution of wear volume from initially flat oxidized Si samples 122
9.11 Measured friction coefficients as function of contact areas and fitted model 123
9.12 MD measurements of the shear strength of Si under pressure. 125
9.13 Atomic structure of a sheared Si system without external pressure 126
9.14 Atomic structure of an Si system under a pressure of 25 GPa 126
9.15 MD measurements of the shear strength of SiO_2 under pressure 127
9.16 Atomic stain in sheared SiO_2 system without external pressure 128
9.17 MD measurements of maximum and dynamical shear strength for Si and SiO_2 under pressure 128
9.18 Simplified models of maximum and dynamical shear strength for Si and SiO_2 under pressure 129
9.19 Example of surface topographies obtained with the BEM model 132
9.20 Friction coefficient and wear volumes obtained with $h_{\mathrm{layer}} = 1\,\mu\mathrm{m}$ 133
9.21 Effect of oxide layer thickness on friction coefficient and wear volume 133

9.22 Effect of rotating non-planarity on surface topographies 134
9.23 Effect of the slope of a rotating non-planarity on friction coefficient and wear volume . 135
9.24 Effect of oxide layer thickness with the presence of a non-planarity of slope 0.02 . . 135
9.25 Comparison of friction coefficient between experiments and simulated planar and non-planar cases 136
9.26 DEM simulation of asperity wear on oxidized Si 137

A.1 Tangential contact setup. 146
A.2 Friction cone for constraints enforcement 148
A.3 Spherical tangential contact 150
A.4 Validation of the BE solver at partial friction in the uncoupled case 150
A.5 Elastic tangential contact of a rough sphere 152

LIST OF TABLES

2.1 Material properties of silicon (Si) and silica (SiO_2) . . . 21
2.2 Silicon and silica names in various languages . . . 21

3.1 List of symbols . . . 33

5.1 List of roughness parameters for the production of wear maps and curves . . . 62

6.1 List of symbols used for lengths and sizes . . . 66
6.2 List of force parameters . . . 69
6.3 List of target material properties . . . 69
6.4 List of target material properties for patch tests . . . 76
6.5 Amorphous silica properties . . . 83
6.6 Estimated time for a simulation of 100 000 nm^3, 10 ns, on 28 2.6 GHz CPUs . . . 86

8.1 Duration and initial roughness of the tests . . . 103

9.1 Duration and oxide layer thickness for experiments . . . 116

NOMENCLATURE

Frequently used symbols

d^*	Critical length scale	[m]
E	Young's modulus	[Pa]
E^*	Equivalent Young's modulus	[Pa]
G	Shear modulus	[Pa]
$\mathcal{H}$	Hurst exponent	[-]
h'_{RMS}	RMS of surface's slopes	[-]
$\mathcal{R}$	Elastic/adhesive energy ratio	[-]
γ	Surface energy	[N/m]
η	Restitution coefficient	[-]
μ	Friction coefficient	[-]
ν	Poisson's ratio	[-]
ρ	Density	[kg/m^3]

Subscripts

$\cdot_{\mathrm{a}}$	Apparent
$\cdot_{\mathrm{ad}}$	Adhesive
$\cdot_{\mathrm{c}}$	Critical
$\cdot_{\mathrm{eff}}$	Effective
$\cdot_{\mathrm{el}}$	Elastic
$\cdot_{\mathrm{j}}$	of junction
$\cdot_{\mathrm{m,N}}$	Maximum in normal direction
$\cdot_{\mathrm{m,T}}$	Maximum in tangential direction
$\cdot_{\mathrm{N}}$	Normal
$\cdot_{\mathrm{T}}$	Tangential

Abbreviations

AFM	Atomic force microscopy
BEM	Boundary element method
DEM	Discrete element method
DFT	Discrete Fourier transform
MD	Molecular dynamics
PSD	Power spectral density
RMS	Root mean square
SEM	Scanning electron microscope
TBL	Third-body layer

PART I

FRAMEWORK

CHAPTER 1

INTRODUCTION

1.1 STATE OF THE ART

1.1.1 *Friction and wear at the macroscopic scale*

WEAR is all around us. We experience it every day in spite of ourselves, with the wear of car brakes and tires on roads being responsible for more than half of traffic-related air pollution according to Grigoratos & Martini (2015). Tire wear in particular has a significant impact on the quantity of microplastics in the environment (Kole *et al.* 2017), which comes with all sorts of respiratory health issues. At larger scales, wear manifests itself in sliding geological faults due to rock pulverization (Scholz 1987; Reches & Dewers 2005), and is responsible for the creation of what is called a *third-body layer*, the two *"first-bodies"* being the two surfaces sliding on each other. This third-body layer, also called a *gouge* by the geomechanics community, directly influences the frictional properties of the interface (Biegel *et al.* 1989; Mair *et al.* 2002), and thus has implications on the triggering and amplitude of seismic events (Mizoguchi *et al.* 2007). Being able to predict the occurrences of earthquakes calls for an understanding of gouge formation, properties, and evolution.

On a more practical level, wear is a primary concern in the field of engineering. When designing mechanical devices, it is desirable to quantify and control the amount of friction and wear, as well as predict their evolution with time. Most systems comprising of moving parts require low friction, for efficiency, and low wear, for reliability and greater lifespan. Yet, some devices need high friction (like brakes), high wear (like machining), or even both (a lighter). As such, it is not always a matter of minimizing these two quantities (even if it is often the case), but rather, being able to control them.

The importance of friction and wear is such that there is a word depicting their examination: "*tribology*", from ancient Greek τρίβω (*tribo*), meaning "to rub", followed by the suffix *-logy* from -λογία (*-logia*), meaning "the knowledge of". Tribology is the science of interacting surfaces in relative motion and refers to the study of friction, wear, lubrication and corrosion. Tribological phenomena have a significant economic impact. Holmberg & Erdemir (2017) estimated that 20% of the world's total energy consumption is used to overcome friction, and that implementing new friction and wear reduction technologies would lead to savings of 1.4% on the gross domestic product annually.

As all dynamical systems, a tribological system has inputs (geometry, materials, and loading

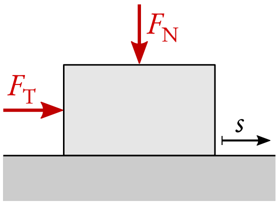

Figure 1.1 – Sliding block with friction. When the tangential force F_T overcomes the static friction force μF_N (Coulomb's friction law) acting between the block and the support, the block starts moving. Other models exist to estimate the friction forces.

conditions) and outputs (for example friction and wear). To know exactly how to predict the behavior of such a system would be like finding the Holy Grail of tribology, and it is what tribologists are after. The study of friction began a long time ago, five centuries from now, with the work of Leonardo da Vinci (Hutchings 2016). He found in his experiments that the friction force is proportional to the normal load and independent of the area of contact. His findings are now well known by the scientific community, being usually attributed to the physicists Guillaume Amontons (1699) and Charles de Coulomb (1785) under the name *"Amontons-Coulomb friction law"*, or simply *"Coulomb's friction law"*:

$$F_T \leqslant \mu F_N, \tag{1.1}$$

which arises in situations like shown in Figure 1.1, where F_N is the *normal load*, F_T is the *tangential load*, and μ is the *friction coefficient* corresponding to the interface. The value of μ depends on the materials constituting the interface, but also on surface finish, lubrication, boundary conditions, *etc.* It usually evolves during sliding.

For the description of sliding wear, as many as 182 equations have been referenced by Meng & Ludema (1995), along with more than 300 equations to describe frictional phenomena. Each model has between 2 and 26 describing parameters. Obviously, not all of the parameters have a direct physical meaning. They must be fitted again experiments, making each model very specific to a given case of interface. One of the first derived and simplest model of wear is the *Archard's wear model* (Archard 1953) giving the *wear volume* V as

$$V = \mathfrak{k}\frac{F_N\, s}{\mathfrak{H}}, \tag{1.2}$$

s being the *sliding distance*, $\mathfrak{H}$ the *hardness* of the softest material, and $\mathfrak{k}$ a fitted *wear coefficient*. Note that, like the Coulomb's friction law, the Archard's wear model shows a proportionality with the normal load F_N. The problem with the formulation of this wear law is the same as for the other wear models, that is $\mathfrak{k}$ is a fitted parameter specific to a given situation, ranging from 10^{-9} to 10^{-2} according to Rabinowicz (1984). Rabinowicz classified wear into different forms, the principal forms being *abrasive wear* and *adhesive wear*, both obeying the Archard's wear model. Abrasive wear involves a hard surface rubbing against a softer one, while adhesive wear takes place between two bodies of similar hardness, typically made of metal. In the case of adhesive wear, various regimes are observed: *low wear* corresponds to $\mathfrak{k}$ in the range 10^{-8} - 10^{-6}, *mild wear* to the range 10^{-6} - 10^{-4}, and *severe* or *catastrophic wear* to the range 10^{-4} - 10^{-2}. Wear particles are formed in the two higher regimes, while in the low wear regime the surfaces are only polished. The wear coefficient is usually not constant over time, and transitions can be observed between different regimes of wear for different sliding durations or different loads (Zhang & Alpas 1997).

Another feature differentiating mild wear from severe wear is that the wear coefficient k is not much dependent on the normal load in the mild wear regime, while it increases with the load in the severe wear regime.

The physical origins of the friction coefficient μ and the wear coefficient k are not yet fully understood. To use these equations in practice, ranges of values can be found in tables, but only for the most usual cases. Therefore, no prediction is readily available without experimentation when working for example with new materials and systems. The flaws and limitations associated with the use of empirical models are the motive to move toward acquiring a more fundamental understanding of tribological processes.

1.1.2 *Rough surfaces and contact*

We may start with some geometrical considerations. All macroscopically flat-looking surfaces are in reality *rough*, whether they are man-made (Mandelbrot *et al.* 1984; Majumdar & Tien 1990) or natural (Thom *et al.* 2017). When put into contact with each other, two rough surfaces create a number of *micro-contacts* (or *junctions*) of various sizes at the interface, depending on the normal load and the amount of roughness (Greenwood & Williamson 1966). The *real contact area* is, for common loading conditions, a small fraction of the apparent area. In an unlubricated contact, the two surfaces only interact through these micro-contacts, so the friction and wear phenomena must initiate from those. Consequently, there is a need to characterize surface roughness and the contact between rough surfaces.

The most common ways of measuring surface roughness, used in industry, give a description of the surface roughness at only one length scale, which is usually the scale that can be directly affected by machining, and therefore that is the most relevant for engineers.

Let us consider a discretized surface of $n_x \times n_y$ points and size $L_x \times L_y$ (for example acquired experimentally), described by its height distribution $h(x_i, y_j)$, with $x_i = i\,L_x/n_x$, $i = 0, 1, \ldots, n_x - 1$ and $y_j = j\,L_y/n_y$, $j = 0, 1, \ldots, n_y - 1$. We also define the *mean* value of any discretized function $f(x_i, y_j)$ as

$$\langle f \rangle = \frac{1}{n_x n_y} \sum_{i=0}^{n_x-1} \sum_{j=0}^{n_y-1} f(x_i, y_j). \tag{1.3}$$

For a surface $h(x_i, y_j)$ with a mean height $\langle h \rangle = 0$, the *arithmetical mean deviation* is defined as

$$Sa = \langle |h| \rangle, \tag{1.4}$$

also called Ra. It is the measurement used through this manuscript to quantify roughness amplitude. Another way of characterizing the mean amplitude of roughness is the *root mean square* (RMS) *of heights*:

$$h_{\text{RMS}} = \sqrt{\langle h^2 \rangle}. \tag{1.5}$$

Alternatively, it is also possible to quantify the gradient of h, with the *RMS of slopes*:

$$h'_{\text{RMS}} = \sqrt{\langle |\nabla h|^2 \rangle}. \tag{1.6}$$

One significant drawback of these measurements is that they depend on the size of the measured sample. Measuring a smaller sample generally leads to a smaller roughness measurement. When performed at large scale, the measurements do not necessarily give a sense of the size of the smallest asperities, which play a major role in the mechanics of contact. There is a need to characterize roughness over multiple scales at once.

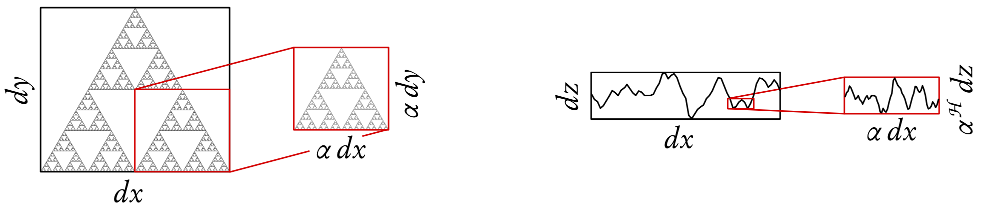

(a) Fractal: Sierpinski triangle

(b) Rough surface

Figure 1.2 – Geometrical interpretation of fractal dimension and Hurst exponent. (a) Fractals are *self-similar*. When scaled by a factor α, the *measure* of the fractal (quantifying its "mass") is scaled by $\alpha^{\mathcal{D}}$, where $\mathcal{D}$ is the fractal dimension. For the Sierpinski triangle shown here, $\mathcal{D} = \log_2(3) \approx 1.585$. (b) Rough surfaces can be modeled by *self-affine* surfaces. When looking at a portion of a size scaled by α, the heights are scaled by a factor $\alpha^{\mathcal{H}}$, where $\mathcal{H}$ is the Hurst exponent.

Hurst exponent

To study rough surfaces over multiple scales, we first need to define the concept of *fractal*. A fractal is an object whose structure is invariant by scaling. In other words, it displays a feature called *self-similarity*, meaning that a zoomed view on one part of the fractal will be *similar* to the whole. Fractals are usually described by their *fractal dimension* $\mathcal{D}$ (see Figure 1.2a). However, in the case of fractal surfaces (or lines) representing rough surfaces, it is easier to consider their *Hurst exponent* $\mathcal{H}$ because it can more easily be understood geometrically (Majumdar & Tien 1990), as shown in Figure 1.2b. Let us consider a rectangular portion of size $dx \times dy$ taken from a fractal surface with a Hurst exponent of $\mathcal{H}$. We call dz the size of its "features" (for example, a mean measurement of the heights). If we now look at a scaled portion of size $\alpha\, dx \times \alpha\, dy$, the features will have a size of $\alpha^{\mathcal{H}} dz$. For a value of $\mathcal{H} = 1$, the initial portion and the scaled potion will look the same, the surface is called *self-similar* in this case. For more general cases, if $0 < \mathcal{H} < 1$, the surface is called *self-affine*, and the vertical features of a scaled-up portion will look shorter. Besides, the Hurst exponent can be related to the fractal dimension, as $\mathcal{H} = 2 - \mathcal{D}$ for rough lines and $\mathcal{H} = 3 - \mathcal{D}$ for rough surfaces.

Self-affinity is a feature observed in real rough surfaces, for example in rocks (Thom *et al.* 2017) or artificial metallic surfaces (Mandelbrot *et al.* 1984; Majumdar & Tien 1990). The surfaces are self-affine over several orders of magnitude and display Hurst exponents usually comprised between $\mathcal{H} = 0.2$ and $\mathcal{H} = 0.8$. Anisotropy of the Hurst exponent can be observed at large scales, but isotropy is restored at smaller scales (Candela & Brodsky 2016). When the Hurst exponent changes across scales in this manner, we qualify the corresponding surfaces as *multi-affine*.

Spectral measurement of roughness

The computation of the Hurst exponent of a given surface, acquired experimentally or numerically generated, is done with the help of spectral analysis (Jacobs *et al.* 2017).

Let us consider a discretized line profile of n_x points and length L_x, described by its height distribution $h(x_i)$. The 1D *discrete Fourier transform* (DFT) of $h(x_i)$ is

$$\hat{h}(q_x) = \sum_{m=0}^{n_x-1} h(x_m)\, e^{-i q_x x_m} \tag{1.7}$$

where $q_x = 2k\pi/L_x$ is the *frequency*, and k is the *wavenumber* ranging from 0 to $\lceil N/2 \rceil$ if we do not consider the redundant periodic and symmetric regions of $\hat{h}(q_x)$. We also give the definition

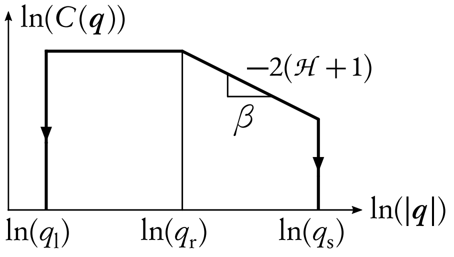

Figure 1.3 – Simplified power spectral density of a rough surface (in logarithmic scale). Its value is zero at frequencies $q < q_\mathrm{l}$ and $q > q_\mathrm{s}$. The slope β between q_r and q_s is related to the Hurst exponent $\mathcal{H}$. For 2D surfaces, the slope is $\beta = -2(\mathcal{H}+1)$ as represented, and for 1D lines, it is $\beta = -(2\mathcal{H}+1)$ instead.

of the *inverse discrete Fourier transform* (IDFT):

$$h(x_i) = \frac{1}{n_x} \sum_{k=0}^{n_x-1} \hat{h}(q_x) e^{i q_x x_i}, \quad q_x = k\frac{2\pi}{L_x}. \tag{1.8}$$

We now consider a discretized surface of $n_x \times n_y$ points and size $L_x \times L_y$, described by its height distribution $h(x_i, y_j)$. The 2D DFT $\hat{h}(q_x, q_y)$ of $h(x_i, y_j)$ is obtained by applying the 1D DFT (1.7) successively in the x and in the y direction.

The *power spectral density* (PSD) of a line or a surface is computed from the DFT of $h(\boldsymbol{x})$:

$$C(\boldsymbol{q}) = A\,|\hat{h}(\boldsymbol{q})|^2 \tag{1.9}$$

where A = L_x/n_x^2 in 1D and $A = L_x L_y / n_x^2 n_y^2$ in 2D. It is equivalently computed by taking the DFT of the autocorrelation of $h(\boldsymbol{x})$. For a 1D line, we obtain $C^{1\mathrm{D}}(q_x)$, which has units of [m^3]. For a 2D surface, we obtain $C^{2\mathrm{D}}(q_x, q_y)$, which has units of [m^4]. If $C^{2\mathrm{D}}$ is radially symmetric, it means that the surface is isotropic, and the PSD can be reduced to a 1D radial average $C^{\mathrm{iso}}(q)$, with $q = |\boldsymbol{q}|$. All the frequencies q_x, q_y and q have units of [1/m] (actually [rad/m]). It is also possible to compute 1D PSDs of a 2D surface by only taking the DFT along one direction and then taking the average along the other one. This maneuver can be used to detect an anisotropy of the surface by comparing a PSD along the x direction against a PSD along the y direction.

Before computing the PSD of a real surface, a window function has to be applied to $h(\boldsymbol{x})$ in order to not have an effect of the aperiodicity of the surface arising in the PSD. For example, a Hann window can be used. If working in 2D, the window has to be radially symmetric to not introduce artificial anisotropy.

The computed 1D PSD ($C^{1\mathrm{D}}$ or C^{iso}) can be used to find the Hurst exponent of a surface. Typical PSDs of natural rough surfaces have the form shown in Figure 1.3 (Yastrebov *et al.* 2015). They follow a *power-law*

$$C(\boldsymbol{q}) \propto q^{\beta} \tag{1.10}$$

in the higher frequencies q (or smaller *wavelengths* $\lambda = 2\pi/q$), characterizing the self-affine part of the surface. The slope β between the frequencies q_r and q_s is linked to the Hurst exponent, which is equal to $\mathcal{H} = -\beta/2 - 1$ for 2D surfaces, and to $\mathcal{H} = -\beta/2 - 0.5$ for 1D rough lines. The frequencies q_l, q_r, and q_s correspond respectively to the *longest* wavelength $\lambda_\mathrm{l} = 2\pi/q_\mathrm{l}$, the *roll-off* wavelength $\lambda_\mathrm{r} = 2\pi/q_\mathrm{r}$ and the *shortest* wavelength $\lambda_\mathrm{s} = 2\pi/q_\mathrm{s}$. For real surfaces, the longest wavelength is the scale at which the surface becomes macroscopically flat, and the shortest wavelength is linked to the size of the smallest asperities.

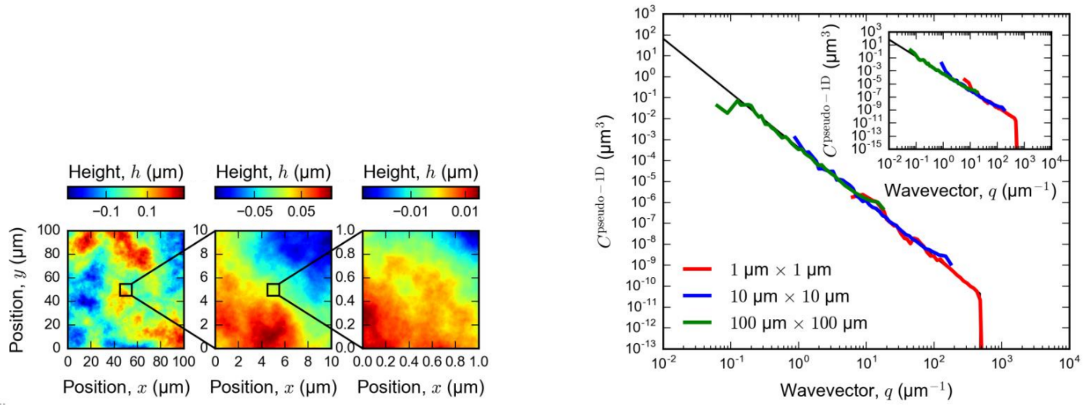

(a) Measurements at multiple scales

(b) PSD and fit

Figure 1.4 – Measuring the PSD of a rough surface, from Jacobs *et al.* (2017). (a) Topographic measurements are taken at multiple scales. (b) The resulting PSD curves span several orders of magnitude. In the case of a self-affine surface, a linear fit (in logarithmic scale) on the data gives the Hurst exponent.

A PSD curve of a real surface ranging multiple scales can be obtained by taking measurements of the surface at different scales, and then stitching the PSD curves obtained for each measurement, as shown in Figure 1.4. One must be careful about the artifacts that a measuring device can create on a PSD curve. For example, white noise will add a $1/q^2$ tail to the curve, which should not be interpreted as self-affinity of the surface. The measuring device can also introduce an artificial cutoff frequency q_s, for example the radius of an *atomic force microscopy* (AFM) tip.

The RMS measurements (h_{RMS} and h'_{RMS}) can actually be computed from the PSD of the surface by integrating it in a certain way (more details in Jacobs *et al.* (2017)). This is an indication that the PSD contains all the information about roughness that we need.

Computer-generated rough surfaces

A rough surface with a desired PSD (like the one shown in Figure 1.3) can be easily created by first generating a surface with random heights $h(x_i, y_j)$, computing its 2D PSD, scaling each of its component to match the desired PSD and finally revert to the spatial domain using the IDFT (1.8). The surface can additionally be rescaled to match a certain Sa, h_{RMS} or h'_{RMS}. Examples of such generated rough surfaces are shown in Figure 1.5. The rough surfaces can be generated for a chosen set of Hurst exponent, frequencies and RMS height or gradient. Usually, q_{r} is taken equal to q_{l} to not account for the plateau in the PSD. Also, λ_{s} (defining q_{s}) cannot be taken smaller than the discretization size of the surface.

Contact of rough surfaces

When two rough surfaces are put into contact with each other, only a fraction of the total apparent area is actually in contact, as Figure 1.6 demonstrates. Many techniques exist to relate the normal load F_{N} to the ratio A/A_0 between the real contact area A and the apparent contact area A_0, being analytical, numerical or experimental. An overview of these techniques is available in Müser *et al.* (2017). Overall, it is shown that for a small load, the ratio A/A_0 is roughly proportional to the load F_{N}, and that the coefficient of proportionality is related to the roughness of the surfaces (and their material properties). For larger loads, the relation becomes sub-linear as the ratio A/A_0 approaches 1.

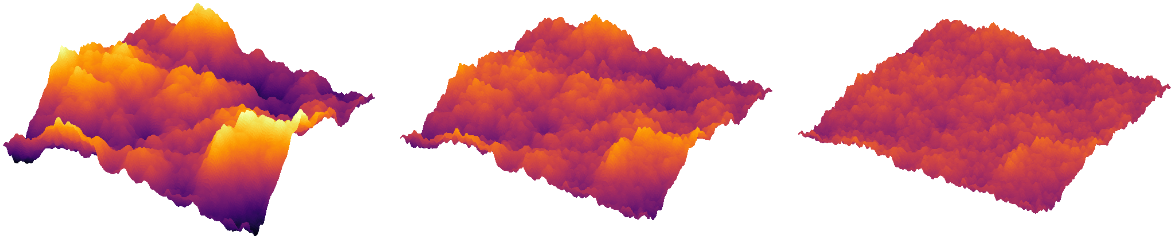

(a) $\mathcal{H} = 0.8$, $\lambda_\mathrm{l} = L$, $\lambda_\mathrm{s} = L/64$ (b) $\mathcal{H} = \mathbf{0.5}$, $\lambda_\mathrm{l} = L$, $\lambda_\mathrm{s} = L/64$ (c) $\mathcal{H} = \mathbf{0.2}$, $\lambda_\mathrm{l} = L$, $\lambda_\mathrm{s} = L/64$

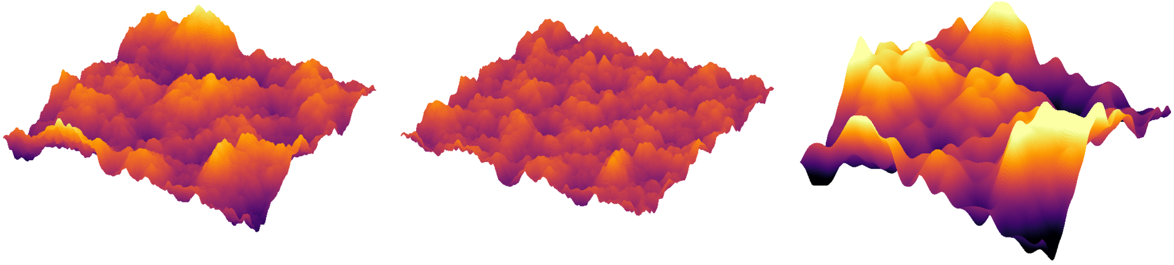

(d) $\mathcal{H} = 0.8$, $\lambda_\mathrm{l} = \boldsymbol{L/2}$, $\lambda_\mathrm{s} = L/64$ (e) $\mathcal{H} = 0.8$, $\lambda_\mathrm{l} = \boldsymbol{L/4}$, $\lambda_\mathrm{s} = L/64$ (f) $\mathcal{H} = 0.8$, $\lambda_\mathrm{l} = L$, $\lambda_\mathrm{s} = \boldsymbol{L/16}$

Figure 1.5 – Example of computer-generated rough surfaces. The parameters in common are $L_x = L_y = L = 1$, $n_x \times n_y = 512 \times 512$, and $h'_\mathrm{RMS} = 1.5$. In all cases, $\lambda_\mathrm{r} = \lambda_\mathrm{l}$. In (a), (b) and (c), only the Hurst exponent is varied, showing the behavior explained in Figure 1.2. In (a), (d) and (e), the largest wavelength λ_l is changed, showing that it controls the size of the largest undulations. Finally, in (a) and (f), only the smallest wavelength λ_s differs, displaying its effect on the smallest roughness components.

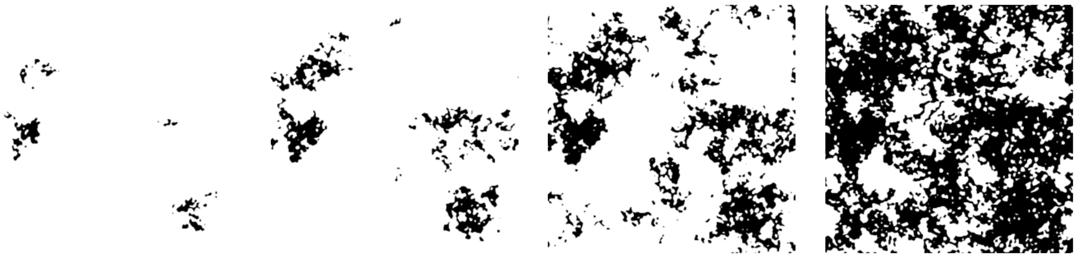

(a) $\frac{p_0}{E^*} = 0.01$, $\frac{A}{A_0} = 1.5\%$ (b) $\frac{p_0}{E^*} = 0.05$, $\frac{A}{A_0} = 7.0\%$ (c) $\frac{p_0}{E^*} = 0.15$, $\frac{A}{A_0} = 20.2\%$ (d) $\frac{p_0}{E^*} = 0.50$, $\frac{A}{A_0} = 56.5\%$

Figure 1.6 – Evolution of contact area with normal pressure. The figures were generated using our boundary element software Tamaas. The simulated rough surface has the same properties as the one shown in Figure 1.5a, with in particular $h'_\mathrm{RMS} = 1.5$. The contact zones are in black. p_0 is the applied normal pressure and E^* is an effective Young's modulus.

Analytical rough contact theories have been derived by considering the interaction of asperities and their statistical distribution on the surfaces (Persson 2006; Bush *et al.* 1975; Ciavarella 2016; Greenwood & Wu 2001). The validity of each model depends on the ranges of roughness parameters (Hyun *et al.* 2004). Still, all models share the same form in the linear range. For example, Bush *et al.* (1975) gives

$$\frac{A}{A_0} = \sqrt{2\pi}\frac{p_\mathrm{N}}{E^* h'_\mathrm{RMS}}, \tag{1.11}$$

where E^* is the equivalent Young's modulus, enclosing the elastic properties of both contacting surfaces:

$$\frac{1}{E^*} = \frac{1-\nu_1^2}{E_1} + \frac{1-\nu_2^2}{E_2}. \tag{1.12}$$

The constant $\sqrt{2\pi}$ in (1.11) varies between the analytical models.

The different numerical techniques presented by Müser *et al.* (2017) are the use of the *finite element method* (FEM), *boundary element method* (BEM) or *molecular dynamics* (MD). Both FEM and MD have the limitation that rough surfaces are very costly to simulate when having a good discretization, especially because a large part of the computational power has to be used for the simulation of the elastic bulk rather than the surfaces. BEM overcomes this limitation by only simulating the surfaces of the solids. Even if the typically used BE formulation is only valid for nominally flat surfaces (surfaces with small slopes), this description is well suited for macroscopically flat rough surfaces, making BEM the best candidate to study the contact between rough surfaces. Furthermore, the contact between two elastic rough surfaces with different Young's moduli is equivalent to the contact between a rigid rough surface and an elastic flat surface (Johnson *et al.* 1971), meaning that only one surface has to be simulated (which is also true for the FEM and MD).

The proportionality of the real contact area with the normal load can be directly related to the macroscopic laws of friction and wear (Coulomb's and Archard's), which both also show a proportionality with the normal load F_N. Regarding the case of friction, Bowden & Tabor (1966) directly linked the tangential sliding resistance to the real contact area and the *shear strength* of the junctions. To investigate the case of wear, we can similarly look at the individual junctions formed by *asperities* in contact.

1.1.3 *Wear at the scale of asperities*

Colliding asperities

Inspired by the theories of Rabinowicz (1958), the wear of a single junction was investigated using MD simulations, leading to a recent breakthrough by Aghababaei *et al.* (2016) in the modeling of adhesive wear. Aghababaei *et al.* looked at the behavior of two colliding asperities located on opposed surfaces under sliding motion, using 2D MD simulations of the setup shown in Figure 1.7a. At the size reachable by current MD simulations, real materials usually exhibit plastic behavior. The novel use of *coarse-grained* materials in the MD simulations allows to witness a transition between *plastic* and *brittle* behaviors: for a *junction size* d between the two asperities smaller than a *critical length scale* d^*, the asperities deform plastically and simply exchange some superficial atoms (Figure 1.7b), while for a junction size larger than d^*, a wear particle detaches from the surfaces (Figure 1.7c). The critical size d^* is found by comparing the *elastic energy* E_el stored by shearing the asperities with the *adhesive energy* E_ad needed to create the new fractured surfaces that lead to the formation of the wear particle. If $E_\mathrm{el} \geqslant E_\mathrm{ad}$, there is enough energy to create the new surfaces and

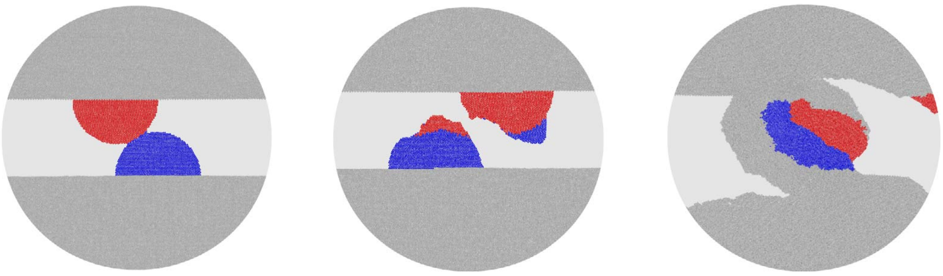

(a) Initial configuration (b) Plastic smoothing (c) Debris formation

Figure 1.7 – MD simulations of colliding asperities under shear, from Aghababaei *et al.* (2016). (a) The asperities and their junction have an overall size d. Depending on d, the two following outcomes are possible: (b) The asperities deform plastically and exchange superficial atoms; (c) A wear particle of size $\sim d$ is detached.

therefore form a particle, whereas if $E_{\mathrm{el}} < E_{\mathrm{ad}}$, new surfaces cannot be created and the asperities can only plastically deform. The expression of the critical size found by Aghababaei *et al.* is

$$d^* = \Lambda \frac{2\gamma G}{\sigma_{\mathrm{j}}^2} \tag{1.13}$$

where Λ is a *geometrical factor* of the order of unity ($\Lambda = 8/\pi$ in the 2D case of protruding asperities), γ is the *surface energy* of the material, G is the *shear modulus* and σ_{j} is the *shear strength* of the junction. We can note that d^* depends mainly on the material properties and not the geometry (considering the fact that $\Lambda \simeq 1$). The expression of d^* was later extended (Brink & Molinari 2019) to take into account a weakened and tilted interface between the joined asperities, resulting in a correction of the term σ_{j}. A distinction is made between having slip or plastic deformations at the junction, but since we are mainly interested in cases of debris formation, we will not consider the two regimes separately here. Another study (Milanese *et al.* 2020) showed that the surface morphology also affects the minimum wear particle size, and that interfacial adhesion impacts the wear rate.

The transition between a case where surfaces only plastically smoothen and a case where a wear particle is formed can be related to the macroscopic manifestations of low wear and mild wear. For light normal loads, we expect to have a small real contact area between macroscopic surfaces, meaning that the junction sizes would be small, resulting in no formation of wear particles. For higher loads, the junction sizes will eventually grow bigger than d^*, resulting in the formation of wear particles, namely wear.

Subsequent MD simulations permitted to link the wear volume created via adhesive wear to the sliding work (Aghababaei *et al.* 2017) and the sliding distance (Zhao & Aghababaei 2020) as in Archard's wear model. These relations are only accurate near the plastic regime, when asperities have a size of the order of d^* (Aghababaei & Zhao 2021).

From asperities to rough surfaces

Having acquired some understanding of the wear process at the single-asperity level, attempts were made to go toward larger scales. Frérot *et al.* (2018) used BEM to numerically simulate the contact between two rough surfaces and obtain a map of the micro-contacts. Each micro-contact size is compared to d^* to assess if it can result in the formation of a wear particle. Ultimately, an instantaneous wear coefficient is estimated. However, relying only on d^* leads to a contradiction: the predicted wear volume increases with the material's hardness, which is opposite to what is

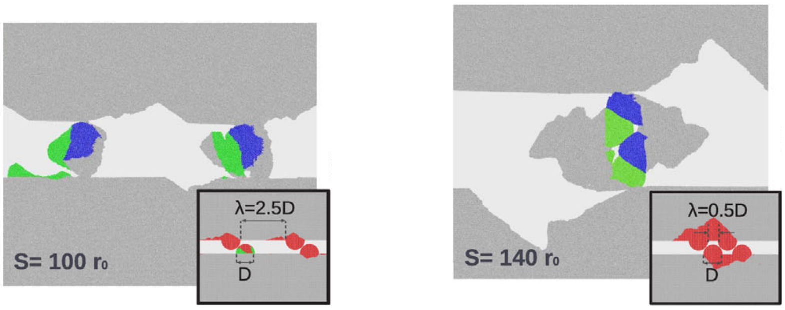

(a) Separate wear particles formation

(b) Combined wear particle formation

Figure 1.8 – MD simulations of two pairs of colliding asperities under shear, from Aghababaei *et al.* (2018). The insets show the initial configurations. The asperities and their junctions have an overall size $d \geqslant d^*$; the space between the pairs is λ. Depending on λ, the two following outcomes are possible: (a) Each pair of asperities creates a wear particle of size d; (b) A combined wear particle of size $d_a = 2d + \lambda$ is detached.

experimentally observed and summarized by Archard's wear model, predicting a wear rate inversely proportional to the hardness. Brink *et al.* (2021) followed the same principle as Frérot *et al.* but added the notion of sliding distance to compute a wear volume over time and get over the hardness inconsistency. These models give promising results, successfully upscaling the transition between the low and mild wear regimes, but they fail to show a clear transition toward a severe wear regime. They assume that each micro-contact can only form a wear particle by itself, and no potential interactions are considered. Somehow, one ingredient seems to be missing.

Interaction of multiple pairs of colliding asperities

Independently of upscaling attempts, a recent work (Aghababaei *et al.* 2018) has studied how two pairs of colliding asperities interact (see insets in Figure 1.8), with each pair having a junction size $d \geqslant d^*$; meaning that each junction can result in the formation of a wear particle under shear. It was shown using 2D MD simulations that when the distance λ between the pairs of asperities is large, each pair of colliding asperities forms its own wear particle of diameter d (Figure 1.8a). However, when λ is smaller than approximately d, a single (larger) wear particle combining the two pairs of asperities is formed with an effective diameter of $d_a = 2d + \lambda$ (Figure 1.8b).

This change of behavior can be an explanation for the transition from mild wear to severe wear regime at large normal loads, observed at the macroscopic scale, with an increase of the wear coefficient. Fracture mechanics were put forward to rationalize the transition (Aghababaei *et al.* 2018). The stress intensity factors K_I of mode I fracture have been analyzed at the corners of each asperity, revealing a mechanism of crack shielding when the pairs of asperities are put closer together, preventing the formation of separate wear particles. Crack shielding mechanisms were later confirmed in the context of finite-element simulations with a phase-field approach to fracture (Collet *et al.* 2020). Even though physical insight has been acquired, no theoretical prediction was given for the critical interaction distance λ, and the influence of the asperities' size d compared to d^* has not been studied systematically. To this end, the existence of elastic interactions could be exploited, as even without the presence of cracks, it is known that multiple neighboring asperities interact elastically over long distances (Block & Keer 2008; Komvopoulos & Choi 1992). It remains to be seen what happens in more complex situations involving many potentially interacting nearby micro-contacts, that typically appear in rough contacts.

Evolution of surfaces and third bodies

All simulations presented until here regarding the wear of asperities only looked at the initiation of wear, up to the detachment of wear particles. In the upscaling attempt of Brink *et al.* (2021), the wear particles are discarded when they are fully detached, to not make strong assumptions on their evolutionary behavior. Still, the presence of wear particles trapped in an interface must have a strong effect on its tribological properties. How wear particles and surfaces in contact evolve over time was studied separately.

Milanese *et al.* (2019) showed using MD simulations that, at the nanoscale, two rough surfaces sliding on each other evolve toward self-affine surfaces with properties independent of the initial roughness profiles. Another feature of these nanoscale simulations is the apparition of a rolling third-body particle, which seems to be a key ingredient in the evolution of the surface roughness to self-affine characteristics. The growth of the rolling third body particle was also investigated analytically (Milanese & Molinari 2020).

The behavior of multiple third-body particles trapped between two sliding surfaces was later studied by Brink *et al.* (2022) using 3D MD simulations. The particles are shown to grow into rolling cylinders, which have low sliding resistance. The cylinders then agglomerate, increasing the tangential resistance. This type of simulation is a rich source of insights, but their computational cost is very high, due to spatial and temporal scales being large for MD simulations.

In both cases, the systems are dynamically evolving. Monitoring this evolution at this scale and larger ones will be crucial for correctly quantifying friction and wear over time.

1.2 OBJECTIVES

Wear involves many phenomena, such as adhesion, abrasion, lubrication, and corrosion. This whole family of processes cannot be reasonably explored in a single thesis. Therefore, we focus solely on *unlubricated adhesive wear*. Even in this form, we saw that wear can be classified into multiple experimentally observed regimes: *low*, *mild*, and *severe*. Through the years, contact mechanics and wear were approached at multiple scales (see Figure 1.9). The *macroscale* is where surfaces can look smooth. It is our everyday scale. Then, we call *mesoscale* the range of scales where roughness is visible, originating from ancient Greek μέσος (*mesos*) for "middle". For most engineering applications, the size of roughness is under 100 µm, whereas in geology, it can be witnessed at a much larger scale. Finally, the scale of the smallest asperities is the *nanoscale*.[1] On the basis of the state of research about adhesive wear modeling, the main objective of this thesis is

---

[1] In the case of metals or ceramics, we can expect an asperity size of the scale of a few nanometers. As a recall, the size of a single atom is around 0.1 nm = 1 Å.

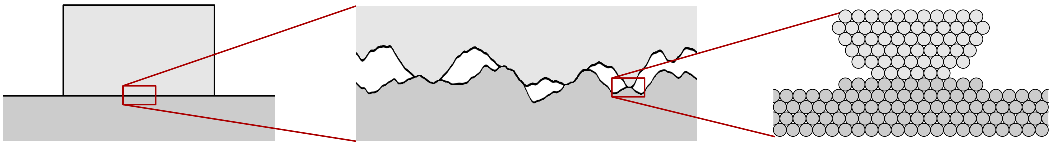
(a) Macroscale (b) Mesoscale (c) Nanoscale

Figure 1.9 – Multiscale view of a macroscopically flat interface. (a) Macroscopic scale: the surfaces are flat, no roughness is visible. (b) Mesoscale: the surfaces are rough over multiple levels of zoom (fractal). (c) Nanoscale: single asperity. Atoms may be visible the following:

Fundamental understanding of wear Acquire a physical grasp of unlubricated adhesive wear from the nanoscale, and establish a link with the expected behaviors at larger scales.

This principal objective can be broken down into several sub-objectives:

Interaction of micro-contacts The wear behavior of a single micro-contact (at the nanoscale) is known. An analytical theory of wear must be formulated for several micro-contacts susceptible of interacting, in order to formalize the emergence of a severe wear regime at the nanoscale. At the mesoscale, rough contacts innately create many clustered micro-contacts, prone to interaction. The investigation of the emergence of severe wear for rough surfaces should naturally follow.

Upscaling All knowledge acquired at the nanoscale, either with analytical or numerical models, must be cast into larger scales. As MD has been shown to reach a computational limit, other numerical methods could be used or developed.

Time evolution As the tribological properties of an interface depend strongly on its geometry (*e.g.* the surface roughness), how this geometry evolves during sliding and whether it reaches a predictable (maybe steady) state must be investigated.

All of the objectives above can be addressed with numerical simulations. Ideally, the resulting models must be applicable to any geometry and material. To give the simulations a practical backing, experiments can be conducted on realistic materials. In this regard, silicon (Si) is a material of choice. It is highly used in the industry, both in mechanics and electronics, and it is also fairly easily simulated using MD, making it an ideal candidate material for our studies. Silicon is a very brittle material that cannot be used as is in its crystalline form for mechanical applications. To mitigate this effect, a thin oxide layer can be grown at the surface of the material (Lai *et al.* 1994), forming a layer of silica (or silicon oxide, SiO_2) by diffusion of oxygen atoms into the surface (Bongiorno & Pasquarello 2002). A more practical objective follows, which is to define how the presence of an oxide layer on interacting pieces of silicon affects their tribological behavior (friction and wear), and to assess the impact of the oxide layer's thickness. Naturally, the objectives stated above can also be addressed with experiments.

1.3 APPROACH

This thesis follows a bottom-up approach, starting from the identification of processes at the scale of asperities, the nanoscale, all the way up to the macroscale.

The nanoscale study of the interaction of micro-contacts is conducted by analytical means, to obtain theoretical predictions, and by using MD simulations, to challenge the predictions. The theory is formulated following the principles laid by Rabinowicz (1958) and Aghababaei *et al.* (2016) by calculating the effect of elastic interactions between multiple junctions on the energy stored by the system under shear, energy available for the creation of wear particles. The MD simulations use the same numerical models as Aghababaei *et al.* to observe the ductile-brittle transition in a fictitious material at a scale reasonable for MD simulations.

At the mesoscale, BEM is used to compute the contact between rough surfaces. From the quantities computed by a BE solver, it is possible to apply the wear principles uncovered at the nanoscale to see their effect on a rough contact, where many micro-contacts susceptible to interact are formed. BEM can also be used at the macroscale by not directly modeling surface roughness, and instead hiding the concepts of roughness and real contact area in field variables. The issue of going for BEM at larger scales is that mechanisms inherently captured by MD, like yield and fracture, are not easily reproduced in BE models. The models obtained with BEM are either static or must include strong assumptions about the formation and evolution of third-body to model dynamic effects. One way of getting around this problem is by using another method for upscaling. To this end, a discrete element (DE) model is formulated to coarse-grain the MD simulations, by merging groups of atoms into larger particles with similar mass and interaction properties, lowering drastically the computational cost of the numerical simulations.

To complement and ground numerical simulations, studying the evolution of tribological systems is also done experimentally at all scales, although with some limitations for the smallest ones. Wear initiation and evolution are observable by optical means, but for a more precise evaluation, the DE model is also used at the nanoscale and up.

Experiments are performed on the silicon samples to measure the effects of the presence of an oxide layer. This approach is backed up by quantitative MD simulations of the materials of interest (Si and SiO_2) at the nanoscale, and BEM simulations at the macroscale.

1.4 OUTLINE

The chapters of this manuscript are organized into three parts. Each section is briefly described below. In the first part, which includes this introductory chapter, the framework of the thesis is presented.

Chapter 2 The numerical methods used during this thesis are presented, namely: molecular dynamics (MD), the discrete element method (DEM), and the boundary element method (BEM).

The second part focuses on the formulation of analytical theories, numerical results, and the development of new numerical models.

Chapter 3 A 2D theoretical model is formulated to predict whether multiple nearby micro-contacts deform plastically, create separated small wear particles under shear, or merge into a single larger wear particle, formalizing the emergence of the three macroscopic wear regimes at the nanoscale. The model is then verified using BEM (in static configurations) and MD simulations (dynamical).

Chapter 4 The theoretical model formulated in the previous chapter is extended to the third dimension to investigate the case of two interacting circular junctions. The analytical problems found in 2D (*e.g.* infinite energy of deformation) are automatically fixed in 3D. A *wear map* is produced from the analytical model, linking the geometrical configuration and material properties to the expected wear behavior of the system.

Chapter 5 This chapter is a natural continuation of the previous one. The analytical model is implemented into a numerical BE model. After verifying that both the analytical and numerical models yield the same results for two micro-contacts, the numerical model is applied to rough surfaces. Wear maps predicting the three different wear regimes are computed.

Chapter 6 To tackle dynamically evolving systems, a coarse-grained DE model is developed, having cohesive forces between the particles to model fracture and reattachment of matter, like in MD. The inter-particular forces are tuned to match target elastic and fracture properties. The model is shown to replicate the adhesive wear mechanisms at the nanoscale.

Chapter 7 Three short DEM studies are carried in this chapter. In the first one, a link between nanoscale and macroscale strengths is found. In the second study, the wear of rough surfaces at different scales is investigated. Finally, in the last study, the transition between two frictional regimes (caused by the presence of wear particles) is explored.

In the final part, experimental campaigns are presented, along with some numerical models supporting the observations.

Chapter 8 *Pin-on-disc* experiments are run on SiO_2 samples. We show how surface roughness is created from flat surfaces, starting with the creation of wear particles at the scale of asperities, which are merging into a rough third-body layer. We demonstrate that, for the explored range of loading conditions, the surface roughness evolves toward a common steady state regardless of the initial surface roughness.

Chapter 9 The same experiments as in the previous chapter are performed on Si samples, comprising of an SiO_2 oxide layer of variable thickness. The effect of the oxide layer on the friction coefficient and the wear volumes is uncovered. To explain the observed behaviors, MD simulations are employed to identify the properties of Si and SiO_2 having a tribological interest, followed by macroscale BEM simulations taking into account the evolution of surfaces.

Material developed during the thesis, but not used in the remaining chapters, is presented in the Appendix.

Appendix A In this section, a BEM contact solver with friction is described. While not being used in the other parts of this thesis, it can prove useful for future works related to this one.

The manuscript is concluded by a summary of the main results and a discussion of the potential future works that can be carried out on the basis of this thesis.

CHAPTER 2

NUMERICAL METHODS

In this chapter, the various numerical methods used throughout the whole thesis are presented. They are: molecular dynamics (MD), the discrete element method (DEM), and the boundary element method (BEM). We do not aim to present a full course on each subject, but rather to give just enough information so that the reader could, in principle, be able to implement a rudimentary version of each method.

2.1 MOLECULAR DYNAMICS

2.1.1 *General principles*

The first chapters of Rapaport (2004) give a nice introduction to MD. In the simplest forms of MD systems, each atom is represented as a point particle, having a position $\boldsymbol{x}_i$ in 2D or 3D,[1] and a mass m_i. The way of describing the interaction between the atoms is via interatomic forces or interatomic potentials. The best known pair potential is the *Lennard-Jones* (LJ) potential. For a pair of atoms i and j, having the respective positions $\boldsymbol{x}_i$ and $\boldsymbol{x}_j$, the potential energy is

$$U(r_{ij}) = \begin{cases} 4\varepsilon\left[\left(\frac{\sigma}{r_{ij}}\right)^{12} - \left(\frac{\sigma}{r_{ij}}\right)^{6}\right] & \text{if } r_{ij} < r_\mathrm{c}, \\ 0 & \text{otherwise,} \end{cases} \tag{2.1}$$

where $r_{ij} = ||\boldsymbol{x}_i - \boldsymbol{x}_j||$ is the interatomic distance, r_c is a cutoff distance, ε is a parameter governing the strength of the interaction, and σ is defining a length scale. A minimum is reached at $r_{ij} = 2^{1/6}\sigma \approx 1.22\,\sigma$. At close range, the resulting force is repulsive, and attractive at high range, dropping to zero above the cutoff distance. The interatomic force is obtained by deriving the potential:

$$\boldsymbol{F}_{ij} = -\nabla U_{ij}(r_{ij}). \tag{2.2}$$

The force acting on each atom is the sum of all the pair forces acting on this atom, which obeys Newton's second law:

$$m_i \ddot{\boldsymbol{x}}_i = \boldsymbol{F}_i = \sum_{\substack{j=1 \\ j \neq i}}^{N} \boldsymbol{F}_{ij}, \tag{2.3}$$

---

[1] In more complex systems considering dipolar particles, they would have additional rotational degrees of freedom.

where N is the number of atoms. To numerically simulate a system governed by these equations of motion, we must resort to a numerical integration method. A popular method is the second-order *leapfrog* method (also called *central difference scheme*), which has good energy conservation properties, despite its low order. The scheme is the following:

$$v_i\left(t+\frac{\Delta t}{2}\right)=v_i\left(t-\frac{\Delta t}{2}\right)+\frac{F_i}{m_i}\Delta t\,, \tag{2.4a}$$

$$x_i(t+\Delta t)=x_i(t)+v_i\left(t+\frac{\Delta t}{2}\right)\Delta t\,, \tag{2.4b}$$

where Δt is the integration time step. The name "leapfrog" comes from having the velocities computed at time steps in-between the positions. The velocity at time t can be obtained by updating the velocity by only half a time step:

$$v_i(t)=v_i\left(t-\frac{\Delta t}{2}\right)+\frac{F_i}{m_i}\frac{\Delta t}{2}\,. \tag{2.5}$$

During this thesis, we used the open source software LAMMPS (Plimpton 1995), which relies on the *velocity-Verlet* method:

$$v_i\left(t+\frac{\Delta t}{2}\right)=v_i(t)+\frac{F_i(t)}{m_i}\frac{\Delta t}{2}\,, \tag{2.6a}$$

$$x_i(t+\Delta t)=x_i(t)+v_i\left(t+\frac{\Delta t}{2}\right)\Delta t\,, \tag{2.6b}$$

$$v_i(t+\Delta t)=v_i\left(t+\frac{\Delta t}{2}\right)+\frac{F_i(t+\Delta t)}{m_i}\frac{\Delta t}{2}\,. \tag{2.6c}$$

It only differs from the leapfrog method in the instants where the velocities are stored (t and $t+\Delta t$), otherwise being strictly equivalent. Note that the *future* force term $F_i(t+\Delta t)$ in (2.6c) depends on the updated position $x_i(t+\Delta t)$, obtained from (2.6b). In the presence of velocity-dependent forces (for example velocity damping), the future force term shoud in principle also depend on the future velocity $v_i(t+\Delta t)$, which is not yet available. To keep the computation *explicit* (not needing the solving of implicit equations), this velocity term can be replaced by the already computed intermediate velocity $v_i(t+\Delta t/2)$ in the evaluation of $F_i(t+\Delta t)$. Thit is the solution opted by LAMMPS.

2.1.2 *Computable quantities*

Energy

The total kinetic energy K of the system is obtained by simply summing the contribution of each atom:

$$K=\frac{1}{2}\sum_{i=1}^{N}m_i v_i^2\,. \tag{2.7}$$

From the expression of the force potential (*e.g.* (2.1)), one can also compute the total potential energy of the system.

Temperature

The absolute temperature $\mathcal{T}$ of the system is directly linked to its kinetic energy. Each translational degree of freedom contributes by $k_\mathrm{B}\mathcal{T}/2$ to the kinetic energy on average, where k_B is the

Boltzmann constant. For a three-dimensional system, where each atom has 3 translational degrees of freedom, the total kinetic energy is therefore

$$K = \frac{3Nk_\mathrm{B}\mathcal{T}}{2}, \tag{2.8}$$

and the temperature can be expressed as a function of the kinetic energy:

$$\mathcal{T} = \frac{2K}{3Nk_\mathrm{B}}. \tag{2.9}$$

Following these expressions, it is possible to initialize a system with a given temperature by randomly assigning initial velocities to the atoms, such that the total kinetic energy matches the desired temperature.

The MD systems simulated throughout this thesis are prone to have local heating due to large localized deformations. In a real system, the temperature would dissipate in the rest of the body, but MD simulations are limited in size. To prevent heat from building up, *thermostats* can be added at the simulation's borders to regulate the temperature. For example, a *Langevin thermostat* (Schneider & Stoll 1978) adds to each atom a damping force

$$\boldsymbol{F}_\mathrm{d} = -\frac{m_i \boldsymbol{v}_i}{c} \tag{2.10}$$

and a force in a random direction

$$F_\mathrm{r} \propto \sqrt{\frac{k_\mathrm{B} T m_i}{c\,\Delta t}}, \tag{2.11}$$

where c is a damping coefficient. This thermostat is the one used in the MD simulations of this thesis.

Stress

A stress tensor can be computed for each atom by factoring the interactions it has with its neighbors. The *virial stress* is a commonly used measure. For an atom of index i, each of its components are defined as

$$\sigma_{ab} = -m(v_{i_a} - \bar{v}_a)(v_{i_b} - \bar{v}_b) + \sum_{j}^{N_\mathrm{n}} (x_{j_a} - x_{i_a}) F_{ij_b} \tag{2.12}$$

where a and b can be the directions x, y or z, $\bar{\boldsymbol{v}}$ is the average velocity, N_n is the number of interacting neighbors, and $\boldsymbol{F}_{ij}$ is the force acting between atoms i and j. The left hand term is the kinetic energy contribution.

Strain

In this thesis, the open source software OVITO (Stukowski 2009) is used to visualize the outputs of MD simulations. In this program, the atomic strain can be computed between a *current* (deformed) configuration and a *reference* (initial) configuration. From the initial and current positions $\boldsymbol{x}_0$ and $\boldsymbol{x}$ of each atom, the atomic *deformation gradient tensor*

$$\boldsymbol{F} = \frac{\partial \boldsymbol{x}}{\partial \boldsymbol{x}_0} \tag{2.13}$$

is computed by averaging the relative motion of neighboring particles around each atom up to a cutoff distance. From $\boldsymbol{F}$, the atomic *Green-Lagrange strain tensor*

$$\boldsymbol{E} = \frac{1}{2}\left(\boldsymbol{F}^\top \boldsymbol{F} - \boldsymbol{I}\right) \tag{2.14}$$

is computed, which can be decomposed into a shear component and a hydrostatic component. Looking at strain distributions can help distinguish between ductile and fragile damage processes, as the fragile case will have more localized strains (where cracks are formed).

2.1.3 *Silicon and silica*

Silicon

Silicon (Si) is known to have an atomic structure which is not fully captured by the widely used LJ pair potentials when working with MD. As for carbon atoms in diamond, silicon atoms arrange into a diamond-like structure, where each atom has four neighbors arranged at the corners of a tetrahedron. Using a pair potential like LJ, each atom can get surrounded by up to 12 neighbors, leading to the incorrect structure. A potential modeling three-body interactions must be considered to account for angles of the bonds, which is achieved for example by the *Stilinger-Weber* (SW) potential (Stillinger & Weber 1985; Stillinger & Weber 1986). Silicon is also known to exist in an amorphous state, that is also well reproduced using the same SW potential (Vink *et al.* 2001). In this thesis, we use the potential parameters given in the original papers, which are shown to give quantitatively acceptable properties for both the diamond-structure crystalline phase and the liquid amorphous phase.

Silica

Silica (SiO_2) can take many stable atomic configurations at usual working conditions, both crystalline or amorphous (Vashishta *et al.* 1990). A layer of oxide grown on an initial sample of silicon is known to have an amorphous configuration. We use the potential by Vashishta *et al.* (1990), which is capable of simulating both crystalline and amorphous forms of silica, taking into account three-body interactions and the presence of two types of atoms (oxygen and silicon). A cutoff parameter of $r_c = 8\,\text{Å}$ is used in place of the one given in the original paper (Luo *et al.* 2016). Other potentials exist to model silica more accurately (*e.g.* Sarnthein *et al.* (1995), an *ab-initio* model), but they are computationally costly.

We are interested in modeling silica in its amorphous state. Initializing a system comprising of atoms arranged in an amorphous fashion is not trivial. To do so, we follow the procedure of Luo *et al.* (2016), starting from a β-crystobalite structure. The system is heated and cooled by equilibrating it for 90000 time steps of 0.5 fs at 5000, 4000, 3000, 2500, 2000, 1500, 1000, 500 and 300 K, with cooling periods with a rate of 166 K/ps between each constant temperature step, except when going to 300 K where a rate of 13 K/ps is used. The pressure is always kept at 0 using a Berendsen barostat. The isotropic material properties of the obtained material at 0 K are $E = 120\,\text{GPa}$, $\nu = 0.22$ and $G = 49\,\text{GPa}$. One sample of $100 \times 100 \times 100\,\text{nm}^3$ was created this way, for it to be used in subsequent simulations involving silica.

Material properties

The known material properties of silicon and silica at room temperature are given in Table 2.1. Since silicon is crystalline, the given properties are either averages or the most critical regarding failure. Being of main interest for tribology, the *ideal strengths* were sought. They are the strength measured at small scale, when no defects are present in the materials (which would decrease the measured strength).

Finally, in order to not get confused with the name of the materials, we will refer to silicon and silica as Si and SiO_2 in the remainder of this document. For readers speaking other languages

Table 2.1 – Material properties of silicon (Si) and silica (SiO_2). For silicon, taken in its crystalline state, some values are averaged or taken in one specific direction. Silica is taken as amorphous. ρ is the density, γ the surface energy, $\sigma_{m,N}$ the ideal tensile strength, and $\sigma_{m,T}$ the ideal shear strength.

Material	E [GPa]	ν [-]	ρ [kg/m³]	γ [N/m]	$\sigma_{m,N}$ [GPa]	$\sigma_{m,T}$ [GPa]
Silicon	150[1]	0.27[1]	2330	1.2[2]	21[3]	11[3]
Silica	73	0.17	2200	1.5	16[4]	9[5]

[1] From Hopcroft *et al.* (2010). Values averaged from multiple directions.
[2] From Jaccodine (1963). Taken in the {111} direction, where it is the smallest compared to other directions.
[3] From Dubois *et al.* (2006). Also taken in the {111} direction for the same reason as above.
[4] From Luo *et al.* (2016).
[5] Estimated using von Mises yield theory (assuming SiO_2 is ductile at small scale, where the ideal strength is measured) to be smaller than the tensile strength by a ratio of $1/\sqrt{3} \approx 0.577$.

Table 2.2 – Silicon and silica names in various languages

	Si	SiO_2	Some celebrities
English	silicon	silica	silicone
Français	silicium	silice	silicone
Deutsch	Silicium	Siliziumoxid	Silikone
Italiano	silicio	silice	siliconi

than the one used to write these lines, you may find useful to refer to Table 2.2 for translations.

2.2 DISCRETE ELEMENT METHOD

DEM is similar to MD in the sense that both methods deal with systems made of particles. The main difference between MD and DEM is that DE particles have a finite size, with three additional rotational degrees of freedom, for a total of six (instead of three).

In their simplest and original form (Cundall & Strack 1979), DE particles are often modeled with normal and tangential springs acting at the contact points between the particles (see Figure 2.1), along with some velocity damping forces. It is also common to replace the linear contact spring by a non-linear Hertzian force, analytically derived for modeling contact between spheres.

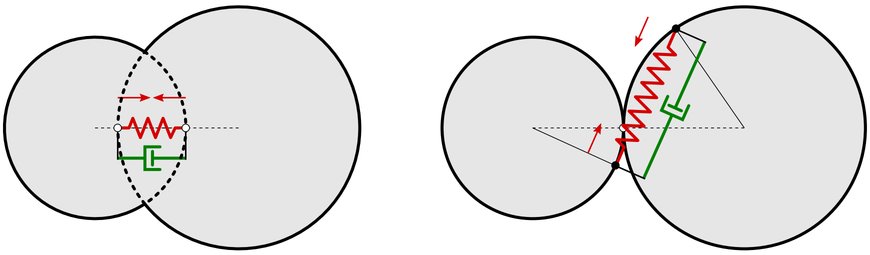

(a) Normal spring (b) Tangential spring

Figure 2.1 – Simple contact in the discrete element method. Each spring can be complemented with a dampener. (a) The particles repel when they interpenetrate. (b) The spring resists against relative tangential motion, which depends on the history of the rotations of the particles.

DEM is a popular method to model the flow of granular media in general, and in particular rocks and gouge in geomechanics (Pande *et al.* 1990). It is also used to model third-body rheology (Fillot *et al.* 2005; Fillot *et al.* 2007), while including other physical effects (*e.g.* thermal in Renouf *et al.* (2011)). The discrete particles are commonly modeled with breakable bonds (Cundall 1971) to represent crushable material. To the best of our knowledge, damage is most often irreversible in DE models modeling plasticity (Nguyen *et al.* 2017), fatigue or fracture (Nguyen *et al.* 2019), and the reattachment of matter is not considered. The particles can be modeled with adhesive/cohesive forces such as JKR (Johnson *et al.* 1971), but the resulting systems made of many particles have elastic properties which are dependent on a confinement pressure and are challenging to predict (Cheng *et al.* 2020; Voisin–Leprince *et al.* 2022).

DEM is also (less commonly) used to model continuum media. However, the link between the particles' interaction properties and the macroscopic elastic properties of the assembly of particles is not straightforward when simple spring forces are used between the particles (Hentz *et al.* 2004; Jerier & Molinari 2012). To exactly match some desired elastic properties, the forces between particles must take into account the neighborhood of each particle (Celigueta *et al.* 2017), making their formulation more complex. Capturing the Poisson's effects is also shown to be challenging using only linear spring forces. Alternatively, spring forces can be replaced by deformable beam elements (Leclerc *et al.* 2017), and even non-spherical particles filling the whole space can be considered (André *et al.* 2019).

We can apply on DEM simulations what is called the *coarse-graining* procedure. It is typically used in the modeling of granular flows (Queteschiner *et al.* 2018; Kanjilal & Schneiderbauer 2021; De *et al.* 2022), possibly coupled with fluids (Jiang *et al.* 2021; Lehuen *et al.* 2020). Multiple small particles are substituted by a larger particle by following principles of scaling similarity (conservation of mass, energy and forces). Some coarse-graining formulations involve dynamically refining or coarsening crucial parts of a system (Queteschiner *et al.* 2018; De *et al.* 2022). It is naturally possible to have multiple coarse-graining ratios in one simulation, which can prove useful when modeling poly-disperse systems (Kanjilal & Schneiderbauer 2021).

2.2.1 *Simulation*

As for MD, the DE systems are also updated using the velocity-Verlet method in LAMMPS. For any given particle, the integration scheme between steps n and $n+1$ can be summarized as

$$\boldsymbol{x}_{n+1} = \boldsymbol{x}_n + \boldsymbol{v}_n \Delta t + \frac{\boldsymbol{F}_n}{m}\frac{\Delta t^2}{2}, \tag{2.15a}$$

$$\boldsymbol{v}_{n+1} = \boldsymbol{v}_n + \frac{\boldsymbol{F}_n + \boldsymbol{F}_{n+1}}{2m}\Delta t, \tag{2.15b}$$

$$\boldsymbol{\omega}_{n+1} = \boldsymbol{\omega}_n + \frac{\boldsymbol{T}_n + \boldsymbol{T}_{n+1}}{2I}\Delta t, \tag{2.15c}$$

where $\boldsymbol{x}_n$, $\boldsymbol{v}_n$ and $\boldsymbol{\omega}_n$ are respectively the position, the velocity and the angular velocity of the particle, $\boldsymbol{F}_n$ and $\boldsymbol{T}_n$ are the force and the torque acting on the particle at step n, m is the mass of the particle, and I is its moment of inertia. This scheme is equivalent to the commonly used central difference scheme (Cundall & Strack 1979). In order for the simulation to be numerically stable, we must define a critical time step.

2.2.2 *Critical time step*

Let us consider a system of two particles of radii r_i and r_j, interacting in linear Hookean regime with a stiffness k_N and a velocity damping c_N. We only consider normal relative motion, so that the system can be reduced to only one dimension. The dynamical equations of the system are:

$$m_i \ddot{x}_i + c_\mathrm{N}(\dot{x}_i - \dot{x}_j) + k_\mathrm{N}(x_i - x_j) = 0\,, \tag{2.16a}$$

$$m_j \ddot{x}_j + c_\mathrm{N}(\dot{x}_j - \dot{x}_i) + k_\mathrm{N}(x_j - x_i) = 0\,. \tag{2.16b}$$

Both equations can be combined into one by subtracting one to the other and taking $x = x_i - x_j$ as the new variable:

$$m_\mathrm{eff}\ddot{x} + c_\mathrm{N}\dot{x} + k_\mathrm{N}x = 0\,, \tag{2.17}$$

where m_eff is the effective mass of the system:

$$m_\mathrm{eff} = \frac{m_i m_j}{m_i + m_j}\,. \tag{2.18}$$

In DEM simulations, it is usual to choose a time step proportional to $\sqrt{m/k_\mathrm{N}}$, with a safety factor that ensures stability (Burns *et al.* 2019). The exact expression of the critical time step guarantying stability was derived for the central difference scheme (O'Sullivan & Bray 2004). For completeness, we present a derivation for the velocity-Verlet scheme we are using.

To compute the critical time step of the system, numerically integrated using equations (2.15), we can drop the velocity damping force[2] so that the remaining force is simply $F = -k_\mathrm{N}x$. The one dimensional integration scheme becomes

$$x_{n+1} = x_n + v_n\,\Delta t - \frac{k_\mathrm{N}x_n}{m_\mathrm{eff}}\frac{\Delta t^2}{2}\,, \tag{2.19a}$$

$$v_{n+1} = v_n - \frac{k_\mathrm{N}x_n + k_\mathrm{N}x_{n+1}}{2m_\mathrm{eff}}\,\Delta t\,. \tag{2.19b}$$

Replacing x_{n+1} in the expression of v_{n+1} and rearranging the terms, we obtain a fully explicit scheme:

$$x_{n+1} = \left(1 - \frac{k_\mathrm{N}}{2m_\mathrm{eff}}\Delta t^2\right)x_n + \Delta t\, v_n\,, \tag{2.20a}$$

$$v_{n+1} = \left(1 - \frac{k_\mathrm{N}}{2m_\mathrm{eff}}\Delta t^2\right)v_n - \frac{k_\mathrm{N}}{m_\mathrm{eff}}\,\Delta t\left(1 - \frac{k_\mathrm{N}}{4m_\mathrm{eff}}\Delta t^2\right)x_n\,. \tag{2.20b}$$

To check for the stability of the system, we can monitor the total energy of the system

$$E_n = \frac{1}{2}k_\mathrm{N}x_n^2 + \frac{1}{2}m_\mathrm{eff}v_n^2 \tag{2.21}$$

and make sure that it does not grow unbounded. The expression of the energy prompts us to perform the substitutions

$$\hat{x}_n = \sqrt{\frac{k_\mathrm{N}}{2E_0}}\,x_n \tag{2.22}$$

$$\text{and}\quad \hat{v}_n = \sqrt{\frac{m_\mathrm{eff}}{2E_0}}\,v_n \tag{2.23}$$

---

[2] We expect the damping force to be sufficiently low, such that it does not significantly affect the critical time step. A safety factor is used afterward, anyway.

for the expression for the initial energy (at $n = 0$) to become

$$1 = \hat{x}_0^2 + \hat{v}_0^2 . \tag{2.24}$$

Using these substitutions and

$$\hat{\Delta t} = \sqrt{\frac{k_\mathrm{N}}{m_\mathrm{eff}}} \Delta t , \tag{2.25}$$

the integration scheme (2.20) becomes

$$\hat{x}_{n+1} = \left(1 - \frac{\hat{\Delta t}^2}{2}\right) \hat{x}_n + \hat{\Delta t}\, \hat{v}_n , \tag{2.26a}$$

$$\hat{v}_{n+1} = \left(1 - \frac{\hat{\Delta t}^2}{2}\right) \hat{v}_n - \hat{\Delta t} \left(1 - \frac{\hat{\Delta t}^2}{4}\right) \hat{x}_n , \tag{2.26b}$$

which can be written in matrix form:

$$\begin{bmatrix} \hat{x}_{n+1} \\ \hat{v}_{n+1} \end{bmatrix} = \begin{bmatrix} 1 - \frac{\hat{\Delta t}^2}{2} & \hat{\Delta t} \\ -\hat{\Delta t}\left(1 - \frac{\hat{\Delta t}^2}{4}\right) & 1 - \frac{\hat{\Delta t}^2}{2} \end{bmatrix} \begin{bmatrix} \hat{x}_n \\ \hat{v}_n \end{bmatrix} , \tag{2.27}$$

or

$$\boldsymbol{p}_{n+1} = A \boldsymbol{p}_n , \tag{2.28}$$

which in turn can be expressed directly as a function of the initial conditions:

$$\boldsymbol{p}_n = A^n \boldsymbol{p}_0 . \tag{2.29}$$

Equation (2.24) tells us that the initial adimensionalized position-velocity vector $\boldsymbol{p}_0$ has a norm of 1. For the integration scheme to be stable, we must ensure that the norm of $\boldsymbol{p}_n$ is not growing toward infinity under the repeated application of A in (2.28). From the eigendecomposition of A, we know that

$$A^n = Q \Lambda^n Q^{-1} , \tag{2.30}$$

where Q is the matrix of the eigenvectors of A and Λ is the diagonal matrix with the eigenvalues:

$$\lambda_{1,2} = \frac{2 - \hat{\Delta t}^2 \pm \hat{\Delta t} \sqrt{\hat{\Delta t}^2 - 4}}{2} . \tag{2.31}$$

For A^n to stay bounded and thus have stability, we must have $\max(|\lambda_1|, |\lambda_2|) \leqslant 1$, which is true when $\hat{\Delta t} \leqslant 2$ (the eigenvalues become complex numbers), or

$$\Delta t \leqslant 2 \sqrt{\frac{m_\mathrm{eff}}{k_\mathrm{N}}} , \tag{2.32}$$

where we have $|\lambda_1| = |\lambda_2| = 1$. Taking $m_i = m_j = m$, we have $m_\mathrm{eff} = \frac{m}{2}$ and the stability condition becomes

$$\Delta t \leqslant \sqrt{\frac{2m}{k_\mathrm{N}}} . \tag{2.33}$$

This is the same stability condition as for the central differences scheme (O'Sullivan & Bray 2004).

2.2.3 *Critical damping*

The system of two particles described by (2.17) is a conventional damped harmonic oscillator. Depending on the value of the damping coefficient c_N, the system will either oscillate with a decreasing amplitude (underdamped regime) or slowly decay toward the equilibrium position without oscillating (overdamped regime). Between these two regimes lies the critically damped regime, where the system decays as quickly as possible toward its equilibrium. The corresponding critical damping coefficient is

$$c_\mathrm{c} = 2\sqrt{k_\mathrm{N} m_\mathrm{eff}}\,. \tag{2.34}$$

2.3 BOUNDARY ELEMENT METHOD

BEM is similar in principle to its more commonly used cousin, the finite element method. When modeling an elastic solid, instead of discretizing its whole volume, only its surface is discretized. The BEM formulation simplifies even further when the considered volume is a half-space (a semi-infinite volume delimited by an infinite plane). Being able to model a single deformable semi-infinite solid is sufficient for solving the contact between two elastic rough surfaces, thanks to the *Jonhson's assumption* (Johnson 1985), stating that the frictionless contact between two nominally flat (having small slopes) elastic surfaces of profile $h_1(x,y)$ and $h_2(x,y)$ is equivalent to the contact between a *flat deformable* surface and a *rigid rough* surface, with a roughness of $h = h_1 - h_2$.

2.3.1 *Elastic deformation*

Modeling an elastic half-space using BEM first comes down to looking at the effect of a single point load applied on its surface. Let us consider the volume Ω shown in Figure 2.2. The effect of a vertical point load P applied at the origin can be calculated using the theory of potential, as it was done by Boussinesq (Johnson 1985). The vertical load induces displacements inside of the solid. At the surface (at $z=0$), these displacements are

$$u_x = -\frac{P}{4\pi G}(1-2\nu)\frac{x}{r^2}\,, \tag{2.35a}$$

$$u_y = -\frac{P}{4\pi G}(1-2\nu)\frac{y}{r^2}\,, \tag{2.35b}$$

$$u_z = \frac{P}{4\pi G}2(1-\nu)\frac{1}{r}\,, \tag{2.35c}$$

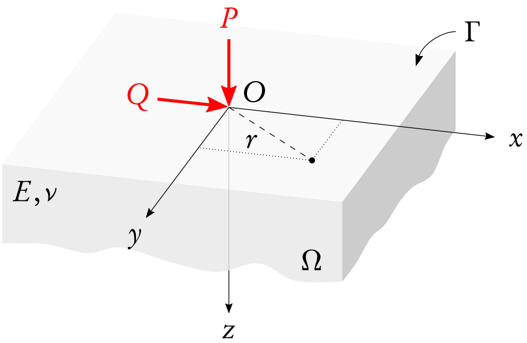

Figure 2.2 – Elastic half-space with point loads applied at its origin

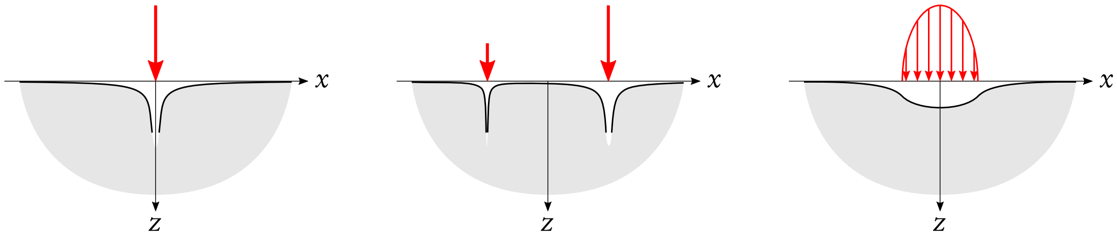

(a) One point load (b) Multiple point loads (c) Distributed load

Figure 2.3 – Different loading condition on an elastic half-space

where G is the shear modulus of the material, and $r=\sqrt{x^2+y^2}$ is the distance of a point on the surface from the origin (see Figure 2.3).

The surface displacements caused by a tangential force Q acting on the origin in the x direction were derived by Cerruti (Johnson 1985). They are:

$$u_x=\frac{Q}{4\pi G}\left[2(1-\nu)\frac{1}{r}+2\nu\frac{x^2}{r^3}\right], \tag{2.36a}$$

$$u_y=\frac{Q}{4\pi G}2\nu\frac{xy}{r^3}, \tag{2.36b}$$

$$u_z=-\frac{Q}{4\pi G}(1-2\nu)\frac{x}{r^2}. \tag{2.36c}$$

From the displacement fields, it is also possible to derive the stress fields caused by the point loads. Full expressions are given in Johnson (1985).

Knowing the effect of a single point load is enough to deduce the effect of several point loads or of a load distribution, thanks to linear elasticity and the superposition principle. Figure 2.3a shows the vertical deflection of the surface caused by a single point load, given by equation (2.35c). In Figure 2.3b, two point loads are present, and the surface deflection is obtained by summing the contribution of each point load. Finally, in Figure 2.3c, the surface is subject to a distributed load $p_x(x,y)$. Similarly, the surface deflection is obtained by integrating the contribution at each patch of surface:

$$u_z(x,y)=\iint_\Gamma u^{\text{ker}}_{z\to z}(x-\xi,y-\eta)p_x(\xi,\eta)\,d\xi\,d\eta \tag{2.37}$$

$$=[u^{\text{ker}}_{z\to z}*p_x](x,y), \tag{2.38}$$

which is a convolution (denoted by the $*$ symbol). Here, $u^{\text{ker}}_{z\to z}$ is the displacement in the z direction caused by a unit load in the z direction. We can call it a *kernel*. According to (2.35c), it is defined as

$$u^{\text{ker}}_{z\to z}=\frac{1}{4\pi G}2(1-\nu)\frac{1}{r}, \tag{2.39}$$

and has units of [m/N]. Loads in the other directions affects the different components of the surface displacements in the same way. In general, we can write

$$u_i(x,y)=[u^{\text{ker}}_{j\to i}*p_j](x,y), \tag{2.40}$$

where the Einstein's summation convention applies, and i and j are the directions x, y or z. The expanded form is

$$u_i=[u^{\text{ker}}_{x\to i}*p_x]+[u^{\text{ker}}_{y\to i}*p_y]+[u^{\text{ker}}_{z\to i}*p_z]. \tag{2.41}$$

The other superposable quantities, such as strains and stresses, behave the same way as the displacement do, and can be calculated with the convolution of a kernel function with the function defining the distributed load.

To numerically use BEM for flat elastic half-spaces, the surface of the solid must be discretized, for example in an uniform grid. The pressure and displacement fields are also discretized on this grid. Using the kernel expressions, one can easily map the application of a load on one cell to the resulting displacement field created in the remaining cells. A (dense) stiffness matrix can be constructed, directly linking the pressure field to the displacement field, and it can be used to solve elasticity problems with the desired boundary conditions (as done for example in Crouch & Starfield (1983)).

2.3.2 *Contact*

We use the open source software Tamaas (Frérot *et al.* 2020b), developed at our laboratory, to solve contact problems using BEM. It works with periodic surfaces, allowing the use of efficient Fourier transforms to compute the necessary convolutions (Rey *et al.* 2017). The kernel function are a bit different from the ones presented earlier, to take into account the periodic boundary conditions.

The contact problem is a minimization problem. In the case of a frictionless contact, only the z components of the displacements and pressure, u and p, are relevant. The functional to minimize is

$$\mathcal{J}(p) = \frac{1}{2}\int_\Gamma p\,u\,dx\,, \tag{2.42}$$

which is the elastic energy of the system. If the rigid surface making contact with the elastic surface has a height profile $h(x)$ the gap between the two surfaces is $g(x) = u(x) - h(x)$ (see Figure 2.4). The constraints of the minimization problem are the Hertz-Signorini-Moreau orthogonality constraints:

$$p(x) \geqslant 0\,, \tag{2.43a}$$
$$g(x) \geqslant 0\,, \tag{2.43b}$$
$$p(x)g(x) = 0\,. \tag{2.43c}$$

The physical meaning of these constraints is that the elastic surface can only be under compression (2.43a) (here without adhesive forces), there is no interpenetration between the surfaces (2.43b), and the rigid surface can only put pressure on the elastic one when they are touching (2.43c). The pressure field must match a target mean pressure p_0. The minimization problem is solved in Tamaas using a conjugate gradient algorithm (Polonsky & Keer 1999).

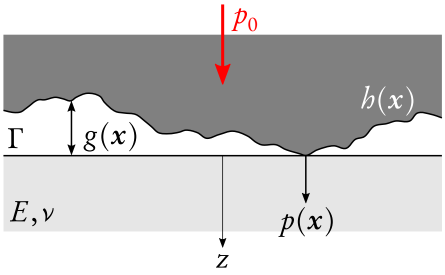

Figure 2.4 – Normal contact with BEM

2.3.3 *Contact with friction*

A tangential contact solver with Coulomb or Tresca friction was implemented. A detailed description is given in Appendix A.

Part II

THEORETICAL AND NUMERICAL ADVANCES

CHAPTER 3

INTERACTION OF MICRO-CONTACTS IN 2D

Disclaimer

This chapter is reproduced in part from S. Pham-Ba *et al.* (2020), "Adhesive wear and interaction of tangentially loaded micro-contacts", *International journal of solids and structures* 188–189, with permission from all authors. My personal contribution was developing the theory, running the simulations, post-processing the results, and writing.

INTRODUCTION

THE objective of this chapter is to derive an analytical description of the transitions between different regimes of wear at the scale of asperities colliding, following the works of Aghababaei *et al.* (2016) and Aghababaei *et al.* (2018). To ease the analytical derivation, we consider flat perfect junctions, or *micro-contacts* (Figure 3.1a), which are shown to have equivalent properties to colliding asperities regarding the transition between a plastic smoothing regime (Figure 3.1b) and a debris formation regime (Figure 3.1c) at a length scale d^* (Aghababaei *et al.* 2016). An analytical theory for the interaction of multiple micro-contacts is derived in 2D, predicting the transition between a mild wear regime (Figure 3.1c) and a severe wear regime (Figure 3.1d) at the scale of the micro-contacts. The various assumptions are verified using BE simulations, and the analytical theory is then validated against MD simulations by simulating perfect adhesive junctions between two solids using model potentials (the same as Aghababaei *et al.*) in quasi-2D setups.

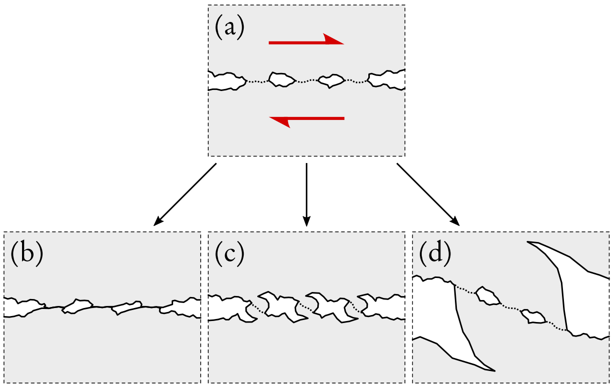

Figure 3.1 – Schematics of sheared micro-contacts and possible outcomes. (a) Initial state. The contact between two solids (top and bottom) viewed at small scale results in the formation of perfect adhesive junctions (micro-contacts) between the two bodies, shown with dotted lines. We consider equally-spaced micro-contacts of identical sizes. The system is under shear. (b) Plastic smoothing. (c) Formation of separate wear particles. (d) Formation of a combined wear particle.

3.1 THEORETICAL MODEL

We derive an analytical prediction for the outcome of the system shown in Figure 3.1a. An energy balance criterion has been effective to predict the transition from plastic shearing to single debris particle creation for both numerical simulations and experimental data (Aghababaei *et al.* 2016), therefore the same argument will be used here. The elastic energy is calculated for systems of increasing complexity, starting from a simple point shear loading. We take advantage of the symmetry of the system by only considering the loaded bottom solid, knowing that the top one will be under a symmetric stress state and thus store the same amount of elastic energy. The adhesive energy corresponding to the different outcomes is derived and compared to the stored elastic energy to obtain an energy criterion for the formation of wear particles.

3.1.1 *Elastic energy*

Point load

Let us consider a semi-infinite solid in 2D, defined by $\Omega = \{(x,z) \in \mathbb{R}, z \geqslant 0\}$. We call B the thickness of the solid in the y direction (see Table 3.1 for a list of symbols used in this chapter). E and ν are respectively the Young's modulus and the Poisson's ratio of the material.

A tangentially loaded micro-contact of negligible size can be modeled as a tangential point load of magnitude Q (in units of force per length) applied at the surface of Ω, as shown in Figure 3.2.

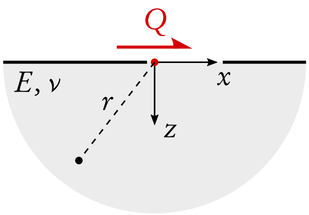

Figure 3.2 – 2D semi-infinite solid under a single tangential point load. Since the point load Q would be represented by a line load in a 3D equivalent setup, Q has units of force per length.

Table 3.1 – List of symbols

Symbol	Description
d	Size of micro-contact
$d^*, d_\mathrm{a}, d_\mathrm{r}$	Critical, apparent and real contact size
h	Height of micro-contact in the MD simulations
a	Distance between point loads
λ	Distance between uniform loads
N	Number of loads
Q	Point load
q	Uniform load
σ_j	Shear strength
$\Omega, \Omega_\mathrm{d}$	Two dimensional semi-infinite solid, continuous and discretized
E, G, ν	Young's modulus, shear modulus and Poisson's ratio
γ	Surface energy
B	Thickness
L, H	Length and height of discretized domain
n_x, n_z	Number of discretization points in x and z direction
$\mathcal{M}$	Spatial discretization factor
$E_\mathrm{el}, E_\mathrm{ad}$	Elastic and adhesive energy
$\mathcal{R}$	Ratio between elastic and adhesive energy
κ	Ratio between real and apparent contact size

For a load applied at $x = z = 0$, the stresses inside Ω are (Johnson 1985)

$$\sigma_x = -\frac{2Q}{\pi}\frac{x^3}{r^4}, \tag{3.1a}$$

$$\sigma_z = -\frac{2Q}{\pi}\frac{xz^2}{r^4}, \tag{3.1b}$$

$$\tau_{xz} = -\frac{2Q}{\pi}\frac{x^2 z}{r^4}, \tag{3.1c}$$

where $r^2 = x^2 + z^2$. In plane strain conditions, the strains are

$$\begin{bmatrix} \varepsilon_x \\ \varepsilon_z \\ \varepsilon_{xz} \end{bmatrix} = \frac{1+\nu}{E} \begin{bmatrix} 1-\nu & -\nu & 0 \\ -\nu & 1-\nu & 0 \\ 0 & 0 & 1 \end{bmatrix} \begin{bmatrix} \sigma_x \\ \sigma_z \\ \tau_{xz} \end{bmatrix}. \tag{3.2}$$

The expression of the elastic energy stored in Ω is

$$E_\mathrm{el} = \frac{1}{2}\int_\Omega \boldsymbol{\sigma} : \boldsymbol{\varepsilon}\, d\Omega \tag{3.3}$$

$$= \frac{1+\nu}{2E}\int_0^\infty \int_{-\infty}^\infty \big[(1-\nu)(\sigma_x^2 + \sigma_z^2) - 2\nu\sigma_x\sigma_z + 2\tau_{xz}^2\big] B\, dx\, dz, \tag{3.4}$$

where $\boldsymbol{\sigma} : \boldsymbol{\varepsilon}$ is the inner product defined as $\sum_{i,j} \sigma_{ij}\varepsilon_{ij}$. For a load in 2D, the elastic energy is infinite. We can still integrate only along the x direction and keep the infinite term within the integral, which for a tangential point load gives:

$$E_\mathrm{el,1Q} = \frac{(1-\nu^2)BQ^2}{\pi E}\int_0^\infty \frac{dz}{z}. \tag{3.5}$$

Subsequent expressions of elastic energy can be compared with each other by looking at the factor in front of the integral term. In this case, we notice that the elastic energy is quadratic to the load Q.

Infinite integral term

The fact that the elastic energy stored in a loaded semi-infinite medium is infinite can be explained in several ways. Since the stored elastic energy is equal to the work of the load, it can be calculated by multiplying the magnitude of the load by the displacement of the loaded point in the direction of the load. In 2D, the displacement caused by a load on the surface is $O(\log r)$, meaning that imposing a zero displacement at $r \to \infty$ as a boundary condition will lead to an infinite displacement under the load (Johnson 1985), therefore to an infinite elastic energy. Also, by looking at the stresses in Eq. (3.1), we see that they are $O(1/r)$, which has a singularity at $r = 0$ and creates the $1/z$ term in the integral of (3.5), decaying too slowly to make the integral finite. The problem of the slow decay is no longer an issue when dealing with systems of finite size. Moreover, the stress singularities disappear in real systems due to plasticity, as well in simulated systems due to the discretization size. Therefore, (3.5) can be rewritten as

$$E_{\mathrm{el},1Q} = \frac{(1-\nu^2)BQ^2}{\pi E}\mathcal{M} \tag{3.6}$$

where $\mathcal{M}$ is a number replacing the infinite integral term, which, again, is finite for a given simulation domain size and discretization size.

Note also that the problem of the infinite elastic energy does not exist in a 3D system (in the absence of stress singularities) because the stresses are $O(1/r^2)$, making the integrals of (3.3) finite, and the displacements are $O(1/r)$, allowing the application of the boundary condition of zero displacement at $r \to \infty$.

Two point loads

We now consider two tangential point loads, each one of magnitude Q, located at $x = a$ and $x = -a$, $z = 0$, as shown in Figure 3.3.

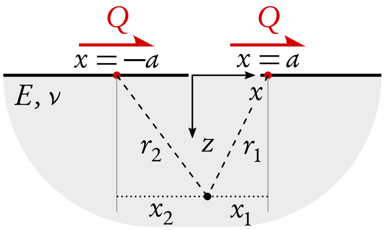

Figure 3.3 – 2D semi-infinite solid under two tangential point loads. The distance between the two point loads is $2a$.

By superposition of (3.1), the stresses are simply

$$\sigma_x = -\frac{2Q}{\pi}\left(\frac{x_1^3}{r_1^4} + \frac{x_2^3}{r_2^4}\right), \tag{3.7a}$$

$$\sigma_z = -\frac{2Q}{\pi}\left(\frac{x_1 z^2}{r_1^4} + \frac{x_2 z^2}{r_2^4}\right), \tag{3.7b}$$

$$\tau_{xz} = -\frac{2Q}{\pi}\left(\frac{x_1^2 z}{r_1^4} + \frac{x_2^2 z}{r_2^4}\right), \tag{3.7c}$$

where $x_1 = x - a$, $x_2 = x + a$, $r_1^2 = x_1^2 + z^2$ and $r_2^2 = x_2^2 + z^2$. The elastic energy is obtained by using these new stresses in (3.3), giving:

$$E_{\mathrm{el,2Q}} = \frac{(1-\nu^2)BQ^2}{\pi E}\left[2\int_0^\infty \frac{dz}{z} + 2\int_0^\infty \frac{z}{a^2+z^2}\,dz\right] \tag{3.8}$$

which is dependent on a, the half spacing between the two point loads. If a goes to 0, the two integral terms are the same and the expression of elastic energy is reduced to

$$E_{\mathrm{el,2Q}}\Big|_{a=0} = 4E_{\mathrm{el,1Q}}\,, \tag{3.9}$$

where $E_{\mathrm{el,1Q}}$ is the elastic energy of a single point load Q given by (3.6). This is consistent with the fact that this situation is equivalent to having a single point load of magnitude $2Q$ (Saint-Venant's principle), the elastic energy being quadratic to the load. If a goes to infinity, the right integral term vanishes, leading to

$$\lim_{a\to\infty} E_{\mathrm{el,2Q}} = 2E_{\mathrm{el,1Q}} \tag{3.10}$$

which corresponds to the case where the two point loads are so far apart that they are not interacting, so the total elastic energy is the sum of their individual elastic energy if they were taken separately. Since a always has a finite value compared to the infinite size of the medium, a is dominated by z and the $1/z$ behavior of $z/(a^2+z^2)$ at infinity, such that a has no effect on the integral if it is not infinite. Therefore, we can assume that we are in the case where a goes to 0, which means that $E_{\mathrm{el,2Q}} = 4E_{\mathrm{el,1Q}}$. This equality will of course not be exactly matched when performing simulations of finite size, where a will no longer be infinitely small compared to the simulated medium.

N point loads

We consider N tangential point loads of magnitude Q. Following the assumption that the distance a between the loads has a finite value compared to the infinite size of the medium, the setup is equivalent to having a single point load of magnitude NQ. The elastic energy being quadratic to the total load, it is also quadratic to the number of point loads:

$$E_{\mathrm{el},NQ} = N^2 E_{\mathrm{el,1Q}}\,. \tag{3.11}$$

Equation (3.11) is subject to the same limitations as (3.9) regarding the simulations of finite size.

Uniform load

A single tangentially loaded micro-contact is better modeled by a uniformly distributed load. We consider a tangential load q (in units of pressure) applied on a region $-d/2 \leqslant x \leqslant d/2$, $z = 0$, as shown in Figure 3.4, where d is the size of the micro-contact.

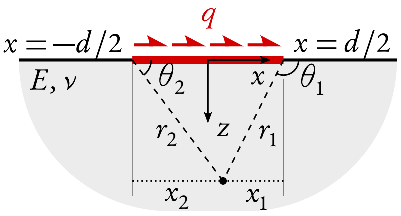

Figure 3.4 – 2D semi-infinite solid under a uniform tangential load q of size d. Since the load q would be represented by a load on a band in a 3D equivalent setup, q has units of pressure.

Integrating (3.1) on this region, the stresses are

$$\sigma_x = \frac{q}{\pi}\left[2\log\left(\frac{r_1}{r_2}\right) - \left(\frac{x_1^2}{r_1^2} - \frac{x_2^2}{r_2^2}\right)\right], \tag{3.12a}$$

$$\sigma_z = -\frac{q}{\pi}\left(\frac{x_1^2}{r_1^2} - \frac{x_2^2}{r_2^2}\right), \tag{3.12b}$$

$$\tau_{xz} = -\frac{q}{\pi}\left[(\theta_1 - \theta_2) - \left(\frac{x_1 z}{r_1^2} - \frac{x_2 z}{r_2^2}\right)\right], \tag{3.12c}$$

where $x_1 = x - d/2$, $x_2 = x + d/2$, $r_1^2 = x_1^2 + z^2$; $r_2^2 = x_2^2 + z^2$; $\tan\theta_1 = z_1/x_1$ and $\tan\theta_2 = z_2/x_2$. For the calculation of the elastic energy, the integral (3.4) cannot be fully evaluated for this distribution of stresses using analytic functions. However, numerical integration shows that the elastic energy is of the form

$$E_{\mathrm{el},1q} = \frac{(1-\nu^2)Bd^2q^2}{\pi E}\int_0^\infty f(z)\,dz \tag{3.13}$$

where $f(z)$ is a function dominated by the term $1/z$ when $z \gg d$. It means that the elastic energy is the same as the one for a point load of equivalent magnitude $Q = dq$:

$$E_{\mathrm{el},1q} = E_{\mathrm{el},1Q}\Big|_{Q=dq}, \tag{3.14}$$

in the case where d is small compared to the size of the medium.

N uniform loads

Using the same assumption as for the N point loads, we can finally derive an expression for the elastic energy of N non-overlapping uniform tangential loads of magnitude q and diameter d:

$$E_{\mathrm{el},Nq} = N^2 E_{\mathrm{el},1q} = \frac{(1-\nu^2)BN^2d^2q^2}{\pi E}\mathcal{M}. \tag{3.15}$$

This is the expression that will be used to compare with the adhesive energy.

3.1.2 *Adhesive energy*

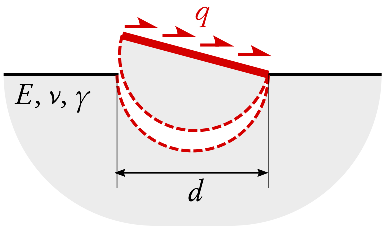

Figure 3.5 – Formation of a debris particle of size d due to the tangential load q. Newly created surfaces are shown in red dashed lines.

The creation of a debris particle under a micro-contact assuming brittle failure involves the creation of new surfaces. To detach a semi-circular particle of diameter d as shown in Figure 3.5, two surfaces of area $B\pi d/2$ have to be created, which requires an adhesive energy of

$$E_{\mathrm{ad}} = \pi\gamma B d \tag{3.16}$$

where γ is the surface energy of the material. The distribution of the stresses forces the crack to initially move into the volume below the surface. We thus assume that the semi-circular path of the crack is close to the minimal path that would relieve the stresses in the solid and allow the pivoting of the forming debris particle. Considering another general crack path would only change the adhesive energy up to a small geometrical factor. This assumption is consistent with what is observed in MD simulations (Aghababaei *et al.* 2016; Aghababaei *et al.* 2017).

We now consider N equally spaced micro-contacts of size d, with λ the distance between the edges of two adjacent micro-contacts, as shown in Figure 3.6.

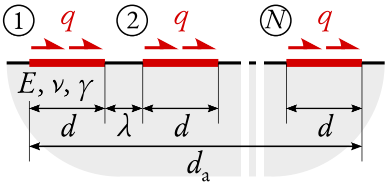

Figure 3.6 – N equally-spaced uniform loads q of size d and spacing λ. The total contact size is $d_\mathrm{r} = Nd$ and the apparent contact size is $d_\mathrm{a} = Nd + (N-1)\lambda$.

Two cases of debris formation can arise. Either N separate debris particles of diameter d are formed, requiring an adhesive energy of

$$E_\mathrm{ad,sep} = \pi\gamma B d_\mathrm{r}\,, \tag{3.17}$$

where

$$d_\mathrm{r} = Nd \tag{3.18}$$

is the real size of the contact, or in other words the sum of the sizes of all the micro-contacts.

The other possible case of debris formation is to create a single debris particle combining all micro-contacts, having an apparent diameter of

$$d_\mathrm{a} = Nd + (N-1)\lambda \tag{3.19}$$

and requiring an adhesive energy of

$$E_\mathrm{ad,comb} = \pi\gamma B d_\mathrm{a}\,. \tag{3.20}$$

Since we always have $d_\mathrm{a} \geqslant d_\mathrm{r}$, $E_\mathrm{ad,comb}$ is always larger than $E_\mathrm{ad,sep}$.

3.1.3 *Energy criterion for debris formation*

Critical micro-contact size

The formation of debris particles is possible if the stored elastic energy is greater than the adhesive energy required to create the particles (Aghababaei *et al.* 2016). In other words, the ratio

$$\mathcal{R} = \frac{E_\mathrm{el}}{E_\mathrm{ad}} \tag{3.21}$$

has to be greater than one to enable the process of debris formation. For a single micro-contact ($N = 1$) of diameter d and uniform load q, the energy ratio is equal to

$$\mathcal{R} = \frac{1-\nu^2}{\pi^2\gamma E} d q^2 \mathcal{M}\,. \tag{3.22}$$

If $\mathcal{R} < 1$, no debris particle can be formed under tangential load, so the micro-contact slips or flows plastically. If $\mathcal{R} \geqslant 1$, there is enough energy to create a debris particle. This allows us to define a critical size d^* for a single micro-contact, which is the size above which a debris particle can be created:

$$d^* = \frac{\pi^2 \gamma E}{(1-\nu^2) q^2 \mathcal{M}} . \tag{3.23}$$

If we set the tangential load q to be equal to the shear strength of the micro-contact σ_{j}, it becomes clear that d^* is a function of the material parameters, similarly to the critical junction size derived by Aghababaei *et al.*, see (1.13). Aghababaei *et al.* derived the critical junction size for two spherical colliding asperities, assuming that the elastic energy is stored inside the volume of the asperities and is therefore independent of the system size. The existence of d^* given by (3.23) means that, as for colliding asperities, flat junctions also have a ductile-to-brittle transition at a length scale d^*, even if the stored elastic energy is radiated into the bulk.

Note that the expression of d^* (3.23) is dependent on the number $\mathcal{M}$, which is linked to the spatial discretization and the size of the domain and therefore is not a physical parameter. We recall that $\mathcal{M}$ disappears in a three-dimensional formulation. In reality, d^* is thus a material parameter, to first-order independent of geometry. The following arguments will therefore be made in terms of d^* rather than $\mathcal{M}$. The material properties E, ν, γ and σ_{j} will all be contained within d^*.

Separated debris particles

To study the possibility of forming separated debris particles from a distribution of N micro-contacts, we have to calculate from (3.15) and (3.17) the ratio

$$\mathcal{R}_{\mathrm{sep}} = \frac{E_{\mathrm{el},Nq}}{E_{\mathrm{ad,sep}}} = \frac{d_{\mathrm{r}}}{d^*} , \tag{3.24}$$

where all material parameters are included in d^*. Note that $\mathcal{R}_{\mathrm{sep}}$ does not depend on the distance between the micro-contacts. Forming N particles is possible if $\mathcal{R}_{\mathrm{sep}} \geqslant 1$, or, in terms of d_{r}, if

$$d_{\mathrm{r}} \geqslant d^* . \tag{3.25}$$

Combined debris particle

To study the possibility of forming a combined debris particle from a distribution of N micro-contacts, we calculate from (3.15) and (3.20) the ratio

$$\mathcal{R}_{\mathrm{comb}} = \frac{E_{\mathrm{el},Nq}}{E_{\mathrm{ad,comb}}} = \frac{d_{\mathrm{r}}^2}{d_{\mathrm{a}} d^*} . \tag{3.26}$$

Forming a combined particle is possible if $\mathcal{R}_{\mathrm{comb}} \geqslant 1$, or, in terms of d_{a}, if

$$d_{\mathrm{a}} \leqslant \frac{d_{\mathrm{r}}^2}{d^*} . \tag{3.27}$$

Transition between behaviors

In summary, the three different behaviors described in Figure 3.1 depend only on the values of the real contact size d_{r} (3.25) and the apparent contact size d_{a} (3.27) and their relation to d^*. Transitions between behaviors are summarized in the wear map shown in Figure 3.7, giving regions where each behavior is energetically plausible. The vertical dashed line shows the transition between a plastic behavior and the formation of separated debris particles, as dictated by (3.25), and the

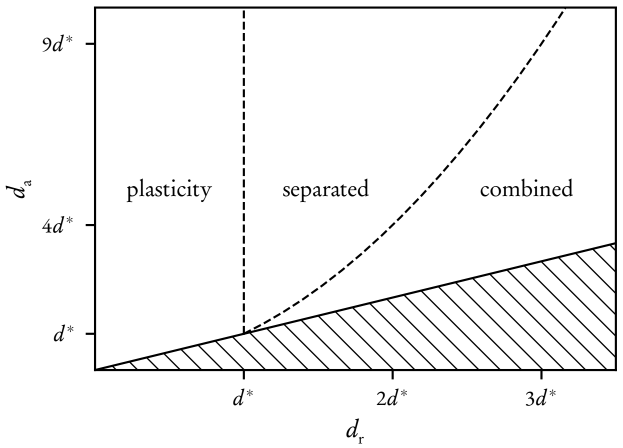

Figure 3.7 – Wear map of the different outcomes for the system of Figure 3.1a. The horizontal axis corresponds to the real contact size d_r and the vertical axis corresponds to the apparent contact size d_a. The hatched area is not accessible because $d_a \geqslant d_r$, and its boundary represents systems with a single micro-contact (thus having $d_a = d_r$).

second dashed line shows the transition to the formation of a single combined debris particle, as dictated by (3.27). The hatched region is inaccessible because $d_a \geqslant d_r$.

Our wear map is compatible with the initial definition of a critical length d^* (1.13), found for a single pair of colliding hemispherical asperities (instead of a flat junction of negligible volume, in our case). However, our wear map is not directly applicable to the geometry of colliding asperities when $N \geqslant 2$, because the elastic energy will not only be stored in the volume under the asperities like we assumed, but will mainly be stored in the protruding hemispherical volume of the deforming asperities, which is not taken into account in our model. Therefore, we will expect less elastic interaction in the case of colliding asperities than established for (3.9), since a large part of the energy is contained in the asperities themselves. This results in a lesser likelihood of the formation of combined debris particles. If the asperities are flatter, as expected in many cases of real contacts, the present theory is expected to apply.

Partial contact

The wear map may be used to define what an asperity is. This definition is far from obvious as, due to the fractal nature of real surfaces, each asperity in contact can be in turn subdivided into smaller contact zones (Archard & Allibone 1957). What appears as a fully compact contact junction at a given scale, becomes fragmented into smaller contact patches at a smaller scale. Yet, interactions between these divided contact spots may be homogenized into a single apparent contact junctions if elastic interactions prevail, which is precisely what Figure 3.7 can help assess. For a contact junction of apparent diameter d_a, we can define the fraction of the real contact size to the apparent contact size as

$$\kappa = \frac{d_r}{d_a}, \tag{3.28}$$

satisfying $\kappa \leqslant 1$. We establish a criterion to determine if this weakened contact can form a single debris particle of size d_a by rewriting the condition for combined debris particle formation (3.27) using κ, leading to the condition

$$\kappa \geqslant \sqrt{\frac{d^*}{d_a}}, \tag{3.29}$$

which is the minimum fraction of contact size necessary to be able to detach a single debris particle. This minimum fraction is only reachable if $\sqrt{d^*/d_\mathrm{a}} \leqslant 1$, or if

$$d_\mathrm{a} \geqslant d^* . \tag{3.30}$$

It implies that a large contact of apparent contact size $d_\mathrm{a} \geqslant d^*$ can be broken down into smaller micro-contacts of total real contact size $d_\mathrm{r} = \kappa d_\mathrm{a}$ with $\kappa \geqslant \sqrt{d^*/d_\mathrm{a}}$ and still form a single debris particle from an energetic point of view. It also shows that only the total contact size d_r matters to determine the formation of debris particles, and not the individual sizes of each micro-contact (assuming full elastic interaction between the micro-contacts).

Limits of the energy criterion

One may have noticed that we always have $\mathcal{R}_\mathrm{sep} \geqslant \mathcal{R}_\mathrm{comb}$, meaning that forming small individual debris particles is always more energetically favorable than forming a single, combined one, even if $\mathcal{R}_\mathrm{comb} \geqslant 1$. In this case, the energy criterion will only suggest that both cases are energetically possible, but will not indicate which one will happen. The outcome can be predicted by looking at the locations of stress concentrations in the material, which indicate the places where cracks can nucleate and thus where debris formation can occur. It implies that in the wear map (Figure 3.7), a separated debris particle formation can energetically happen in the "combined" region.

3.2 VALIDATION USING SIMULATIONS

3.2.1 *Boundary element method*

Before validating the wear map (Figure 3.7), BEM is used to verify the effects of a finite size system on the computation of the elastic energy $E_{\mathrm{el},Nq}$ (3.15), which was derived assuming an infinite medium. Instead of a semi-infinite plane Ω, a region $\Omega_\mathrm{d} = \{|x| \leqslant L/2,\ 0 \leqslant z \leqslant H\}$ of $n_x \times n_z$ points is considered. The BEM simulation is periodic in the x direction. Desired loads are applied at the nodes located at $z = 0$, and the elastic energy is computed by discretizing the integral of (3.3) as

$$E_\mathrm{el} = \frac{1}{2} \sum_{i=0}^{n_x-1} \sum_{j=0}^{n_z-1} \boldsymbol{\sigma}(x_i, z_j) : \boldsymbol{\varepsilon}(x_i, z_j) \frac{L}{n_x} \frac{H}{n_z} . \tag{3.31}$$

The stress and strain tensors $\boldsymbol{\sigma}(x_i, z_j)$ and $\boldsymbol{\varepsilon}(x_i, z_j)$ are evaluated using a code based on the application of Green's functions defined for a tangential point load applied at the surface of a semi-infinite medium (Polonsky & Keer 1999; Rey *et al.* 2017). The comparison of the results from the BEM with the analytical expression of $E_{\mathrm{el},Nq}$ is shown in Figure 3.8. H is chosen to be large compared to the maximum d_a (with $H/d_\mathrm{a} > 45$) to match the assumption of a large medium made for the analytical prediction. Having periodicity in the x direction and computing the elastic energy only between $-L/2$ and $L/2$ does not seem to affect the match between the analytical and numerical $E_{\mathrm{el},Nq}$, even if d_a is not significantly small compared to L (we always have $L/d_\mathrm{a} > 2.8$). No improvement was found by increasing the value of L.

Overall, there is a good match between the analytical predictions and the numerical values. The discrepancy between the computed and theoretical values is the smallest for lower values of λ and N (low d_a). The decrease of the elastic energy recorded when λ increases can be seen as a transition between a complete interaction of the N loads at $\lambda = 0$, and an absence of interaction for $\lambda \to \infty$. At complete interaction, $E_{\mathrm{el},Nq}$ is verified to be quadratic to N, while for no interaction,

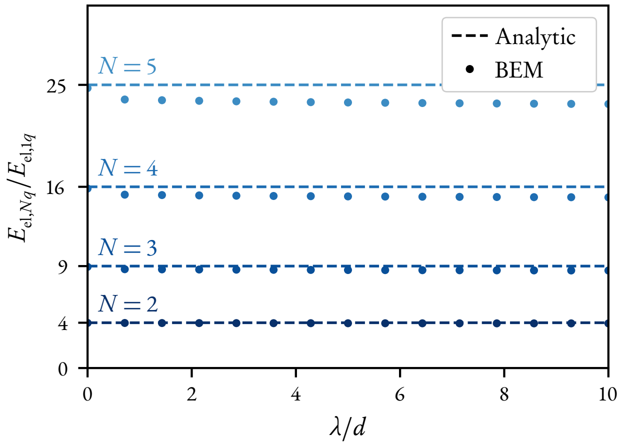

Figure 3.8 – BEM simulations of the elastic energy $E_{\mathrm{el},Nq}$ of N equally-spaced uniform loads q compared to analytical prediction. The values were computed with $L=128$, $H=2048$, $B=1$, $n_x=n_z=2048$, $d=1$, $E=1$, $\nu=0.3$, $q=0.001$. The energies are normalized by $E_{\mathrm{el},1q}$, computed with a single uniform load, to check the validity of (3.11). The agreement is better when the apparent contact size d_{a} is small compared to L and H.

it should decrease to become proportional to N, which is not seen in Figure 3.8 because of the small value of λ.

The theoretical elastic energy slightly overestimates the value computed inside a finite domain, but it still provides a good approximation. Therefore, the criteria for debris formation we derived using the analytical expression of elastic energy can reasonably be applied for systems of finite size.

3.2.2 *Molecular dynamics*

We use MD simulations of perfect junctions to check the validity of the predictions for debris formation, (3.25) and (3.27). A model potential (P4 in Aghababaei *et al.* (2017)) is used to simulate a material brittle enough to have a critical length d^* observable at the scale of the simulations while maintaining a reasonable size. We have $d^* \simeq 35 r_0$ in all our simulations, where r_0 is the interatomic distance at absolute zero temperature. The size of all the simulations is kept constant at $L=900 r_0$ in the x direction and $H=1200 r_0$ in the z direction. The atoms are arranged in a face-centered-cubic lattice with a thickness of three close-packed layers of atoms in the y direction to stay in a quasi-2D plane strain representation. The $[111]$ lattice direction is aligned with the y axis and the $[110]$ direction is in the (x,z) plane at an angle of 15° with the x axis, so that the junctions are not aligned with weak crystal planes. Periodic boundary conditions are used in the x and y directions and the possible lattice mismatch at the boundary is resolved using a step of energy minimization. The temperature of the system is kept constant using Langevin thermostats at the non-periodic boundaries of the simulation. Instead of applying a shear force, a constant velocity is imposed on the boundary of the top solid, and a small constant normal load is applied to prevent the system from drifting apart. The maximum resultant shear force is limited by the shear strength σ_{j} of the material. All the MD simulations are performed with LAMMPS (Plimpton 1995) and visualized with OVITO (Stukowski 2009).

The critical length d^* is first found by simulating single junctions of increasing sizes d. The perfect junctions are modeled by rectangles of width d and fixed height $h=6r_0$. The observation of a transition between plastic behavior and debris particle formation validates the existence of the

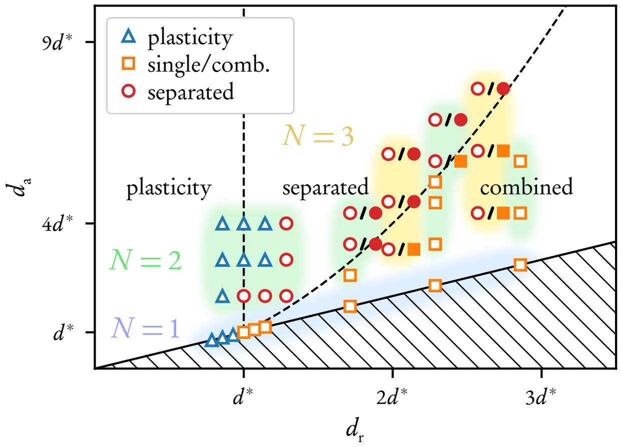

Figure 3.9 – Distribution of the MD simulations' outcomes on the wear map (Figure 3.7). Each symbol corresponds to one MD simulation. Empty and color-filled symbols are simulations with sharp corners and rounded corners respectively, sometimes leading to a different outcome. Rounding the corners has the effect of slightly increasing d_r, shifting the symbol to the right in the diagram. The highlighted areas show the different values of N used for the simulations.

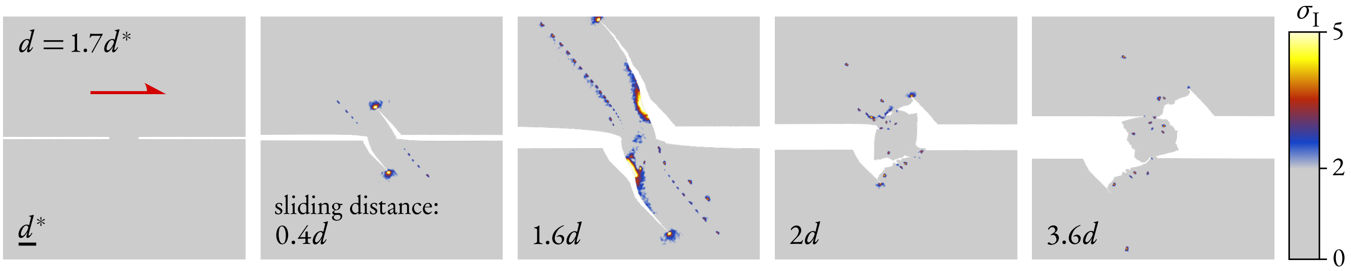

Figure 3.10 – Formation of a debris particle from a single micro-contact of size $d = 1.7d^*$. The red arrow indicates the shear direction. The bottom boundary is fixed. The colors show the first principal stress σ_I (if positive: maximum tensile stress) in reduced dimensionless Lennard-Jones units, with brighter regions corresponding to higher values. Regions of stress concentration are visible near the tips of the growing cracks and at the locations of crack nucleation. The smaller bright spots are mismatches in the crystallographic structure propagating in the material, which is the nanoscale manifestation of shear plasticity. Notice that the cracks extend way past the necessary length before closing at the formation of the debris particle, which is due to an excess of stored elastic energy ($\mathcal{R} > 1$).

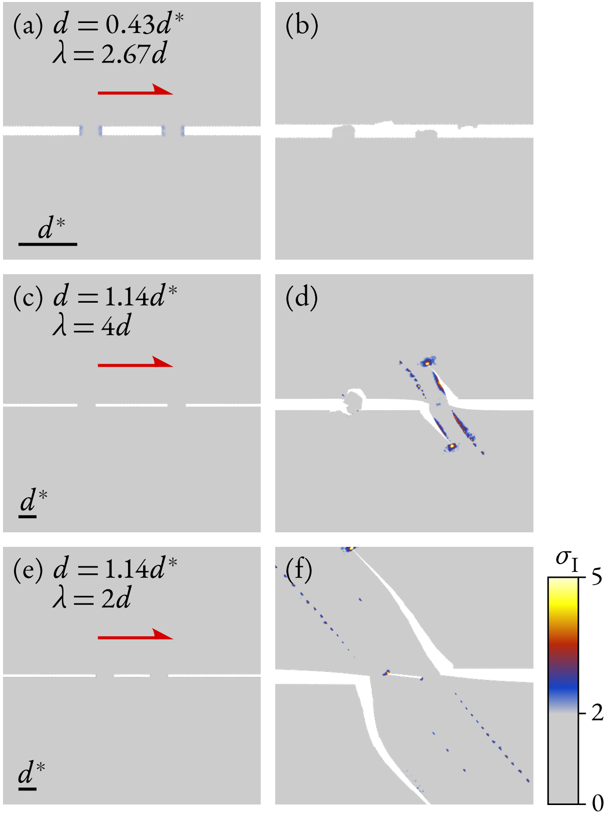

Figure 3.11 – Three different outcomes from two sheared micro-contacts. (a), (c), and (e) show the initial states of (b), (d), and (f) respectively. (b) Case of slip. (d) Case of separated debris particle formation. The left one is detached and the right one is under formation. (f) Case of combined debris particle formation. The length of the cracks is a characteristic of this behavior.

critical size d^* (3.23), which is defined as the value of d at which this transition occurs. The points in Figure 3.9 show that these simulations are located on the line $d_\text{a} = d_\text{r}$ and are highlighted in light blue. An example of debris particle formation is shown in Figure 3.10. Two types of damaging processes are witnessed during the formation of the debris particle: cracks are opened under tensile stress, and dislocations move across the material, which is a nanoscopic manifestation of plastic shear deformations. When varying d, the length reached by the opening cracks becomes larger when d increases relative to d^*. This phenomenon is enabled by $\mathcal{R}$ increasing with d (and being greater than 1 because $d > d^*$), meaning that more elastic energy is stored than what is needed to create the minimal crack path. This excess energy can be used in the formation of larger cracks.

Several simulations were performed with $N = 2$ (highlighted in green in Figure 3.9) and $N = 3$ (highlighted in orange) with different values of d and λ. Examples of the three possible outcomes are shown in Figure 3.11 for $N = 2$. We recall that it is possible to observe the formation of separated debris particles even when the formation of a combined debris particle is energetically possible ($\mathcal{R}_\text{sep} \geqslant \mathcal{R}_\text{comb}$). Therefore, when an MD simulation leads to the formation of separated debris particles, it is relaunched with the same geometric parameters but adding rounded corners where the cracks forming separated debris particles can initiate, in order to prevent their formation, leading to a different outcome if energetically possible (shown by color-filled symbols in Figure 3.9). This shows that the outcome is also controlled by the presence or absence of stress concentrations.

Some simulations reach an asymmetric end-state even if the initial state seems symmetrical, as shown in Figure 3.11d. This is due to the system being very sensitive to stress concentrators (sharp corners) where even the presence or absence of a single atom can make the system's evolution asymmetrical. This is a side effect of using a brittle interatomic potential for the simulations. The fact of imposing a shearing velocity only on the upper half of the system can also contribute to the asymmetry. This is still consistent with our model since particles form as predicted.

The prediction of the transition between a separated and a combined debris particle formation behavior (3.27) is well matched by the $N = 2$ and $N = 3$ simulations, as no combined particles are ever formed outside of the "combined" region of the wear map. Some simulations with sharp corners lead to a behavior consuming less energy, but their rounded corners counterparts are in agreement with the wear map.

The prediction of the transition between a plastic behavior and the formation of separated debris particles (3.25) is however not perfectly matched by the $N = 2$ simulations when d_{a} increases, as seen in Figure 3.9 near the $d_{\mathrm{r}} = d^*$ dashed line. It means that when the distance between the micro-contacts λ gets bigger, there is not enough energy to create the separated debris particles. The decrease of the elastic energy for increasing values of λ was identified with the BEM simulations (Figure 3.8) and is also present in the MD simulations because they both take place in a finite discretized medium. In the wear map (Figure 3.9), taking the decrease of elastic energy into account for increasing values of λ, thus increasing values of d_{a}, would be represented by shifting the dashed lines (showing the transitions between behaviors) to the right for the higher values of d_{a}. The disagreement of the MD simulations with our theory near $d_{\mathrm{r}} = d^*$ might also be an effect of having the sizes of the individual micro-contacts $d \simeq 0.5d^*$ being close to their height $h = 0.17d^*$, enabling unwanted geometrical effects like the concentration of elastic energy in the now non-negligible volume of the micro-contacts, resulting in even less elastic interaction between the micro-contacts.

In general, the criteria (3.25) and (3.27) work well to predict the transitions of behavior, and the transition between the separated and combined debris formation is especially well matched by the MD simulations.

Concluding remarks

We derived and validated analytical criteria for the formation of separated or combined debris particles in an adhesive wear regime at the microscale, leading to a wear map of the different behaviors. The outcome is dictated by the sum of the sizes of the micro-contacts (the real contact area), and by the total length covered by all of them (the apparent contact area), in comparison to the critical length scale d^* of the material, at which a ductile-to-brittle transition occurs. The different microscopic behaviors of debris particle formation give a physical interpretation for the different regimes of macroscopic unlubricated adhesive wear, and the emergence of a regime of severe wear can be physically explained by the energetic feasibility of forming combined debris particles under multiple micro-contacts. The next chapter generalizes these findings to a 3D setting, which has the notable benefit of getting rid of the infinite energy issue, that led to the presence of the unphysical $\mathcal{M}$ factor in some expressions (like the expression of the critical size d^* (3.23)).

CHAPTER 4

INTERACTION OF MICRO-CONTACTS IN 3D

Disclaimer

This chapter is reproduced in part from S. Pham-Ba and J.-F. Molinari (2021a), “Adhesive wear regimes on rough surfaces and Interaction of micro-contacts”, *Tribology letters* 69.3, with permission from all authors. My personal contribution was developing the theory and writing. This paper was highlighted in the *Tribology & lubrication technology* magazine (November 2021) in the Editors’ Selections: Best from STLE’s research community.

INTRODUCTION

IN the previous chapter, elastic interactions between nearby micro-contacts were explored analytically in a rather academic two dimensional setting. Using an energy balance criterion, a wear map was obtained to predict how a set of multiple tangentially loaded micro-contacts transition from multiple small wear particles to a single larger wear particle. This chapter extends the two-dimensional analytical model to three dimensions.

Before diving into the contact between two rough surfaces, we take a look at a simplified contact between two flat surfaces, joined at a small number of cold-welded perfect junctions that we call micro-contacts. To study the elastic interaction between multiple micro-contacts during adhesive wear, we model them with uniform loads of magnitude q acting along the x direction at the surface Γ of a semi-infinite solid Ω (see Figure 4.1). Out of the two solids in contact, only the

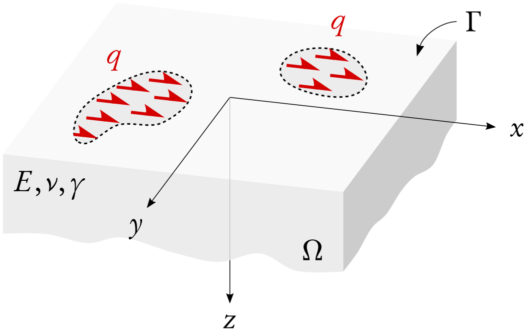

Figure 4.1 – Micro-contacts under uniform tangential load on a semi-infinite solid bottom one is considered because of symmetry.

In this chapter, adhesive wear is incorporated into this model by introducing two wear criteria, one energy-based and one stress-based, which are then both used to find the definition of a critical size of micro-contact d^* for the geometric configuration of Figure 4.1. We then study analytically the interaction between two circular micro-contacts and produce a *mechanism wear map*.

4.1 ENERGY BALANCE CRITERION

Elastic energy

When loaded, the solid Ω of Figure 4.1 accumulates elastic energy of deformation. If it is made of a linear elastic material, no energy is dissipated in the loading process, which implies that the elastic energy is equal to the work of the load on the surface:

$$E_{\mathrm{el}} = \frac{1}{2}\int_{\Gamma} \boldsymbol{u}\cdot\boldsymbol{p}\, d\Gamma\,, \tag{4.1}$$

where $\boldsymbol{u}$ and $\boldsymbol{p}$ are respectively the displacement and traction fields on the surface Γ. In our case, the imposed tractions are only in the x direction, so (4.1) reduces to

$$E_{\mathrm{el}} = \frac{1}{2}\int_{\Gamma} u_x p_x\, d\Gamma\,. \tag{4.2}$$

Here, the field p_x describes the distribution of the tangential tractions in the x direction on Γ, which are equal to q wherever there is a micro-contact, and 0 otherwise (see Figure 4.1). The surface displacements in the x direction u_x are determined from the fundamental solution established by Cerruti (Johnson 1985):

$$u^{\mathrm{ker}}_{x\to x} = \frac{1}{4\pi G}\left[2(1-\nu)\frac{1}{r} + 2\nu\frac{x^2}{r^3}\right], \tag{4.3}$$

which is the displacement field in the x direction caused by a unit point load at the origin of Ω, also in the x direction. G is the shear modulus of the material, ν the Poisson's ratio, and r is the distance from the origin: $r^2 = x^2 + y^2 + z^2$. The full displacement field u_x is obtained by linear superposition of the contributions of all tractions:

$$\begin{align} u_x(x,y) &= \iint u^{\mathrm{ker}}_{x\to x}(x-\xi, y-\eta)p_x(\xi,\eta)\, d\xi\, d\eta \tag{4.4}\\ &= [u^{\mathrm{ker}}_{x\to x} * p_x](x,y), \tag{4.5}\end{align}$$

which is a convolution (denoted by the $*$ symbol). The tractions p_x in the x direction also induce displacements in the y and z direction, but they do not intervene in (4.2). We can rewrite (4.2) as

$$E_{\mathrm{el}} = \frac{1}{2}\int_{\Gamma} [u^{\mathrm{ker}}_{x\to x} * p_x]\, p_x\, d\Gamma\,. \tag{4.6}$$

In order to be calculable analytically for simple cases, the convolution can be turned into a cross-correlation. Following the definition of u_x caused by p_x (4.5), we can find any component i of the displacement as

$$\begin{align} u_i(x,y) &= \iint u^{\mathrm{ker}}_{j\to i}(x-\xi, y-\eta)\, p_j(\xi,\eta)\, d\xi\, d\eta \tag{4.7}\\ &= [u^{\mathrm{ker}}_{j\to i} * p_j](x,y), \tag{4.8}\end{align}$$

which is a convolution, where i and j can be either of the three coordinates x, y or z and the Einstein summation convention is used. The full expression of the elastic energy can be written as

$$E_{\mathrm{el}} = \frac{1}{2} \int_{\Gamma} [u^{\mathrm{ker}}_{j \to i} * p_j]\, p_i \, d\Gamma , \tag{4.9}$$

now taking into account the components of $\boldsymbol{u}$ and $\boldsymbol{p}$ in all directions.

Alternatively, the integrand $[u^{\mathrm{ker}}_{j \to i} * p_j]\, p_i$ of the elastic energy can be written as

$$\begin{aligned} [u^{\mathrm{ker}}_{j \to i} * p_j]\, p_i &= \iint u^{\mathrm{ker}}_{j \to i}(x-\xi, y-\eta)\, p_j(\xi,\eta)\, p_i(x,y)\, d\xi \, d\eta & (4.10)\\ &= \iint u^{\mathrm{ker}}_{j \to i}(\xi',\eta')\, p_j(x-\xi', y-\eta')\, p_i(x,y)\, d\xi' \, d\eta' , & (4.11) \end{aligned}$$

which, injected into the E_{el} expression, gives

$$\begin{aligned} E_{\mathrm{el}} &= \frac{1}{2} \iint [u^{\mathrm{ker}}_{j \to i} * p_j]\, p_i \, dx \, dy & (4.12)\\ &= \frac{1}{2} \iiiint u^{\mathrm{ker}}_{j \to i}(\xi',\eta')\, p_j(x-\xi', y-\eta')\, p_i(x,y)\, dx \, dy \, d\xi' \, d\eta' & (4.13)\\ &= \frac{1}{2} \iint u^{\mathrm{ker}}_{j \to i}(\xi',\eta')[p_j \star p_i](\xi',\eta')\, d\xi' \, d\eta' & (4.14) \end{aligned}$$

which now contains a cross-correlation, denoted by the $\star$ symbol. Using a lighter notation:

$$E_{\mathrm{el}} = \frac{1}{2} \int_{\Gamma} u^{\mathrm{ker}}_{j \to i} [p_j \star p_i]\, d\Gamma . \tag{4.15}$$

Adhesive energy

To detach a wear particle from Ω, new surfaces have to be created, requiring adhesive energy (or fracture energy). We assume a simple spherical geometry. Therefore, the detachment of a single particle of diameter d requires the creation of two hemispherical surfaces, needing an adhesive energy of

$$E_{\mathrm{ad,1}} = \pi \gamma d^2 . \tag{4.16}$$

Criterion

When a wear particle is detached from the bulk, it can no longer carry a tangential load applied at the surface. If a particle is detached where micro-contacts were present, those micro-contacts get unloaded and no longer contribute to the traction field p_x, resulting in a decrease ΔE_{el} of the elastic energy. This energy does not disappear, and in fact contributes to the formation of the cracks resulting in the particle detachment. Therefore, to determine if the particle can be fully detached, we consider the energy ratio

$$\mathcal{R} = \frac{\Delta E_{\mathrm{el}}}{E_{\mathrm{ad}}} , \tag{4.17}$$

and the particle can be detached if

$$\mathcal{R} \geqslant 1 , \tag{4.18}$$

which is the energy balance criterion.

Effect of normal load

The creation of micro-contacts between two surfaces often results from the application of a normal load, which means that all the terms p_x, p_z, u_x and u_z contribute to the elastic energy (4.1). Nevertheless, the change ΔE_{el} in elastic energy due to unloading can still be solely attributed to the change of p_x and u_x, neglecting the effect of the constant p_z. A proof is given below.

Let us consider a surface with micro-contacts, loaded tangentially and vertically. The traction field is

$$\boldsymbol{p} = p_x \boldsymbol{e}_x + p_z \boldsymbol{e}_z \,, \tag{4.19}$$

and the elastic energy, obtained with (4.15), is therefore

$$E_{\mathrm{el}} = \frac{1}{2} \int_{\Gamma} \left(u^{\mathrm{ker}}_{x\to x}[p_x \star p_x] + u^{\mathrm{ker}}_{x\to z}[p_x \star p_z] + u^{\mathrm{ker}}_{z\to x}[p_z \star p_x] + u^{\mathrm{ker}}_{z\to z}[p_z \star p_z] \right) d\Gamma \,. \tag{4.20}$$

When the micro-contacts are unloaded, they can no longer carry the tangential load, so p_x goes to 0. However, the normal load remains, so that the unloaded elastic energy is

$$\Delta E_{\mathrm{el}} = \frac{1}{2} \int_{\Gamma} \left(u^{\mathrm{ker}}_{x\to x}[p_x \star p_x] + u^{\mathrm{ker}}_{x\to z}[p_x \star p_z] + u^{\mathrm{ker}}_{z\to x}[p_z \star p_x] \right) d\Gamma \,, \tag{4.21}$$

where

$$u^{\mathrm{ker}}_{x\to z} = \frac{1}{4\pi G} \left[(1-2\nu) \frac{x}{r^2} \right] = -u^{\mathrm{ker}}_{z\to x} \tag{4.22}$$

and $u^{\mathrm{ker}}_{x\to x}$ is given by (4.3). In the particular case where $p_x(x,y) = p_x(-x,-y)$ and $p_z(x,y) = p_z(-x,-y)$, we have $p_x \star p_z = p_z \star p_x$, so that the unloaded elastic energy becomes

$$\Delta E_{\mathrm{el}} = \frac{1}{2} \int_{\Gamma} u^{\mathrm{ker}}_{x\to x} \, d\Gamma \,, \tag{4.23}$$

which is independent of p_z. Therefore, in this particular case, the unloaded elastic energy does not depend on the normal load, if it is conserved during the unload of the tangential load. The symmetry conditions on p_x and p_z are fulfilled in the simple analytical cases derived in this chapter, and they are also satisfied (approximately) in the case of a contact between rough surfaces, which should be statistically similar upon axial symmetry.

4.2 CRACK INITIATION CRITERION

Since the formation of wear particles results from the formation of cracks, their creation must start with the nucleation of such cracks, which can only be initiated at a point on a surface if

$$\sigma_{\mathrm{I}} \geqslant \sigma_{\mathrm{m}} \,, \tag{4.24}$$

where σ_{I} is the first principal stress at this point, which is the maximum tensile stress if it is positive, and σ_{m} is the tensile strength of the material.

Until now, we only considered the bottom solid to simplify the problem. Let us also reconsider the top solid for a moment. In order to detach a spherical wear particle, two diametrically opposed cracks have to be initiated, as shown in Figure 4.2 as thick red lines at locations (a) in the bottom solid and (b') in the top one. The cracks can be nucleated if the tensile stress at those points, shown by red arrows, is sufficiently large. Thanks to the symmetry of the loading, we can state that the maximum tensile stress at the point (b') in the top solid is equal in magnitude to the maximum

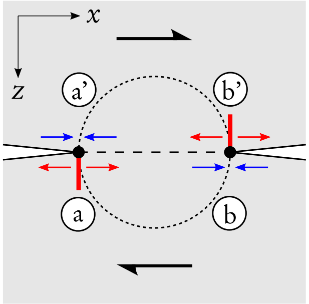

Figure 4.2 – Cross section view of the required crack nucleation sites for the formation of a spherical wear particle at a micro-contact. Points (a) and (b) are slightly below the junction, and points (a') and (b') slightly above. The thick red lines show the cracks which must be nucleated in order to detach the particle. Tensile stresses (red arrows) must overcome the tensile strength of the material. Equal and opposite compressive stresses (blue arrows) appear by symmetry.

compressive stress at the point (b) in the bottom solid, so that the conditions for crack opening can be defined by looking only at the bottom solid. In summary, when considering only the bottom solid, a particle can be detached if it has a sufficiently large tensile stress at its trailing edge (a) and a sufficiently large compressive stress at its leading edge (b). The crack initiation criterion can therefore be written as:

$$\sigma_{\mathrm{I}} \geqslant \sigma_{\mathrm{m}} \quad \text{at point (a)}, \tag{4.25a}$$

$$\sigma_{\mathrm{III}} \leqslant -\sigma_{\mathrm{m}} \quad \text{at point (b)}. \tag{4.25b}$$

In the way our micro-contacts are defined (Figure 4.1), the tangential traction field at the interface oriented in the x direction has discontinuities from 0 to q at the borders of the micro-contacts, which leads to stress singularities (regions of infinite stresses) in the other directions inside the solid around those places (Johnson 1985), also leading to infinite principal stresses. Therefore, the crack initiation criterion (4.25) can always be satisfied somewhere on the borders of the micro-contacts.

4.3 SINGLE SHEARED MICRO-CONTACT AND CRITICAL SIZE

In order to define a critical junction size as in Aghababaei *et al.* (2016), we consider a single circular micro-contact of diameter d. The stored elastic energy stored by tangentially loading the micro-contact can be calculated analytically from (4.6). Only the component p_x of $\boldsymbol{p}$ is non-zero, and we can write p_x as

$$p_x(x,y) = c_q(x,y)q \tag{4.26}$$

where q is the value of the uniform tangential load and $c_q(x,y)$ is a function describing the shape of the micro-contact, in this case equal to 1 when $r = \sqrt{x^2+y^2} < d/2$ and 0 otherwise. $p_x \star p_x$ is easier to calculate than $u^{\mathrm{ker}}_{x\to x} * p_x$, which means that we can use (4.15) to calculate the elastic energy. We have

$$p_x \star p_x = (c_q \star c_q)q^2 \tag{4.27}$$

which is an autocorrelation, calculable geometrically. As c_q is a circle of diameter $d/2$, $[c_q \star c_q](x,y)$ is equal to the area of the intersection between two circles of diameter $d/2$ with a distance $r = \sqrt{x^2+y^2}$ between their centers:

$$C(x,y) = [c_q \star c_q](x,y) = \frac{d^2}{2}\cos\left(\frac{r}{d}\right) - \frac{r}{2}\sqrt{d^2-r^2}, \tag{4.28}$$

where we called C the autocorrelation of c_q. In (4.15), this autocorrelation multiplies $u^{\text{ker}}_{x\to x}$ (4.3)

$$u^{\text{ker}}_{x\to x} = \frac{1}{4\pi G}\left[2(1-\nu)\frac{1}{r} + 2\nu\frac{x^2}{r^3}\right],$$

which has a $1/r$ component and a x^2/r^3 component. Using polar coordinates and with the help of the *Python* symbolic library *Sympy* (Meurer *et al.* 2017), we get the integrals of the products with the components:

$$\int_\Gamma \frac{1}{r} C\, d\Gamma = \frac{2\pi d^3}{3}, \tag{4.29}$$

$$\int_\Gamma \frac{x^2}{r^3} C\, d\Gamma = \frac{\pi d^3}{3}. \tag{4.30}$$

From those, we easily recover the expression of the elastic energy for a single circular micro-contact:

$$E_{\text{el},1} = \frac{1}{2}\int_\Gamma \frac{1}{4\pi G}\left[2(1-\nu)\frac{1}{r} + 2\nu\frac{x^2}{r^3}\right] C q^2\, d\Gamma \tag{4.31}$$

$$= \frac{1}{8\pi G}\left[2(1-\nu)\frac{2\pi d^3}{3} + 2\nu\frac{\pi d^3}{3}\right] q^2 \tag{4.32}$$

$$= \frac{(2-\nu) d^3 q^2}{12 G}. \tag{4.33}$$

The corresponding adhesive energy required to detach a hemispherical wear particle under this circular micro-contact is given in (4.16). From these two expressions, we obtain the energy ratio from (4.17):

$$\mathcal{R} = \frac{(2-\nu) d q^2}{12\pi\gamma G}. \tag{4.34}$$

The maximum tangential load q which can be applied on the micro-contact is equal to the shear strength σ_j of the junction between the two surfaces in contact. After setting $q = \sigma_\text{j}$ in the expression of $\mathcal{R}$, we look for the value of d which makes $\mathcal{R}$ satisfy the energy balance criterion (4.18). We find a critical diameter:

$$d^* = \frac{12\pi\gamma G}{(2-\nu)\sigma_\text{j}^2} \tag{4.35}$$

which only depends on material parameters. The energy balance criterion is satisfied whenever $d \geqslant d^*$. Note that the expression of d^* found in this geometrical configuration is in accordance with the expression found by Aghababaei *et al.* (1.13) with a newly defined geometrical factor. The infinite factor $\mathcal{M}$ found in 2D (previous chapter) is now absent from the expressions of $\mathcal{R}$ and d^*.

A single sheared micro-contact of diameter d can result in the detachment of a wear particle if $d \geqslant d^*$ and otherwise flows plastically.

4.4 INTERACTION OF TWO MICRO-CONTACTS

To study the elastic interactions between multiple micro-contacts in the same manner as the two-dimensional model of the previous chapter, we start by considering two tangentially loaded circular micro-contacts of diameters d and having a distance l between their centers, as shown in Figure 4.3. They are tangentially loaded in the x direction with a pressure of magnitude σ_j and the line going through both of their centers makes an angle θ with the x axis.

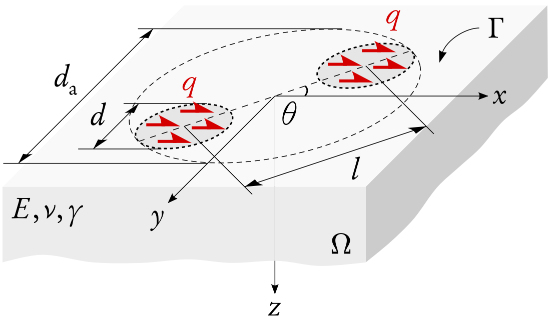

Figure 4.3 – Two circular contacts under uniform tangential load. d_a is the "apparent" diameter of a hemispherical particle that would encompass both micro-contacts, and θ is the angle between the direction of the load and the line going through the centers of the micro-contacts.

Elastic energy

Again, we use (4.15) to calculate the stored elastic energy by hand. In this case, following the notation of Section 4.3, c_q is made of two circular regions of diameter d with a space l between their centers and having the line connecting their centers making an angle θ with the x axis. The autocorellation $\mathcal{C}_2$ of c_q in this case can be written as a function of $\mathcal{C}$ (4.28) for a single micro-contact:

$$\mathcal{C}_2(x,y) = 2\mathcal{C}(x,y) + \mathcal{C}(x - l\cos\theta, y - l\sin\theta) + \mathcal{C}(x + l\cos\theta, y + l\sin\theta), \tag{4.36}$$

which has a centered component $2\mathcal{C}(x,y)$ and two side components. The centered component simply gives a $2E_{\mathrm{el},1}$ contribution to the total elastic energy. The integrals of the products of the side components with the terms $1/r$ and x^2/r^3 of $u^{\mathrm{ker}}_{x\to x}$ have to be approximated by assuming that x and r do not vary much in the region where the side components of $\mathcal{C}_2$ are non-zero. We have :

$$\int_\Gamma \frac{1}{r}\mathcal{C}(x \pm l\cos\theta, y \pm l\sin\theta)\, d\Gamma \approx \frac{1}{l}\int_\Gamma \mathcal{C}(x \pm l\cos\theta, y \pm l\sin\theta)\, d\Gamma \tag{4.37}$$

$$= \frac{\pi^2 d^4}{16 l}, \tag{4.38}$$

$$\int_\Gamma \frac{x^2}{r^3}\mathcal{C}(x \pm l\cos\theta, y \pm l\sin\theta)\, d\Gamma \approx \frac{\cos^2\theta}{l}\int_\Gamma \mathcal{C}(x \pm l\cos\theta, y \pm l\sin\theta)\, d\Gamma \tag{4.39}$$

$$= \frac{\pi^2 d^4 \cos^2\theta}{16 l}. \tag{4.40}$$

Using (4.15), we finally get:

$$E_{\mathrm{el},2} = \frac{1}{2}\int_\Gamma \frac{1}{4\pi G}\left[2(1-\nu)\frac{1}{r} + 2\nu\frac{x^2}{r^3}\right]\mathcal{C}_2 q^2\, d\Gamma \tag{4.41}$$

$$\approx 2E_{\mathrm{el},1} + 2\frac{1}{8\pi G}\left[2(1-\nu)\frac{\pi^2 d^4}{16 l} + 2\nu\frac{\pi^2 d^4\cos^2\theta}{16 l}\right]q^2 \tag{4.42}$$

$$= 2E_{\mathrm{el},1} + \frac{1}{32\pi G}\left[\frac{\pi^2 d^4}{l} + \nu\frac{\pi^2 d^4(\cos^2\theta - 1)}{l}\right]q^2 \tag{4.43}$$

$$= \frac{(2-\nu)d^3 q^2}{6G} + \frac{\pi d^4 q^2}{32 G}\frac{1-\nu\sin^2\theta}{l}. \tag{4.44}$$

The approximation (4.44) is only exact in the limit when $l \gg d$, but is still very accurate when l reaches $l = d$, which is when the two micro-contacts are adjacent. The accuracy is verified by

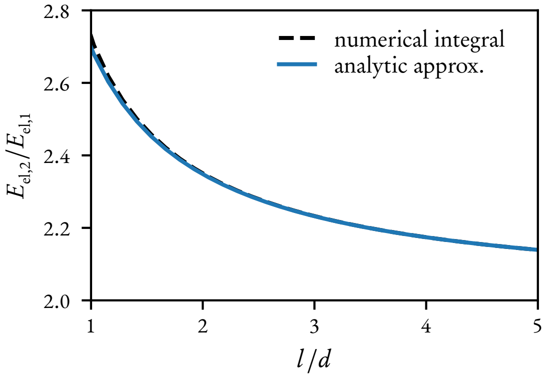

Figure 4.4 – Comparison of the numerical integration and the analytical approximation of the elastic energy stored under two tangentially loaded circular contacts. Here, $\nu = 0.3$ and $\theta = 0$. The analytical approximation is more accurate when l is large.

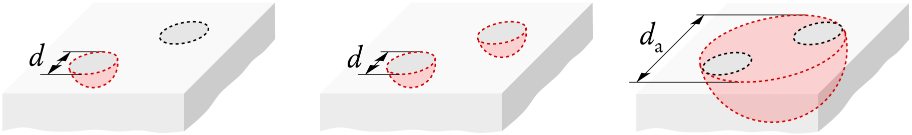

(a) One separated

(b) Two separated

(c) Combined

Figure 4.5 – Different cases of wear particle formation with two micro-contacts. The red surfaces show the surfaces created when a particle is detached. The case where no wear particle is detached is not shown. In case (a), either one of the junctions is equally likely to form a particle, as the stress state is symmetric (when also considering the sliding body on the top).

numerically integrating (4.6) for fixed values of d and l and comparing the results with (4.44), as shown in Figure 4.4.

The expression (4.44) consists in the sum of two terms. The left term is equal to $2E_{\mathrm{el},1}$ (4.33) and represents the energetic contributions of each circular micro-contact. The right term is proportional to $1/l$ and represents the effect of the elastic interactions between the two micro-contacts. When l is large compared to d, the right term vanishes and the two micro-contacts do not interact: the total energy is just the sum of their energies taken separately. When l decreases, the two micro-contacts get closer and the interaction term increases (see Figure 4.4).

Note that if the two micro-contacts were to be superimposed into a single circular micro-contact loaded at $2q$, the resulting elastic energy would reach $4E_{\mathrm{el},1}$, as (4.33) has a quadratic dependence on q. This would not happen in practice when $q = \sigma_\mathrm{j}$ since the tangential load is limited to σ_j, but it explains why the $E_{\mathrm{el},2}$ is necessarily bounded between $2E_{\mathrm{el},1}$ and $4E_{\mathrm{el},1}$.

Adhesive energy

With two loaded micro-contacts, several cases of wear particle formation may arise, as shown in Figure 4.5. There can be either zero, one or two separated wear particles at each micro-contact, or a single combined wear particle encompassing both micro-contacts. We call d_a (for *apparent* diameter) the diameter of the potentially formed combined wear particle. We have $d_\mathrm{a} = d + l$.

In the case of the formation of a single separated particle[1] the required adhesive energy to detach the particle is the same as (4.16):

---

[1] When there is enough energy to form only a single particle, a slight asymmetry in the system would select one of the two contact junctions and the other junction would deform plastically.

$$E_{\mathrm{ad,1sep}} = \pi\gamma d^2 . \tag{4.45}$$

In the case of the formation of two wear particles, the required adhesive energy is twice as big:

$$E_{\mathrm{ad,2sep}} = 2\pi\gamma d^2 , \tag{4.46}$$

and in the case of the formation of a combined wear particle, it is

$$E_{\mathrm{ad,comb}} = \pi\gamma d_{\mathrm{a}}^2 . \tag{4.47}$$

Energy balance criterion

Assuming that both micro-contacts get unloaded when the two separated wear particles or a single combined one are formed, the decrease of elastic energy ΔE_{el} in (4.17) is equal to $E_{\mathrm{el},2}$ (4.44). From the expression of ΔE_{el} and the different expressions of the adhesive energy for each case, we get the energy ratio

$$\mathcal{R} = \left(C_{\mathrm{n}} + \frac{3\pi}{8} C_{\mathrm{inter}} \frac{d}{l} \right) \frac{d}{d^*} C_{\mathrm{case}} \tag{4.48}$$

where $C_{\mathrm{n}} = 2$, and

$$C_{\mathrm{inter}} = \frac{1 - \nu \sin^2\theta}{2 - \nu} \tag{4.49}$$

is a constant controlling the amount of interaction, which only depends on the Poisson's ratio and the angle θ and has always a value between $1/3$ and $2/3$. Choosing $\nu = 0.5$ and $\theta = 0$ (micro-contacts aligned with the direction of the load) provides the most interaction with $C_{\mathrm{inter}} = 2/3$, whereas $\theta = \pi/2$ (line of the micro-contacts perpendicular to the direction of the load) gives the least amount of interaction with $C_{\mathrm{inter}} = 1/3$. We will discuss the implications of this in the next sub-section. The constant C_{case} has a value which depends on the case of particle formation. From the different adhesive energies $E_{\mathrm{ad,2sep}}$ (4.46) and $E_{\mathrm{ad,comb}}$ (4.47), we have $C_{\mathrm{case}} = 1/2$ or $C_{\mathrm{case}} = d^2/d_{\mathrm{a}}^2$ respectively. Note that the material parameters G, σ_{j} and γ do not appear directly in (4.48) and were conveniently replaced by the critical diameter d^* (4.35) which contains all those missing terms.

When only one micro-contact out of the two forms a wear particle and gets unloaded, the elastic energy goes from $E_{\mathrm{el},2}$ (4.44) to $E_{\mathrm{el},1}$ (4.33) with $q = \sigma_{\mathrm{j}}$, as the remaining micro-contact, flowing plastically, still carries a load of σ_{j}. Therefore, the decrease of elastic energy is $\Delta E_{\mathrm{el}} = E_{\mathrm{el},2} - E_{\mathrm{el},1}$, which with the expression of the adhesive energy $E_{\mathrm{ad,1sep}}$ (4.45) gives the energy ratio (4.48) with $C_{\mathrm{n}} = 1$ and $C_{\mathrm{case}} = 1$.

4.5 WEAR MAP

When we derived the energy ratio for a single micro-contact and the formation of a single wear particle (4.17), we were able to find a critical diameter d^* which easily defines which behavior is expected (plastic flow or formation of a particle). The expressions of the energy ratio $\mathcal{R}$ for two micro-contacts (4.48) are more complicated, as they now depend on d, l, d^* and C_{inter}.

Figure 4.6 shows our best attempt to represent the different possible scenarii of wear particle formation as a function of model parameters. We refer to Figure 4.6 as a *wear map*. Each colored region shows where $\mathcal{R} \geqslant 1$ for a selected value of C_{case} and therefore tells that the indicated behavior

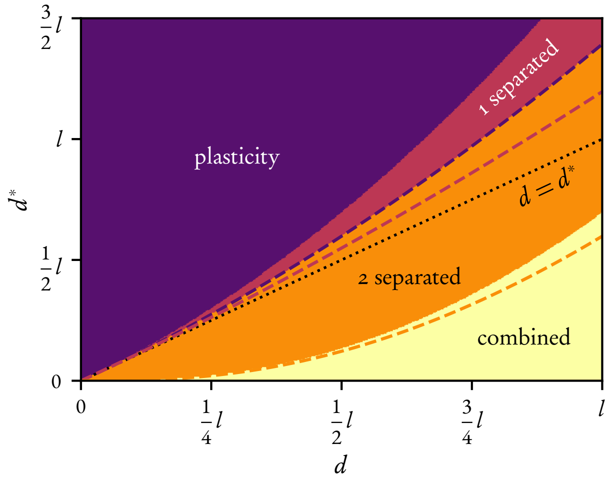

Figure 4.6 – Wear map of the different cases of wear particle formation under tangentially loaded two micro-contacts. The colored regions are computed at maximum possible elastic interaction ($\nu = 0.5$, $\theta = 0$). The dashed colored lines show the boundaries the regions would have at minimum interaction ($\nu = 0.5$, $\theta = \pi/2$).

is energetically feasible, depending on the contact junction size d and the critical junction size d^*, both expressed relative to l. The colored regions in Figure 4.6 are computed at maximum interaction with $C_{\text{inter}} = 2/3$. The dashed colored lines show the boundaries that those regions would have if $C_{\text{inter}} = 1/3$, that is at minimum interaction. Clearly, increasing elastic interactions favors wear particle formation.

The black dotted line $d = d^*$ in Figure 4.6 is given for comparison with the single micro-contact case. Indeed, such a system would be in a plastic regime when $d < d^*$, which is the whole region above the dotted line, and it would allow the formation of a wear particle when $d \geqslant d^*$, which is the region below the line. The wear map predicts that with two interacting micro-contacts, it is possible to form one and even two wear particles, even if the size of each micro-contact is smaller than the minimum required d^*. Once more, we emphasize that this is because of elastic interactions, which make the available stored elastic energy larger than trivially expected, as explained by (4.44).

The wear map hints toward the emergence of multiple wear regimes. The "plasticity" region corresponds to theoretically no wear volume, as the sliding surfaces only get plastically remodeled. This behavior can be linked to the experimental observations of low wear. In contrast, the jump in wear volume between the "2 separated" and the "combined" regions is significant and can be related to the transition between a mild and a severe wear regime.

CONCLUDING REMARKS

It is possible to derive wear maps for larger numbers of micro-contacts and other arrangements, following the same derivation for the analytical approximation of the elastic energy. Molinari & Pham-Ba (2022) takes this idea even further by optimizing a distribution of micro-contacts on a surface that leads to a maximized stored elastic energy under shear. We will show in the next chapter that more interesting results involving wear can be obtained using numerical simulations with generic rough surfaces while following the same energetic principles.

CHAPTER 5

FROM MICRO-CONTACTS TO WEAR REGIMES

Disclaimer

This chapter is reproduced in part from S. Pham-Ba and J.-F. Molinari (2021a), “Adhesive wear regimes on rough surfaces and Interaction of micro-contacts”, *Tribology letters* 69.3, with permission from all authors. My personal contribution was developing the model, designing and performing the numerical study, and writing.

INTRODUCTION

ELASTIC interactions between a large number of micro-contacts with varying sizes and shapes, as occurs during loading of self-affine surfaces, is largely unexplored and is the focus of the present chapter. As already briefly mentioned in the introduction of this document, Frérot *et al.* (2018) and Brink *et al.* (2021) used BEM to simulate the contact between two rough surfaces and obtain a map of the micro-contacts. Each micro-contact size is compared to d^* to assess if it can result in the formation of a wear particle. Frérot *et al.* estimate an instantaneous wear coefficient, while Brink *et al.* (2021) added the notion of sliding distance to compute a wear volume over time. These models give promising results, but their downside is that they do not take into account elastic interactions and assume that each micro-contact is isolated from the others, overlooking the potential transition to a severe wear regime. An interesting study by Popov & Pohrt (2018) also relies on BEM to compute the contact between rough surfaces. They use an energy balance criterion to determine if a wear particle can be detached, therefore accounting for elastic interactions. However, we will discuss how the approximation that was made in the released energy, while allowing for high computational efficiency, does not capture the full effect of the elastic interactions. As a consequence, they obtain wear particles that can enclose several junctions, but do not observe a transition to a severe wear regime.

This chapter explores a mesoscale mechanistic model for adhesive wear. In the context of self-affine surfaces in contact, the model aims to explain the emergence of different wear regimes as a function of normal load. The model of the previous chapter, formulated for only two micro-contacts, is numerically extended to the contact between self-affine rough surfaces, resulting in the description of three well-identified regimes of wear. A salient feature of the model is that the produced wear maps are function of well-defined physics-based model parameters, including material properties, surface roughness, and load.

5.1 Numerical model for random rough surfaces

Distribution of micro-contacts

We use our software Tamaas to generate discretized self-affine rough surfaces $h(x,y)$ with the PSD shown in Figure 5.1. The rough surfaces are discretized on a grid of $n \times n$ points, with $n = 512$, and of side-length L. Their parameters are the root mean square (RMS) of slopes $h'_{\mathrm{RMS}} = \sqrt{\langle |\nabla h|^2 \rangle}$, the Hurst exponent $\mathcal{H}$ and the frequencies q_{l} and q_{s} corresponding respectively to the largest and smallest wavelengths contained in the spectrum, where a frequency of the surface is given by $q = 2k\pi/L$, also called wavenumber, and k is a number ranging from 0 to $\lceil n/2 \rceil$. We set the roll-off frequency q_{r} at $q_{\mathrm{r}} = q_{\mathrm{l}}$.

Tamaas, primarily a BEM software, is used to efficiently solve the elastic contact between two rough surfaces, equivalently considered as the contact between a rigid rough surface (with equivalent roughness) and a flat deformable elastic solid. Figure 5.2 shows distributions of the contact pressure on a rough surface with $\mathcal{H} = 0.8$, $q_{\mathrm{l}} = 8$ and $q_{\mathrm{s}} = n/8$ for different normal loads. We normalize the normal load (Hyun *et al.* 2004):

$$\tilde{p}_{\mathrm{N}} = \frac{\sqrt{2\pi}}{h'_{\mathrm{RMS}}} \frac{p_{\mathrm{N}}}{E^*}, \tag{5.1}$$

where p_{N} is the normal load and

$$E^* = \frac{E}{1-\nu^2} \tag{5.2}$$

is the effective Young's modulus. At low normal loads, the normalized normal load $\tilde{p}_{\mathrm{N}}$ is a good approximation of the ratio between the real and the apparent contact area.

For given rough surface parameters q_{l}, q_{s} and $\mathcal{H}$, the normalized load $\tilde{p}_{\mathrm{N}}$ is the only free parameter for the description of the rough contact, and it combines the effect of the normal load and the RMS of heights. In the contact simulations, all the grid points where the local normal pressure is non-zero are in contact. They give the needed locations of micro-contacts.

Detachment of wear particles

We use the energy balance and the crack initiation criteria on the distribution of micro-contacts to determine the potential wear particle formation sites. Assuming a constant tangential load σ_{j} in the contact areas, the elastic energy can be numerically computed with (4.6). The procedure to find the maximum wear volume is the following:

1. Consider largest particle fulfilling crack initiation criterion;

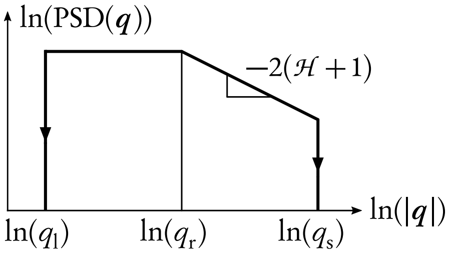

Figure 5.1 – Target PSD of generated rough surfaces. Its value is zero at frequencies $q < q_{\mathrm{l}}$ and $q > q_{\mathrm{s}}$. $\mathcal{H}$ is the Hurst exponent, q_{l}, q_{r}, and q_{s} are respectively the frequencies corresponding to the largest, roll-off and smallest wavelengths.

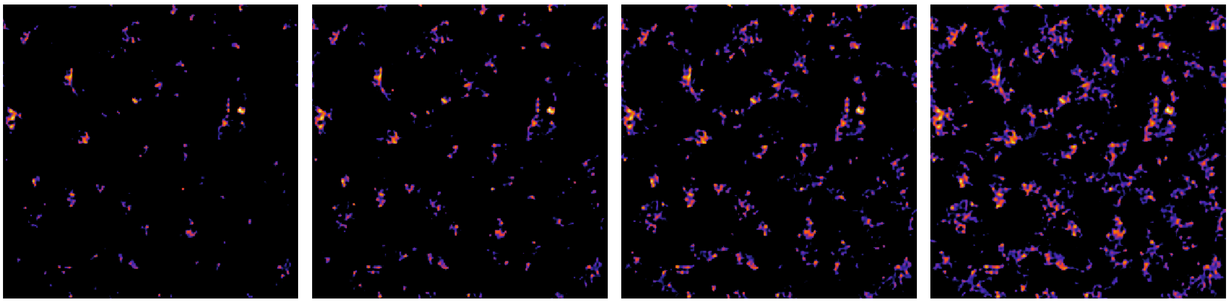

(a) $\tilde{p}_{\mathrm{N}} = 0.02$ (b) $\tilde{p}_{\mathrm{N}} = 0.05$ (c) $\tilde{p}_{\mathrm{N}} = 0.1$ (d) $\tilde{p}_{\mathrm{N}} = 0.2$

Figure 5.2 – BE simulations of the micro-contacts and local contact pressures for increasing normal load. The normalized normal load is indicated, which also corresponds to the ratio of real contact area to apparent contact area. Brighter color corresponds to a higher local pressure. For increasing normal load, the number and size of the micro-contacts increase, until micro-contacts become large enough to merge together, resulting in a drop in the number of contacts but a sharp rise of their average size. The surface roughness parameters are $n = 512$, $\mathcal{H} = 0.8$, $q_{\mathrm{l}} = 8$ and $q_{\mathrm{s}} = n/8$.

2. Unload corresponding region $\mathcal{C}$ (remove tangential loads) and compute the drop in elastic energy ΔE_{el};
3. If ΔE_{el} greater than needed E_{ad} (for a given d^*), save this particle removal; Else, try next largest particle;
4. Repeat until no more particles can be added.

After those steps, the remaining elastic energy should be small and insufficient to allow the creation of further particles. The position and size of each created particle are recorded for analysis.

As a result of this procedure, a list of wear particles (position and size) is obtained for any given value of $\tilde{p}_{\mathrm{N}}$ (controlling the micro-contacts) and d^* (controlling the ductile to brittle transition).

Note that this algorithm requires many consecutive explicit calculations of ΔE_{el} for testing the unloading of each possible particle (according to the crack initiation criterion) and is computationally expensive. Indeed, the creation of a particle unloads a portion $\mathcal{C}$ of the domain Ω, affecting the displacements, going from u_x to u_x' (computed with (4.5) for each possible $\mathcal{C}$), with $u_x' < u_x$ at every point of Ω (by the principle of superposition, less tractions are applied after unloading). The resulting expression of elastic energy release is therefore:

$$\begin{aligned}
\Delta E_{\mathrm{el}} &= \frac{1}{2}\int_{\Omega} p_x\, u_x\, d\Omega - \frac{1}{2}\int_{\Omega\setminus\mathcal{C}} p_x\, u_x'\, d\Omega \\
&= \frac{1}{2}\int_{\mathcal{C}} p_x\, u_x\, d\Omega + \frac{1}{2}\left(\int_{\Omega\setminus\mathcal{C}} p_x\, u_x\, d\Omega - \int_{\Omega\setminus\mathcal{C}} p_x\, u_x'\, d\Omega\right) \\
&= \frac{1}{2}\int_{\mathcal{C}} p_x\, u_x\, d\Omega + \frac{1}{2}\int_{\Omega\setminus\mathcal{C}} p_x\,(u_x - u_x')\, d\Omega. \qquad (5.3)
\end{aligned}$$

In comparison, to find at each iteration a detached particle, the approach of Popov and Pohrt (Popov & Pohrt 2018) estimates the energy release by integrating the local elastic energy density, without computing u_x'. In this case, the drop in elastic energy takes the form:

$$\Delta E_{\mathrm{el}} = \frac{1}{2}\int_{\mathcal{C}} p_x\, u_x\, d\Omega,$$

which misses the additional positive term present in (5.3). While less computationally intensive, the procedure adopted by Popov and Pohrt leads to an underestimation of elastic interactions.

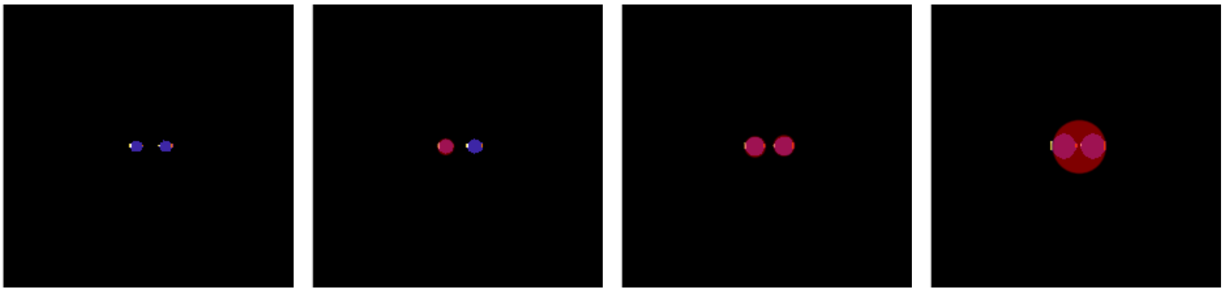

(a) Plasticity (b) 1 separated (c) 2 separated (d) Combined

Figure 5.3 – Different cases of wear particle formation with two micro-contacts in the numerical model. The blue regions are the micro-contacts. The red circles are the wear particles that can be detached. The small brighter spots are the regions of tensile and compressive stresses where the crack initiation criterion can be fulfilled.

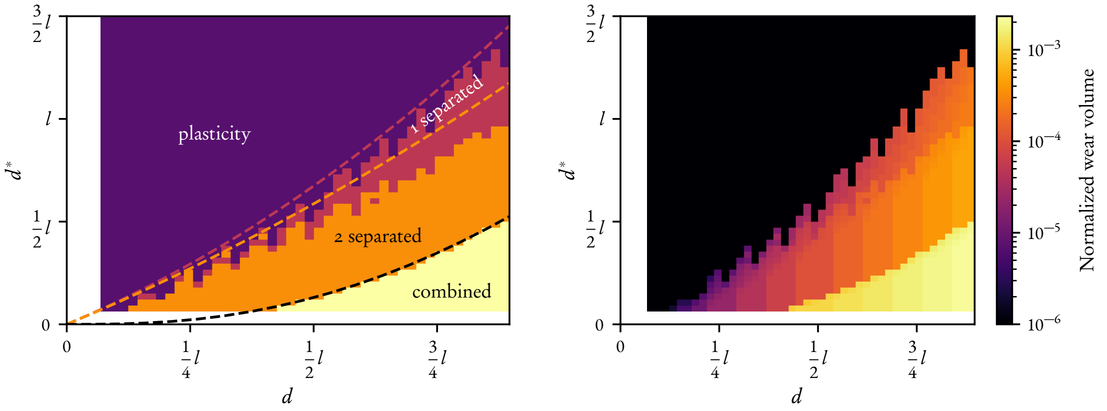

(a) Wear map (b) Wear volume

Figure 5.4 – Numerical wear maps for two circular micro-contacts. Here, $\theta = 0$ and $\nu = 0.3$. The jagged edges of the regions are due to the coarse discretization of the simulated surface. (a) Wear map deduced from the number of formed particles (0, 1, or 2) and their volume. The four regions of the analytical wear map (Figure 4.6) are recovered, and the analytical boundaries are shown with dashed lines. (b) The wear volume is normalized by L^3, where L is the side-length of the discretization surface.

As a consequence, a single power-law between wear volume and the applied pressure is found. There is no visible transition to severe wear, which only arises with proper accounting of elastic interactions.

5.2 Verification

The computation of the detachment of wear particles in the numerical model was tested with a setup consisting of two micro-contacts, for which we previously derived an analytical theory and constructed a wear map. We are choosing the micro-contacts to be aligned with the load ($\theta = 0$). Figure 5.3 shows the effect of increasing d for constant values of l and d^*. Looking at the wear map (Figure 4.6), this means moving on a horizontal line from left to right. As predicted by the wear map, there is a transition between all the possible behaviors of wear particle formation.

The numerically generated wear maps are shown in Figure 5.4. They are generated by varying the values of d and d^* and by computing the possible detachment of wear particles. Figure 5.4a shows the different behaviors deduced by the number of formed particles and their volume. It agrees with the analytical wear map (Figure 4.6) superimposed by dashed lines. Figure 5.4b indicates the corresponding wear volumes. It shows that in the lower right region of the wear map, a much higher wear volume is created, which corresponds to the “combined” behavior of particle formation. Note that the transition to this behavior is quite sharp.

5.3 WEAR MAPS AND WEAR REGIMES

The numerical model was run on five randomized rough surfaces with the roughness parameters $\mathcal{H} = 0.8$, $q_\mathrm{l} = 8$ and $q_\mathrm{s} = n/8$ (with $n = 512$). Examples of wear particle distributions are shown in Figure 5.5 and the averaged computed wear maps are given in Figure 5.6. Regions similar to the ones of the wear map for two micro-contacts can be found. The “plasticity” region is where no wear particles are detached. Then, for a constant d^* (*i.e.* for a given material), the number of particles increases with the load until reaching a maximum value, defining a region “separated” where separated particles can be formed, as shown in Figure 5.5a to g. Then, the number of particles decreases with the higher loads, entering the “combined” region, where large wear particles can encompass multiple micro-contacts. The wear volume increases monotonically with the load and reaches a plateau (the crossed areas in the wear maps), which is a non-physical numerical artifact caused by the fact that wear particles reach the size of the discretized system.

The effects of the material parameters can also be read on the wear maps since they are contained into d^*. According to our model, a material with a lower d^*, that would be harder or more fragile, should form smaller particles. The model also predicts that harder materials are more prone to generate combined particles from neighboring contact junctions.

However, the full volume of debris production is higher for a harder material, which seems in opposition to Archard’s wear model. This is a limitation of not accounting for the sliding history, as we discuss further below. It is also a consequence of assuming that our junctions all carry the material-specific shear strength σ_j, implying that harder materials are loaded tangentially with a larger force. As more mechanical work is imparted to the interface for hard materials, this results in larger wear volume production. The exact distributions of shear forces at micro-contacts should be examined in future work.

For an easier interpretation, the wear maps can be represented as curves (Figure 5.7), where each curve corresponds to a constant value of d^* and vary with the imposed load. Every point of each curve is the average between five measurements done with different randomized rough surfaces, and the standard deviation is indicated. To find the maximum number of particles reached by one curve without being sensitive to the statistical noise, a smoothed version is first computed using a Savitzky-Golay filter of degree 3 on a window of 11 points, and the maximum is determined on the filtered smooth curve. A study of the evolution of the wear volumes (Figure 5.7b) reveals the emergence of three wear regimes:

- There is no wear particle production until the normal load reaches a critical value. This range is the “plastic” region: the surfaces are only deformed plastically. This would correspond to the regime of *low wear*.
- Above a critical load, wear increases monotonically. This range goes roughly up to the point of maximum number of particles and would correspond to the regime of *mild wear*.
- For loads higher than the point of maximum number of particles, the slope of the curves increases quickly. This drastic increase of the wear volume would correspond to the regime of *severe wear*.

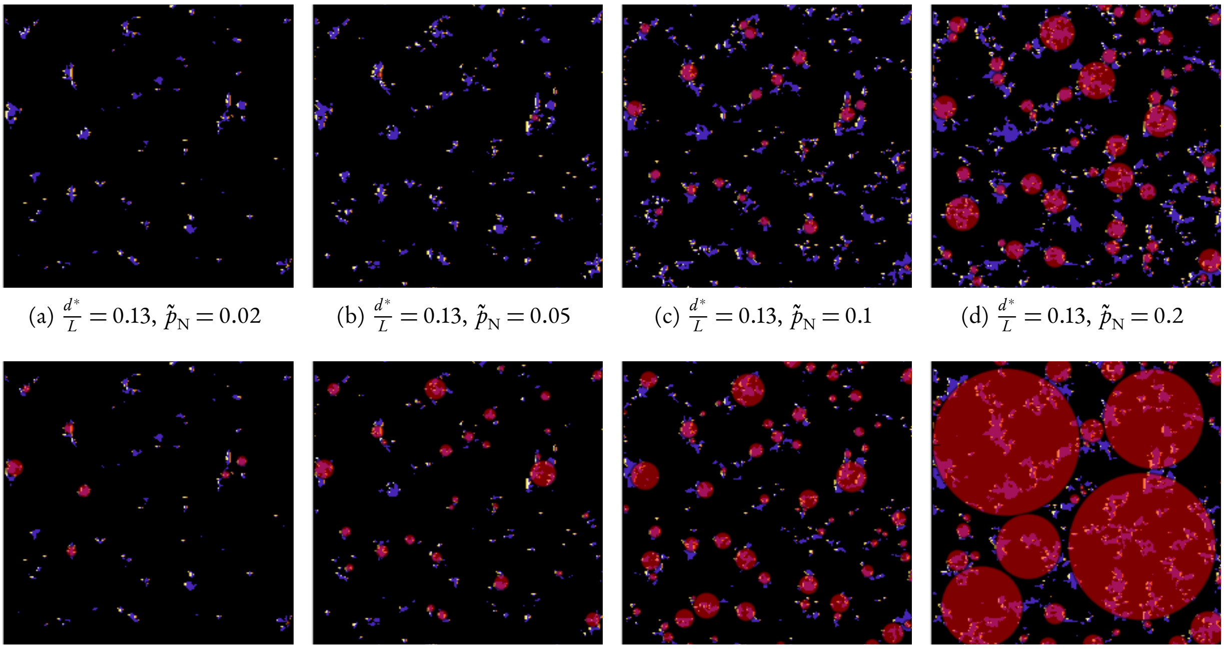

(a) $\frac{d^*}{L} = 0.13$, $\tilde{p}_{\mathrm{N}} = 0.02$
(b) $\frac{d^*}{L} = 0.13$, $\tilde{p}_{\mathrm{N}} = 0.05$
(c) $\frac{d^*}{L} = 0.13$, $\tilde{p}_{\mathrm{N}} = 0.1$
(d) $\frac{d^*}{L} = 0.13$, $\tilde{p}_{\mathrm{N}} = 0.2$

(e) $\frac{d^*}{L} = 0.04$, $\tilde{p}_{\mathrm{N}} = 0.02$
(f) $\frac{d^*}{L} = 0.04$, $\tilde{p}_{\mathrm{N}} = 0.05$
(g) $\frac{d^*}{L} = 0.04$, $\tilde{p}_{\mathrm{N}} = 0.1$
(h) $\frac{d^*}{L} = 0.04$, $\tilde{p}_{\mathrm{N}} = 0.2$

Figure 5.5 – Different cases of wear particle formation in a rough contact. (a)-(d) When the normal load increases, the number and size of wear particles increase, following the trend of the micro-contacts. (e)-(h) With a lower d^*, particles are generated at lower loads. Also, at high loads, elastic interactions promote the formation of less numerous and larger particles encompassing multiple micro-contacts, even if the distributions of micro-contacts are the same as above.

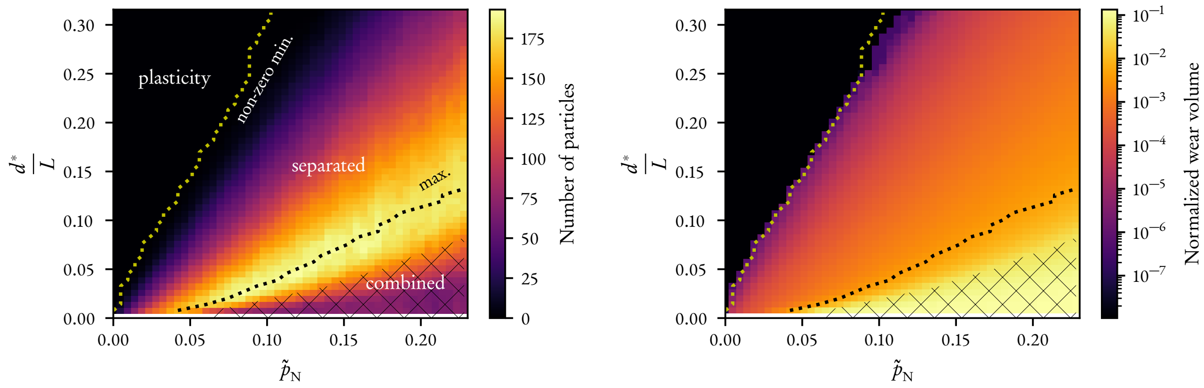

(a) Number of particles
(b) Wear volume

Figure 5.6 – Wear maps of the contact between rough surfaces. The map of the number of particles shows clearly distinct regions. Between the "separated" and "combined" regions, the number of particles decreases but the wear volume increases. The wear volume spans multiple orders of magnitude. The crossed area is the region where the numerical simulation validity is not guaranteed because the size of the wear particles becomes comparable to the size of the simulated system.

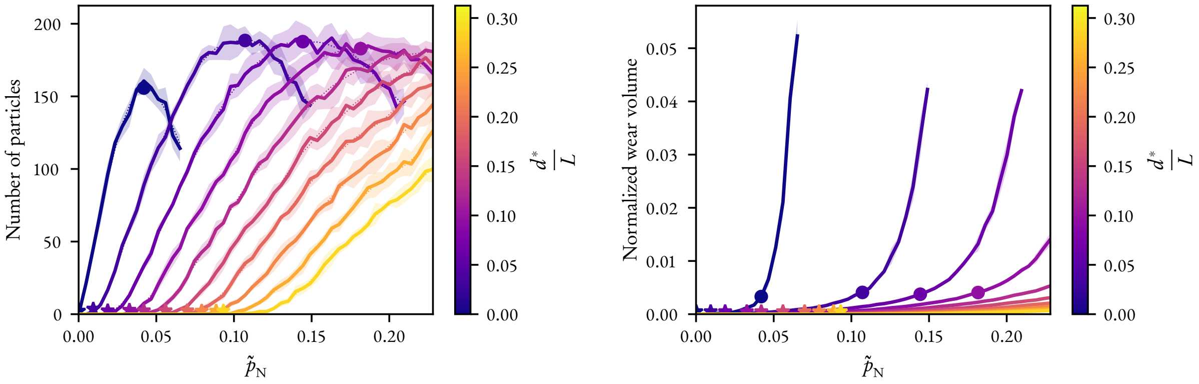

(a) Number of particles

(b) Wear volume

Figure 5.7 – Wear curves of the contact between rough surfaces. Each curve follows a horizontal line in the wear maps of Figure 5.6. The filled areas represent the standard deviation. The first non-zero value of each curve is shown by a star. The maximum number of particles reached by each curve is shown by a dot. The invalid parts of the curves (shown crossed in the wear maps) are cut. (b) The evolution of the wear volume with $\tilde{p}_N$ notably shows the transition between a regime with zero wear volume (to the left of each star) to a regime where the wear volume increases with the load. All the curves follow the same trend, although with a horizontal shift. For a given curve, between the star and the dot, the wear volume increases steadily. The slope increases drastically around the dot, indicating a transition to a severe wear regime.

The ability of our model to predict a regime of severe or catastrophic wear is novel among the similar existing models (Frérot *et al.* 2018; Brink *et al.* 2021), as these models limit the formation of each wear particle to occur under a single micro-contact. The maximum instantaneous wear volume is thus limited by the size and number of micro-contacts, whereas our model takes into account elastic interactions and permits the creation of wear particles larger than a single micro-contact. One advantage of the model of Brink *et al.* is that it simulates the sliding process, and reaches a steady-state wear rate. This procedure is unfortunately not applicable for our model because of the high computational cost to compute even a single pixel of a wear map. In consequence, our model can only predict an instantaneous wear volume and has no notion of sliding distance. Brink *et al.* showed that simulating the sliding history is key to recovering Archard's model, stating that harder materials wear less. The current model gives the opposite trend. A computationally efficient procedure to account both for the sliding history, as in Brink *et al.*, as well elastic interactions for wear particle generation, will be the topic of future work.

It is also worth noting that our model predicts the possibility of forming wear particles smaller than d^*, as shown by Figure 4.6 and Figure 5.5a to d, which is surprising since d^* is generally thought of as the minimum possible wear particle size. This effect can also be related to sliding not being considered in our model. As sliding dissipates energy, it would affect the remaining energy available for the creation of such small wear particles. The possibility of forming wear particles smaller than d^* in the absence of sliding is worthy of investigation either experimentally or numerically using FE or MD simulations. In the case where the possibility of creating wear particles smaller than d^* were to be invalidated, our results would not be significantly impacted. The "plasticity" zone in Figure 5.6 would simply extend on a larger range of normal load, and the three identified wear regimes would remain present.

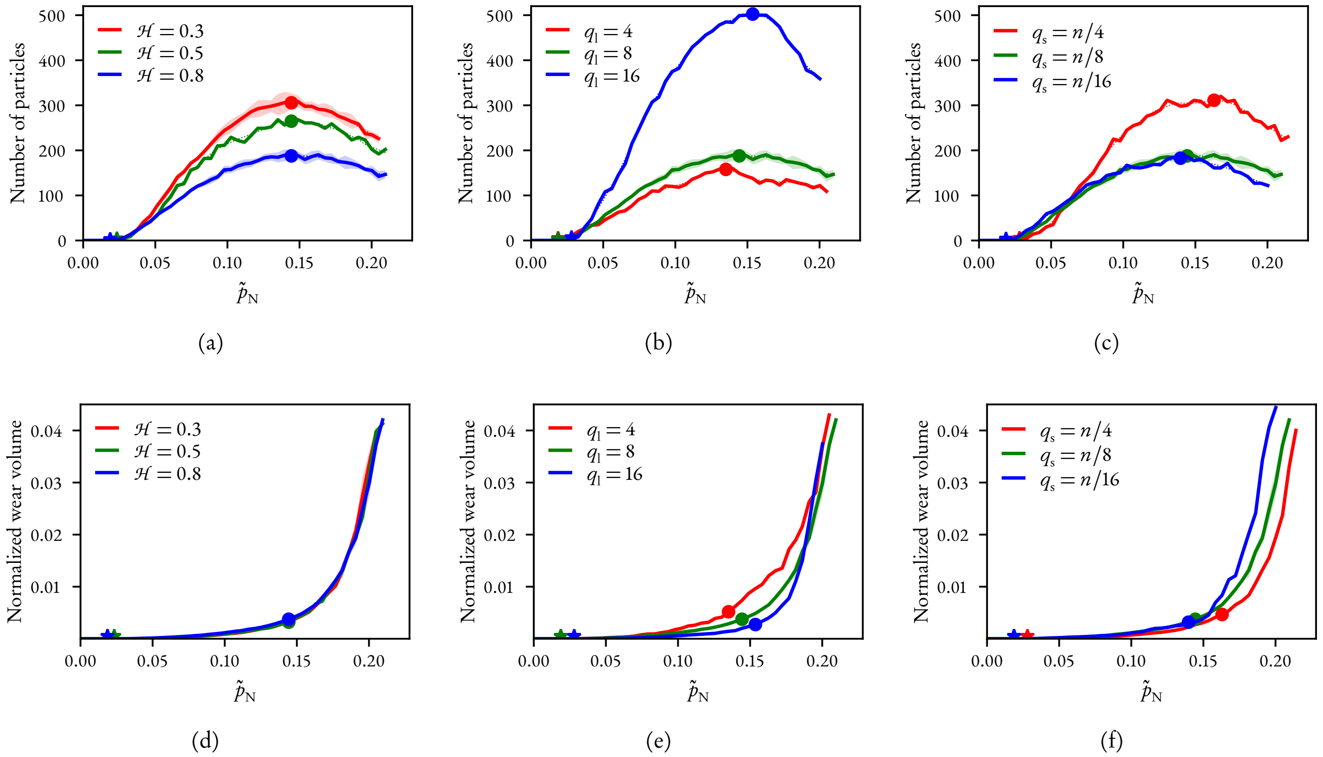

(a) (b) (c)

(d) (e) (f)

Figure 5.8 – Effect of the roughness parameters on the wear curves. Here, $d^*/L = 0.07$ and $n = 512$. Only the curves with the sets of parameters $\mathcal{H} = 0.8$, $q_l = 8$, $q_s = n/8$ and $\mathcal{H} = 0.3$, $q_l = 8$, $q_s = n/8$ were computed with five repetitions, so their wear curve is averaged and a standard deviation is shown. The curves for the other sets of parameters are computed from only one rough surface and thus are more subject to statistical noise.

5.4 ROUGHNESS PARAMETERS

The wear maps and curves of the previous section were computed for a unique set of roughness parameters, namely $\mathcal{H} = 0.8$, $q_l = 8$ and $q_s = n/8$. The effects of varying the parameters $\mathcal{H}$, q_l and q_s is assessed by running the simulations listed in Table 5.1 and comparing the curves of number of particles and wear volume. The Figure 5.8 shows such comparison for a single value of $d^*/L = 0.07$ in order to not overload the plots. Note that the RMS of slopes h'_{RMS} is also a roughness parameter, but its effect is already taken into account in the normalized imposed load $\tilde{p}_N$.

Table 5.1 – List of roughness parameters for the production of wear maps and curves

$\mathcal{H}$	q_l	q_s	Repetitions
0.8	8	$n/8$	5
0.5	8	$n/8$	1
0.3	8	$n/8$	5
0.8	4	$n/8$	1
0.8	16	$n/8$	1
0.8	8	$n/4$	1
0.8	8	$n/16$	1

The Figures 5.8a and d show the effect of the Hurst exponent $\mathcal{H}$. One physical interpretation of $\mathcal{H}$ in the context of self-affine rough surfaces is that a surface of size L with a roughness of characteristic height H can be viewed on a window of size αL, and the new roughness viewed on this window would have a roughness with characteristic height $\alpha^{\mathcal{H}} H$. It means that for $\mathcal{H} = 1$, the surface roughness always look the same in the range of self-affinity (*i.e.* with $q_\mathrm{l} < q < q_\mathrm{s}$) regardless of the scale of observation. A surface with a smaller $\mathcal{H}$ will look flatter if zoomed-out and rougher if looked at from a smaller scale. In Figure 5.8a, we see that the rough surfaces with a lower $\mathcal{H}$ can produce more wear particles, but smaller, as the overall wear volume (Figure 5.8d) is surprisingly independent of $\mathcal{H}$.

The frequency parameters q_l and q_s control the region (scaling) of fractal self-affinity of a rough surface. q_l controls the lower frequencies, so a lower value means higher large-scale features. q_s controls the smaller length scales, so a higher value means smaller rough features. The trends shown by the Figures 5.8b and c are in accordance with this description: at higher values of q_l, a rough surface look flatter because the lower frequency shapes are absent, which promotes more contact on the smaller "bumps" on the surface and thus the creation of more wear particles. The trend is the same when q_s decreases, as more smaller bumps appear and contribute to the rise of the number of wear particles. Still, the total wear volume remains only weakly affected by the change of these roughness parameters.

Overall, while the number of produced particles varies with the roughness parameters, the wear volumes remain relatively unaffected. The three previously identified wear regimes also remain untouched. This invariance with the roughness parameters implies that the wear mechanisms are supposedly not affected by the details of the fractal description of the rough surfaces in contact, and that they can be described solely by d_c^* which includes the material parameters E, ν, σ_j and γ, and by $\tilde{p}_\mathrm{N}$, which is linked to the imposed normal load p_N and the RMS of slopes h'_RMS of the rough surface. However, this only takes into account an instantaneous measurement of the total wear volume. Actually, the size of the produced wear particles is dictated by the fractal parameters, and the size of the detached particles may dictate how the surface roughness *evolves* over time (effectively changing h'_RMS, thus $\tilde{p}_\mathrm{N}$). The wear particles themselves may contribute to the tribological properties of the interface, so that their size would be a matter of importance.

CONCLUDING REMARKS

A model of adhesive wear was developed analytically and implemented numerically. The model takes into account elastic interactions between several nearby micro-contacts and allows for the formation of combined wear particles encompassing multiple micro-contacts. A salient result is that a wear particle is not necessarily formed under a single junction, which challenges the definition of what amounts to a contact junction in the context of adhesive wear. The model is based on two criteria: an energy balance and a crack initiation criteria. It predicts the transition from a regime of low wear (with zero wear volume) to a regime of mild wear, and finally to a regime of severe wear, emerging thanks to the consideration of the elastic interactions. The instantaneous wear volume is predicted from the material parameters, the loading conditions, and roughness parameters. Hard materials favor elastic interactions and combined wear particles.

Chapter 6

Bridging scales with a coarse-grained discrete element model

Disclaimer

This chapter is reproduced in part from S. Pham-Ba and J.-F. Molinari (2022), "Adhesive wear with a coarse-grained discrete element model", *Computer methods in applied mechanics and engineering* 397, with permission from all authors. My personal contribution was developing and implementing the model, running the simulations, post-processing the results, and writing.

Introduction

Molecular dynamics simulations were used to study systems ranging from the wear of a single asperity (Aghababaei *et al.* 2016; Aghababaei *et al.* 2017; Zhao & Aghababaei 2020; Aghababaei & Zhao 2021) to the growth of multiple third-body particles trapped between two sliding surfaces in three dimensions (Aghababaei *et al.* 2018; Milanese *et al.* 2019; Brink *et al.* 2022). The latter simulations show that the rolling particles grow into rolling cylinders and merge together into a gouge layer, with a noticeable effect on the macroscopic tangential force resisting the sliding motion. The formation of rolling cylinders and of a gouge layer from third-body particles is also observed experimentally (Chen *et al.* 2017; Pham-Ba & Molinari 2021b), showcasing the importance of modeling multiple third-body particles and their interactions during sliding. However, the largest adhesive wear MD simulations (*e.g.* by Brink *et al.* (2022)) start to reach a computational barrier, having around 35 000 000 atoms per simulation. Due to the very small size of the atoms simulated in MD (order of 1 Å), the simulations are limited both in space and in time (the time step must also be small, of the order of 1 ps).

Having possibly reached the maximum capabilities of MD regarding scale, other methods must be used to further increase the size of the simulated worn systems and explore the effects of collective mechanisms, as these mechanisms are ultimately responsible for the macroscopic wear response. Despite the small scale disadvantage, the benefit of MD simulations is to seamlessly model, with simple force potentials, particle rearrangements such as fracture and mixing of materials, which is much more challenging to achieve in continuum methods like the widely used finite element method. To preserve the advantages of MD while going to larger scales, we propose to resort to DEM to coarse-grain the particle interactions. The current capabilities and usages of DEM are enumerated in Section 2.2.

To perform the same kind of adhesive wear simulation as with MD but using DEM, we aim to model a solid with known elastic and fracture properties, and the fracture process must be reversible to capture the growth of rolling third-body particles in a sheared interface, which involves reattachment of matter due to adhesive forces. We formulate a DE method suited for this problem, with relatively simple pair forces to remain computationally inexpensive. The interaction forces have a repulsive part and a reversible cohesive part, inspired by the most simple MD pair forces (*e.g.* Lennard-Jones). However, instead of applying coarse-graining to atoms with known properties, the parameters of the pair forces are directly expressed in terms of macroscopic material properties and particle size. In Section 6.1, we present our formulation of pair forces and explain how its parameters are tuned to match elastic and fracture properties with an assembly of many particles. Then, in Section 6.2, the model and the choice of its parameters are validated using simple patch tests. Finally, we show in Section 6.3 an example of application of the adhesive wear of a single junction between two sliding surfaces, similar to what was done using MD (Aghababaei *et al.* 2016).

6.1 METHOD

The three dimensional physical system is discretized into many spherical particles (each identified by an index i) of radius r_i and density ρ (see Table 6.1 for a list of used symbols). Forces of interaction are acting between every pair of distinct particles, and the particles' velocities and positions are updated accordingly using the second-order velocity-Verlet with a time step Δt. For any given particle, the integration scheme between steps n and $n+1$ is

$$\boldsymbol{x}_{n+1} = \boldsymbol{x}_n + \boldsymbol{v}_n \Delta t + \frac{\boldsymbol{F}_n}{m} \frac{\Delta t^2}{2}, \tag{6.1a}$$

$$\boldsymbol{v}_{n+1} = \boldsymbol{v}_n + \frac{\boldsymbol{F}_n + \boldsymbol{F}_{n+1}}{2m} \Delta t, \tag{6.1b}$$

$$\boldsymbol{\omega}_{n+1} = \boldsymbol{\omega}_n + \frac{\boldsymbol{T}_n + \boldsymbol{T}_{n+1}}{2I} \Delta t, \tag{6.1c}$$

where $\boldsymbol{x}_n$, $\boldsymbol{v}_n$ and $\boldsymbol{\omega}_n$ are respectively the velocity, the position and the angular velocity of the particle, $\boldsymbol{F}_n$ and $\boldsymbol{T}_n$ are the force and the torque acting on the particle in step n, m is the mass of the particle, and I is its moment of inertia. This integration scheme is the one currently implemented in the open-source software LAMMPS (Plimpton 1995) we are using.

Table 6.1 – List of symbols used for lengths and sizes

Symbol	Description
d	Particle diameter
$d_{\min}$	Minimum acceptable particle diameter
d_c	Critical particle diameter
d_0	Average particle size
d_s, d_l	Smallest and largest bounds in size distribution
d^*	Critical material length scale
D	Junction size
r_i, r_j	Particle radii
δ_N, δ_T	Normal and tangential particle separations
δ_e	Elastic separation
δ_f	Fracture separation

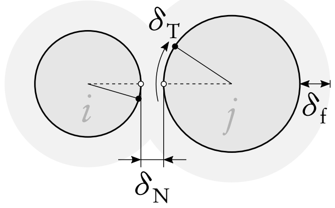

Figure 6.1 – Two interacting particles

For each pair of particles (i, j), we define the normal distance δ_N between their surfaces, and the tangential sliding distance δ_T (see Figure 6.1). The normal distance is simply equal to $d_{ij} - r_i - r_j$, with d_{ij} being the distance between the particles' centers. We have $\delta_N = 0$ when the particles are touching and $\delta_N < 0$ when they are interpenetrated. The tangential sliding distance δ_T is only defined when the particles are within their range of interaction (shaded area around particles in Figure 6.1, more details later). δ_T is equal to 0 when the particles start interacting, and is updated using the relative rolling velocity (Wang *et al.* 2015). δ_T is always positive (or equal to zero).

6.1.1 *Forces between particles*

The force $\boldsymbol{F}$ acting between a given pair of particles is the sum of a normal component F_N, a tangential component F_T, and velocity damping forces:

$$\boldsymbol{F} = -(F_N + c_N v_N)\boldsymbol{n}_N - (F_T + c_T v_T)\boldsymbol{n}_T, \tag{6.2}$$

where $\boldsymbol{n}_N$ and $\boldsymbol{n}_T$ are the unit vectors pointing respectively in the normal and tangential directions, the latter being computed using the evolution of the rolling velocity (Wang *et al.* 2015), v_N and v_T are the corresponding relative velocities at the point of interaction, and c_N and c_T are damping factors. Since the total force $\boldsymbol{F}$ acts on the surface of the particles, it also induces torques $\boldsymbol{T}$ (when seen from the centers of the particles), computed directly from $\boldsymbol{F}$ and the appropriate moment arms. In order to model an elastic solid with discrete particles, cohesive forces between particles are needed in addition to the usually modeled repulsive contact forces, all of which are defined thereafter.

Normal force

The normal component of the pairwise force depends on the inter-particular distance δ_N and has the profile shown in Figure 6.2. When the particles are interpenetrating ($\delta_N \leqslant 0$), they feel a Hookean repulsive force $F_N = k_N \delta_N$, where k_N is the normal stiffness. When the particles are not touching ($\delta_N > 0$), we model a cohesive force by keeping the Hookean force up to a separation

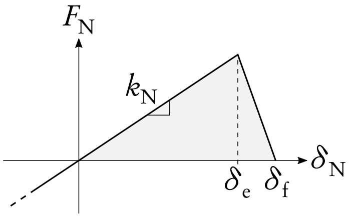

Figure 6.2 – Normal force between two particles as a function of inter-particular distance δ_N. There is interpenetration when $\delta_N < 0$. The force has a cohesive part when $\delta_N > 0$.

δ_e, until which the interaction between the particles is *elastic* (hence the subscript letter "e" in δ_e). The fracture process is modeled by a linear weakening zone between the elastic separation δ_e and a *fracture* separation δ_f (see Figures 6.1 and 6.2). When $\delta_N > \delta_f$, the particles are not interacting, and the total force is zero. The full expression of the normal force is

$$F_N = \begin{cases} k_N \delta_N & \text{if } \delta_N \leqslant \delta_e, \\ -\dfrac{k_N \delta_e}{\delta_f - \delta_e}(\delta_N - \delta_f) & \text{if } \delta_e < \delta_N \leqslant \delta_f, \\ 0 & \text{otherwise.} \end{cases} \tag{6.3}$$

The value of the normal force F_N is independent of the history of δ_N. Therefore, the fracture process is fully reversible, and particles can create or recreate new "bonds" with neighboring particles. We make the simplifying assumption that newly created bonds have the same properties (stiffness, strength) as previously existing bonds, which is not always the case in reality, as some phenomena can weaken the reattachment (*e.g.* surface roughness or oxidation).

Tangential force

The tangential component of the force depends on the sliding distance δ_T and has the profile shown in Figure 6.3. When the particles are interpenetrating, the force has the expression $F_T = k_T \delta_T$ up to a maximum value of $F_{m,T}$. When the particles are not touching but still in their range of interaction ($0 < \delta_N \leqslant \delta_f$), the maximum reachable force $F_{m,T}$ is decreased from its original value (at $\delta_N = 0$) toward zero at $\delta_N = \delta_f$. The full expressions of the tangential force F_T and the rescaled maximal tangential force $F'_{m,T}$ are

$$F_T = \min(k_T \delta_T, F'_{m,T}), \tag{6.4}$$

$$F'_{m,T} = \min\left(\frac{\delta_f - \delta_N}{\delta_f}, 1\right) F_{m,T}. \tag{6.5}$$

The considered tangential force is not a frictional force, typically used in DEM. It is instead an elastic force, originating from the attraction between the atoms constituting the discrete particles. This explains how a non-zero tangential force can exist even if the particles are separated ($\delta_N > 0$).

List of force parameters

In summary, there are 7 parameters, listed in Table 6.2.

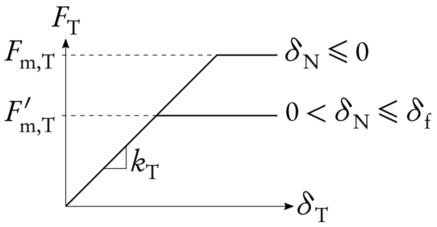

Figure 6.3 – Tangential force between two particles as a function of sliding distance δ_T. When the particles are in contact ($\delta_N \leqslant 0$), the tangential force is bounded by $F_{m,T}$, whereas when they are not touching but still in their range of interaction ($0 < \delta_T \leqslant \delta_f$), the force is bounded by $F'_{m,T}$. The corrected bound force $F'_{m,T}$ is equal to $F_{m,T}$ when $\delta_N = 0$ and decreases linearly down to 0 when $\delta_N = \delta_f$.

Table 6.2 – List of force parameters

Name	Symbol
Normal stiffness	k_N
Tangential stiffness	k_T
Elastic separation	δ_e
Fracture separation	δ_f
Maximum tangential force	$F_\mathrm{m,T}$
Normal damping	c_N
Tangential damping	c_T

Simulations' time step

In equations (6.1), we stated the integration scheme used with our model, which depends on a time step Δt. In order for the simulation to be numerically stable, we define the critical time step for our particular integration scheme (derived in Section 2.2.2)

$$\Delta t_\mathrm{c} = \sqrt{\frac{2m}{k_\mathrm{N}}}, \tag{6.6}$$

which is the maximum time step at which a simulation comprised of two particles in contact in the linear Hookean range ($\delta_\mathrm{N} \leqslant \delta_\mathrm{e}$) remains stable. For a system with many particles, we typically choose a time step being a fraction of the critical time step.

6.1.2 *Matching macroscopic material properties*

For each pair (i, j) of particles, the parameters of the interaction forces can be tuned such that the assembly of many particles exhibit the desired mechanical properties. The choice of the normal and tangential stiffnesses k_N and k_T determines the macroscopic Young's modulus E and the Poisson's ratio ν. The elastic domain extends up to the interparticular distance $\delta_\mathrm{N} = \delta_\mathrm{e}$, so δ_e controls the macroscopic tensile strength $\sigma_\mathrm{m,N}$. In the same manner, the maximum tangential force $F_\mathrm{m,T}$ controls the macroscopic shear strength $\sigma_\mathrm{m,T}$.[1] The interaction distance δ_f defines the surface energy γ, which is linked to the fracture energy (shaded area in Figure 6.2 under the force-displacement curve). Finally, the damping factors c_N and c_T influence the restitution coefficient η, which is the ratio between final and initial relative velocities when two particles collide. The list of material properties needed to fully determine the force parameters is given in Table 6.3.

Table 6.3 – List of target material properties

Name	Symbol
Young's modulus	E
Poisson's ratio	ν
Tensile strength	$\sigma_\mathrm{m,N}$
Shear strength	$\sigma_\mathrm{m,T}$
Surface energy	γ
Restitution coefficient	η
Density	ρ

---

[1] This is a simplified view. In fact, in an assembly of many particles, a tensile stress will displace the particles both in the normal and in the tangential directions relative to each other, so that both the tensile and the shear strength will contribute to the actual strength of the assembly. The same is true for a shear motion.

Choosing the right force properties to obtain some desired macroscopic material properties is a knowingly challenging task for this kind of DEM model. As a first guess in the process of calibrating the parameters, they can be expressed in terms of material properties.

Derivation of force parameters

Let us consider two particles of indexes i and j. They interact via normal forces F_N and tangential forces F_T. These forces can be converted into stresses by dividing them by effective contact cross sections A_N and A_T in the normal and tangential direction, respectively:

$$\sigma_\mathrm{N} = \frac{F_\mathrm{N}}{A_\mathrm{N}}, \tag{6.7}$$

$$\sigma_\mathrm{T} = \frac{F_\mathrm{T}}{A_\mathrm{T}}. \tag{6.8}$$

The value of the cross sections will be derived later.

The equilibrium distance between the particles is equal to $r_i + r_j$. From it, we can convert the normal separation δ_N into a normal deformation:

$$\varepsilon_\mathrm{N} = \frac{\delta_\mathrm{N}}{r_i + r_j}. \tag{6.9}$$

In the elastic range, we must have

$$\sigma_\mathrm{N} = E\varepsilon_\mathrm{N} \tag{6.10}$$

where E is the target Young's modulus of the material to model. From this relation, we find the expression for the normal stiffness in the elastic range:

$$k_\mathrm{N} = \frac{F_\mathrm{N}}{\delta_\mathrm{N}} \tag{6.11}$$

$$= \frac{A_\mathrm{N}\sigma_\mathrm{N}}{(r_i + r_j)\varepsilon_\mathrm{N}} \tag{6.12}$$

$$= \frac{A_\mathrm{N}E}{(r_i + r_j)}. \tag{6.13}$$

We give a similar expression to the tangential stiffness:

$$k_\mathrm{T} = \frac{A_\mathrm{T}E}{(r_i + r_j)}. \tag{6.14}$$

In our model, the elastic limit is found from the maximum tensile stress of the material:

$$\varepsilon_\mathrm{e} = \frac{\sigma_\mathrm{m,N}}{E}, \tag{6.15}$$

from which we deduce the elastic limit in terms of normal separation:

$$\delta_\mathrm{e} = \frac{(r_i + r_j)\sigma_\mathrm{m,N}}{E}. \tag{6.16}$$

The maximum tangential force is obtained directly from the maximum tangential stress:

$$F_\mathrm{m,T} = A_\mathrm{T}\sigma_\mathrm{m,T}. \tag{6.17}$$

We can compute the energy needed to break the bond between the two particles, which is equal to the area under the force-separation curve (Figure 6.2):

$$U_\gamma = \frac{1}{2}\delta_\mathrm{f} k_\mathrm{N} \delta_\mathrm{e} \tag{6.18}$$

$$= \frac{A_\mathrm{N}\sigma_\mathrm{m,N}\delta_\mathrm{f}}{2}. \tag{6.19}$$

This energy can be linked to the surface energy of the material (two surfaces of area A_N are created during fracture):

$$\gamma = \frac{U_\gamma}{2A_\mathrm{N}}. \tag{6.20}$$

We obtain the expression for the fracture separation distance:

$$\delta_\mathrm{f} = \frac{4\gamma}{\sigma_\mathrm{m,N}}. \tag{6.21}$$

To compute the expressions for the damping coefficients, we can express the dynamical equation of the system as in (2.17). One solution to this equation is the motion

$$x = \frac{v_0}{\omega} e^{-\frac{c_\mathrm{N}}{2m_\mathrm{eff}}t} \sin(\omega t), \tag{6.22}$$

$$\dot{x} = -\frac{c_\mathrm{N} v_0}{2\omega m_\mathrm{eff}} e^{-\frac{c_\mathrm{N}}{2m_\mathrm{eff}}t} \sin(\omega t) + v_0 e^{-\frac{c_\mathrm{N}}{2m_\mathrm{eff}}t} \cos(\omega t), \tag{6.23}$$

where ω is the natural frequency of the system in the linear elastic range:

$$\omega = \sqrt{\frac{k_\mathrm{N}}{m_\mathrm{eff}}} \sqrt{1 - \frac{c_\mathrm{N}^2}{4k_\mathrm{N} m_\mathrm{eff}}} \tag{6.24}$$

$$\approx \sqrt{\frac{k_\mathrm{N}}{m_\mathrm{eff}}} \tag{6.25}$$

when c_N is small. This particular solution is the motion of an impact between two particles happening at a time $t = 0$ with a relative velocity of v_0 (neglecting the cohesive range, when the particles are not touching). The duration of the impact is approximately $t_\mathrm{f} = \pi/\omega$ when c_N is small (half of a period of oscillation). The final relative velocity after impact is therefore

$$v_\mathrm{f} = \dot{x}(t_\mathrm{f}) \tag{6.26}$$

$$= v_0 e^{-\frac{\pi c_\mathrm{N}}{2\omega m_\mathrm{eff}}}. \tag{6.27}$$

The restitution coefficient is defined as the ratio between the initial and the final velocity:

$$\eta = \frac{v_0}{v_\mathrm{f}} \tag{6.28}$$

$$= e^{-\frac{\pi c_\mathrm{N}}{2\omega m_\mathrm{eff}}} \tag{6.29}$$

$$\approx 1 - \frac{\pi c_\mathrm{N}}{2\omega m_\mathrm{eff}} \tag{6.30}$$

$$\approx 1 - \frac{\pi c_\mathrm{N}}{2\sqrt{k_\mathrm{N} m_\mathrm{eff}}}, \tag{6.31}$$

from which we obtain the expression for the damping coefficient

$$c_\mathrm{N} \approx \frac{2(1-\eta)}{\pi}\sqrt{k_\mathrm{N} m_\mathrm{eff}}, \tag{6.32}$$

which can also be expressed as a fraction of the critical damping:

$$c_\mathrm{N} \approx \frac{1-\eta}{\pi} c_\mathrm{c}. \tag{6.33}$$

We give a similar expression to the tangential damping coefficient:

$$c_\mathrm{T} \approx \frac{2(1-\eta)}{\pi}\sqrt{k_\mathrm{T} m_\mathrm{eff}}. \tag{6.34}$$

Effect of particle size

Almost all the force parameters depend on the size of the particles, except for the fracture separation distance δ_f (6.21). In particular, we can focus on δ_e (6.16) and δ_f, which are represented in Figure 6.2. Since δ_e increases with the size of the particles while δ_f remains fixed, there is a point at which δ_e becomes larger than δ_f, which happens when $r_i + r_j > d_\mathrm{c}$, where

$$d_\mathrm{c} = \frac{4\gamma E}{\sigma^2_\mathrm{m,N}} \tag{6.35}$$

is a critical diameter. For large particles (bigger than d_c), we are in the situation shown in Figure 6.4, with $\delta_\mathrm{e} > \delta_\mathrm{f}$. The plot shows that the elastic limit ($\delta_\mathrm{N} = \delta_\mathrm{e}$) is not reached, and the fracture energy (shaded area) is smaller than expected, meaning that neither the target tensile strength $\sigma_\mathrm{m,N}$ nor the target surface energy γ will be matched.

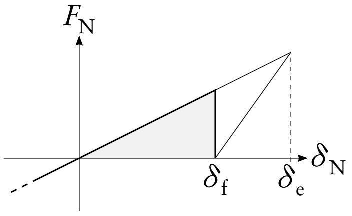

Figure 6.4 – Normal force when $r_i + r_j > d_\mathrm{c}$

To mitigate this undesirable behavior, we rescale the fracture separation distance δ_f to

$$\delta'_\mathrm{f} = \delta_\mathrm{e}\left(\frac{r_i + r_j}{d_\mathrm{c}}\right)^{-s}, \tag{6.36}$$

where s is a scaling factor, resulting in the force plotted in Figure 6.5.

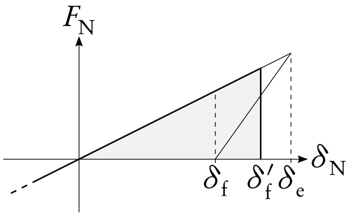

Figure 6.5 – Normal force when $r_i + r_j > d_\mathrm{c}$ with corrected δ_f

By tuning the scaling factor s, we can choose to either match the correct elastic limit ($s=0$, implying $\delta_\mathrm{f}=\delta_\mathrm{e}$), match the target surface energy ($s=0.5$), or have another behavior. The tensile strength resulting on the choice of s is plotted in Figure 6.6.

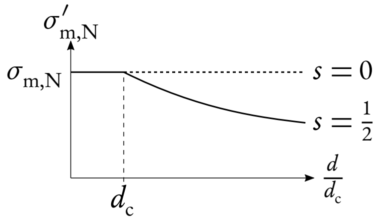

Figure 6.6 – Matched tensile strength with corrected δ_f

Effective cross sections

The magnitude and the balance between the normal stiffness (6.13) and the tangential stiffness (6.14) are controlled by the effective cross sections A_N and A_T, and they directly influence the obtained elastic properties (*i.e.* Young's modulus and Poisson's ratio). The effective cross sections must be chosen accordingly.

Following the two-dimensional analysis of Griffiths & Mustoe (2001), we must express the strain energy stored when deforming a body made of many particles. We start by considering only two particles of the body, both having a radius r. The center of one particle is taken as the origin of an arbitrary frame, and the other particle has the spherical coordinates $(2r,\theta,\phi)$ in this frame (θ is the polar angle, ϕ is the azimuthal angle). The deformation of the whole body ε_x and ε_z in the x and z directions (z is the zenith direction) directly influence the separation vector $\boldsymbol{\delta}$ between the two particles, which can be expressed in the Cartesian frame:

$$\delta_x = 2r\varepsilon_x\cos\phi\cos\theta \tag{6.37}$$

$$\delta_z = 2r\varepsilon_z\sin\theta, \tag{6.38}$$

and in the spherical frame:

$$\delta_r = \delta_x\cos\phi\cos\theta + \delta_z\sin\theta \tag{6.39}$$

$$\delta_\theta = -\delta_x\cos\phi\cos\theta + \delta_z\cos\theta \tag{6.40}$$

$$\delta_\phi = -\delta_x\sin\theta. \tag{6.41}$$

Note that $\delta_r=\delta_\mathrm{N}$. In the linear elastic range, the strain energy of the single pair of particles is

$$U_\mathrm{pair} = \frac{1}{2}k_\mathrm{N}\delta_\mathrm{N}^2 + \frac{1}{2}k_\mathrm{T}(\delta_\theta^2+\delta_\phi^2). \tag{6.42}$$

The total strain energy stored by all possible pairs with neighbors surrounding a single particle is obtained by integrating the strain energy of a single pair:

$$U = \frac{1}{2}\int_{\phi=0}^{2\pi}\int_{\theta=-\frac{\pi}{2}}^{\frac{\pi}{2}} U_\mathrm{pair}\cos\theta\,d\theta\,d\phi, \tag{6.43}$$

where the leading $1/2$ factor distributes the energy between the single considered particle and its neighborhood. This energy assumes that one particle can be fully surrounded by 4π neighbors, while the number of neighbors in the most densely packed arrangement of particles (*e.g.* HCP) is 12. We can rescale the strain energy to take this into account:

$$U' = \frac{12}{4\pi}U. \tag{6.44}$$

In an HCP lattice, the particle is surrounded by 12 neighbors positioned at the edges of a cube of side length $2\sqrt{2}r$ (or at the centers of the faces of a rhombic dodecahedron). Each particle can be assigned a piece of the deformable body having a volume of

$$V = 4\sqrt{2}r^3, \tag{6.45}$$

which is a bit larger than the volume of the spherical particle itself, $4\pi r^3/3$ (the ratio between the two volumes is around 74%). From the volumetric strain energy, we can make the elastic constants of the granular body appear:

$$\frac{1}{V}\frac{\partial U'}{\partial \varepsilon_x} = C_{11}\varepsilon_x + C_{12}\varepsilon_z \tag{6.46}$$

Plugging all the expressions of δ into this last equation and identifying the leading factors of ε_x and ε_z, we obtain the expression of the elastic constants:

$$C_{11} = \frac{\sqrt{2}}{5r}(3k_{\mathrm{N}} + 2k_{\mathrm{T}}), \tag{6.47}$$

$$C_{12} = \frac{\sqrt{2}}{5r}(k_{\mathrm{N}} - k_{\mathrm{T}}). \tag{6.48}$$

Inverting these, we get the expressions for the stiffness coefficients (expressed directly in terms of the Young's modulus and the Poisson's ratio):

$$k_{\mathrm{N}} = \frac{\sqrt{2}Er}{2(1-2\nu)}, \tag{6.49}$$

$$k_{\mathrm{T}} = \frac{\sqrt{2}Er(1-4\nu)}{2(1+\nu)(1-2\nu)}. \tag{6.50}$$

Expressing these in terms of the effective cross sections ((6.13) and (6.14)), we finally obtain the expressions for the latter:

$$A_{\mathrm{N}} = \sqrt{2}r^2\frac{1}{1-2\nu}, \tag{6.51}$$

$$A_{\mathrm{T}} = \sqrt{2}r^2\frac{1-4\nu}{(1-2\nu)(1+\nu)}. \tag{6.52}$$

From these expressions, we note that the target Poisson's ratio can only take values up to $\nu = 1/4$, and values between $1/4$ and $1/2$ cannot be modeled. Having such a restriction on the allowed Poisson's ratios is a known issue when working with only pair forces between particles (Celigueta *et al.* 2017). This problem also notably arises in the field of peridynamics (Trageser & Seleson 2020). To mitigate this drawback, more complex forces involving more than two particles should be considered, which is out of the scope of this work.

Henceforth, all force parameters have been identified. For now, the effective cross sections are defined for particles all having the same radius of r.

Effective particle radius

In the expressions of the effective cross sections, we can replace the particle radius r by an effective radius r_{eff} to take into consideration the two different radii of the pair of particles for which the force is being computed. There are many ways to define the effective radius. Since the projected contact area between the particles is necessarily bounded by the size of the smallest one, we choose

$$r_{\mathrm{eff}} = \min(r_i, r_j), \tag{6.53}$$

which results in the macroscopic elastic and strength properties to be controlled by the presence of large particles in the system (as demonstrated in Section 6.2.3).

Expression of force parameters

In summary, the force parameters take the following expressions:

$$k_\mathrm{N} = \frac{A_\mathrm{N} E}{r_i + r_j}, \tag{6.54}$$

$$k_\mathrm{T} = \frac{A_\mathrm{T} E}{r_i + r_j}, \tag{6.55}$$

$$\delta_\mathrm{e} = \frac{(r_i + r_j)\sigma_\mathrm{m,N}}{E}, \tag{6.56}$$

$$\delta_\mathrm{f} = \begin{cases} \dfrac{4\gamma}{\sigma_\mathrm{m,N}} & \text{if } r_i + r_j \leqslant d_\mathrm{c}, \\ \delta_\mathrm{e}\left(\dfrac{r_i + r_j}{d_\mathrm{c}}\right)^{-s} & \text{otherwise,} \end{cases} \tag{6.57}$$

$$F_\mathrm{m,T} = A_\mathrm{T}\,\sigma_\mathrm{m,T}, \tag{6.58}$$

$$c_\mathrm{N} = \frac{2(1-\eta)}{\pi}\sqrt{k_\mathrm{N} m_\mathrm{eff}}, \tag{6.59}$$

$$c_\mathrm{T} = \frac{2(1-\eta)}{\pi}\sqrt{k_\mathrm{T} m_\mathrm{eff}}. \tag{6.60}$$

A_N and A_T are effective contact cross section defined by (6.51) and (6.52) and by an effective particle radius (6.53). In (6.59) and (6.60), m_eff is the effective mass of the oscillatory system comprised of the two interacting particles:

$$m_\mathrm{eff} = \frac{m_i m_j}{m_i + m_j}. \tag{6.61}$$

In the expression of the fracture distance δ_f (6.57), d_c is a critical diameter, defined by (6.35), and $s \geqslant 0$ is a scaling parameter.

Choice of particle size

Note that nearly all parameters depend on the size of the particles. In particular, δ_f takes two different expressions depending on the particles' sizes. When the particles are smaller than the critical diameter ($r_i + r_j \leqslant d_\mathrm{c}$), it is possible to capture both the shear strength $\sigma_\mathrm{m,N}$ and the surface energy γ of the target material. In this lower range of particles' sizes, δ_f has a constant value. However, the particles cannot be given an arbitrary small size. Since δ_f represents the size of the neighborhood of a particle (see Figure 6.1), it indicates from how far a particle can feel a force from another particle. In the case where the diameter of a particle becomes smaller than the neighborhood size δ_f, the particle will be able to "communicate" with others located further than its closest neighbors, increasing a lot the computational cost of the simulation. Therefore, it is reasonable to keep the particles' sizes over a minimum value of

$$d_\mathrm{min} = \frac{4\gamma}{\sigma_\mathrm{m,N}} \tag{6.62}$$

(which is the maximum value of δ_f). Note that for physically realistic target properties, d_min can be comparable to the size of atoms, for which the interaction distance is roughly the same as their size. Having the lower limit on the size of the discrete particles bounded by the size of an atom is consistent with our coarse-graining approach. On the other side of the spectrum of particle sizes, when $r_i + r_j > d_\mathrm{c}$, the shear strength $\sigma_\mathrm{m,N}$ and the surface energy γ of the target material cannot be both matched at the same time. Depending on the value of the scaling parameter s, the tensile strength will be matched to a lower value of

$$\sigma'_{\mathrm{m,N}} = \sigma_{\mathrm{m,N}} \left(\frac{r_i + r_j}{d_{\mathrm{c}}} \right)^{-s} . \tag{6.63}$$

When $s = 0$, the matched tensile strength remains constant, but the matched surface energy is larger than it should be. With $s = 1/2$, the surface energy stays constant, but instead, the matched tensile strength decreases with the size of the particles. The decrease of the strength between the particles can be related to the same decrease of the strength of a material when tested with samples of increasing sizes, where the larger samples have a higher chance of containing defects and thus have a lower strength. If one wishes to use this model in both the lower sizes range $d_{\mathrm{min}} \leqslant r_i + r_j \leqslant d_{\mathrm{c}}$ and with the larger sizes, the target tensile strength $\sigma_{\mathrm{m,N}}$ can be taken as the *ideal* tensile strength of the material to model, which is the strength measured at a small scale when no defects are present in the tested sample, and the scaling parameter s can be chosen to represent the desired behavior.

It is worth noting that d_{c} (6.35) shares the same expression (ignoring a geometrical multiplication factor) with the *critical length scale* of the target material, established by Aghababaei *et al.* (2016), under which the material has a ductile behavior and exhibits a higher strength (Luo *et al.* 2016).

6.2 VALIDATION

The choice of force parameters given by equations (6.54) to (6.60) does not ensure that the resulting macroscopic properties will be exactly equaled since they strongly depend on the coordination number, which in turn is dependent on the volume fraction and the size of the neighborhood of the particles. To eliminate these unknowns, we first perform patch tests on systems made of particles arranged in a hexagonal close-packed (HCP) lattice, so that the coordination number is fixed.

We are interested in adhesive wear, which can be regarded as a fracture process at small scale. Ordered systems may have preferential planes for fracture propagation, and we ultimately want to model isotropic materials. Consequently, we also build amorphous systems of particles and perform the same kind of patch tests, this time without full control over the coordination number.

The force parameters are chosen to match the material properties listed in Table 6.4. No units are specified, so any coherent system of units can be considered. The value of the target ν is varied for the lattice tests. From the material properties, we compute the minimum allowed particle size $d_{\mathrm{min}} = 30$ (6.62) and the maximum particle size $d_{\mathrm{c}} = 150$ (6.35) over which the tensile strength and the surface energy cannot be both equaled. For particle sizes greater than d_{c}, scaling factors of $s = 0$ (constant strength) and $s = 1/2$ (constant surface energy) are investigated.

The elastic properties are determined by applying a unidirectional compressive load of 0.01 on a confined sample (see Figure 6.7a), up to a deformation of the order of $\varepsilon \sim 0.01$, and measuring the

Table 6.4 – List of target material properties for patch tests

E	ν	$\sigma_{\mathrm{m,N}}$	$\sigma_{\mathrm{m,T}}$	γ	η	ρ
1	0.15	0.2	0.1	1.5	0.95	1

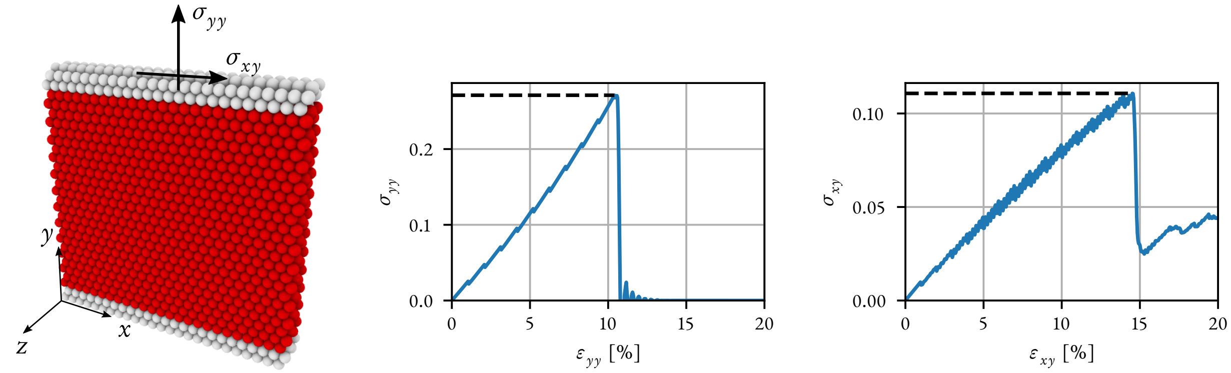

(a) Crystalline (HCP) system for patch test

(b) Tensile strength test

(c) Shear strength test

Figure 6.7 – Example of patch test's system and outputs. (a) White particles are part of rigid walls. The bottom wall is fixed and a stress or displacement is imposed on the top wall, depending on the type of test. Boundaries are periodic in the x and z directions. To measure E and ν, a small compressive stress σ_{yy} is applied, then σ_{xx} and ε_{yy} are measured. (b)-(c) A displacement is imposed on the top wall in the appropriate direction to deform the system, and the stresses are monitored. The strengths are defined as the peak measured stresses (dashed lines).

stiffness coefficients C_{11} and C_{12}, from which E and ν are deduced. The loading is performed with a time step of $\Delta t = 0.1\,\Delta t_{\mathrm{c}}$ and a global damping of $c = 0.2\,c_{\mathrm{c}}$, where Δt_{c} and c_{c} are respectively the critical time step (6.6) and the critical damping

$$c_{\mathrm{c}} = \sqrt{2k_{\mathrm{N}} m} \tag{6.64}$$

for a system of two particles (see Section 2.2.3), evaluated for the smallest particle present in the system (leading to the most restrictive time step).

The tensile and shear strengths are determined by deforming the system in the appropriate direction using rigid walls moving at a constant rate of $\dot{\varepsilon} = 10^{-5}/\Delta t$ (with periodic boundary conditions) and measuring the peak stress before failure (see Figures 6.7b and 6.7c). The stresses are obtained by computing the average virial stress (Morante *et al.* 2006) inside the deformable part of the system. The simulations are performed with a time step of $\Delta t = 0.1\,\Delta t_{\mathrm{c}}$ and a global damping of $c = 0.01\,c_{\mathrm{c}}$.

6.2.1 *Crystalline lattice*

Different particle sizes (diameters) are tested, ranging from $d_0 = 0.6\,d_{\mathrm{c}}$ to $d_0 = 76.8\,d_{\mathrm{c}}$. The target Poisson's ratio is also varied from $\nu = 0$ to $\nu = 1/4$ (which is the maximum Poisson's ratio acceptable by our model). The size of each tested sample is equal to $L \times L \times W$, with $L = 25\,d_0$ and $W = 3\,d_0$.

The measured Young's moduli and Poisson's ratios match the target properties, with an acceptable deviation (low enough to allow for an easy later adjustment of the force parameters). The error is smallest when ν is near 0 and reaches a maximum of 12% when $\nu = 1/4$. Figures 6.8 and 6.9 depict the actual deviations. Since the organization of particles is always an HCP lattice regardless of the size of the particles d_0, the latter has no influence on the measured elastic properties measured at small strain.

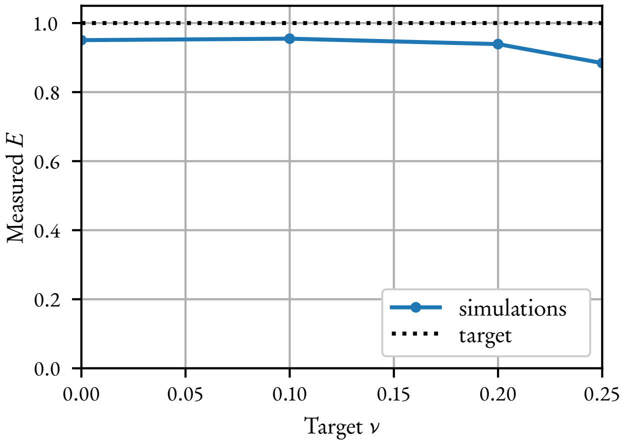

Figure 6.8 – Effect of target ν on the measured E

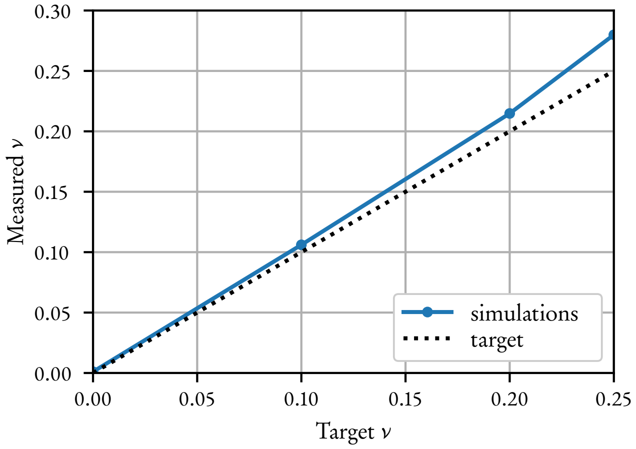

Figure 6.9 – Effect of target ν on the measured ν

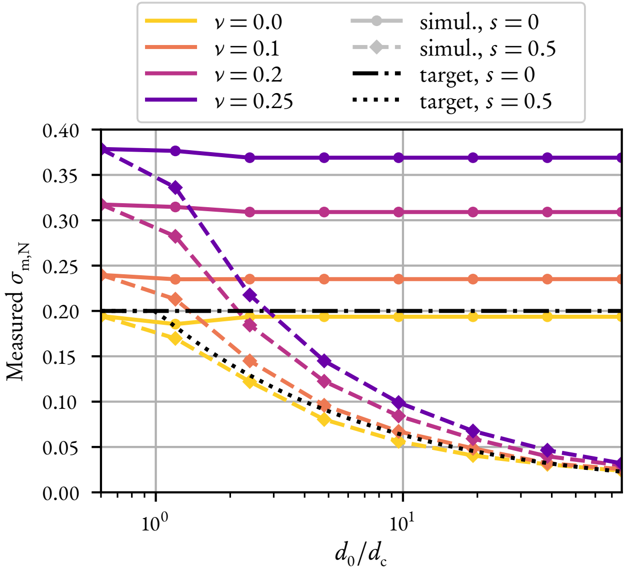

Figure 6.10 – Effect of d_0, s and target ν on the measured tensile strength $\sigma_{\mathrm{m,N}}$. Colored curves show simulations and black curves are target values. There is one set of curves for $s = 0$ (continuous lines) and one set for $s = 0.5$ (dashed lines). For both values of s, the measured $\sigma_{\mathrm{m,N}}$ matches the target one when $\nu = 0$. For higher values of ν,the strengths are larger than the target ones, but their dependence on d_0 remains the same.

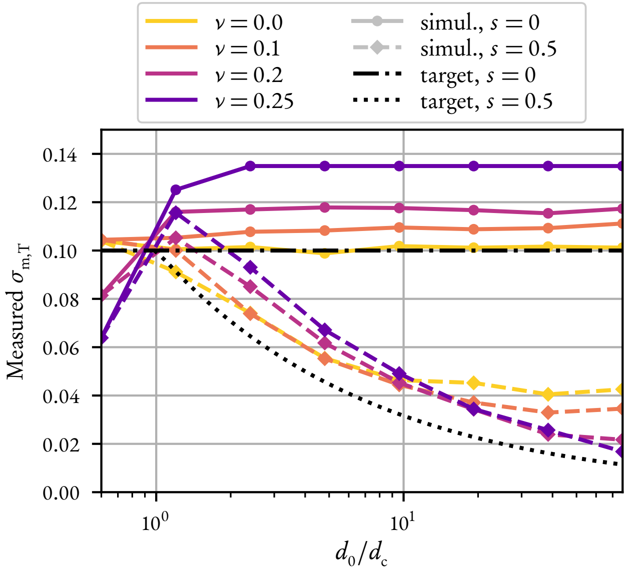

Figure 6.11 – Effect of d_0, s and target ν on the measured shear strength $\sigma_{\mathrm{m,T}}$. The behavior of the measured shear strength is mostly the same as the tensile one, except for $d_0 < d_\mathrm{c}$ where the measured strengths are lower than the target ones.

The measured tensile and shear strengths are shown in Figures 6.10 and 6.11. They depend on ν, d_0, and the scaling parameter s. For a scaling of $s = 0$, the target tensile and shear strengths (shown by the black dash-dotted curves) are constant with respect to d_0, whereas for $s = 0.5$, the target strengths (black dotted curves) decrease with respect to d_0, as described by (6.63). The measured strengths match the target ones when the target Poisson's ratio is equal to 0. Otherwise, the strengths are higher than the target ones, while following the same trend with respect to the value of d_0. For the shear strength, the measured values are instead lower than the target ones when $d_0 < d_\mathrm{c}$. We did not try to analytically predict the gap between the target and measured strengths. To accurately capture the measured strengths, the values of the target strengths must be adjusted according to the target ν and to the plots (Figures 6.10 and 6.11).

6.2.2 *Amorphous sample*

Particles' size distribution

In order to obtain an amorphous sample, the particles must have various sizes. Otherwise, particles of identical sizes would arrange into a crystalline lattice or crystalline grains with weaker grain boundaries. We distribute the particles' sizes around a diameter of d_0, within the bounds d_s (the smallest diameter) and d_l (the largest). The particles' diameters are distributed along a log-normal distribution of mode d_0 (most frequent value) and standard deviation $0.2(d_\mathrm{l} - d_\mathrm{s})$. The distribution is truncated between d_s and d_l. When d_0 is at the midpoint between the bounding diameters, the log-normal distribution is similar to a Gaussian distribution. In other cases, this particular distribution allows us to choose a larger d_l to add a small amount of larger particles inside the sample, while keeping the smallest diameter d_s and the average diameter d_0 the same. The particles are inserted into the system at random positions until they fill it up to a given volume fraction of 0.75.

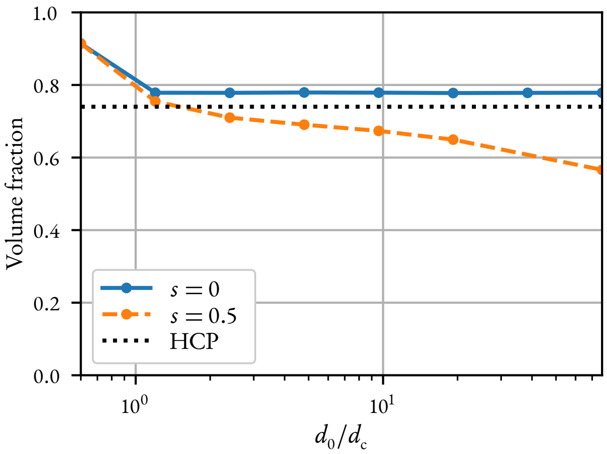

Figure 6.12 – Effect of d_0 and s on the relaxed volume fraction. The volume fraction of HCP lattice systems is shown for comparison. The relaxed volume fraction is independent of d_0 when the target shear strength is kept constant ($s = 0$). When the target shear strength decreases with d_0 ($s = 0.5$), the relaxed volume fraction also decreases.

Relaxation

The system of randomly placed particles is relaxed in two phases by simulating it dynamically with a global velocity damping until an equilibrium state is reached. In the first phase, only normal repulsive forces are considered in addition to the global damping forces, allowing the particles to rearrange into a state with no completely overlapped particles. This phase is run for 3000 time steps of $\Delta t = 0.1\,\Delta t_c$ with a damping of $c = c_c$, inside a system with fixed periodic boundaries. For the second phase, the adhesive normal forces are added, and the periodic boundaries are allowed to move in order to adapt to the internal stresses of the system. No tangential forces are considered to avoid the formation of stable holes in the system. This phase is run with a damping of $c = 0.02\,c_c$ until all the internal stresses become lower than $10^{-14}E$, where E is the target Young's modulus. Typically, around 20000 time steps are required for this phase. At the end, the mass of all the particles is adjusted such that the density of the whole system matches the target one. The final volume fraction is likely to change during the relaxation process, along with the movement of the system boundaries.

Patch tests results

We test samples of size $L \times L \times W$, with $L = 100\,d_0$, $W = 3\,d_0$, and d_0 ranging from $d_0 = 0.6\,d_c$ to $d_0 = 76.8\,d_c$. The bounds of the particles' size distribution are chosen as $d_s = 0.75\,d_0$ and $d_l = 1.25\,d_0$. For each relaxed system, the final volume fraction is measured (see Figure 6.12). The scaling parameter s starts to play a role whenever $d_0 > d_c$. When $s = 0$, the ratio between the interaction distance δ_f and the particles' diameter d_0 remains constant, so the particles can get organized in the same fashion regardless of d_0. However, when $s = 0.5$, this same ratio gets smaller when the particles are larger. Less interaction are allowed between the particles, resulting in a system being less densely packed.

The decreased volume fraction has a direct impact on the coordination number of each particle, and thus on the macroscopic elastic properties of the system, as shown by the drastic effect of d_0 on the measured Young's modulus when $s = 0.5$ (Figure 6.13). As d_0 increases, the distance of interaction becomes comparatively smaller, resulting in fewer links between particles and a more fragile network. When $d_0 > 20\,d_c$, the system no longer resists the compression stress of 0.01

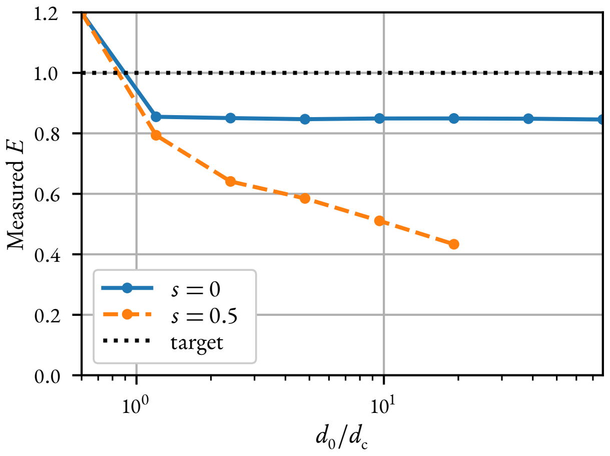

Figure 6.13 – Effect of d_0 and s on the measured E. The measured Young's modulus follows the same trend as the volume fraction (Figure 6.12). For $d_0 > 20\,d_c$, the system fails under the compression used to measure the elastic properties.

imposed to measure the elasticity parameters, which is why no values are reported beyond this value of d_0. The measured Poisson's ratio stays constant at $\nu \approx 0.20$ regardless of s (see Figure 6.14), which is higher than the target value ($\nu = 0.15$).

Finally, the measured strengths follow the correct trends with respect to d_0 and s (see Figures 6.15 and 6.16). However, the tensile strengths are reduced to 50% of the target one, and the shear strengths are at 56%. This is likely due to the particles not being in direct contact with their neighbors ($\delta_N = 0$), therefore not benefiting from the whole adhesive range $0 \leqslant \delta_N \leqslant \delta_f$, resulting in a decreased strength in both normal and tangential directions. This phenomenon is not present in the lattice systems.

6.2.3 *Discretization*

We saw that when the scaling factor s is not equal to 0, the measured mechanical properties of simulated systems are significantly affected by d_0. If one desires to simulate multiple samples having the same size but different discretizations by varying d_0, the obtained samples will have different elastic properties because of d_0. To mitigate this effect, the distribution of the particles' sizes can be adapted by having the largest bounding diameter d_l constant throughout all samples (*i.e.* $d_l = 1.25 \max(d_0)$). The larger particles act like defects in the samples, keeping the strengths as low as when all particles are large. The effect of keeping a constant d_l for multiple discretizations is presented in detail below. This method is shown to work well to harmonize the strengths across multiple samples of the same size when $s = 0.5$.

We test samples of size $L \times L \times W$, with L ranging from $L = 60\,d_c$ to $L = 7680\,d_c$. The discretization of each system is determined by d_0, chosen such that the coarsest systems have $d_0 = L/25$, and the finest have $d_0 = L/100$, while keeping d_0 between $0.6\,d_c$ and $76.8\,d_c$. The smallest bound of the particles' size distribution is chosen as $d_s = 0.75\,d_0$, and the largest bound is set to $d_l = 0.05\,L$, such that it remains fixed with respect to the system size and is not affected by d_0. The thickness of the systems is fixed at $W = 3\,d_0$. The measured tensile strengths are plotted in Figure 6.17. The simulations show that, given one system size L, having the same largest size particle d_l for all discretizations results in the systems exhibiting roughly the same tensile strengths.

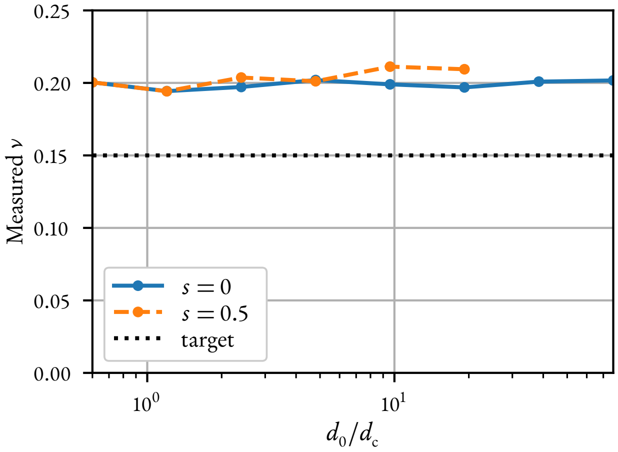

Figure 6.14 – Effect d_0 and s on the measured ν

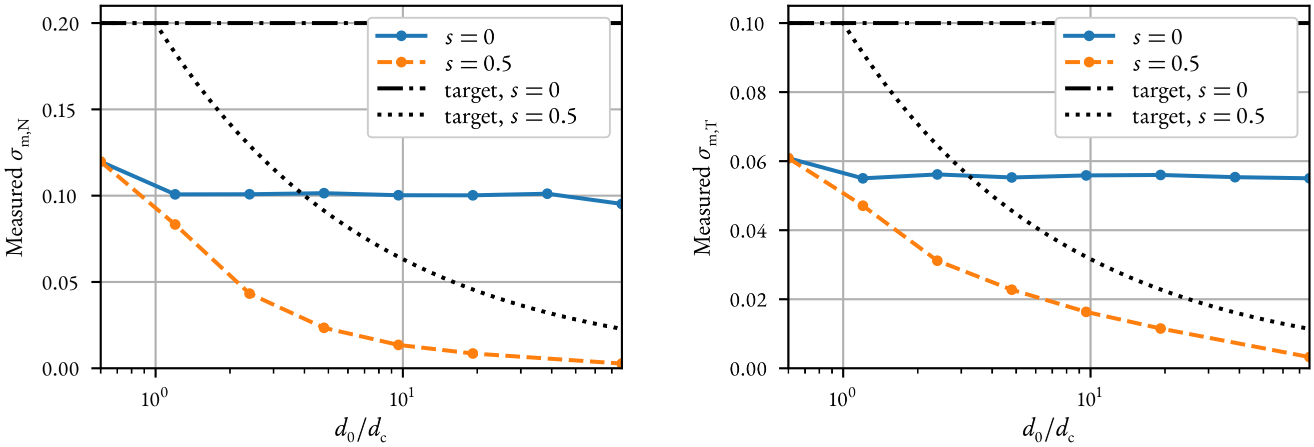

Figure 6.15 – Effect d_0 and s on the measured tensile strength

Figure 6.16 – Effect d_0 and s on the measured shear strength

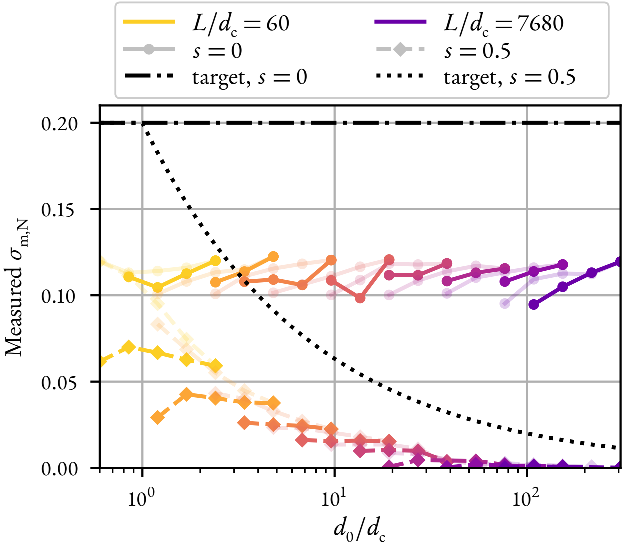

Figure 6.17 – Effect of d_0 and s on the measured tensile strength $\sigma_{m,T}$ for systems of various sizes and discretizations. Each color corresponds to a fixed system size. The semi-transparent curves correspond to a varying $d_l = 1.25\, d_0$, whereas the fully-visible ones have a fixed $d_l = 0.05\, L$.

6.2.4 *Calibration*

As already known (Cheng *et al.* 2020; Hentz *et al.* 2004) and witnessed once more here, obtaining the correct continuum behavior with DEM is a challenging task. Nevertheless, we have shown that our estimates for the force parameters (equations (6.54) to (6.60)) result in measured elastic and fracture properties being approximately at the target value, especially for a scaling factor of $s = 0$. The force parameters can be further adjusted if necessary, after running the relevant patch tests.

6.3 APPLICATION: NANOSCALE ADHESIVE WEAR

MD simulations of adhesive wear have been performed (Aghababaei *et al.* 2016) by modeling two surfaces being in contact at a single junction of a given size and moving in a shear motion relative to each other. In accordance with theoretical predictions (Rabinowicz 1958), it was shown that junctions smaller than a critical size d^* are subjected to plastic smoothening, while junctions larger than d^* can detach and form a wear particle. The critical size d^* at first order only depends on material parameters, and defines the boundary between ductile and fragile behaviors in a material.

We use our coarse-grained model to perform the same kind of nanoscale adhesive wear simulation and see if we can reproduce both the ductile and the fragile behaviors for a given material. We choose to model amorphous silica (SiO_2), which has the material properties listed in Table 6.5. The coarse-grained model was implemented in LAMMPS (Plimpton 1995).

Table 6.5 – Amorphous silica properties. The ideal (atomic scale) tensile strength $\sigma_{\mathrm{m,N}}$ is from Luo *et al.* (2016) and the shear strength is estimated from the tensile one. The restitution coefficient η is arbitrarily chosen.

E	ν	$\sigma_{\mathrm{m,N}}$	$\sigma_{\mathrm{m,T}}$	γ	η	ρ
73 GPa	0.17	16 GPa	9 GPa	1.5 N/m	0.9	2200 kg/m^3

From the material parameters, we compute the critical length scale from the expression of Aghababaei *et al.* (2016) for the geometrical configuration we will use:

$$d^* \approx \frac{32\gamma G}{\sigma_{\mathrm{m,T}}^2} = 18\,\mathrm{nm}\,. \tag{6.65}$$

We simulate systems of $60 \times 40 \times 40\ \mathrm{nm}^3$ made of two solids linked by a cylindrical junction of diameter $D = 10\,\mathrm{nm}$ or $20\,\mathrm{nm}$ and of height $H = D/2$ (see Figures 6.18a and 6.18c). The two values of D are chosen to have one smaller than d^* and the other one larger.

From the material properties of SiO_2, we compute the minimum allowed DEM particle size $d_{\mathrm{min}} = 0.37\,\mathrm{nm}$ (6.62) and the critical particle size $d_{\mathrm{c}} = 1.7\,\mathrm{nm}$ (6.35). From those, we chose to use DEM particles of size $d_0 = 1.5\,\mathrm{nm}$, 3 nm and 6 nm. For comparison, the bond lengths between atoms in silica are (Vashishta *et al.* 1990) SiO_2: 0.16 nm, SiO_2: 0.26 nm and SiO_2: 0.31 nm. DEM particles are therefore at least 10 times larger than atoms. For each average particle size d_0, we take the bounds of the particles' sizes distribution as $d_{\mathrm{s}} = 0.75\,d_0$ and d_{l} fixed to $d_{\mathrm{l}} = 7.5\,\mathrm{nm}$, so that every system has the same mechanical properties regardless of d_0. We chose the scaling parameter $s = 0.5$ for the dependence of strength on d_0.

The amorphous systems are created and relaxed using the same procedure as for the validation tests, resulting in boxes fully filled with particles. The systems are then carved by removing

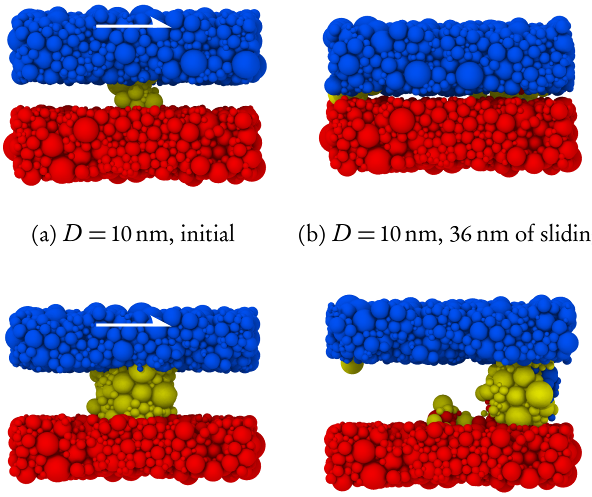
(a) $D = 10\,\text{nm}$, initial (b) $D = 10\,\text{nm}$, 36 nm of sliding

(c) $D = 20\,\text{nm}$, initial (d) $D = 20\,\text{nm}$, 32 nm of sliding

Figure 6.18 – Sheared junctions with $d_0 = 1.5\,\text{nm}$. The colors of the particles indicate to which body they initially belong to. The bottom surface is fixed and the top one is dragged from left to right. The system length is 60 nm with periodic boundary conditions. (a)-(b) The smaller junction deforms plastically and gets squished. (c)-(d) The larger junction detaches into a rolling wear particle. The two mechanisms observed with MD simulations are remarkably recovered with the coarse-graining method.

particles to obtain the desired shapes (two surfaces with one cylindrical junction). Two rigid walls of width equal to $1.5\,d_0$ are used to impose a shear motion on the systems, with the bottom one remaining fixed and to top one moving with a constant shear velocity of $10\,\text{m/s}$, which is sufficiently small compared to the pressure wave velocity in the medium $c = \sqrt{E/\rho} = 5760\,\text{m/s}$. A constant normal load of 100 MPa is applied on the top wall to prevent it from drifting apart, but similar results are obtained with smaller normal loads. The time step is $\Delta t = 0.1\,\Delta t_c$.

The results of the simulations are shown in Figure 6.18 for the finest discretization ($d_0 = 1.5\,\text{nm}$), Figure 6.19 for the medium discretization ($d_0 = 3\,\text{nm}$), and Figure 6.20 for the coarsest ($d_0 = 6\,\text{nm}$). All visualizations were rendered using OVITO (Stukowski 2009). For all levels of discretization, the same behaviors emerge. The small junction ($D = 10\,\text{nm}$) gets deformed plastically and squished under the imposed shear, because it is smaller than the critical size d^* of the material. In turn, the large junction ($D = 20\,\text{nm}$), which is larger than the critical d^*, is detached (by fracture) from the surfaces and starts rolling. The coarse-grained DEM approach is able to reproduce both the ductile and brittle behaviors of the simulated material. From the simulations, we deduce that the critical size of the material is in the bounds $10\,\text{nm} < d^* < 20\,\text{nm}$, which is consistent with the theoretical estimate (6.65).

We can assume that the ductile behavior $D < d^*$ can only be observed if the DEM particles are sufficiently smaller than d^*, which is the case with all our discretizations. Taking larger particles would result in losing the ability to model the ductile behavior.

Our method is successfully able to reproduce results that are obtained using MD while having to simulate fewer particles and with a larger time step. In addition, silica is a relatively complex and costly material to simulate in MD. For example, the potential of Vashishta *et al.* (1990) can be used, taking into account 3-body interactions to accurately simulate the bounds between SiO_2 atoms. Table 6.6 compares the estimated computational cost of MD and coarse-grained DEM simulations to perform a simulation equivalent in size and duration to the sheared junction of

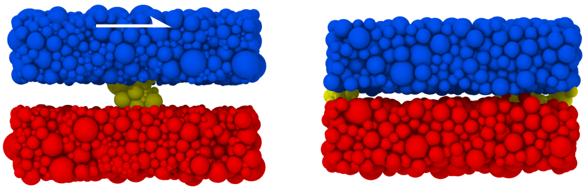

(a) $D = 10\,\text{nm}$, initial (b) $D = 10\,\text{nm}$, after sliding

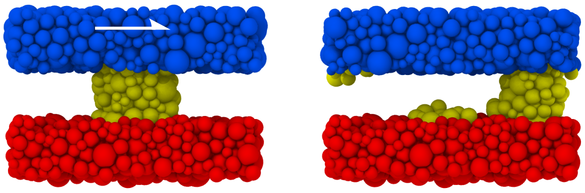

(c) $D = 20\,\text{nm}$, initial (d) $D = 20\,\text{nm}$, after sliding

Figure 6.19 – Sheared junctions with $d_0 = 3\,\text{nm}$. The observed behaviors are the same as with the finer and coarser discretizations of $d_0 = 1.5\,\text{nm}$ and $d_0 = 6\,\text{nm}$ (Figures 6.18 and 6.20).

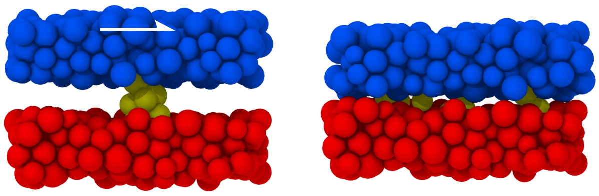

(a) $D = 10\,\text{nm}$, initial (b) $D = 10\,\text{nm}$, 80 nm of sliding

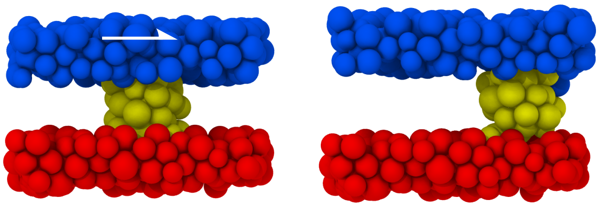

(c) $D = 20\,\text{nm}$, initial (d) $D = 20\,\text{nm}$, 32 nm of sliding

Figure 6.20 – Sheared junctions with $d_0 = 6\,\text{nm}$. The observed behaviors are the same as with the finer discretizations of $d_0 = 1.5\,\text{nm}$ and $d_0 = 3\,\text{nm}$ (Figures 6.18 and 6.19).

$D = 20\,\mathrm{nm}$. The computational time for MD simulations is estimated by scaling the time needed to simulate a smaller system on a shorter period of time (from Section 8.2.1). The coarse-grained DEM simulations show a definite advantage. However, it should be clear to the reader that the coarse-grained approach results in losing atomistic details (such as three-body interactions and the presence of two types of atoms), and that we only aimed to capture rough material properties, in particular for the ductile to brittle transition.

Table 6.6 – Estimated time for a simulation of 100 000 nm^3, 10 ns, on 28 2.6 GHz CPUs. N is the number of atoms/particles. The simulations are equivalent in size and duration to the sheared junction of $D = 20\,\mathrm{nm}$.

	d_0	N	Δt	Time
MD	$\approx 0.2\,\mathrm{nm}$	7 800 000	1 fs	530 days
DEM	1.5 nm	6000	20 fs	4 min
DEM	3 nm	2600	40 fs	2 min
DEM	6 nm	600	80 fs	25 s

In more general terms, the time and length scales reachable by our model are controlled by the critical time step (6.6) and the critical particle diameter (6.35), which, in turn, depend on the material parameters. For example, going back to the case of silica, we could choose a particle diameter near $d_c = 1.7\,\mathrm{nm}$ and simulate three-dimensional systems of 200 nm wide (around $120 \times 120 \times 120$ atoms) for 1 µs (50 million time steps), which is sufficient to observe interesting adhesive wear behaviors over time.

6.4 EXAMPLES OF APPLICATION

The newly developed coarse-grained DEM model was successfully used to model a macroscopic process (Ghesquière *et al.* 2022). A scooping tool was optimized (Molinari & Pham-Ba 2022) and tested using a robotic arm (Mikelis & Molinari (2021), see Figure 6.21) to scoop into *kinetic sand*, a material mimicking the properties of wet sand, but that never dries out. The experiment was reproduced using DEM, fitting the measured properties of kinetic sand, which resulted in a stunningly similar qualitative behavior (see Figure 6.22).

The Section 9.3.3 briefly presents another application, at the nanoscale, directly related to the study of Si and SiO_2. The simulations can reach a size of $220 \times 220 \times 75\ \mathrm{nm}^3$, with around a million particles, while modeling realistic materials, which would be unreasonable to try using MD simulations.

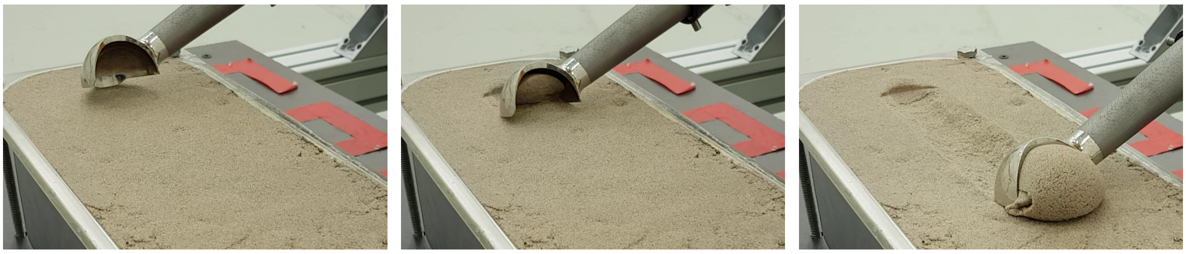

(a) Initial position (b) Scooping (c) End

Figure 6.21 – Scooping experiments on kinetic sand. The material behaves like wet sand or ice cream. The imposed motion is vertical at the beginning, then purely horizontal during scooping.

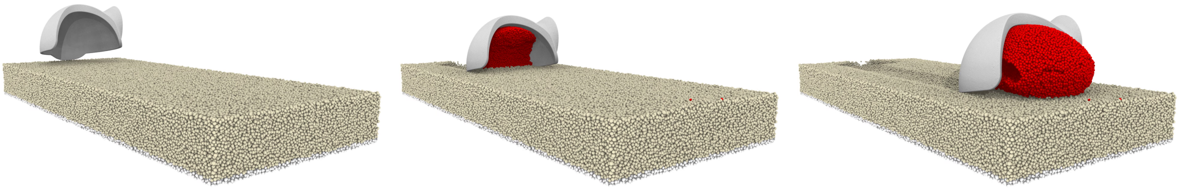

(a) Initial position (b) Scooping (c) End

Figure 6.22 – DEM scooping simulations. The experiment shown in Figure 6.22 is remarkably well represented.

CONCLUDING REMARKS

We formulated a pair force to be used with DEM, featuring a reversible cohesive part mimicking the simplest pair potentials used in MD. We derived expressions for the parameters of the pair force to match the elastic and fracture properties of a chosen isotropic and homogeneous material and showed that the calibration process can be greatly helped by using these expressions. Restricting our model to rely only on pair forces limits the achievable Poisson's ratio to values under $1/4$. Solids can be modeled with an organized (crystalline) or amorphous arrangement of particles. Finally, we showed that our model can be used to perform coarse-grained simulations of adhesive wear at the scale of asperities, with particles having a diameter 10 times larger than the atoms they replace, and with a computational cost reduced by at least 5 orders of magnitude. This method can be used to perform simulations at a scale inaccessible to MD, for example involving the evolution of rough surfaces and third-body elements at a tribological interface.

Chapter 7

Friction and wear from nanoscale up

We are now equipped with a method able to reproduce the microscopic behavior of brittle or ductile material, and capable of reaching scales orders of magnitude larger than MD. The method is therefore suited to help us find a link between the microscopic and macroscopic behaviors of a material. In Section 7.1, DEM simulations are used as a basis for the establishment of a model linking the nanoscale shear strength of a material to a macroscopic strength. In Sections 7.2 and 7.3, rubbed rough surfaces are simulated, and the friction and wear behaviors are examined. Section 7.3 focuses on an identified transition of frictional regime, dependent on the type of third-body. The newly developed DEM model being still quite young, the informations shown in this chapter are still preliminary results.

7.1 Linking local and macroscopic strengths

The most interesting material property for us in tribology is the *shear strength*, which plays a key role in adhesive wear when viewed from the atomic scale. At the smallest scale, when no defects are present in a material (typically at a size smaller than the critical size d^* of the material), the measured shear strength of a sample (measured experimentally or numerically) is equal to its ideal shear strength $\sigma_{\mathrm{m,T}}$. In contrast, when two surfaces are put into contact, the resultant shear strength will be a fraction of the ideal shear strengths of the materials constituting the surfaces. We show in this section how the resultant shear strength can be estimated from the ideal strength, the normal load, and some geometrical parameters.

7.1.1 *Simulations*

As we have already established, two surfaces put into contact will meet only at a fraction of their total apparent area of contact. Small junctions are created between the surfaces, where asperities are touching. The imposed normal and shear stresses can only be carried by those junctions.

A single one of these junctions can be modeled as shown by Figure 7.1. The choice of the parameters of the pair-forces defines the intrinsic shear strength of the material. A shearing motion is applied on the system, with an imposed normal load, and the resultant tangential load is measured. The size of the junction relative to the size of the system reflects the fraction of real contact area that would appear between two rough surfaces in contact.

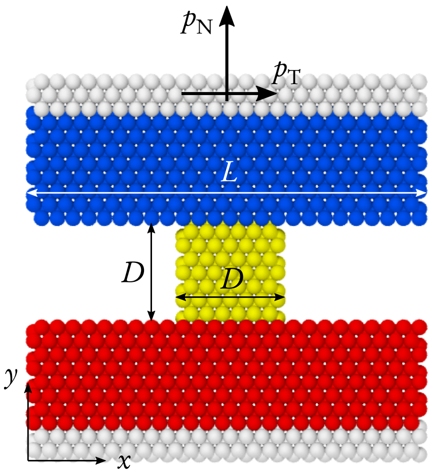

Figure 7.1 – DEM model of a junction between two sliding surfaces. Different materials can be attributed to each set of colored particles. White particles are part of rigid walls. The bottom wall is fixed. A normal load and a tangential displacement are applied on the top wall, and the tangential resistance is measured.

We model systems of size $37.5 \times 37.5 \times 2.4\text{nm}^3$ with an initial junction having a size ranging from $D = 5\,\text{nm}$ to the full length of the system ($D = L = 37.5\,\text{nm}$). The normal imposed load ranges from $p_N = 0$ to $p_N = 6\,\text{GPa}$. The material properties of SiO_2 are still used, with particles of size $d_0 = 1.5\,\text{nm}$ arranged in a crystalline HCP lattice. The top wall of the system is displaced in the y direction with a velocity $v = 10\,\text{m/s}$. The simulations are performed with a time step of $\Delta t = 0.1\,\Delta t_c$ and no global damping (internal damping between the particles, due to the restitution coefficient, are still present). As with the patch tests, the peak virial shear stress p_T is measured for each case.

The results are shown in Figure 7.2. The general tendency is to have a larger shear resistance p_T when the junction is wider. At $D = L$, the resistance is equal to the shear strength of the material. Junctions smaller than L usually detach into a rolling particle, and the maximum measured resistance seems to be proportional to the initial size of a junction. Meanwhile, junctions with the smallest initial sizes ($D = 5\,\text{nm}$ and $10\,\text{nm}$) deviate from this general trend by sometimes exhibiting higher resistances. This is caused by the junctions being smaller than the critical size d^* of the material (order of $10\,\text{nm}$) and not being detached into a rolling particle, but rather being flattened into a wider junction, therefore increasing their size and their ability to resist shear. The same crushing phenomenon happens to larger junctions when the normal load p_N is greater, and is responsible for all the points lying above the dashed line in Figure 7.2, representing $p_T = p_N$. An explanation can be found by analytically modeling the system, as we do in the next section.

Only the largest measured shear stress is reported here. During sliding, the rolling particles originating from the junctions are less resistant to tangential motion. For simplification, we report in the next section only the modeling of the initial shear resistance. The resistance met during the rolling regime can be estimated following the same principles.

7.1.2 *Model*

The simulations show that there is a strong link between the system's shear resistance and the actual size of the junction between the surfaces (which can be different from its initial size). As we established earlier, the junction must carry all the normal and tangential loads between the two

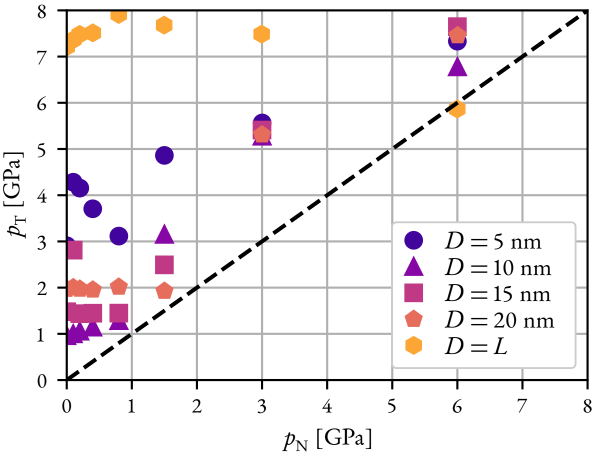

Figure 7.2 – Shear resistance of DEM systems with one junction. The size of the system is $L = 37.5$ nm in the direction of sliding. The initial junction size is indicated in the legend. Overall, the larger junctions give a higher resistance. The resistance is maximal when $D = L$ and is equal to the shear strength of the material. Junctions with a small initial size get wider under the normal load p_N, resulting in a higher resistance. All the points seem to lie above the $p_T = p_N$ line.

sliding surfaces.

The external normal pressure p_N acts on a surface of size

$$A_0 = L \times B\,, \tag{7.1}$$

where L and B are respectively the length and the width of the system in the x and z directions. We can refer to A_0 as the *apparent* contact area. The imposed load is therefore equal to

$$F_N = A_0\, p_N\,. \tag{7.2}$$

The imposed load is transmitted through the junction, having a surface area

$$A = D \times B\,, \tag{7.3}$$

which is the *real* contact area. The normal pressure felt *locally* by the junction is then

$$p_N^{\mathrm{loc}} = \frac{F_N}{A}\,. \tag{7.4}$$

The junction can only resist (keep its shape) to a normal pressure lower than its compressive strength $\sigma_{\mathrm{m,c}}$, meaning that there exists a critical normal pressure p_N^{crit} above which the junction gets crushed, up to the point where its new contact area A gets large enough to accommodate for the normal load F_N and have a local pressure p_N^{loc} not larger that the compressive strength $\sigma_{\mathrm{m,c}}$. In the general case where the compressive strength is dependent on the local normal pressure (we will write it as $\sigma_{\mathrm{m,c}}(p_N^{\mathrm{loc}})$), the critical pressure is defined as

$$p_N^{\mathrm{crit}} = \sigma_{\mathrm{m,c}}(p_N^{\mathrm{crit}})\,, \tag{7.5}$$

and can be found by solving this equation (which could be non-linear, depending on the chosen expression of $\sigma_{\mathrm{m,c}}(p_N^{\mathrm{loc}})$). Knowing the critical local pressure, we can deduce the minimum contact area the junction must have to resist being flattened, which is simply

$$A_{\mathrm{min}} = \frac{F_N}{p_N^{\mathrm{crit}}} = A_0\,\frac{p_N}{p_N^{\mathrm{crit}}}\,. \tag{7.6}$$

The size D of the junction will grow under the normal load to have at least this contact area (see (7.3)). Let us assume that the amount of tangential resistance the junction can withstand is proportional to its area A and to its local shear strength $\sigma_{\mathrm{m,T}}(p_{\mathrm{N}}^{\mathrm{loc}})$, which in the general case can be dependent on the local normal pressure. The resistance can be expressed as a tangential force

$$F_{\mathrm{T}} = A\,\sigma_{\mathrm{m,T}}(p_{\mathrm{N}}^{\mathrm{loc}}), \tag{7.7}$$

and since the junction area A has a minimum value A_{min}, the tangential force also has a minimum value of

$$F_{\mathrm{T,min}} = \frac{\sigma_{\mathrm{m,T}}(p_{\mathrm{N}}^{\mathrm{loc}})}{p_{\mathrm{N}}^{\mathrm{crit}}} F_{\mathrm{N}}\,. \tag{7.8}$$

When viewed from the whole system perspective, this force translates into a tangential stress:

$$p_{\mathrm{T}} = \frac{A}{A_0}\sigma_{\mathrm{m,T}}\left(\frac{A_0}{A}p_{\mathrm{N}}\right), \tag{7.9}$$

with a minimum value of

$$p_{\mathrm{T,min}} = \frac{p_{\mathrm{N}}}{p_{\mathrm{N}}^{\mathrm{crit}}}\sigma_{\mathrm{m,T}}(p_{\mathrm{N}}^{\mathrm{crit}}), \tag{7.10}$$

where $p_{\mathrm{N}}^{\mathrm{loc}}$ has been replaced by its definition (7.4).

Equations (7.5), (7.9) and (7.10) summarise the model for estimating the macroscopic tangential resistance p_{T} from the normal stress p_{N}, the contact area ratio A/A_0, and local material properties, the later being the shear strength $\sigma_{\mathrm{m,T}}$ and the critical crushing pressure $p_{\mathrm{N}}^{\mathrm{crit}}$.

To apply this new model to the simulated system of the previous section, we must define the shear strength $\sigma_{\mathrm{m,T}}$ and the critical crushing pressure $p_{\mathrm{N}}^{\mathrm{crit}}$. Looking at the simulation data in Figure 7.2, the shear strength seems to have a value around $\sigma_{\mathrm{m,T}} = 7.5\,\mathrm{GPa}$, independent of the local normal pressure. To find the critical normal pressure, we must first define the compressive strength of the material, which can be approximated as being equal to the shear strength, thus $\sigma_{\mathrm{m,c}} = 7.5\,\mathrm{GPa}$. Solving the trivial equation (7.5), we obtain the critical pressure $p_{\mathrm{N}}^{\mathrm{crit}} = 7.5\,\mathrm{GPa}$. Injecting these values in (7.9) and (7.10), we obtain the fitted model

$$p_{\mathrm{T}} = \frac{A}{A_0} \times 7.5\,\mathrm{GPa}, \tag{7.11}$$

$$p_{\mathrm{T,min}} = p_{\mathrm{N}}\,. \tag{7.12}$$

The model is plotted in Figure 7.3 using the same values for p_{N} and A/A_0 as in the simulations. Two main behaviors previously observed in the simulations are recovered with the model:

- The resistance is proportional to the initial size of the junction and is maximal when $D = L$ (7.9);
- There is a minimum value for the resistance, which depends on the normal load p_{N} (7.10). In the tested case, the limit follows the $p_{\mathrm{T}} = p_{\mathrm{N}}$ line.

We did not take into account the effect of the material's critical size d^*, responsible for pulling up the resistances of junctions initially smaller than d^*. In fact, our simple model also applies to systems where multiple junctions are present. Only the contact area ratio A/A_0 needs to be monitored. The downside is that using A/A_0 does not give any information about the actual size of each junction, which in turn cannot be compared to d^*. So, we chose to let the effect of d^* aside in this model. Besides, the model predicts resistances which are overall higher than the ones measured in DEM simulations. We can attribute this to the central assumption made at the

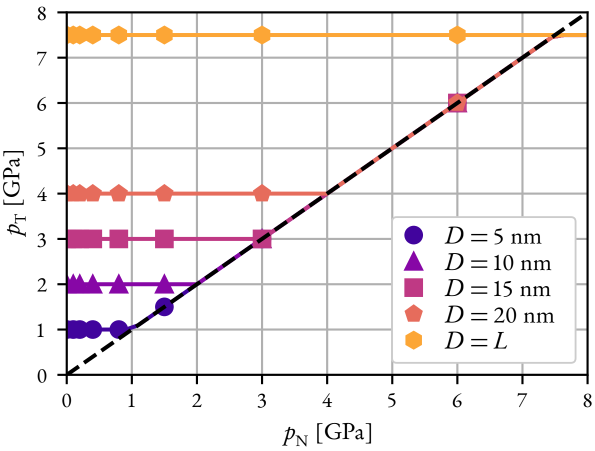

Figure 7.3 – Predicted shear resistance of systems with one junction. Points are shown wherever the set of parameters has been tested with a DEM simulation (see Figure 7.2). The model predicts the same trend as the results of DEM simulations. In particular, it shows that the $p_T = p_N$ line indeed is the lower limit for the resistance p_T.

establishment of equation (7.7), neglecting the effects of geometry and the potential presence of stress concentrations, which could both be responsible for lower resistance.

The established simple model, described by equations (7.9) and (7.10) can be used to predict the tangential resistance of a sliding system when the normal load and the real contact area are know. The local shear strength has to be given as an input to the model, ideally along with its dependence on the normal pressure. For tribological systems, it makes sense to provide the dynamical shear strength. The compressive strength must also be provided, but can be reasonably approximated by the shear strength. While this model can only output rough estimates for the tangential resistance, it is worth noting that it does not rely on any empirical parameter.

7.2 WEAR OF ROUGH SURFACES AT MULTIPLE SCALES

In this study, we leave the single-asperity scale to move up to the scale of surface roughness. Two SiO_2 rough surfaces are considered. The average size of the discrete particles is varied from $d_0 = 1.5\,\text{nm}$ up to $96\,\text{nm}$. For each particle size d_0, three system sizes are tested: $L = 25\,d_0$, $L = 50\,d_0$, and $L = 100\,d_0$. The initial roughness of the surfaces is set to $Sa = 0.01\,L$, $0.02\,L$ and $0.04\,L$. The systems are sheared with a sliding velocity ranging from $v = 0.1\,\text{m/s}$ to $10\,\text{m/s}$. A constant normal pressure is applied on the system, taking values from $p_N = 0.1\text{GPa}$ to $1\,\text{GPa}$. The effect of each parameter on the friction force and the wear process (wear volume and surface roughness) is investigated. To know whether a particle is "worn", its list of current neighbors is compared to the list of neighbors it has at the initial step. If more than half of the initial neighbors are no longer in the current list, the particle is considered as worn. It is given a red color in the post-processed images.

7.2.1 *Qualitative results*

The system's behavior is dependent on its size and on the average size of particles d_0. Sizes can be compared to the material's critical length scale d^*, which is around 18 nm for the simulated

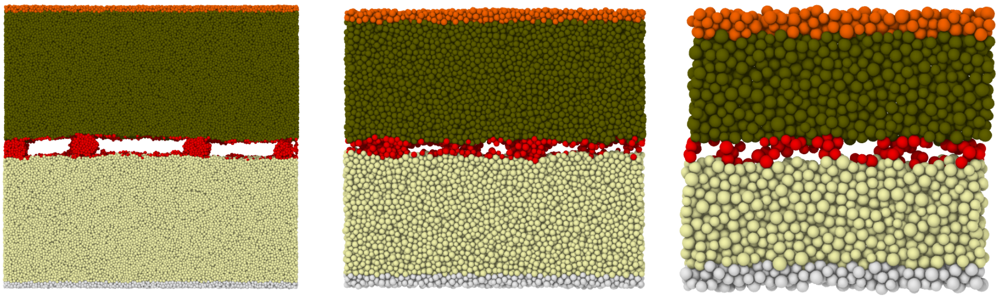

(a) $d_0 = 2\,\text{nm}$ (b) $d_0 = 4\,\text{nm}$ (c) $d_0 = 8\,\text{nm}$

Figure 7.4 – Formation of wear particles from rough surfaces in DEM. Worn particles are shown in red. The size of the systems is $L = 200\,\text{nm}$, the initial surface roughness is $Sa = 2\,\text{nm}$, and the current sliding distance is $s = 480\,\text{nm}$. For comparison, $d^* \approx 18\,\text{nm}$.

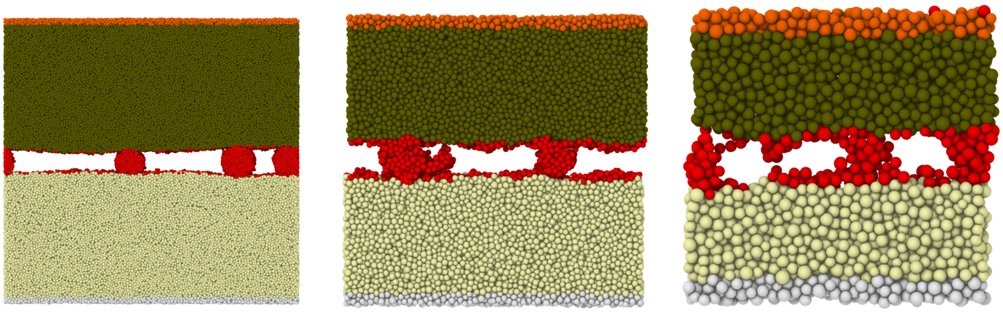

(a) $d_0 = 2\,\text{nm}$ (b) $d_0 = 4\,\text{nm}$ (c) $d_0 = 8\,\text{nm}$

Figure 7.5 – Growth of wear particles trapped between sliding rough surfaces. The sliding distance is now $s = 4\,\mu\text{m}$. Ultimately, all rolling particles merge into a single one (not shown here).

material (SiO_2). At small scale, when $d_0 < d^*$, wear particles are formed (see Figure 7.4) and then grow with the increasing sliding distance (Figure 7.5). They usually merge into larger rolling particles after some time. The same behavior is recovered using different levels of discretization. At large scale, when d_0 is significantly larger than d^*, the formation of wear particles is not observed anymore. Instead, a growing shear band appears (Figure 7.6).

7.2.2 *Quantitative results*

The evolution of the tangential force is tied to the qualitatively observed regime (see Figure 7.7). When wear particles are formed, the tangential force drops to a low value, whereas the opposite behavior is measured when a shear band is formed. Note that for systems having the same size L but different particle sizes d_0, the quantitative measurements only match if the method stated in Section 6.2.3 is applied (have the same largest particle size d_1 in all systems regardless of d_0).

The normal pressure p_N affects the regime reached by a given system. At low pressure, the wear particles formation regime is favored. No system featuring a transition between having rolling wear particles and forming of a shear band was found, motivating the study reported in the next section.

The sliding velocity does not affect any measured quantity, which may not seem physical,

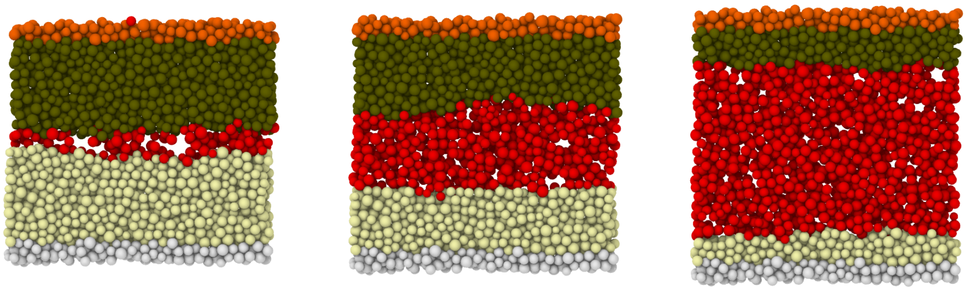

(a) $s = 1.28\,\mu\mathrm{m}$ (b) $s = 8.96\,\mu\mathrm{m}$ (c) $s = 35.84\,\mu\mathrm{m}$

Figure 7.6 – Growth of a shear band. The average particle size is $d_0 = 64\,\mathrm{nm}$, the size of the systems is $L = 1.6\,\mu\mathrm{m}$, and the initial surface roughness is $Sa = 16\,\mathrm{nm}$.

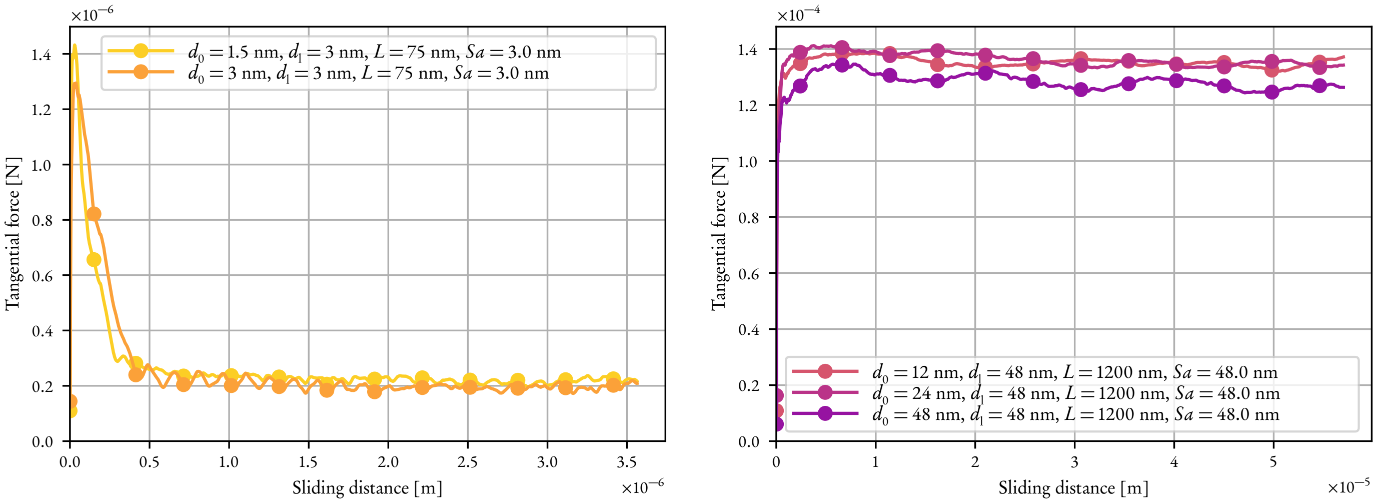

(a) Formation of wear particles. $L = 75\,\mathrm{nm}$. (b) Shear band. $L = 1200\,\mathrm{nm}$.

Figure 7.7 – Tangential force measured in both frictional regimes. The multiple curves correspond to systems with different discretizations (d_0), having otherwise identical geometrical parameters (largest particle size d_1, system size L, and initial Sa roughness). Keeping d_1 constant for different discretizations leads to quantitatively matching forces. (a) Regime where rolling wear particles are formed and merge together. The rolling motion gives a low resistance against sliding. (b) Formation of a shear band, with large tangential resistance.

since higher velocities should involve heating effects. However, temperature is not implemented in our DEM model, so it cannot represent these effects. The fact that shear bands seem to grow unbounded (see Figure 7.6) is also likely due to the lack of temperature effects. Indeed, it is known that materials are subject to thermal softening, which has the effect of keeping the strain localized in shear bands (Fleitout & Froidevaux 1980; Lewandowski & Greer 2006).

Initial surface roughness does not affect the frictional force. In fact, it evolves toward a similar Sa value regardless of the initial one, which explains why the frictional force does not differ after the running-in period. The evolution of surface roughness is explored in more depth in Chapter 8, with experiments.

7.3 Transition between frictional regimes with wear particles

This study is motivated by the previous one, where two frictional regimes arise, but no transition between them is observed. To answer this issue, the same kind of simulations are run, but without initial surface roughness, and with circular particles already present initially between the surfaces. Between $n = 2$ and $n = 4$ particles are inserted. The normal pressure is still varied from $p_\mathrm{N} = 0.1\,\mathrm{GPa}$ to $1\,\mathrm{GPa}$.

As before, two regimes can be reached (see Figure 7.8). However, this time, a transition is observed, as shown in Figure 7.9, at a specific normal load, and when 3 or 4 particles are initially present in the system. Having multiple evenly sized loose particles trapped in the systems seems to be the main ingredient allowing the transition between the two regimes. The transition also happens at a very specific normal load. In the previous study, all systems where particles formed ultimately resulted in them merging into a single rolling wear particle.

Whether rolling particles remain or get crushed into a shear band seems to depend on the normal load and the compressive strength of the material. When multiple particles are present, they share the compressive stress applied on the system. When two loose particles merge together, the compressive force felt by the resulting particle is multiplied by 2, but its contact area with the first-body surfaces is only multiplied by $\sqrt{2}$. In the right conditions, multiple surviving rolling particles can merge into a single one that cannot withstand the compressive stress, making the transition toward the shear band. On the other hand, when a single rolling particle is present, its size will grow upon sliding, but the compressive stress does not, meaning that the particle can survive indefinitely. It explains why no transitions were observed in the study of previous section.

Concluding remarks

We showed that our coarse-grained DEM model is capable of tackling dynamic wear systems at the nanoscale and up. It is possible to simulate the apparition of wear particles when the discretization size is smaller than the material's critical size d^*_r and the formation of a shear band under a larger normal load. d^* and the material compressive strength seem to play an important role in the evolutionary behavior of the systems, which calls for a more extensive and systematic study. While all simulations were performed in quasi-2D setups (3D but with a small thickness), they can be naturally run in 3D. One ingredient missing in the DEM model is temperature (and heat transfer), which should play a role when modeling larger scales.

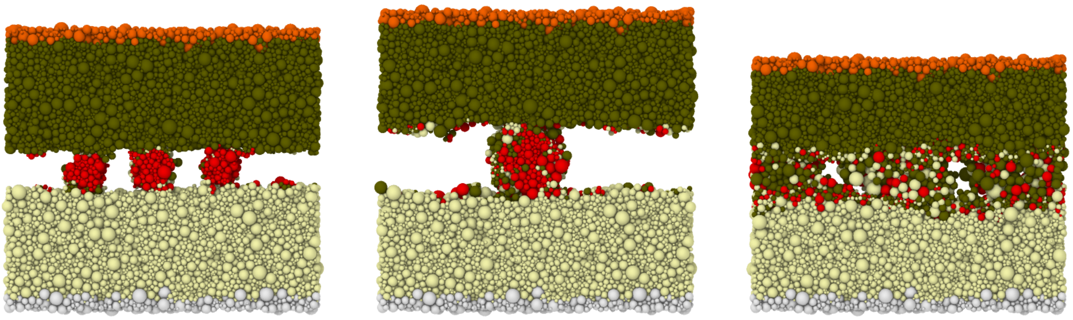
(a) Initial rolling particles. $p_\mathrm{N} = 0.1\,\mathrm{GPa}$, $s = 600\,\mathrm{nm}$.

(b) Fusion into one particle. $p_\mathrm{N} = 0.3\,\mathrm{GPa}$, $s = 7.2\,\mathrm{\mu m}$.

(c) Shear band. $p_\mathrm{N} = 1\,\mathrm{GPa}$, $s = 7.2\,\mathrm{\mu m}$.

Figure 7.8 – Reaching two frictional regimes from trapped wear particles. The average particle size is $d_0 = 3\,\mathrm{nm}$ and the initial system size is $L = 300\,\mathrm{nm}$. (a) 3 loose particles are initially present. (b) When the normal load is low, the particles ultimately merge into a single one. (c) With a higher normal load, the particles are crushed into a growing shear band.

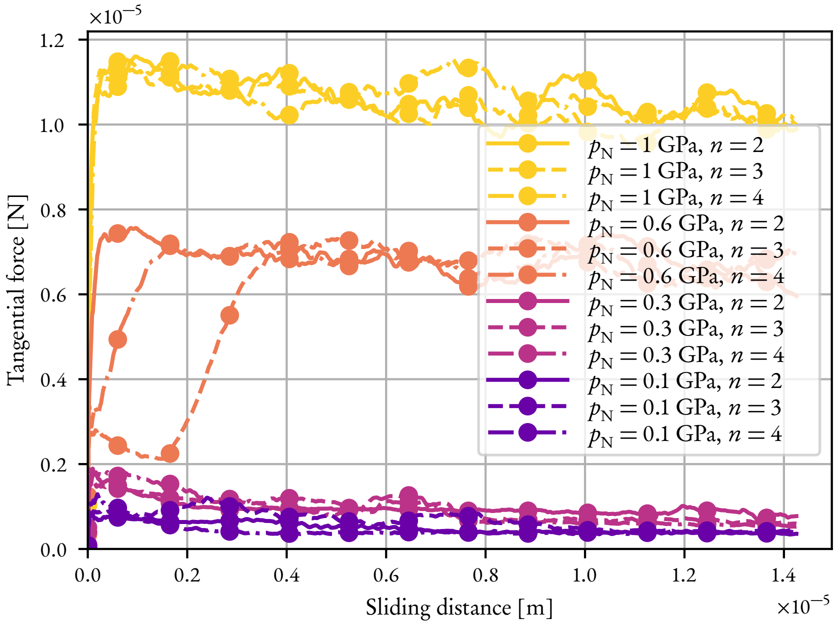

Figure 7.9 – Evolution of frictional force during a transition of regime. For low normal loads $p_\mathrm{N} \leqslant 0.3\,\mathrm{GPa}$ (blue and purple curves), the initial wear particles fuse into a single larger one, inducing low tangential forces due to the rolling motion. At an intermediate load $p_\mathrm{N} = 0.6\,\mathrm{GPa}$ (in orange) and for $n = 3$, the system evolves with rolling particles for some time, and then transitions to a regime with a shear band, with a much higher tangential resistance. All other cases (high load or few particles) directly go to the shear band state. Note that in the case with $p_\mathrm{N} = 0.6\,\mathrm{GPa}$ and $n = 4$ (mixed orange curve), the system should in principle be able to sustain a rolling particles regime. However, having more closely spaced particles allows them to merge earlier, rapidly transitioning toward a shear band regime.

PART III

EXPERIMENTAL STUDIES AND MODELING

CHAPTER 8

CREATION AND EVOLUTION OF ROUGHNESS

Disclaimer

This chapter is reproduced in part from S. Pham-Ba and J.-F. Molinari (2021b), “Creation and evolution of roughness on silica under unlubricated wear”, *Wear* 472–473, with permission from all authors. My personal contribution was planning and performing the experiments, making the measurements, running the numerical simulations, post-processing the results, and writing. We thank Tobias Brink[1] for sharing his expertise in MD simulations and for providing insightful discussions.

INTRODUCTION

FRICTION coefficients and the way they evolve over time are currently hardly predictable. To better understand friction, it is useful to relate it to known geometrical and physical characteristics of the tribological system. As the most simple friction laws suggest, like the Coulomb’s friction law, friction forces are mostly independent of the apparent contact area, and are instead linked to the real contact area (Bowden & Tabor 1966). Indeed, contacting rough surfaces only touch where protruding asperities meet, resulting in a real contact area being only a fraction of the total apparent contact area in most operating conditions. The ratio between real and apparent contact area is positively correlated with the normal load and is smaller for increasing surface roughness. Since frictional processes can only take place at the contact spots in an unlubricated contact, this highlights a direct relation between friction and surface roughness. This relation applies to all engineered (Mandelbrot *et al.* 1984; Majumdar & Tien 1990) or natural surfaces (Thom *et al.* 2017), as they all display some roughness within a certain range of length scales.

Surface roughness itself can evolve thanks to wear. MD simulations of adhesive wear (Milanese *et al.* 2019) show that, at the nanoscale, two rough surfaces sliding on each other evolve toward fractal self-affine rough surfaces with the same fractal dimension regardless of the initial roughness. Another feature of these nanoscale simulations is the apparition of a rolling third-body particle, which seems to be a key factor behind the evolution of the surface roughness to self-affine characteristics.

At the engineering scale, experiments show that wear leads to the modification of the rubbed surfaces, with the formation of a third-body layer made of sintered worn material (Wirth *et al.*

---

[1] Department of Structures and Nano/Micromechanics of Materials, Max-Planck-Institut für Eisenforschung, 40237 Düsseldorf, Germany

1994; Meierhofer *et al.* 2014), also called tribo-layer (Riahi & Alpas 2001) or tribofilm (Gosvami *et al.* 2015; Kato & Komai 2007), which contributes to a change in the frictional properties of the interface.

The same evolutionary behavior is found at the geological scale. Gouge formation is omnipresent in brittle faults (Scholz 1987; Wilson *et al.* 2005). It is made of crushed and worn rock particles and dictates the frictional properties of the interface, as seen experimentally (Starfield & Cundall 1988; Biegel *et al.* 1989; Mair *et al.* 2002) and numerically (Morgan 1999; Guo & Morgan 2007).

Studies also considered the evolution of surface roughness due to wear, for example in engineering applications using *pin-on-disc* setups, where metallic samples can go through multiple wear regimes over time (Kubiak *et al.* 2011) and settle down to a steady state after a certain amount of time. At steady state, the worn surfaces of the samples are seen to exhibit identical geometrical characteristics (wear track and surface roughness) regardless of the initial surface roughness for the same operating conditions (Yuan *et al.* 2008). Other studies reproducing or looking at geological phenomena observe a steady-state self-affine roughness upon sliding after a running-in period (Power *et al.* 1988; Brodsky *et al.* 2011; Candela & Brodsky 2016; Thom *et al.* 2017). However, overall, the mechanisms of the onset of wear and their link with following wear processes are not studied in detail. A direct non-empirical relation between material properties and wear processes remains to be found.

Here, an experimental study of friction and wear was performed on amorphous silica (SiO_2) using a rotating tribometer in a *pin-on-disc* configuration. From observations of worn surfaces after various sliding distances, we deduced the steps giving rise to the creation of surface roughness from comparatively flat initial surfaces — from the formation of the first third-body particles, often overlooked in the literature, to the full third-body layer — while attempting to directly relate the very first events of wear to material properties. The observations linked to the onset of wear are complemented by MD simulations. We also assessed the evolution of the friction coefficient and the surface roughness given different initial surface roughnesses, and we provide a mechanistic description of the factors behind surface roughness evolution.

8.1 EXPERIMENTAL SETUP

The tribological tests have been performed using 6 mm spheres of amorphous SiO_2 sliding (rotating) on discs made of the same material (see Figure 8.1). A *Bruker UMT 3* tribometer was used. The sliding velocity of the ball was 8 mm/s and it followed a circular path of radius 1 mm with a normal load of $F_N = 1\,\mathrm{N}$. Using Hertz contact theory, we get that in the elastic case the diameter of the contact zone between the unworn ball and the disc is 78.2 µm and the maximum pressure (reached

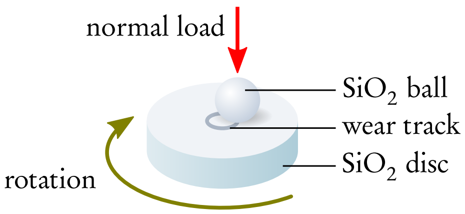

Figure 8.1 – Experimental setup on tribometer. The disc is fixed to a rotating motor. The ball can only move vertically and is kept against the disc with a constant normal load.

Table 8.1 – Duration and initial roughness of the tests. The table is subdivided into three sections according to the polishing of the discs. The latter are manually polished using sandpaper with the indicated grain sizes. Each test has a duration and a corresponding sliding distance, known from the fixed sliding velocity of 8 mm/s. The third column indicates the number of repetitions for each set of parameters, and the multiple initial disc Sa are indicated for each repetition when they differ significantly.

Duration	Distance	Rep.	Polishing	Disc Sa [μm]
1 s	8 mm	1	none	≈ 0.01
15 s	12 cm	1		
30 s	24 cm	1		
1 min	48 cm	1		
15 min	7.2 m	1		
30 min	14.4 m	1		
1 h	28.8 m	3		
2h30	72 m	2		
5 h	144 m	3		
2h30	72 m	3	P120	0.78, 0.91, 0.74
5 h	144 m	3		0.79, 0.63, 0.58
2h30	72 m	3	P80	1.54, 0.75, 1.51
5 h	144 m	3		1.51, 1.56, 1.58

at the center of the contact zone) is 312 MPa.[2]

For comparison, the compressive strength of SiO_2 is $\sigma_{\mathrm{m}} = 1150\,\mathrm{MPa}$. The initial untreated surface roughness of the balls and the discs has been identified using atomic force microscopy (AFM) and is around $Sa \approx 10\,\mathrm{nm}$, which is very small from an engineering point of view. Some discs have been manually polished using P120 and P80 sandpaper, resulting in roughened surfaces with $Sa = 0.74\,\mu\mathrm{m}$ and $Sa = 1.41\,\mu\mathrm{m}$ in average respectively (see Section 8.1.1 for details about the computation of the Sa surface roughness). Only the discs were treated to have an initial surface roughness, while the balls were kept flat, with their initial roughness of $Sa \approx 10\,\mathrm{nm}$. It is indeed difficult to polish the SiO_2 balls in the same way as the discs without disrupting their spherical shape. Shot peening or sandblasting could have been used to roughen the balls, but having them initially smooth is not very important for this study since a surface roughness (dissimilar to the one on the discs) eventually develops on them.

Table 8.1 lists the tests that were performed. The initial Sa of the discs are indicated. Some variation in the Sa roughnesses can be seen amongst the discs which were polished with the same grain size. This is in part due to the inherent variability of the manual polishing process. The fact that those roughness measurements were only performed in a single small window on each disc can also imply some uncertainty.

For each test, the Sa roughness of the disc is measured before and after the experiment (details in the following section). The vertical reaction force F_z and the lateral force F_x parallel to the direction of sliding are recorded during the whole test, from which a dynamical friction coefficient $\mu = F_x/F_z$ is deduced. Roughness measurements cannot be similarly performed over the whole duration of a test because they are not *in situ* measurements. Finally, scanning electron microscope (SEM) images of the wear tracks and wear particles formed on the initially flat discs were taken after various durations.

---

[2] The material properties of SiO_2 are $E = 73\,\mathrm{GPa}$ and $\nu = 0.17$. The contact radius a is given by (Johnson 1985): $a = \sqrt[3]{\frac{3F_{\mathrm{N}}R}{4E^*}} = 39.1\,\mu\mathrm{m}$, where $R = 3\,\mathrm{mm}$ and E^* is the equivalent Young's modulus: $E^* = \frac{E}{2(1-\nu^2)} = 37.6\,\mathrm{GPa}$. The maximum pressure reached at the center of the contact zone is: $p_0 = \frac{3F_{\mathrm{N}}}{2\pi a^2} = 312\,\mathrm{MPa}$.

8.1.1 *Sa roughness measurement*

Surface topography measurements are acquired using a *Sensofar S-Neox* confocal microscope on a 117 µm × 88 µm window of 1360 px × 1024 px, resulting in data points $h(x,y)$ with discrete x and y. Missing data points are filled by iteratively solving a Laplace equation at those points:

$$\frac{\partial^2 h}{\partial x^2} + \frac{\partial^2 h}{\partial y^2} = 0 \,. \tag{8.1}$$

A plane is fitted by least-squares minimization and subtracted to the points to obtain a zero-mean topography $h_0(x,y)$. The Sa roughness is defined as:

$$Sa = \frac{1}{N}\sum_{x,y} |h_0(x,y) - \overline{h}_0| \tag{8.2}$$

where N is the number of data points and $\overline{h}_0$ is the mean value of h_0.

Since the value of Sa is dependent on the size of the measurement site due to the fractal nature of the rough surfaces, all measurements of Sa roughness have to be performed at the same window size to be comparable. Usually, the Sa roughness decreases when the window size gets smaller.

To obtain the Sa roughness of the unpolished and polished discs before the tests, only one topographic measurement is performed at the center of the sample. For the Sa of the circular wear tracks left on the discs, four locations on the track are measured and the computed Sa are averaged.

8.2 RESULTS AND DISCUSSION

8.2.1 *Initial wear particle size*

Figure 8.2 shows SEM images of wear particles found on a flat disc after only 1 s of sliding, corresponding to a sliding distance of 8 mm. The images were obtained using a *Zeiss SUPRA 55-VP* SEM. The formation of wear particles is the first and only evidence of wear found on the disc at this stage (there is no wear track). An adhesive nickel patch was rubbed against the surface of the worn disc to capture the wear particles in order to more easily observe them with SEM. No particle smaller than 30 nm was observed. Whether this size depends on the material properties or the loading conditions is discussed thereafter.

Recent theoretical work (Aghababaei *et al.* 2016) has confirmed the existence of a critical length scale d^* which governs a transition between ductile and brittle behavior for any given material. The expression of d^* for the detachment of spherical wear particles is

$$d^* = \frac{12\gamma G}{\sigma_\mathrm{j}^2} \,, \tag{8.3}$$

where γ is the surface energy of the material, G is the shear modulus and σ_j is the shear strength (or flow stress) of cold-welded junctions. Note that d^* is mainly dependent on material parameters and weakly depends on geometry and loading conditions (which influence the “12” factor), thus

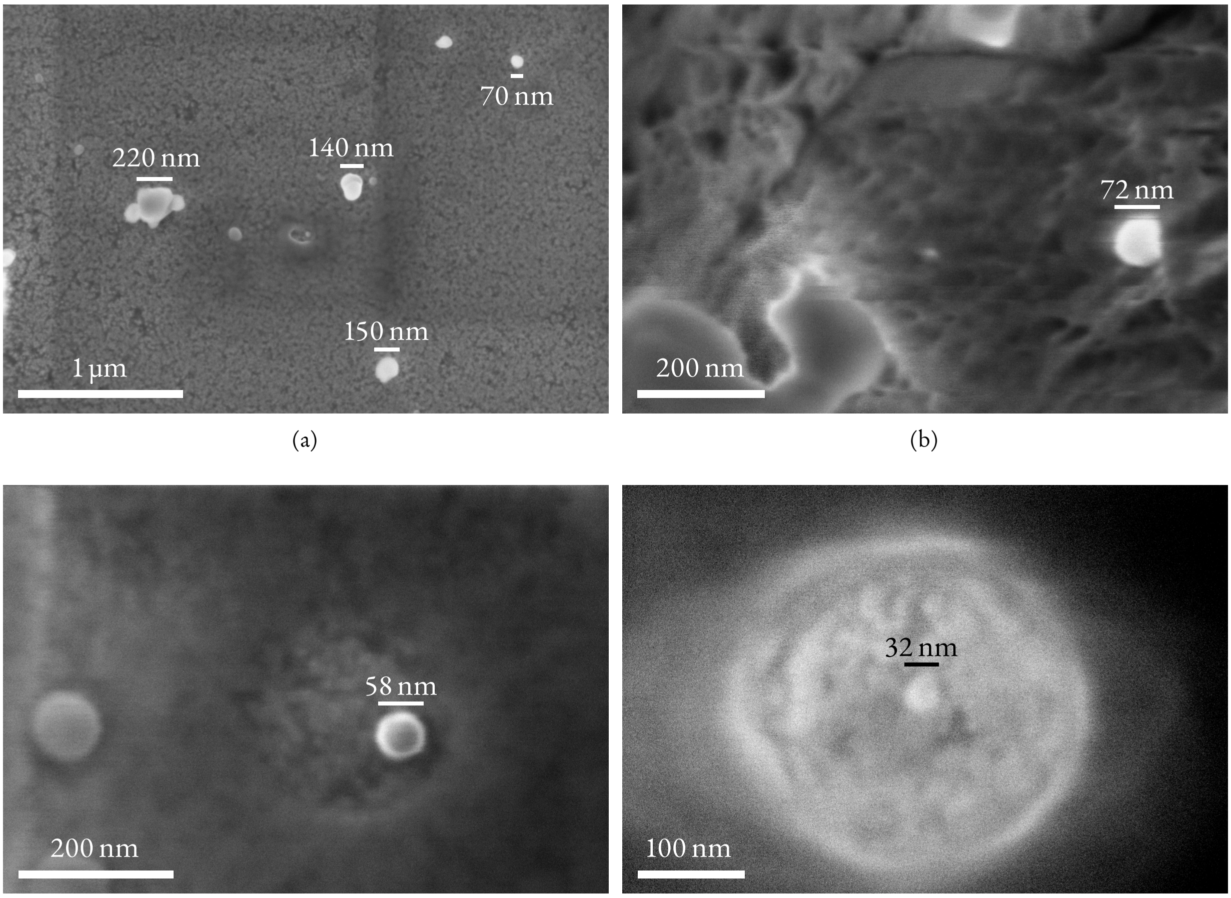

(a)

(b)

(c)

(d) The silica was discriminated from the nickel background using energy-dispersive X-ray (EDX) spectroscopy

Figure 8.2 – SEM images of wear particles taken from a flat disc after 1 s (8 mm) of sliding. The particles were collected from the disc using an adhesive nickel patch for an easier observation.

it can be itself considered as a material parameter. A sheared junction between two surfaces can only be detached into a wear particle if its size d is larger than d^*. Otherwise, it flows plastically. It implies that no wear particles smaller than d^* should be observed in wear experiments, because they cannot be created.

Using MD simulations, we computed estimates for the unknown material parameters of amorphous SiO_2 using a potential by Vashishta *et al.* (1990) taking into account three-body interactions, using a cutoff parameter of $r_c = 8\,\text{Å}$. The amorphous SiO_2 MD system is prepared following the procedure of Luo *et al.* (2016), as described in Section 2.1.3. A shear strength of $\sigma_j = 7.2\,\text{GPa}$ is obtained from a bulk shear test without fracture, with periodic boundary conditions, at a strain rate of $4 \times 10^7\,\text{s}^{-1}$. A surface energy of $1.5\,\text{N/m}$ is estimated by cutting the sample at 10 random planes and averaging the results, while the charge neutrality is being preserved by keeping periodic boundary conditions. Using (8.3) with those material parameters leads to the estimate:

$$d^* \approx 15\,\text{nm}\,.$$

Luo *et al.* (2016) observed a similar ductile-to-brittle transition size of 18 nm in MD simulations of glass SiO_2 nanofibers, also using the Vashishta potiential. It is also shown that this potential can provide quantitatively correct values for Young's modulus and tensile strength, so that the value found for d^* is likely to also be quantitatively accurate.

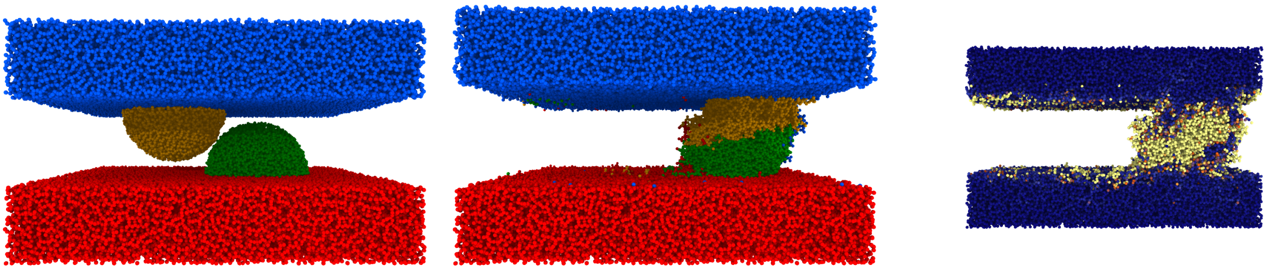

(a) Initial configuration (b) After collision (c) Shear strain (cross section)

Figure 8.3 – MD simulation of a collision between two amorphous SiO_2 asperities of diameter $d = 7\,\text{nm}$. The initial simulation size is $20.2\,\text{nm} \times 21.0\,\text{nm} \times 11.8\,\text{nm}$ (in the figures: length × height × depth). The non-localized shear strain (brighter is higher) shows a plastic deformation of the asperities, indicating that $d < d^*$.

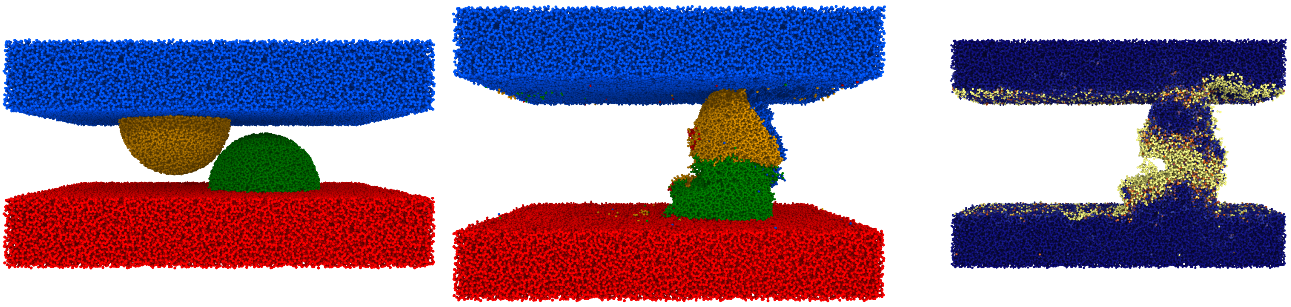

(a) Initial configuration (b) After collision (c) Shear strain (cross section)

Figure 8.4 – MD simulation of a collision between two amorphous SiO_2 asperities of diameter $d = 10\,\text{nm}$. The initial simulation size is $30.3\,\text{nm} \times 21.0\,\text{nm} \times 16.0\,\text{nm}$. The behavior is in-between ductile and brittle, indicating that $d \simeq d^*$.

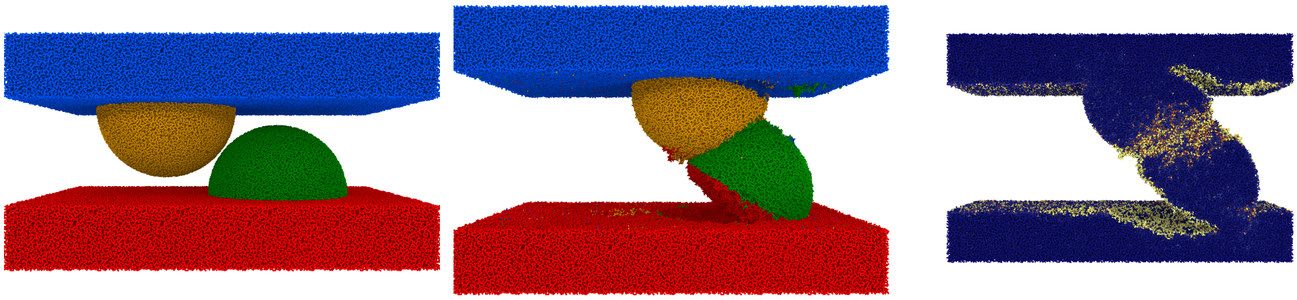

(a) Initial configuration (b) After collision (c) Shear strain (cross section)

Figure 8.5 – MD simulation of a collision between two amorphous SiO_2 asperities of diameter $d = 20\,\text{nm}$. The initial simulation size is $50.5\,\text{nm} \times 31.6\,\text{nm} \times 27.5\,\text{nm}$. The presence of clear cracks (regions of high strain) indicates a brittle behavior, implying that $d > d^*$.

To confirm that the estimated d^* really corresponds to the transition of interest for amorphous SiO_2, we simulated a setup equivalent to Aghababaei *et al.* using the Vashishta potential in LAMMPS (Plimpton 1995). The setup consists of two hemispherical asperities of diameter d, each attached to a flat body (as shown in Figure 8.3a). The amorphous SiO_2 structure is created following the same procedure as before. A periodic cubic unit cell of side $\approx 10\,\text{nm}$ containing amorphous SiO_2 was generated and used to build the whole setup by tiling the space with the SiO_2 cells and carving the desired shapes by removing the atoms, while making sure to preserve charge neutrality. A constant lateral velocity of 10 m/s is applied on the upper body to make the asperities collide. Normal loads are applied on the top and bottom bodies to obtain pressures of 100 MPa to 200 MPa on the loaded surfaces, which prevents the system from flying apart. Periodic boundary conditions are applied in the horizontal directions. Langevin thermostats are applied at the non-periodic boundaries to keep the temperature of the system constant at 300 K with a damping constant of 0.01 ps. A timestep of 1 fs is used. The simulation results are shown in the Figures 8.3 to 8.5, visualized using OVITO (Stukowski 2009), for the asperity diameters $d = 7\,\text{nm}$, $d = 10\,\text{nm}$ and $d = 20\,\text{nm}$. These values were chosen around the theoretical estimate $d^* \approx 15\,\text{nm}$. The atomic shear strain (computed relative to the initial configuration) is used to determine whether the wear regime is ductile or brittle. In the ductile case (Figure 8.3), the colliding asperities are plastically deformed, resulting after the collision in high permanent shear strains between all the atoms located in the plasticized region. In the brittle case (Figure 8.5), a wear particle combining the two asperities is formed, and high strains only remain in the fractured regions, whereas inside the wear particle, the strains increase during the collision and return to a low value after the formation of cracks, since the atoms retain their original configuration. According to Aghababaei *et al.*, the critical length scale d^* is defined as the size of the junction between the colliding asperities corresponding to the transition between ductile and brittle behaviors. In our case, instead of measuring the size of the junction, we assume for simplicity that it has a size roughly equal to the diameter of the asperities d. The simulations show that the d^* of amorphous SiO_2 is indeed located between 7 nm and 20 nm. Note that there is no sharp transition between the ductile and brittle behavior (see Figure 8.4 which shows an in-between behavior), which is why d^* is called a *length scale* rather than a definite length.

The theoretical estimate $d^* \approx 15\,\text{nm}$ and the lower and upper bounds ($d^* > 7\,\text{nm}$ and $d^* < 20\,\text{nm}$) found using simulations for the value of d^* for SiO_2 are in line with the minimum size of wear particles found experimentally (no particles smaller than 30 nm were observed). This supports the idea that no wear particles smaller than d^* can be created, which is expected because a junction smaller than d^* cannot be detached into a wear particle. Due to the nature of d^* being mainly dependent on material parameters and only weakly on geometry or loading conditions, we can infer that the minimum size of wear particles formed when rubbing two surfaces together is equal to d^* and similarly only dependent on the materials of the two surfaces.

Having established the notion of minimum wear particle size, we know that wear particles can be formed when two asperities located on rubbed surfaces and having a diameter greater than d^* collide with each other. Therefore, wear particles can understandably form from rough surfaces. The formation of wear particles is still possible if the surfaces are flat and free of protruding asperities. When put in contact under a normal load, the surfaces will meet at some points and create adhesive junctions. A tangential load applied on an adhesive junction will enable the formation of wear particles if the size of the junction is greater than d^*. If it is smaller, the junction may grow in size due to plastic deformations, if the adhesive forces are strong enough, until reaching the critical size when a wear particle can finally be detached.

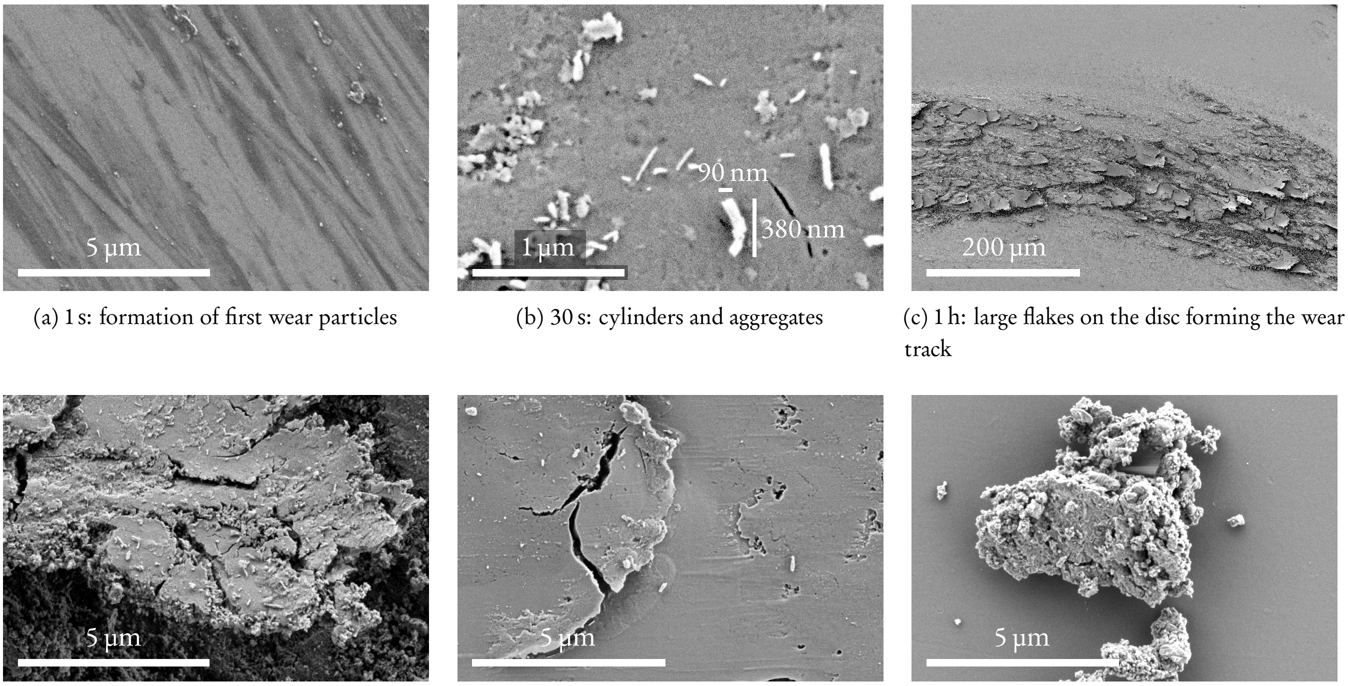

(a) 1 s: formation of first wear particles

(b) 30 s: cylinders and aggregates

(c) 1 h: large flakes on the disc forming the wear track

(d) 1 h: detail: aggregates forming a large flake

(e) 1 h: detail: cylinders and aggregates on top of a flake

(f) 1 h: detail: aggregated wear particle fallen outside the wear track

Figure 8.6 – SEM images of wear tracks on flat discs after different amounts of time

8.2.2 *Roughness formation*

Figure 8.6 shows SEM images of the wear track left by a ball on flat discs after various sliding durations in chronological order. From an initially almost flat surface of the disc, the process of creation of surface roughness goes through different steps. At first, small spherical wear particles of minimum size d^* are created in the way described in the previous section (see Figure 8.2 and 8.6a). The newly created particles enter a rolling motion between the two rubbed surfaces and start growing in size by chipping away some material from the flat surfaces thanks to adhesive forces (larger particles in Figure 8.2). The increase of the diameter of the rolling spherical particles is limited by the normal pressure applied by the opposed surfaces, so that the spherical particles will instead continue to grow by elongating into rolling cylinders. With the current loading conditions, the cylinders reach a maximum length of about 500 nm and a maximum diameter of 100 nm (see Figure 8.6b). When the cylinders become numerous and meet each other, they agglomerate into larger aggregates. The accumulation of aggregates takes the form of large flakes being left on the initially flat disc, creating a third-body or gouge layer and resulting in the macroscopic surface roughness. The flakes have an average width of 20 µm (see Figure 8.6c). The same mechanisms of wear formation continue to take place on top of the already formed third-body layer, as seen in Figures 8.6d and 8.6e, where cylinders are visible on top of the large aggregated flakes.

While the creation of wear particles and their accumulation into a third-body layer is commonly seen in engineering (Ajayi & Ludema 1990; Kato & Komai 2007; Kirk *et al.* 2019; Kirk *et al.* 2020) or at geological scales (Reches & Dewers 2005), the formation of rolling cylinders is interesting in itself and subject to recent discussions in literature. Rolling cylinders have been observed in lubricated (Varga *et al.* 2019) and unlubricated (Zanoria & Danyluk 1993; Zanoria *et al.* 1995) wear. In the latter case, the cylinders are believed to decrease the interfacial tangential stresses. Chen *et al.*

(2017) have conducted rock friction experiments and observed the formation of rolling cylinders along the sliding direction. They believe the occurrence of these worn cylindrical bodies is a mechanism that leads to slip weakening, with implications in earthquake physics.

8.2.3 *Roughness evolution*

Figure 8.7 shows topographic images of disc surfaces with different initial roughnesses (one in each category of Table 8.1) acquired using a *Sensofar S-Neox* confocal microscope, before and after an experiment with a sliding duration of 5 h. Initially, the roughened samples exhibit strong rough features, also revealing the direction of polishing. After the experiments, a wear track is left on each disc, which is visible in the topographic images as well as to the naked eye. When the disc is initially flat, the resulting wear track is comparatively rougher (Figure 8.7c). Conversely, when the disc is initially very rough, the roughness inside the wear track is decreased by the flattening of the high features (Figure 8.7e). In-between, when starting from relatively moderate surface roughness, the created wear track keeps the same roughness, resulting in a topographic image with uniform heights (Figure 8.7d).

This observed trend in the evolution of surface roughness can be complemented by more accurate topographic computations. Figure 8.8 shows measurements of friction coefficient and of the two-dimensional Sa roughness of the wear tracks left on the discs for all the tests listed in the Table 8.1.

The evolution of the friction coefficients indicates that an almost steady state is reached after a running-in period. The running-in period itself does not seem to last a constant time between the different tests. For example, the wear track on the disc can start to become visible to the naked eye on the initially flat discs after 30 seconds or only after 5 seconds of sliding for two repetitions of the same test. The running-in period may be very dependent on small non-controlled variations of the initial conditions (like dust, temperature, or hygrometry). The friction coefficient still increases slowly in the "steady" region, which is probably linked to the non-constant contact area between the worn ball and the disc, which increases as the ball wears out.

The dashed curves of the Figure 8.8a are fitted to all the evolution curves of a given category of initial surface roughness of the disc (corresponding to the three categories of the Table 8.1). Functions of the form $a+bx+ce^{dx}$ are empirically chosen, only for visual comparison purposes, as they can represent a steadily increasing regime with the $a+bx$ terms and an exponential convergence to this regime with the ce^{dx} term. The friction coefficient is on average higher when the initial surface roughness is higher. However, the fitted curves are within a standard deviation apart from each other, so this trend is not statistically significant.

In contrast, the evolution of the surface roughness of the discs over time has an interesting dependence on the initial disc roughness: when the initial roughness is in the explored range (from $Sa = 0.01\,\mu\text{m}$ to $Sa = 1.58\,\mu\text{m}$), the roughness evolves toward a common value of $Sa \approx 0.65\,\mu\text{m}$ (the black dashed line in Figure 8.8b) irrespective of the initial value.

Note that the average values of initial roughnesses of $Sa \approx 0.74\,\mu\text{m}$ and $Sa \approx 1.41\,\mu\text{m}$ were chosen after witnessing that initially almost flat discs evolved toward a roughness of $Sa \approx 0.65\,\mu\text{m}$. The grain sizes of the sandpapers used in the creation of the rough discs were selected to obtain a roughness being around 1 time and 2 times the value $Sa \approx 0.65\,\mu\text{m}$ after polishing.

While convenient at larger scales, one drawback of the Sa roughness measurement is its dependence on the scale of measurement for fractal surfaces. Typically, the measured Sa roughness

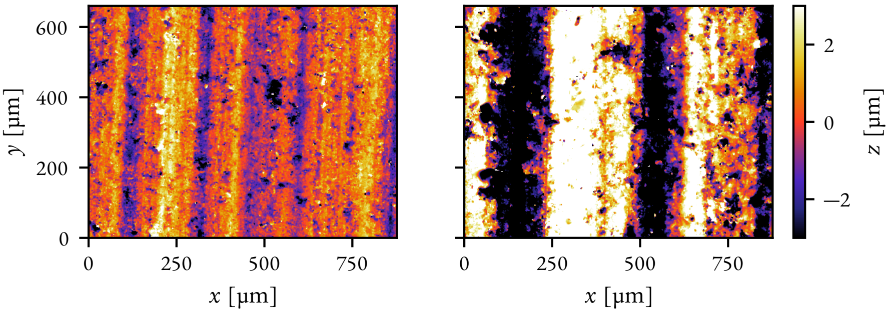

(a) Initial surface with $Sa = 0.63\,\mu\mathrm{m}$

(b) Initial surface with $Sa = 1.58\,\mu\mathrm{m}$

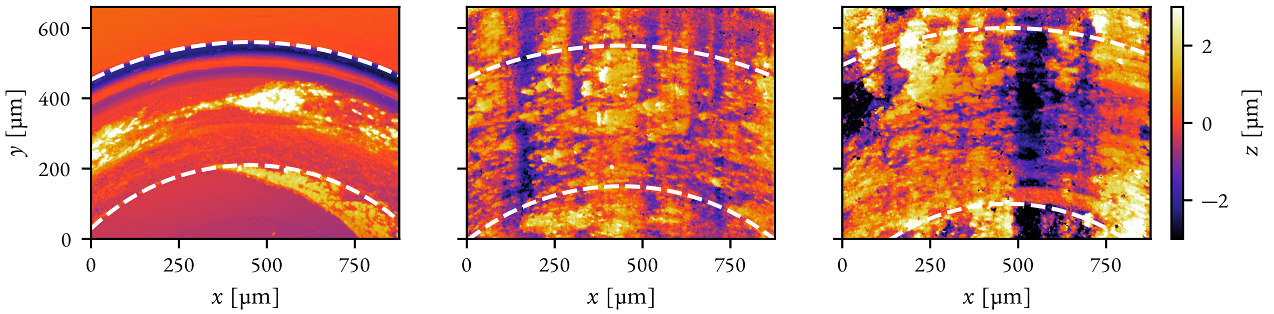

(c) Wear track from an initial surface with $Sa \approx 0.01\,\mu\mathrm{m}$ (not shown). $Sa = 0.23\,\mu\mathrm{m}$ inside the wear track.

(d) Wear track from an initial surface with $Sa = 0.63\,\mu\mathrm{m}$. $Sa = 0.61\,\mu\mathrm{m}$ inside the wear track.

(e) Wear track from an initial surface with $Sa = 1.58\,\mu\mathrm{m}$. $Sa = 0.64\,\mu\mathrm{m}$ inside the wear track.

Figure 8.7 – Topographic images of discs' initial surfaces and wear tracks after 5 h of sliding. In (a) and (b), the captions indicate the Sa roughnesses when measured on a window of size $117\,\mu\mathrm{m} \times 88\,\mu\mathrm{m}$ like in the rest of the text. The portions of circular wear tracks shown in (c), (d), and (e) have a radius of 1 mm. Note that the pairs of images (a)-(d) and (b)-(e) were taken on the same discs, before and after the experiment, but not at the exact same location. The wear track is clearly visible on (c) because it is rougher than the initial surface surrounding it (completely smooth at this scale). The situation is reversed in (e): the wear track exhibits less dramatic heights than the rougher initial surface. In (d), the surface roughnesses are similar and the wear track boundaries are harder to distinguish. Note that in (c), the value of Sa roughness may look smaller than expected. Actually, the roughness averaged over four locations on the wear track is $Sa = 0.77\,\mu\mathrm{m}$.

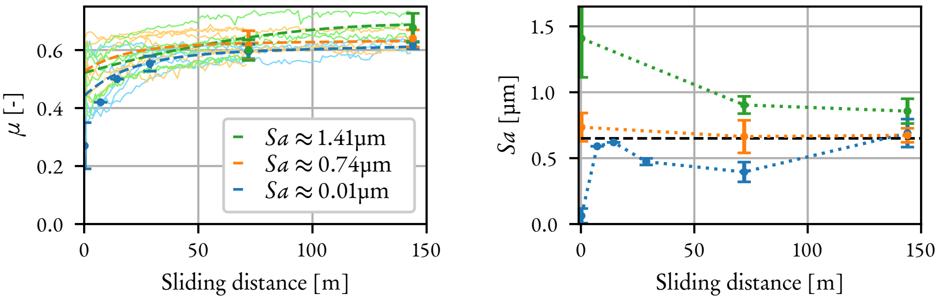

(a) Friction coefficient

(b) Roughness of the wear tracks on the discs

Figure 8.8 – Evolution of friction coefficient and surface roughness from initially smooth and rough SiO_2 surfaces. Errors bars show the standard deviation. (a) Empirical functions of the form $a + bx + ce^{dx}$ (thick dashed lines) are fitted to the measurements (all thiner curves) for visual comparison. (b) The roughnesses converge toward the black dashed line placed at $Sa = 0.65\,\mu\text{m}$. Dotted lines are added to guide the eye and are not representative of the actual evolution paths. The Sa roughnesses are computed from $117\,\mu\text{m} \times 88\,\mu\text{m}$ topographic images of $1360\,\text{px} \times 1024\,\text{px}$ (details in Section 8.1.1).

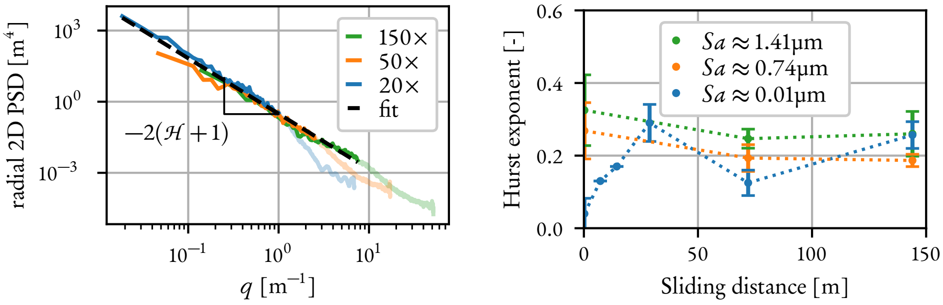

(a) Example of computation of Hurst exponent on a disc with an initial roughness of $Sa = 0.79\,\mu\text{m}$ after 5 h (144 m) of sliding

(b) Hurst exponent of the wear tracks on the discs

Figure 8.9 – Example of computation of the Hurst exponent and its evolution from initially smooth and rough SiO_2 surfaces. (a) Three radial PSDs are obtained using three different magnifications on a sample, centered on the same spot. The black dashed line is fitted to all the three curves, leading to the Hurst exponent $\mathcal{H} = 0.17$ in this case. The transparent parts of the curves are above the cutoff frequency and do not contribute to the fit. The PSD obtained from the lowest magnification (20×) gives low-frequency information while the one obtained from the highest (150×) provides high frequencies. Numerical data for the three PSD curves shown here and for other cases can be found in Supplementary material S1. (b) The Hurst exponents start scattered and evolve toward a similar value. Errors bars show the standard deviation. Dotted lines are added to guide the eye and are not representative of the actual evolution paths.

is lower at smaller scales. Instead, the computation of the PSD of the surface heights[3] (one example shown in Figure 8.9a) shows that all PSD curves follow a power-law over several orders of magnitude, which is typical of self-affine surfaces, meaning that all initial and worn surfaces in our experiments are remarkably self-affine. Our results reveal that the resulting surfaces are self-affine on over two orders of magnitude (Figure 8.9a). For such self-affine surfaces, another measure of roughness besides the Sa roughness is the Hurst exponent, which is independent of the measuring scale and is related to the slope of the PSD in a logarithmic plot (Jacobs *et al.* 2017). The PSD $C(q)$ of a self-affine surface takes the form

$$C(q) \propto q^{-2(\mathcal{H}+1)} \tag{8.4}$$

in a certain range, where q is the radial spatial frequency and $\mathcal{H}$ is the Hurst exponent. The Hurst exponent of a self-affine surface is related to its fractal dimension, and it describes how the roughness changes when viewing the surface from a larger or smaller perspective (Mandelbrot *et al.* 1984).

The Hurst exponent of the rough surfaces is computed from topographic measurements. Three measurement are made using the three magnifications $20\times$, $50\times$ and $150\times$, leading to images of $1360\,\mathrm{px} \times 1024\,\mathrm{px}$ on windows of size $877\,\mu\mathrm{m} \times 660\,\mu\mathrm{m}$, $351\,\mu\mathrm{m} \times 264\,\mu\mathrm{m}$ and $117\,\mu\mathrm{m} \times 88\,\mu\mathrm{m}$ respectively. Note that when performing a measurement for a wear track at the lowest magnification (the largest scale), the wear track does not fill the whole image (see Figure 8.7), so it has to be cropped.

For each topographic data $h(x,y)$, a radial Hann window is applied and the discrete Fourier transform $\hat{h}(q_x,q_y)$ of the windowed data is computed, as well as the PSD:

$$C(q_x,q_y) = \frac{L_x L_y}{n_x^2 n_y^2} |\hat{h}(q_x,q_y)|^2, \tag{8.5}$$

where q_x and q_y are the spatial frequencies, L_x and L_y are the window size and n_x and n_y are the window resolution. The radial PSD $C(q)$ with $q^2 = q_x^2 + q_y^2$ is computed form the cartesian PSD $C(q_x,q_y)$ by binning into 512 linearly spaced bins. Due to physical limitations in the measuring hardware, higher frequencies of the PSDs are not representative and have to be dropped. A cutoff of $0.05\,\mathrm{m}^{-1}$ times the magnification (20, 50 or 150) is applied to the radial PSDs. A line is fitted to the three PSDs in a log-log graph, ignoring the values after the cutoff frequencies. The slope of the line is $-2(\mathcal{H}+1)$, where $\mathcal{H}$ is the searched Hurst exponent. The Figure 8.9a shows an example of Hurst exponent computation from three radial PSDs obtained at the different magnifications.

Figure 8.9b shows measurements of the Hurst exponent of the wear tracks left on the discs for the tests listed in the Table 8.1. Remarkably, while the initial Hurst exponents differ depending on the initial roughness, all our measured Hurst exponents converge toward a common value of $\mathcal{H} \approx 0.25$.

The different behaviors of surface roughness evolution can be qualitatively explained with a simple physical intuition like shown in Figure 8.10. When the surface roughness is low, wear particles can be chipped away from the contacting surfaces thanks to adhesive forces, as described in Section 8.2.1. The cracks created by the detachment of particles contribute to increasing the surface roughness. Conversely, when the surface roughness is large, high peaks on the surfaces can meet and knock each other out, and created wear particles can fill up holes in the surfaces,

---

[3] It is defined as the squared norm of the two-dimensional Fourier transform of the surface heights. See Section 1.1.2 for details.

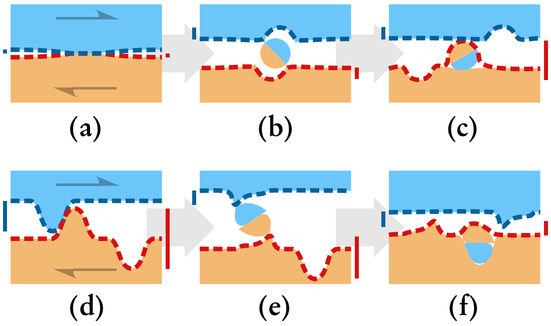

Figure 8.10 – Schematics of roughness evolution behaviors. The vertical bars on the sides of each panel represent the total height contributing to surface roughness. (a) Starting from low initial roughness. An adhesive junction forms between the two surfaces. (b) Formation of a wear particle. The roughness increases with the newly formed cracks. (c) The particle attaches itself to one surface, increasing again the roughness. (d) Starting from high initial roughness. (e) Formation of a wear particle from the colliding asperities. The roughness decreases with their destruction. (f) The particle falls into a hole, decreasing again the roughness.

reducing the surface roughness. The two mechanisms continuously happen simultaneously over the contacting surfaces, balancing each other. Thus, stable surface roughness can be reached after a running-in period. Nonetheless, this simple description does not explain the remarkable finding that the final roughness profile does not seem to retain any memory of the initial roughness.

Note that while the surface roughness of the worn parts obtained after a running-in period appears to be independent of their initial surface roughness, the final steady-state friction coefficient and surface roughness are likely dependent on the loading parameters (normal load, turning radius, and sliding velocity) and the material properties. Thus, the particular value of $Sa \approx 0.65\,\mu\text{m}$ is specific to the current set of parameters. A change in those parameters might change the target value of Sa, a behavior that has not been studied here.

All of our analyses on roughness evolution and formation were performed on the discs and not on the spherical pins. The loading conditions (*pin-on-disc*) imply that the pins are more locally solicited than the discs, resulting in an asymmetric evolution of the worn surfaces. Overall, the worn caps of the balls have a Sa surface roughness two orders of magnitude lower than their disc counterparts, so that the most interesting features created by wear could only be found on the discs. The third-body layer is indeed only deposited on the discs, creating the macroscopic roughness.

CONCLUDING REMARKS

We performed tribological experiments on amorphous SiO_2 samples of different surface roughnesses. We found that for the employed loading conditions (load, sliding velocity), a self-affine surface roughness emerges from initially comparatively flat surfaces via the following steps:

1. Formation of small spherical wear particles, whose minimum size is mainly dependent on the material properties. These initial wear particles are the fundamental bricks in the formation of the third-body layer;
2. The wear particles grow into rolling cylinders and larger aggregates;
3. The large aggregates take the form of flakes, creating a third-body layer and the macroscopic roughness.

Alternatively, when starting with an initially high surface roughness, the latter gets reduced by wear to a value similar to the one obtained from initially flat surfaces. The initial surface roughness does not influence the state (surface roughness) and behavior (friction coefficient) of the worn parts attained after a running-in period. Thus, a stable value for the coefficient of friction could be achieved by machining an initial surface roughness that matches the expected final roughness, which depends on the materials and loading conditions. Further studies can be considered to explore the effects of the loading conditions and material properties (and therefore the minimum wear particle size) on the steady-state values of surface roughness and friction coefficient, if such steady state can be reached, which could be conducted either experimentally or using computer simulations.

CHAPTER 9

ADDING AN OXIDE LAYER

THE previous experimental campaign involved samples made of bulk (or plain) SiO_2. The same experiments are run, but this time we are interested in how mechanical pieces made of Si behave in dynamical contact, and how the presence of an oxide layer can impact this behavior, depending on its thickness. In Sections 9.1 and 9.2, the experimental setup and results are presented and discussed. Then, in Section 9.3, numerical models are devised to physically support the experimental findings.

9.1 EXPERIMENTAL SETUP

For this second experimental campaign, the setup remains essentially the same. The SiO_2 discs are switched with monocrystalline Si discs treated to have an amorphous oxide layer of controlled thickness (up to 3 µm). Untreated discs also have a native oxide layer caused by a mere exposition to ambient air, measuring only a few nanometers. Plain SiO_2 balls are still used because of the difficulty to manufacture monocrystalline Si spheres. They can nonetheless be considered as objects coated with a very large thickness of SiO_2. The surface of the crystalline discs making contact with the spheres has the direction (100).

We keep a sliding velocity of 8 mm/s, a turning radius of 1 mm and a normal load of $F_\mathrm{N} = 1\,\mathrm{N}$. The durations of the tests and the thicknesses of the discs' oxide layers are given in Table 9.1. The initial roughness of all samples is left untreated and has been identified using AFM measurements to be less than $Sa = 20\,\mathrm{nm}$.

For each test, the vertical reaction force F_z and the lateral force F_x parallel to the direction of sliding are recorded, from which a dynamical friction coefficient $\mu = F_x/F_z$ is computed. The surface topography of the worn discs and pins is measured at the end of each experiment, from which we compute the Sa roughness and an estimation of the wear volume coming from each part. Finally, SEM images of the wear track are taken after sliding, viewed from the top and as a cross-section.

Table 9.1 – Duration and oxide layer thickness for experiments. Each test has a duration and a corresponding sliding distance, known from the fixed sliding velocity of 8 m/s.

Oxide	Duration	Distance	Repetitions
native	2h30	72 m	3
	5 h	144 m	3
0.5 µm	2h30	72 m	3
	5 h	144 m	3
1.0 µm	2h30	72 m	3
	5 h	144 m	3
2.0 µm	2h30	72 m	3
	5 h	144 m	3
3.0 µm	2h30	72 m	3
	5 h	144 m	3

9.2 RESULTS AND DISCUSSION

Figures 9.1 and 9.2 show the measurements of friction coefficient μ and final surface roughness Sa for each tested oxide thickness, as well as for tests performed on initially flat ($Sa \approx 10\,\text{nm}$) samples of bulk SiO_2 (taken from the previous experimental campaign). Figure 9.3 shows the same measurements regrouped in a single graph for comparison.

9.2.1 *Friction coefficient*

The friction coefficients (Figures 9.1 and 9.3a) evolve toward a steady state after a running-in period, whose duration is variable and very dependent on uncontrolled initial parameters. It is more interesting to look at the final values reached at the steady state. The averaged curves represent the mean behavior for each oxide thickness. They show the following trend: as the oxide layer's thickness increases, the coefficient of friction increases toward the value for bulk SiO_2, which is expected since the Si beneath a thick layer of oxide will not be felt at the surface, therefore acting like a plain SiO_2 surface. The friction coefficients obtained on samples with an oxide layer between $h_\text{layer} = 0\,\mu\text{m}$ (native) and 1.0 µm are all within a standard deviation from each other, so that it is not statistically possible to tell whether one specific oxide thickness leads to a minimal friction coefficient.

Figure 9.4 shows two empirical curves fitted to the friction coefficients measured at the end of each test (after 2h30 and 5 h). One fit is performed on the measurements from oxidized Si discs, while the other one also accounts for the tests performed on bulk SiO_2, for which an arbitrary value of $h_\text{layer} = 6\,\mu\text{m}$ is assigned to permit the fitting of a function. The empirical fits are

$$\mu \approx 0.337 + 0.070 h_\text{layer}\,, \tag{9.1}$$

$$\mu \approx 0.331 + 0.092 h_\text{layer} - 0.008 h_\text{layer}^2\,, \tag{9.2}$$

$$\tag{9.3}$$

with root-mean-square (RMS) errors of respectively 0.065 and 0.058. The models are equivalent in the region where the first one has been fitted. Overall, μ is increasing monotonically with

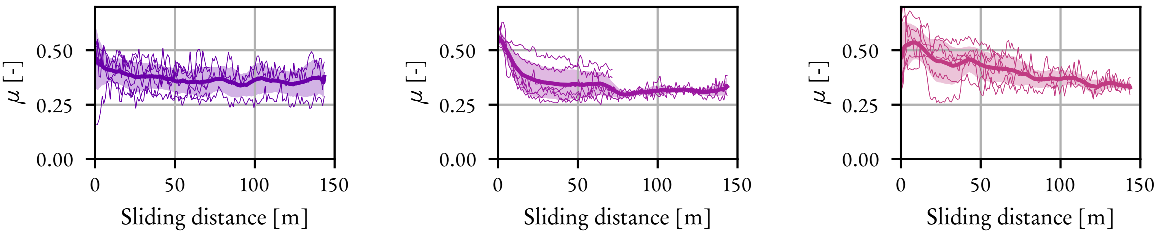

(a) Native (b) 0.5 µm (c) 1.0 µm

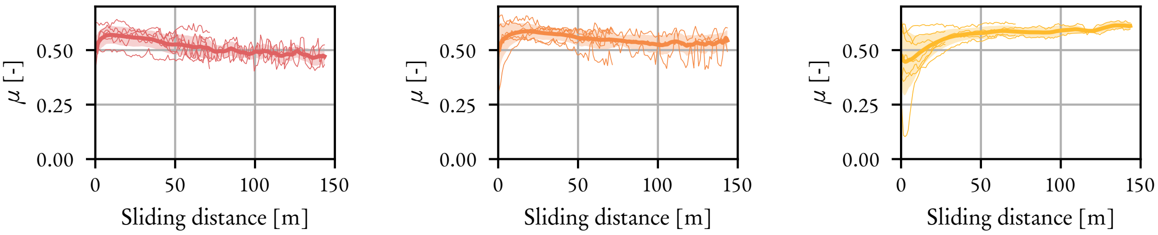

(d) 2.0 µm (e) 3.0 µm (f) Bulk

Figure 9.1 – Evolution of friction coefficient for each oxide thickness and averaged curves. The thinnest curves are the experimental measurements, and the thick curves are averages, obtained by taking the mean of all available measurements at every sliding distance, and applying a moving average filter on the resulting curves to smoothen the oscillations. The shaded area around the averaged curves represents one standard deviation.

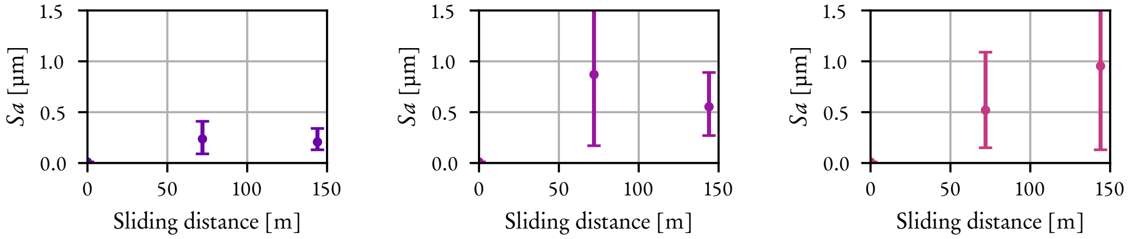

(a) Native (b) 0.5 µm (c) 1.0 µm

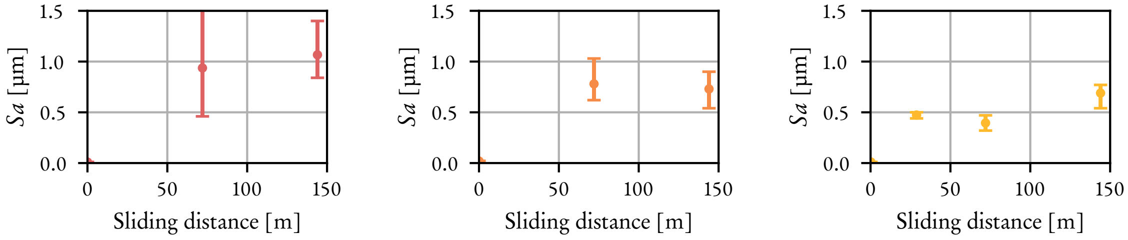

(d) 2.0 µm (e) 3.0 µm (f) Bulk

Figure 9.2 – Evolution of surface roughness for each oxide thickness. The points are averages and the error bars are ranges from minimum to maximum value. The measurements are only taken at the end of each test, after a sliding distance of 72 m or 144 m, since real-time *in-situ* measurements were not possible with our equipment. Samples with an oxide layer have the largest deviations.

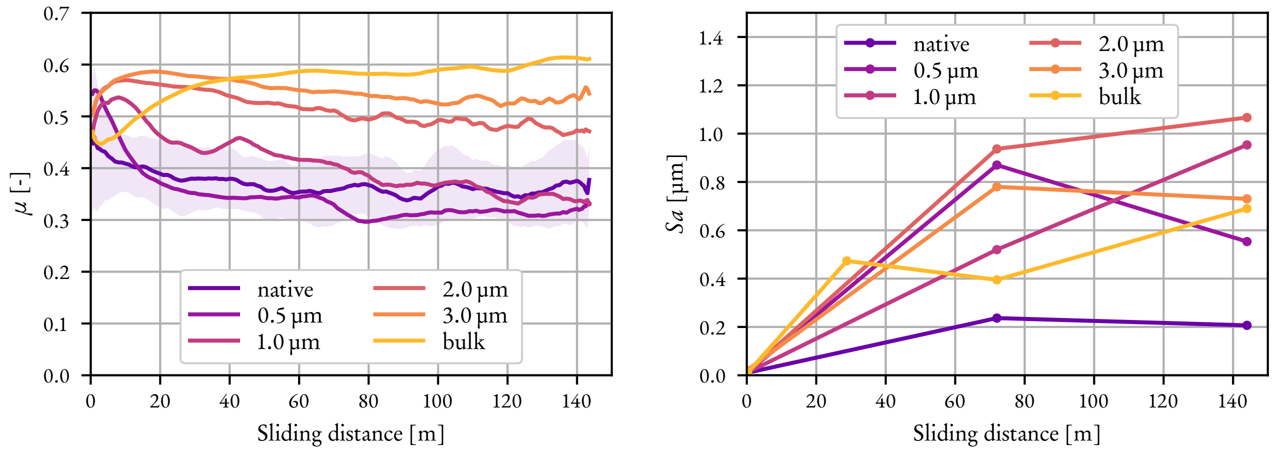

(a) Friction coefficient

(b) Roughness of the disc

Figure 9.3 – Evolution of friction coefficient and surface roughness from initially flat oxidized Si samples. (a) The curves are averages from measurements, and the shaded area represents one standard deviation for the "native" curve, which has larger deviations compared to the other (see Figure 9.1). Overall, the friction coefficient increases with the thickness of the oxide layer, toward the value obtained with plain SiO_2 discs. (b) The points are average measurements, and lines are drawn to guide the eye. All final roughnesses are similar, except for the non-oxidized samples which evolve toward a lower one.

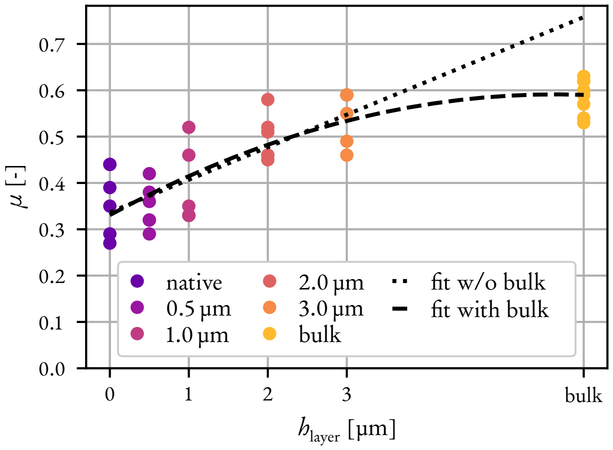

Figure 9.4 – Friction coefficient as a function of oxide layer thickness and empirical fits. The bulk measurements are arbitrarily set to $h_{\text{layer}} = 6\,\mu\text{m}$. One curve is linear and the other is quadratic. They indicate a monotonous increase of μ with h_{layer} and a saturation for large layer thicknesses.

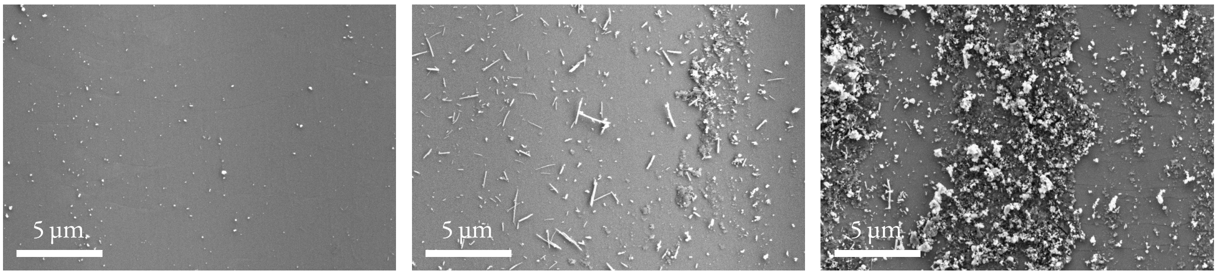

(a) Particles

(b) Cylinders

(c) Aggregates

Figure 9.5 – Wear track on an Si disc after 5 hours.

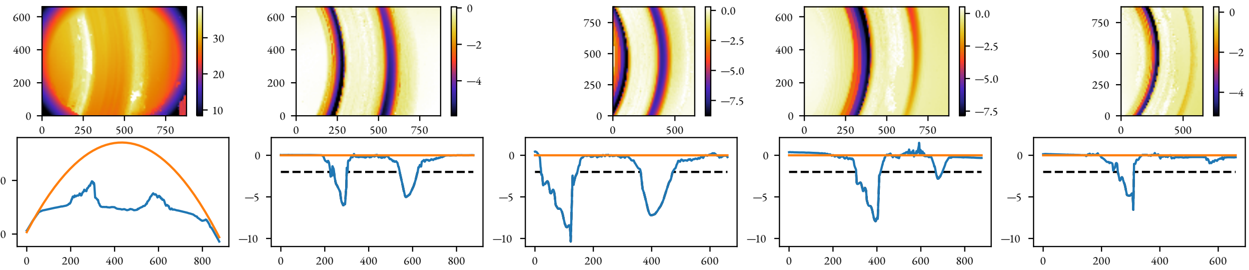

Figure 9.6 – Topographies (top) and cross-sections (bottom) of a worn pin and an oxidized disc at multiple locations after the experiment. All the dimensions are in µm. The shape of the worn region of the pin (leftmost) conforms to the wear track on the disc. The red lines are estimated initial surfaces and the black dashed lines show the thickness of the oxide layer.

h_{layer}. Even when including higher-order terms, no model having a significant[1] local minimum has been found. Moreover, μ has no significant influence on sliding duration, which is an indication of reached steady states. We will show later that the friction coefficient is correlated with other measurable quantities.

9.2.2 *Surface roughness*

The measurements show that all samples evolve from having a relatively flat surface to being rough. The discs made of only one material (Si with negligible native oxide layer, and bulk SiO_2) are those with the smallest amount of variation in the roughness measurement (we can also include the samples with the thickest 3.0 µm oxide layer). The non-oxidized samples exhibit the lowest surface roughness with statistical significance. The large variance observed for the oxidized samples can be explained by the diverse topography of the wear tracks on which the roughness measurements are performed. Indeed, the wear tracks on the non-oxidized Si discs are smooth, as shown in Figure 9.5, and the wear tracks on the bulk SiO_2 discs are rough (see Figure 8.6c). The wear tracks left on the oxidized discs have both smooth and rough regions. The topographic measurements in Figure 9.6 are an example of wear track created on an oxidized disc, and Figure 9.7 shows schematic cross-sections of typical wear tracks in all cases. The wear tracks on the oxidized discs are similar to those on the SiO_2 discs but with multiple grooves (up to three) reaching the Si underneath the oxide layer. The grooves have the same appearance as the wear tracks on non-oxidized Si discs. The physical explanation for the formation of grooves, which only happens with discs made of layered materials, is not trivial. It could be caused by irregularities initially present on the surfaces of the samples, but the reason we found (revealed in the numerical simulations section) is more unexpected, and we challenge the reader to find it prior to reading.

The presence of a third body layer (TBL) of worn SiO_2 is verified using SEM. The observation of a cross-section of the TBL can be carried out using an SEM equipped with EDX. Thanks to the latter, the chemical contrast between Si and SiO_2 can be associated with a color (brightness) contrast in the images obtained using back-scattered electrons. Figures 9.8 and 9.9 show such images, with different colors given to parts made of Si and those made of SiO_2. Figure 9.8 shows a TBL formed in the oxide layer of a disc, having not yet reached the Si beneath. The roughness created by the accumulation of debris in the TBL is clearly apparent. Figure 9.9 shows a groove, where the underlying Si has been worn out. The surface finish inside the groove is much smoother.

---

[1] For the fitting of empirical models, terms are added until the improvement of the RMS error drops under 5%. Further terms are labeled as *statistically non-significant*.

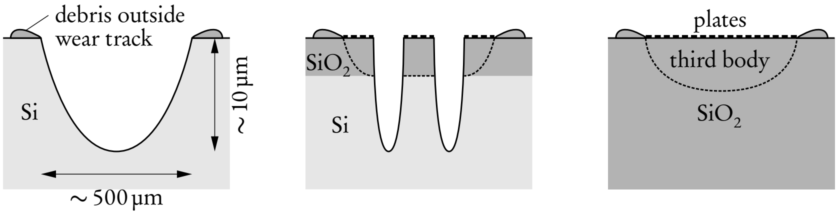

(a) Non-oxydized Si (b) Oxydized Si (c) SiO_2

Figure 9.7 – Schematic cross-sections of the wear tracks on the different discs. The vertical scale is largely exaggerated for visualization. The wear tracks in Si are smooth compared to those in SiO_2, where the visible roughness is inherent to the formed plates represented in thick dashed lines. The regions marked with "third body" are where third body layers (TBL) can form under local contact spots.

Note the presence of a thin layer of SiO_2 on top of the Si inside the groove.

9.2.3 *Wear*

The evolution of the wear volume on the discs and on the pins is shown in Figure 9.10. It is estimated by comparing the final surface topography to an idealized initial surface (a sphere for the pins and a plane for the discs). The total wear volume seems to evolve linearly with the sliding distance, which is in accordance with Archard's wear model. The nature (oxidation) of the disc's surface does not significantly affect the evolution of the total wear volume. However, the comparison of the wear volumes on the pins and on the discs indicates that the discs with a thicker layer of SiO_2 wear more slowly, which is compensated by having the pins wearing more against those surfaces. The bulk SiO_2 discs look like they were almost not worn out, which is not the case considering the surface roughness created on them (see Figure 9.2f). Actually, the wear and the reattachment of matter are such that not much material is carried outside of the wear track.

The data shows that the presence of an oxide layer on the discs lowers the volume of wear debris they emit.

A simple empirical model for the friction coefficient can be fitted to the measurements to establish its link with the contact areas between the worn pins and the discs. By looking at the topographic images of the worn part of a pin (see Figure 9.6, leftmost), we can extract the projected contact area A_{Si} between the pin and the Si parts of the wear track, and the projected contact area $A_{\mathrm{SiO_2}}$ between the pin and the SiO_2 parts of the wear track, using the knowledge that the salient rails on the pin are in contact with the Si grooves in the disc. The total contact area is $A_{\mathrm{tot}} = A_{\mathrm{Si}} + A_{\mathrm{SiO_2}}$. We can assume that there is one (dynamical) friction coefficient for each of two kinds of interface:

- μ_{Si} at the interface between the SiO_2 pin and the Si part of the disc's wear track;
- and $\mu_{\mathrm{SiO_2}}$ at the interface between the SiO_2 pin and the SiO_2 part of the disc's wear track.

With these friction coefficients, the tangential resistance to sliding under a supposedly uniformly distributed normal load F_{N} is

$$F_{\mathrm{T}} = A_{\mathrm{Si}}\mu_{\mathrm{Si}}\frac{F_{\mathrm{N}}}{A_{\mathrm{tot}}} + A_{\mathrm{SiO_2}}\mu_{\mathrm{SiO_2}}\frac{F_{\mathrm{N}}}{A_{\mathrm{tot}}}, \tag{9.4}$$

so that the resulting homogenized friction coefficient is

$$\mu = \frac{A_{\mathrm{Si}}}{A_{\mathrm{tot}}}\mu_{\mathrm{Si}} + \frac{A_{\mathrm{SiO_2}}}{A_{\mathrm{tot}}}\mu_{\mathrm{SiO_2}}. \tag{9.5}$$

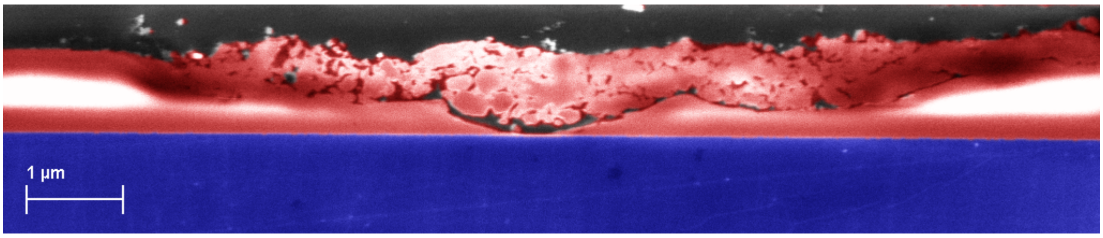

Figure 9.8 – Colored SEM image of a TBL in a portion of the wear track of a worn oxidized Si disc. Si is in blue and SiO_2 in red. The full wear track (about 500 µm long) contains multiple occurrences of TBL zones. The colors are obtained by superimposing images obtained using back-scattered electrons. The initial oxide thickness is 1.0 µm.

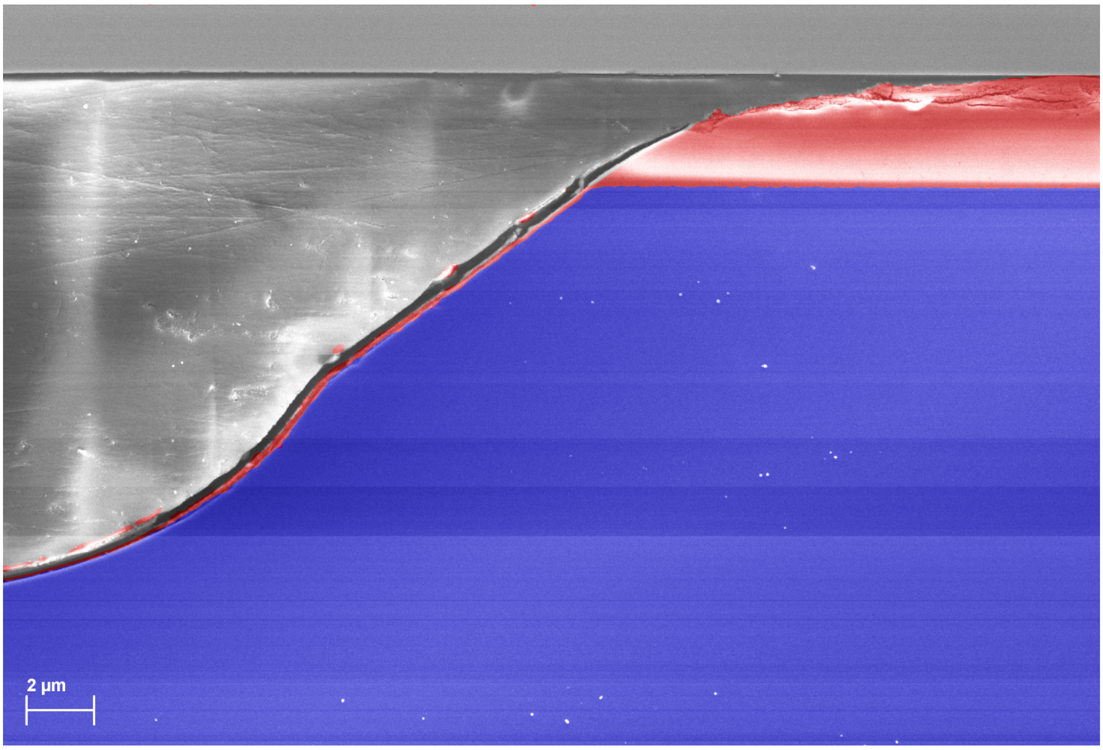

Figure 9.9 – SEM image of the cross-section of a groove in the wear track on an oxidized disc. Si is in blue and SiO_2 in red. The initial oxide thickness is 3.0 µm. A TBL of approximately 1 µm is visible on top of it.

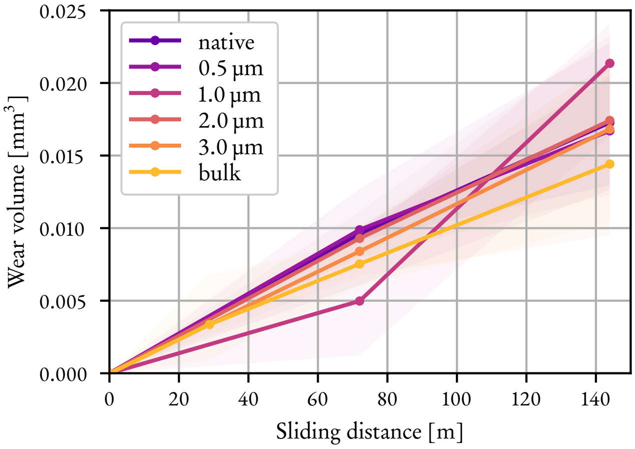

(a) Total

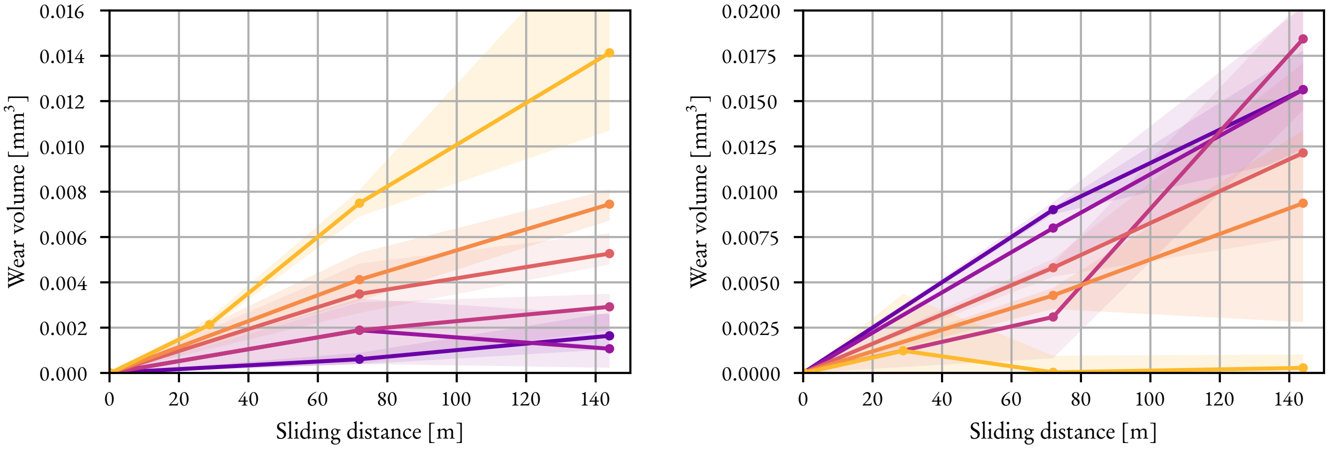

(b) Pin (c) Disc

Figure 9.10 – Evolution of wear volume from initially flat oxidized Si samples. The points are average measurements and the shaded areas are ranges from minimum to maximum measured values. (a) All curves statistically evolve the same way. (b) The pins wear more on discs with a thicker oxide layer. (c) Conversely, the discs with an oxide layer wear less. The pure SiO_2 discs seem to not wear away, which is due to the worn material remaining attached inside the wear tracks.

Using least-squares regression on the friction coefficient and contact areas measurements, the following estimate is obtained:

$$\mu \approx \frac{A_{\mathrm{Si}}}{A_{\mathrm{tot}}}\mu_{\mathrm{Si}} + \frac{A_{\mathrm{SiO_2}}}{A_{\mathrm{tot}}}\mu_{\mathrm{SiO_2}}\,, \tag{9.6}$$

$$\mu_{\mathrm{Si}} = 0.326\,, \tag{9.7}$$

$$\mu_{\mathrm{SiO_2}} = 0.548\,, \tag{9.8}$$

with a RMS error of 0.077. The fitted model and the measured friction coefficients are represented in Figure 9.11. As we could expect from the observed relation between oxide thickness and evolution of friction coefficient, the coefficient for the SiO_2–Si interface is lower that the one for the SiO_2–SiO_2 interface.

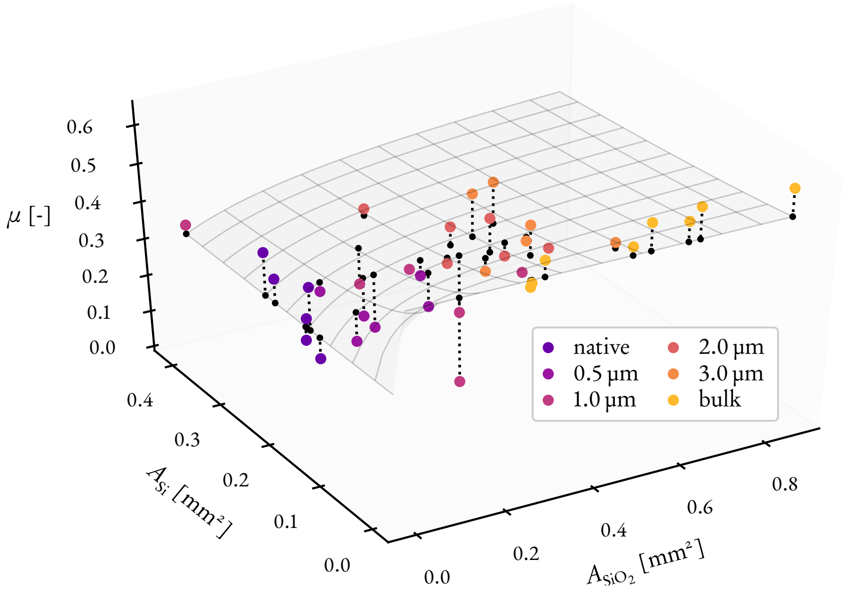

Figure 9.11 – Measured friction coefficients as function of contact areas and fitted model. The dotted lines represent the distance between the measurements (colored dots) and the empirical model (grey surface). The RMS error is 0.077. The contact between SiO_2 and Si (obtained from mostly blue points) has a fitted friction coefficient of $\mu_{Si} = 0.326$, whereas the contact between SiO_2 and SiO_2 (mostly from yellow points) has a $\mu_{SiO_2} = 0.548$.

9.3 NUMERICAL SIMULATIONS

With the experiments, we captured the effect of the oxide layer on the friction coefficient and the wear volumes. In essence, adding a SiO_2 layer on a Si sample increases its resistance to wear, but as a trade-off, also increases friction. We were able to establish a simple empirical model for the friction coefficient, depending solely on the contact area between the pin and the disc, taking into account the types of material in contact. However, the contact zone evolves toward a singular shape (with grooves) on samples possessing an oxide layer, which could not be explained from our observations. This shape is influencing directly the frictional and wear properties. Using numerical simulations, we attempt to uncover the processes leading to the formation of this kind of contact zone.

As a first step, we use MD simulations to find the shear strength properties of Si and SiO_2 at the atomic scale. Then, using the simple model established in Section 7.1, we project the small scale strengths into a BEM model at the experimental scale to simulate the wear process.

9.3.1 *MD: tangential strength at the atomic scale*

From the experimental measurements, we found that the SiO_2–SiO_2 interface is stronger (delivers more tangential resistance) than an interface involving Si. This fact can intuitively be attributed to a discrepancy in the shear strengths of the two materials.

The ideal strengths[2] of Si and SiO_2 can be found in the literature, obtained either with experiments, theoretical calculations, or numerical simulations. In its crystalline state, Si does not have the same properties in all directions. The smallest shear strength has a value of 11 GPa, in the {111} direction (Dubois *et al.* 2006). For SiO_2, the ideal shear strength is not easily found, but the ideal tensile strength is reported at about 16 GPa (Luo *et al.* 2016), and the shear strength can be estimated from the tensile one using the von Mises yield theory (assuming SiO_2 is ductile at small scale, where the ideal strength is measured) to be smaller by a ratio of $1/\sqrt{3} \approx 0.577$. We find a shear strength of 7 GPa for SiO_2.

---

[2] As a reminder: the ideal strengths are the ones measured when no defects are present in the material, typically at a small scale.

The found shear strengths seem to contradict our initial findings, since the shear strength of Si is larger. But those strengths are *static* strengths, measured or computed from unperturbed samples, where a *dynamical* strength would be more at stake in a tribological interface. Another factor not taken into account in these estimates is the confinement pressure, which can reach several GPa in our experiments[3] We found no studies linking directly pressure and strength for Si and SiO_2. But in more general terms, the strength of materials was shown to be meaningfully dependent on pressure and temperature (Towle 1967), following the empirical estimate

$$\sigma_{\mathrm{m}} = \sigma_{\mathrm{m,0}} \exp\left(-a \frac{T}{T_{\mathrm{m}}(p)}\right), \tag{9.9}$$

where $\sigma_{\mathrm{m,0}}$ is the unconfined strength, p is the pressure, T is the temperature, T_{m} is the melting temperature (dependent on pressure), and a is an empirical parameter. From this equation, we deduce that an increase in the melting temperature leads to an increase in the strength. For SiO2, we find that increasing the pressure also increases the melting temperature (González-Cataldo *et al.* 2016), which by inference also increases the strength. This is a typical behavior. For Si, increasing the pressure has the opposite effect of decreasing the melting temperature (Yang *et al.* 2003), consequently decreasing the strength.

In summary, our current knowledge on the shear strength properties of our materials is the following:

Si: shear strength $\sigma_{\mathrm{m,T}} = 11\,\mathrm{GPa}$, decreases under pressure;
SiO_2: shear strength $\sigma_{\mathrm{m,T}} = 7\,\mathrm{GPa}$, increases under pressure.

The dynamical and pressure effects are more likely to have a noticeable effect on Si, whose crystalline structure might be disturbed. To gather more quantitative information on the shear strengths, we resort to MD simulations.

Setup

We simulate systems of $10 \times 10 \times 10\,\mathrm{nm}^3$. At the top and bottom, 0.4 nm rigid walls are used to impose loads and displacements on the system, and Langevin thermostats are put on adjacent layers of 0.4 nm to keep the temperature of the systems at 300 K, using a damping factor of 0.01. The bottom rigid wall is fixed. A normal pressure p_{N} between 0 and 50 GPa and a shear motion are imposed on the top wall, with a shear rate of 10 m/s, and up to a shear deformation of 0.5. The lateral boundaries are periodic. A time step of 1 fs (10^{-15} s) is used. During the simulation, the tangential resistance is measured on the top wall, from which a tangential stress p_{T} is computed. The evolution of p_{T} over time gives us the maximum (static) shear stress $\sigma_{\mathrm{m,T}}^{\mathrm{max}}$ and the dynamical shear strength $\sigma_{\mathrm{m,T}}^{\mathrm{dyn}}$ after failure.

Si potential

To model Si in MD, we use the Stillinger-Weber potential (Stillinger & Weber 1985; Stillinger & Weber 1986), which takes into account three-body interactions to correctly model the crystalline

---

[3] The initial pressure is around 400 MPa, but the real contact area between the roughened surfaces is a few percent of the total apparent area, cranking up the local pressure acting on asperities.

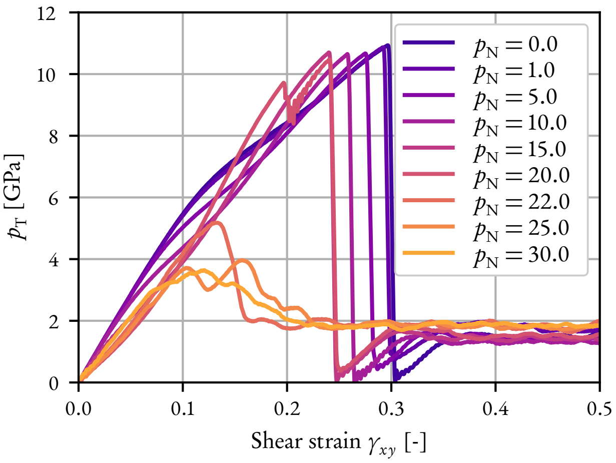

Figure 9.12 – MD measurements of the shear strength of Si under pressure. All systems reach a maximum shear stress, then drop to a dynamical regime with a lower resistance. The static strength drops for compressions higher than $p_N = 20\,\text{GPa}$.

phase of Si, having a diamond structure, where each atom has four neighbors arranged at the corners of a tetrahedron. We use the potential parameters given in the original paper, which are shown to give quantitatively acceptable properties for both the diamond-structure crystalline phase and the liquid amorphous phase.

Si results

The shear strength of Si is tested for compressions ranging from 0 to 30 GPa. The resulting evolutions of tangential stress are shown in Figure 9.12. At low compression (up to 20 GPa), the tangential stress increases up to shear strength of $\sigma_{\text{m,T}}^{\text{max}} \approx 11\,\text{GPa}$ independent on compression, and then suddenly drops to a much lower value of dynamical shear strength $\sigma_{\text{m,T}}^{\text{dyn}} \approx 1.5\,\text{GPa}$. Looking at the arrangements of atoms during sliding (Figure 9.13), we see that it transitions from a fully crystalline structure to becoming amorphous in a shear band. The lowered tangential resistance can be attributed to the transition from crystalline to amorphous state. For larger compression (from 22 GPa and above), the maximum strength $\sigma_{\text{m,T}}^{\text{max}}$ gets lower, dropping to around 4 GPa, and the same transition to a dynamical shear strength of $\sigma_{\text{m,T}}^{\text{dyn}} \approx 2\,\text{GPa}$ follows. The lower strength seems caused by the atomic structure becoming amorphous under the compression alone, as shown in Figure 9.14.

SiO_2 potential

The MD modeling of SiO_2 is performed using the potential by Vashishta *et al.* (1990), using a cutoff parameter of $r_c = 8\,\text{Å}$ (Luo *et al.* 2016). The amorphous system is prepared following the same procedure as Luo *et al.*, by heating and progressively cooling an initial crystalline sample (see Section 2.1.3 for more details).

SiO_2 results

The shear strength of SiO_2 is tested for compressions ranging from 0 to 50 GPa. The results are shown in Figure 9.15. In all compression cases, the system transitions from an elastic loading to a dynamical regime, with a change in the measured tangential resistance. Overall, a higher compression force leads to a larger strength (both the maximal strength $\sigma_{\text{m,T}}^{\text{max}}$ and the dynamical one $\sigma_{\text{m,T}}^{\text{dyn}}$). During the elastic phase, the strain is homogeneously distributed in the system (Figure 9.16a),

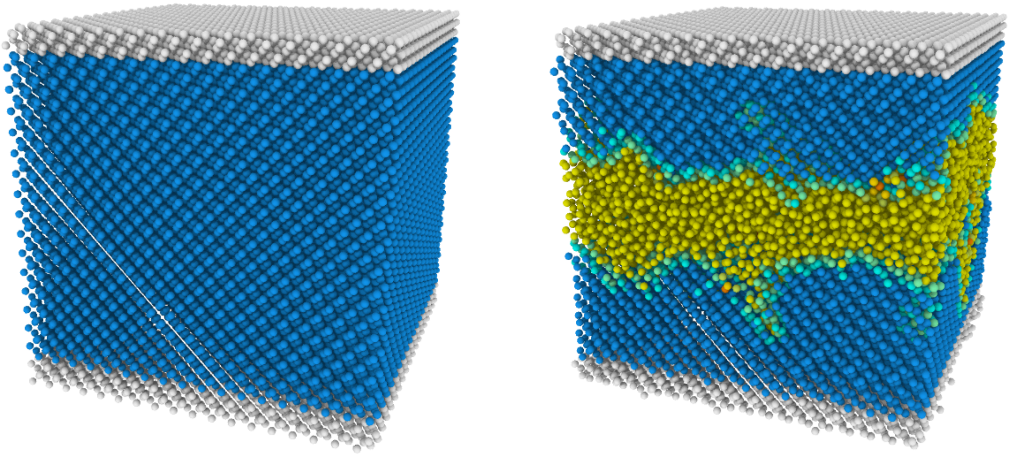

(a) Initial configuration

(b) After shearing

Figure 9.13 – Atomic structure of a sheared Si system without external pressure. Blue atoms are in a diamond-like structure (4 neighbors arranged tetrahedrally) and yellow atoms are unstructured (amorphous). The sheared system forms an amorphous shear band, responsible for the lower strength measured in the dynamical regime.

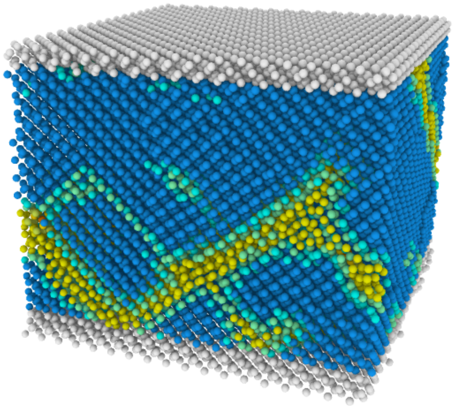

Figure 9.14 – Atomic structure of an Si system under a pressure of 25 GPa. The normal pressure forces the system into an amorphous structure, reducing the strength to a value similar to the dynamical shear strength.

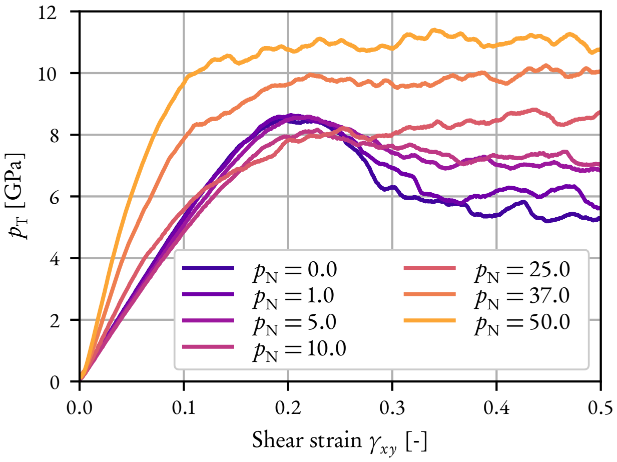

Figure 9.15 – MD measurements of the shear strength of SiO_2 under pressure. All systems reach a maximum shear stress, then transition into a dynamical regime. The strength increases under compression.

whereas in the dynamical phase, the strain is localized inside a shear band (Figure 9.16b). The non-equilibrium state of the atoms inside the shear band, being attached to less than their ideal number of neighbors, is responsible for the decrease of strength when transitioning to the dynamical regime. For high compression forces, the system is already disturbed during the static phase, reducing the difference with the dynamical phase.

Tangential strengths

The maximum and dynamical tangential strengths and their dependence on the compression stress can be extracted from the plots of tangential resistance evolving with shear (Figures 9.12 and 9.15), resulting in the summarizing curves in Figure 9.17. The empirical tendencies we established prior to the MD simulations are verified, and we have obtained numerical estimates for the strengths.

9.3.2 *BEM: modeling experiments*

The BEM can be employed to model the contact between the pin and the disc used in the experiments, providing the distribution of local pressures between the two objects and their deformation. In this section, we explain in detail how the tangential resistance is computed from the BEM outputs and how the contacting surfaces are evolved by simulating the wear process.

Pressure distribution

The pin and the disc are represented respectively as a portion of a sphere $h_{\mathrm{pin}}(x,y)$ of radius $R = 3\,\mathrm{mm}$ and a plane $h_{\mathrm{disc}}(x,y)$. The two surfaces have a size of $L \times L$, and are discretized into $n \times n$ cells. Each cell has an area of $A_0 = (L/n)^2$. Since layered systems cannot be currently modeled in our BEM software Tamaas, both surfaces are given the properties of SiO_2 for solving contact. The BEM outputs the normal pressure $p_{\mathrm{N}}(x,y)$ applied on each discretized cell.

Tangential resistance

Thanks to MD, we have obtained quantitative tangential strength measurements for Si and SiO_2 at the atomic scale. Using the model established in Section 7.1.2, we can link the newly found small scale properties to macroscale strengths, for them to be used in a model of wear at the experimental scale.

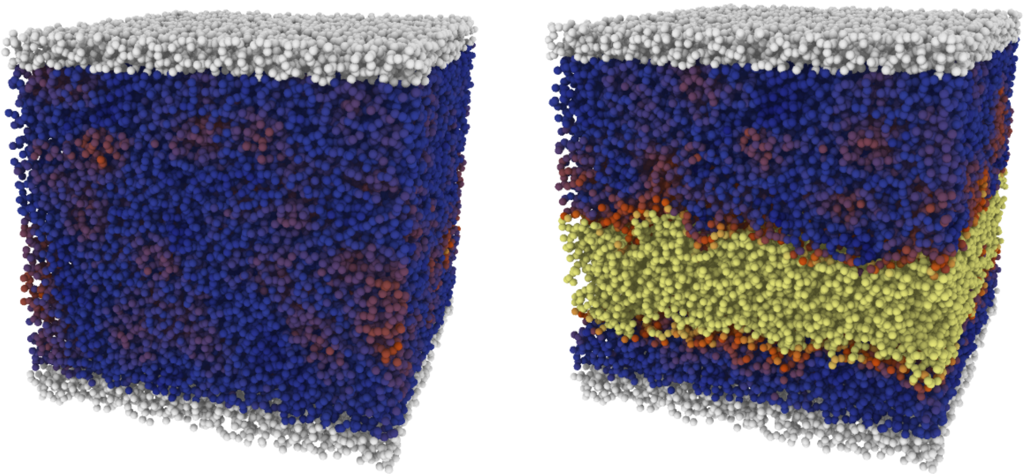

(a) Elastic loading

(b) After shearing

Figure 9.16 – Atomic stain in sheared SiO_2 system without external pressure. The stain is uniform during elastic loading and localises into a shear band in the dynamical regime. The same behavior is observed for SiO_2 systems under pressure.

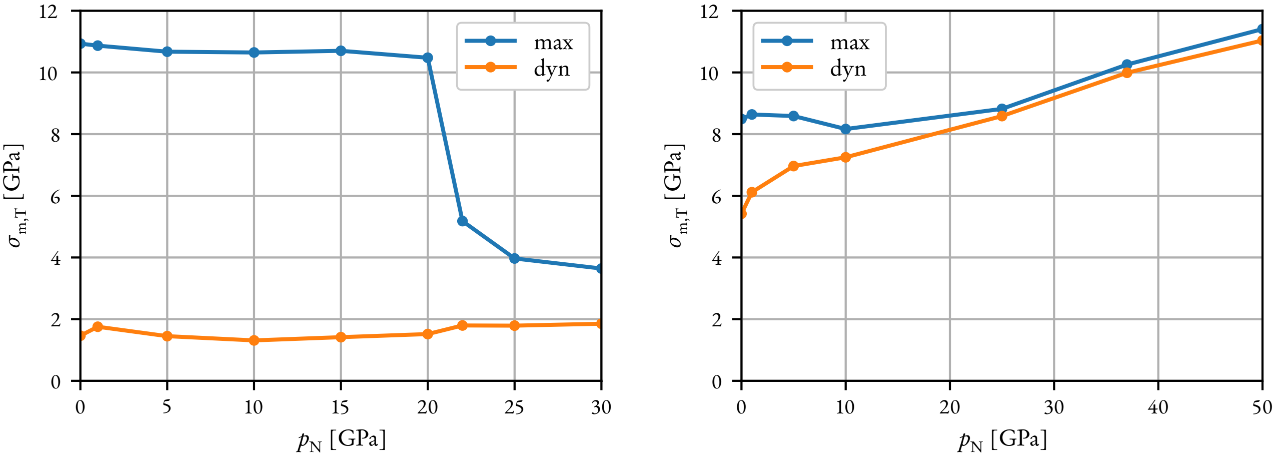

(a) Si

(b) SiO_2

Figure 9.17 – MD measurements of maximum and dynamical shear strength for Si and SiO_2 under pressure. (a) Si has a large drop of strength when entering the dynamical regime. Pressure decreases the shear strength. (b) The maximum and dynamical strength are close to each other. Pressure increases the strength.

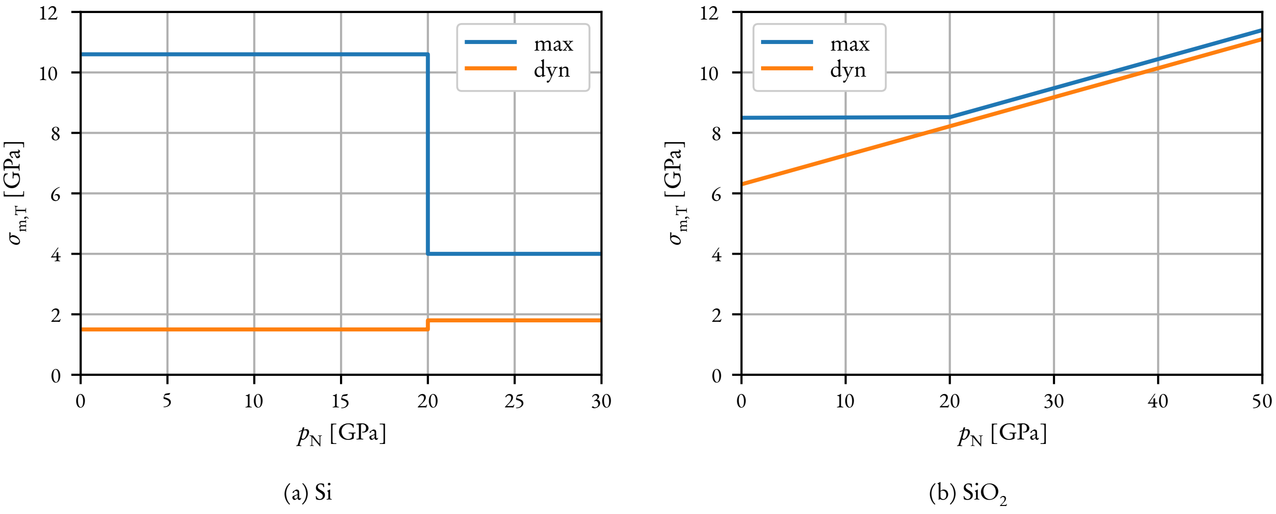

(a) Si

(b) SiO_2

Figure 9.18 – Simplified models of maximum and dynamical shear strength for Si and SiO_2 under pressure. (a) The maximum strength goes from 10.6 GPa to 4 GPa and the dynamical strength from 1.5 GPa to 1.8 GPa, with a transition at $p_{\mathrm{N}} = 20\,\mathrm{GPa}$. (b) The maximum strength begins at 8.5 GPa and starts increasing from $p_{\mathrm{N}} = 20\,\mathrm{GPa}$ with a slope of 0.096. The dynamical strength starts at 6.3 GPa and increases with the same slope.

We start by introducing simplified governing laws for the strengths and their dependence on compression, shown in Figure 9.18, based on the MD results, but which can be more easily implemented in a macroscopic model.

Since the compressive strength $\sigma_{\mathrm{m,c}}$ of the materials was not assessed, it can be reasonably approximated by the maximum shear strength of each respective material:

$$\sigma_{\mathrm{m,c}}(p_{\mathrm{N}}^{\mathrm{loc}}) = \sigma_{\mathrm{m,T}}^{\mathrm{max}}(p_{\mathrm{N}}^{\mathrm{loc}}), \tag{9.10}$$

plotted in blue in Figure 9.18, where $p_{\mathrm{N}}^{\mathrm{loc}}$ is the pressure measured at the asperity level. We input the compressive strengths in (7.5) to obtain the critical pressures, which are $p_{\mathrm{N}}^{\mathrm{crit}} = 10.6\,\mathrm{GPa}$ for Si and $p_{\mathrm{N}}^{\mathrm{crit}} = 8.5\,\mathrm{GPa}$ for SiO_2. These are the maximum pressure an asperity can withstand before collapsing, therefore increasing its contact size.

To use the scale-linking model, the ratio between real contact area A and apparent contact area A_0 in each discretized BEM cell must be identified. In a physical tribological system, this ratio A/A_0 is constantly changing with the wear of the contacting asperities. When wear particles are detached, holes are left in the surfaces, increasing the surface roughness and decreasing the contact ratio A/A_0. Conversely, when A/A_0 is small, the asperities collapse to reach the critical pressure, increasing A/A_0. We saw experimentally that the evolution of the surface roughness (and therefore of A/A_0) eventually reaches a steady state, where the two mechanisms of increase and decrease are at an equilibrium. The minimum value of the contact ratio (which satisfies that the local pressures do not exceed the critical $p_{\mathrm{N}}^{\mathrm{crit}}$) is given by (7.6) and depends on a macroscopic normal pressure:

$$\frac{A_{\mathrm{min}}}{A_0} = \frac{p_{\mathrm{N}}}{p_{\mathrm{N}}^{\mathrm{crit}}}. \tag{9.11}$$

Since we cannot reasonably model the micromechanics of asperity wear in a macroscopic model, we make the broad assumption that the contact area ratio remains at a steady-state value, chosen as (9.11), while keeping in mind that the steady-state ratio in a real system could be larger. With this contact ratio, the resulting tangential resistance is given by (7.10), using the dynamical shear strength:

$$p_{\mathrm{T}} = \frac{p_{\mathrm{N}}}{p_{\mathrm{N}}^{\mathrm{crit}}} \sigma_{\mathrm{m,T}}^{\mathrm{dyn}}(p_{\mathrm{N}}^{\mathrm{crit}}), \tag{9.12}$$

and a steady-state friction coefficient is deduced:

$$\mu_0 = \frac{p_{\mathrm{T}}}{p_{\mathrm{N}}} = \frac{\sigma_{\mathrm{m,T}}^{\mathrm{dyn}}(p_{\mathrm{N}}^{\mathrm{crit}})}{p_{\mathrm{N}}^{\mathrm{crit}}}. \tag{9.13}$$

This friction coefficient is independent on the loading conditions and geometrical configuration (bearing in mind our assumptions) and can be read directly from the shear strain curves (plotted in orange in Figure 9.18), giving

$$\mu_{\mathrm{Si}} = 0.14, \tag{9.14}$$

$$\mu_{\mathrm{SiO_2}} = 0.84. \tag{9.15}$$

The coefficient μ_{Si} is calculated for an Si–Si interface, but we can expect the same resistance from an $\mathrm{SiO_2}$–Si interface, since the more fragile Si underneath the interface is the first that will give up under a tangential stress.

The friction coefficient estimates we just obtained deviate from the experimental computations (9.7) and (9.8), which is not surprising considering the very simplified nature of our model. Still, the higher friction coefficient obtained in $\mathrm{SiO_2}$–$\mathrm{SiO_2}$ interfaces is qualitatively recovered. In order to not introduce any empirical parameter in our model, we will stick to the newly derived values.

As a side note, (9.11) can be compared to the equation linking the contact ratio to the normal pressure and the surface roughness in an elastic rough contact:

$$\frac{A}{A_0} = \frac{\sqrt{2\pi}\, p_{\mathrm{N}}}{E^* h'_{\mathrm{RMS}}}, \tag{9.16}$$

from which we deduce the alleged steady-state roughness

$$h'_{\mathrm{RMS}} = \frac{\sqrt{2\pi}\, p_{\mathrm{N}}^{\mathrm{crit}}}{E^*}. \tag{9.17}$$

The estimated stead-state RMS of slopes amounts to $h'_{\mathrm{RMS}} = 0.57$ for $\mathrm{SiO_2}$–$\mathrm{SiO_2}$ interfaces and to $h'_{\mathrm{RMS}} = 0.71$ for $\mathrm{SiO_2}$–Si interfaces. The experimental measurements show that in the $\mathrm{SiO_2}$–$\mathrm{SiO_2}$ case, this value is around 1.

Wear volume

To build a model with surface evolving over time, the instantaneous wear volume must be computed. According to Archard's assumption (Archard 1953), a contact junction of size $a \times a$ is detached into a wear particle after a sliding distance of $ds = a$, creating a wear volume of $dV = a^3$. The increase in wear volume can be expressed as a function of sliding:

$$dV = a^2\, ds. \tag{9.18}$$

For multiple contact junctions, each having a size $a_i \times a_i$, the increase of wear volume is just the sum of the contributions of each junction:

$$dV = \sum_i a_i^2\, ds, \tag{9.19}$$

which can be written as

$$dV = A\,ds\,, \tag{9.20}$$

where A is the contact area formed by all the junctions. This last equation is reminiscent of Archard's wear model, where the wear volume is also proportional to the sliding distance. According to (9.11), the contact area A can be replaced by its assumed steady-state value, leading to

$$dV = \frac{p_\mathrm{N}}{p_\mathrm{N}^\mathrm{crit}} A_0\,ds\,. \tag{9.21}$$

The reattachment of worn particles and the effect of wear on the contact area A are not taken into account in the equation, meaning that the predicted wear volume will be greater than what we would observe in a real system. Therefore, we should not expect quantitatively correct results regarding timescales using this simple model. This complements the assumption made earlier that the contact area ratio A/A_0 remains at a steady-state value.

The instantaneous wear rate dV/ds is computed at each discretized cell of size A_0 from their current pressure $p_\mathrm{N}(x,y)$. The resulting change in surface height is

$$\begin{align} dh &= \frac{1}{A_0}\frac{dV}{ds}v\,dt \tag{9.22}\\ &= \frac{p_\mathrm{N}}{p_\mathrm{N}^\mathrm{crit}} v\,dt\,, \tag{9.23}\end{align}$$

where v is the sliding velocity and dt is the discretized time step. Depending on the type of interface (SiO_2–SiO_2 or SiO_2–Si), the worn surface height is applied to the pin or to the disc. For SiO_2–SiO_2 interfaces, since both materials in contact are the same, the change in height is applied equally to the two surfaces:

$$\begin{align} dh_\mathrm{pin} &= 0.5\,dh\,, \tag{9.24}\\ dh_\mathrm{disc} &= -0.5\,dh\,. \tag{9.25}\end{align}$$

For SiO_2–Si interfaces, since Si is more fragile, we set the wear to

$$\begin{align} dh_\mathrm{pin} &= 0\,, \tag{9.26}\\ dh_\mathrm{disc} &= -dh\,. \tag{9.27}\end{align}$$

To know the nature of the interface, we simply compare the current worn disc height $h_\mathrm{disc}(x,y)$ with the initial height of oxide layer h_layer. For now, we assume that the worn volume is ejected from the contact zone and no longer contributes.

The length L_path of the path of the pin on the disc can be different from the size L of the system considered with the BEM (to lessen the computational cost). To account for this difference, dh_disc is multiplied by L/L_path.

Instead of shifting the two surfaces relative to each other to simulate sliding, the surface of the disc $h_\mathrm{disc}(x,y)$ is simply averaged at every time step along the sliding direction, chosen as the y axis, so that h_disc is always invariant with respect to y.

Model summary

Let us sum up the working of the model. At each time step dt:

1. Solve for the contact between the current surfaces using BEM. We get the pressure distribution $p_\mathrm{N}(x,y)$;

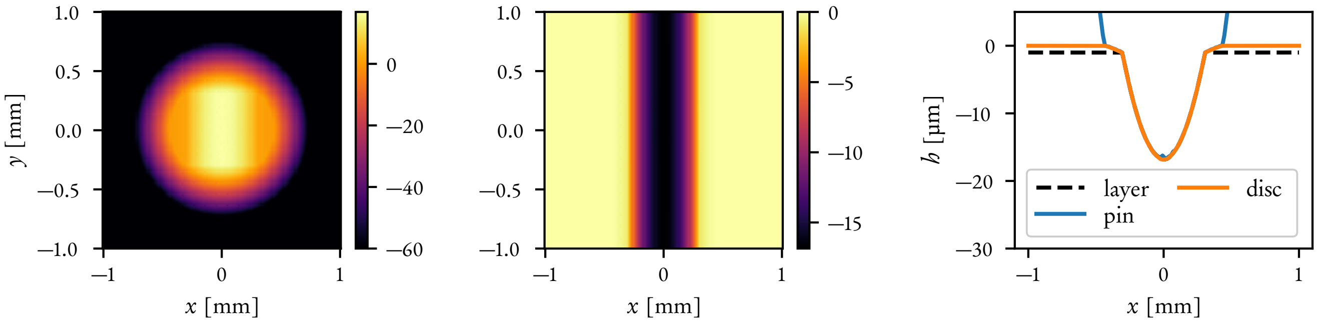

(a) Ball. The heights are in µm.

(b) Disc. The heights are in µm.

(c) Disc cross-section

Figure 9.19 – Example of surface topographies obtained with the BEM model. The oxide layer has an initial thickness of 1 µm. Parts of the SiO_2 pin are in contact with the SiO_2 oxide layer while the rest is in contact with the disc's Si beneath the layer. A single groove is formed in the disc.

2. Compute the tangential resistance p_T at each cell using (9.12);
3. Compute the worn heights from p_N using (9.11), (9.21) and (9.23), and update the surfaces accordingly;

The friction coefficient is obtained by integrating the tangential stresses $p_T(x, y)$ of every cell and dividing by the imposed normal load F_N.

Setup

We consider a system of size $L = 2\,\text{mm}$ with a discretization of $n = 128$. The length of the pin's path is $L_{\text{path}} = 6.28\,\text{mm}$. The sliding velocity is $v = 8\,\text{mm/s}$, the time step is $dt = 0.02\,\text{s}$, and the simulations are run up to a sliding distance of 0.5 m. For solving contact, a constant normal load of $F_N = 1\,\text{N}$ is imposed. The oxide layer thickness is varied from $h_{\text{layer}} = 0$ to 3 µm, like in the experiments, and an infinite layer is also considered, reproducing experiment on bulk SiO_2.

Results

Examples of outputs for an oxide layer of 1 µm are shown in Figure 9.19 and 9.20. As in some experiments, a single groove is created in the disc. The pin has parts in contact with the SiO_2 oxide layer, and a rail in contact with the underlying SiO_2. The evolution of the friction coefficient clearly displays an initial phase where the pin is in contact with the SiO_2 layer, with a high value near μ_{SiO_2}, and a transition to a phase where the pin starts contacting the Si beneath the layer, with μ progressively decreasing toward μ_{Si}. The two phases are also visible in the wear rates dV/ds, with the wear rate of the pin suddenly decreasing when reaching the Si. The total wear rate remains almost constant.

The dependence of the friction coefficient and the disc wear with the oxide layer thickness is shown in Figure 9.21. The same two phases of wear are identifiable on the plots, with a transition happening later for thicker layers. Looking at temporal averages, the presence of an oxide layer increases the average friction coefficient and decreases the wear rate on the disc. It seems that with a longer sliding distance, all systems would converge to the same behavior of contact on an Si disc without any oxide layer, which is expected since the oxide layer is worn out.

All simulations result in the formation of a unique groove in the disc, whereas in experiments, the wear tracks left on oxidized Si discs most often feature several grooves. Introducing initial irregularities on the surfaces does not result in the formation of multiple grooves, as the wear

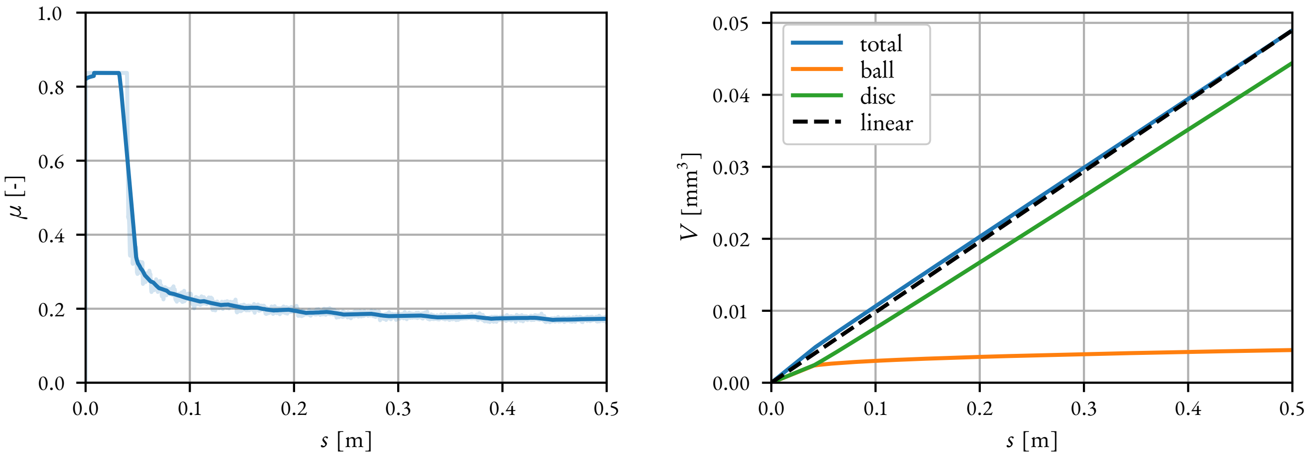

(a) Friction coefficient

(b) Wear volumes

Figure 9.20 – Friction coefficient and wear volumes obtained with $h_{\text{layer}} = 1\,\mu\text{m}$. In both plots, two phases are identifiable. The first phase spans from $s = 0$ to $s = 0.03\,\text{m}$, and corresponds to the moment when the pin is only in contact with the SiO_2 layer of the disc, resulting in a high friction coefficient and an equivalent wear between the pin and the disc. The second phase follows with the pin starting to make contact with the Si beneath the SiO_2 layer. The relative contact area with Si progressively increases, resulting in a lower friction coefficient and a stronger wear of the disc. (a) The transparent curve shows the unfiltered noisy data. A moving average filter is applied, with a window just large enough to remove the noise, resulting in the fully visible curve.

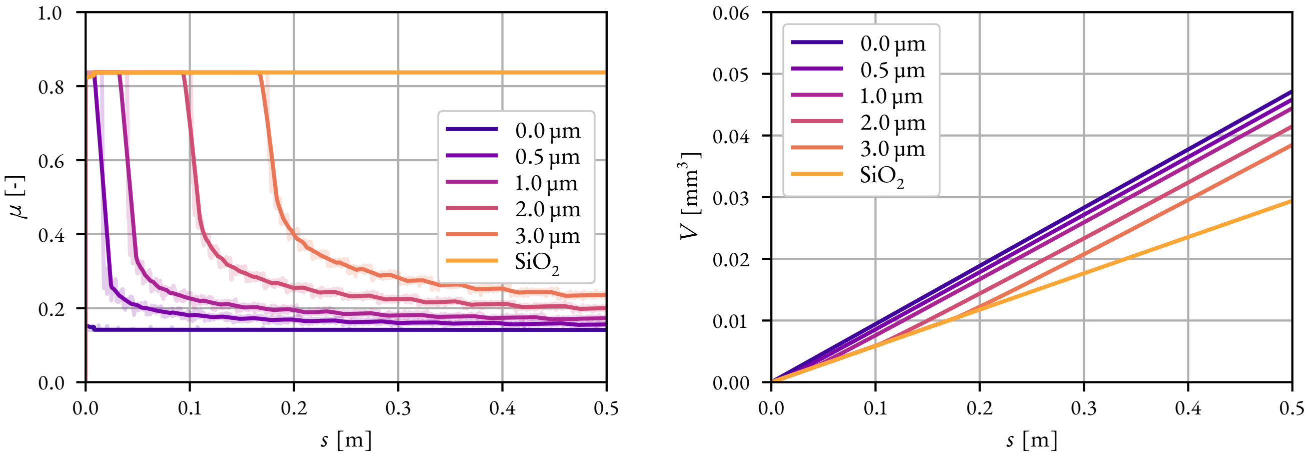

(a) Friction coefficient

(b) Wear volume from the disc

Figure 9.21 – Effect of oxide layer thickness on friction coefficient and wear volume. (a) Plain Si ($h_{\text{layer}} = 0\,\mu\text{m}$) and SiO_2 discs simply result in constant friction coefficients. The presence of an oxide layer increases μ. All curves for oxidized discs seem to converge toward the same value of μ_{Si}. (b) The presence of the oxide layer decreases the wear of the disc. All curves for oxidized discs seem to converge toward the same wear rate (dV/ds slope).

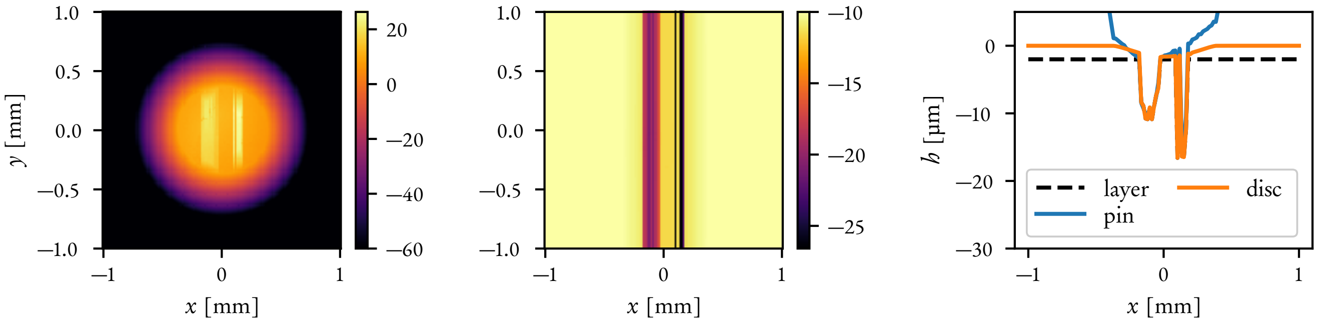

(a) Pin. The heights are in µm.

(b) Disc. The heights are in µm.

(c) Disc cross-section

Figure 9.22 – Effect of rotating non-planarity on surface topographies. Two grooves are created in the disc, with corresponding rails on the pin. The rails are in contact with the Si, while the rest of the pin is in contact with the SiO_2 layer. The relative contact area with SiO_2 is larger than in the perfectly planar case.

process has a smoothening effect.

Non-planarity

In the experiments, the planarity of the disc on the tribometer was not ensured nor measured. Oscillations in the raw measurements of normal and tangential forces during the tests hinted at the presence of this non-planarity. It can easily be implemented in the model by adding a tilted plane to h_{disc} when solving the contact, with the direction of the slope rotating at the desired frequency.

Figure 9.22 shows an example of surface topographies obtained with an oxide layer of 2 µm and with an added slope of 0.01 on the disc, rotating with a period equivalent to 0.05 m of sliding. Two grooves have emerged from the presence of the rotating non-planarity!

The presence of non-planarity also has a noticeable effect on the evolution of the friction coefficient (see Figure 9.23) and on the final behavior at steady state. Without slope, all systems with an oxidized Si disc reach a state where the majority of the contact between the pin and the disc is made of an SiO_2–Si interface, with a friction coefficient converging toward μ_{Si}. Here, the friction coefficient converges to a higher value when the slope is larger. This is explained by the pin keeping a larger contact area with the top of the SiO_2 layer of the disc thanks to the alternating slope. The wear volume is not significantly impacted.

The dependence on the oxide layer thickness is assessed again, adding a non-planarity with a rotating slope of 0.02. The results are shown in Figure 9.24. As observed with the single $h_{\text{layer}} = 2\,\mu\text{m}$ case, the two phases have disappeared, and the friction coefficients are higher than in the planar case. Overall, the trends are the same: having a thicker oxide layer increases the friction coefficient and decreases the wear rate on the disc.

All the final friction coefficients obtained in the planar and non-planar cases are compared between themselves and to the empirical experimental model in Figure 9.25. This figure does not have the purpose of quantitatively comparing the data, since we called earlier that the BEM model is not quantitatively accurate. Still, it clearly shows the effect of non-planarity, and the experimentally observed trend is recovered with the model.

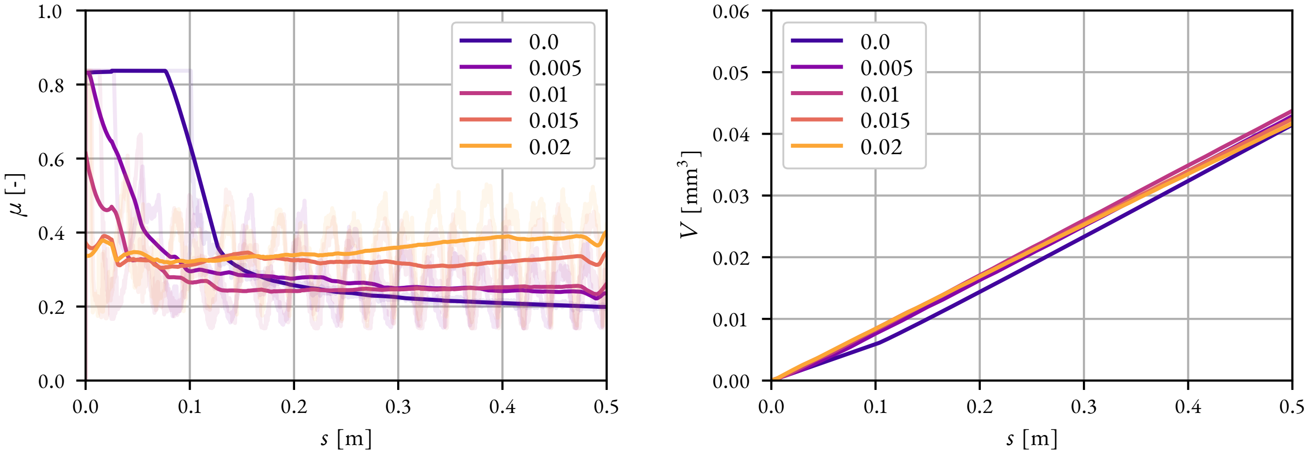

(a) Friction coefficient

(b) Wear volume from the disc

Figure 9.23 – Effect of the slope of a rotating non-planarity on friction coefficient and wear volume. (a) The transparent curves show the unfiltered noisy data, oscillating with the rotation of the non-planarity. The fully visible curves have a moving average filter applied, with a window size equal to the period of rotation. The presence of non-planarity increases the friction coefficient, and the presence of two phases is less evident at larger slopes. (b) There is not much effect on the wear rate.

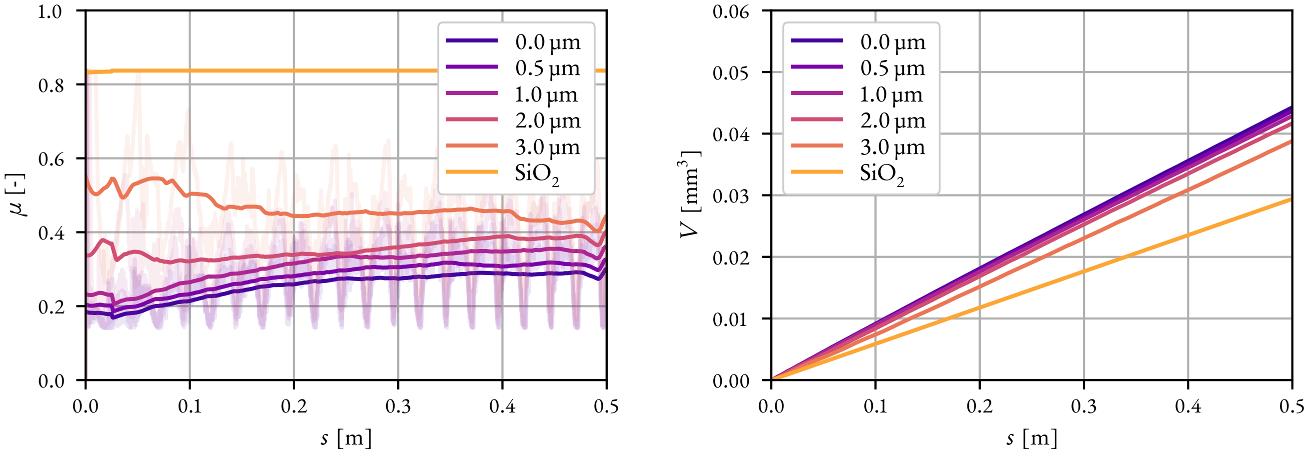

(a) Friction coefficient

(b) Wear volume from the disc

Figure 9.24 – Effect of oxide layer thickness with the presence of a non-planarity of slope 0.02. The same trends as in the planar case are observed, although with overall higher friction coefficients. Contrary to the planar case, the curves do not seem to converge toward a unique value.

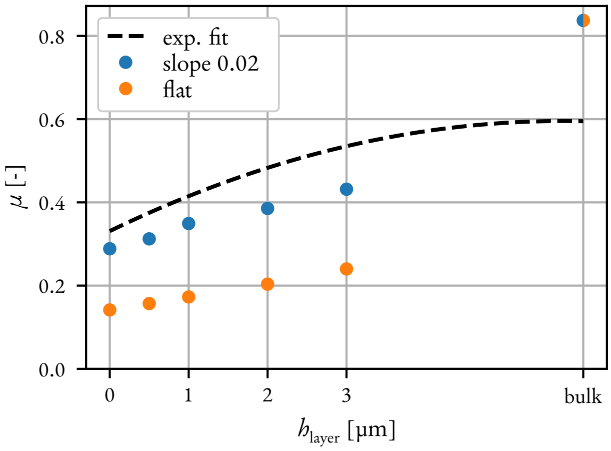

Figure 9.25 – Comparison of friction coefficient between experiments and simulated planar and non-planar cases. The bulk measurements are arbitrarily set to $h_{\text{layer}} = 6\,\mu\text{m}$. The dashed curve is an empirical experimental fit. All sets of data have the same qualitative behavior, with μ increasing monotonously with h_{layer}. The presence of non-planarity significantly increases μ (doubling it in this case).

9.3.3 *Going further with coarse-grained DEM simulations*

The assumption of steady-state surface roughness was made mainly because there is no knowledge of the nanoscale and mesoscale wear processes happening at the interface. To address this issue, it is conceivable to use the coarse-grained DE model developed during this thesis to model a dynamic interface at the scale of asperities with accurate material properties.

Figure 9.26 shows an example of what is achievable, with a system of size $150 \times 150 \times 75\ \text{nm}^3$ made of 400 000 particles. Si can be modeled with an ordered arrangement of particles to replicate (to a certain extent) the differences in strength between the initially crystalline structure and the weakened amorphous structure. SiO_2 is represented with an amorphous arrangement of particles. Here, we simulate an initially cylindrical SiO_2 loose body, of size 50 nm (in green in Figure 9.26). It is trapped between an upper SiO_2 surface (actually rigid) and a lower Si surface, overlayed with an oxide layer of thickness 5 nm. An average particle size of $d_0 = 1.5\,\text{nm}$ was chosen to correctly capture the surface energy and the strength of both Si and SiO_2 (see definitions of minimum and critical particle diameters in Section 6.1.2).

With a sliding motion imposed on the top surface, the loose cylinder rolls and deforms. It picks up particles from the oxide layer and grows in size. It eventually reaches the Si underneath the layer, leaving a trench in its path. The wear particle growth and the creation of a wear track match experimentally observed phenomena.

Modeling the same system with MD would be totally untractable. Atoms have a size roughly 10 times smaller than the current d_0, so around 400 million atoms would be needed. Moreover, the time step would drop from 20 fs (femtoseconds) to the usual 1 fs used in our other MD simulations. Methodically running more DEM simulations of this kind is unfortunately out of the time frame available for this thesis. We leave this task to the future minds that would find an interest in pursuing it.

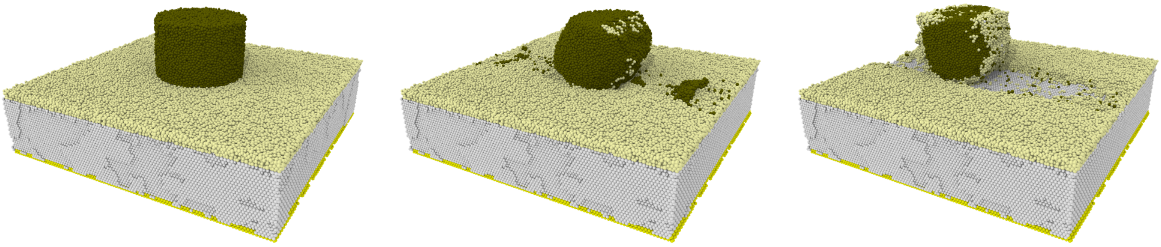

(a) $s = 0\,\mu m$ (b) $s = 0.44\,\mu m$ (c) $s = 7.7\,\mu m$

Figure 9.26 – DEM simulation of asperity wear on oxidized Si. Green and beige particles are amorphous SiO_2, white and yellow particles are crystalline Si. The system size is $150 \times 150 \times 75$ nm³. The average particle size is $d_0 = 1.5$ nm. The shear motion is caused by a rigid plate made of SiO_2 particles (not shown). A pressure of 100 MPa is applied on the system. (b) The rolling wear particle rolls and grows by taking SiO_2 particles from the surface. (c) The wear particle reaches the Si underneath the layer, creating a trench.

Concluding remarks

Both the experiments and numerical simulations show that the presence of an oxide layer on Si samples increases the friction coefficient while decreasing the wear volume originating from the oxidized piece. In the experiments, the measured friction coefficient goes from $\mu \approx 0.33$ for non-oxidized samples to $\mu \approx 0.55$ for fully oxidized ones (made completely of SiO_2). MD simulations reveal that the lowest tangential resistance offered by Si, despite its higher static strength, is caused by a transition between the initial crystalline state of the material toward a weaker amorphous state.

The wear tracks left on oxidized samples feature multiple grooves reaching the Si underneath the oxide layer. Such grooves were not observed in the previous experimental campaign involving only SiO_2. BEM simulations revealed that the grooves originate from a non-planarity in the *pin-on-disc* experiments. They are therefore specific to this kind of test and should not be expected in every tribological system involving oxidized Si pieces. The presence of the non-planarity is shown to increase the friction coefficient (*e.g.* up to 2 times for a slope of $dh/dx = 0.02$) without significantly impacting the wear rate.

The BEM model is able to qualitatively reproduce the experimentally observed phenomena without the need for any empirical parameter. However, the predicted wear volumes are higher than the experimental ones by three orders of magnitude. Indeed, strong assumptions were formulated for this BEM model. Still, there is one ingredient missing in the model, whose presence could mitigate this discrepancy: it is the modeling of the TBL. It was shown in the previous chapter that the TBL stays inside the contact zone thanks to the adhesive reattachment of matter, creating the surface roughness. Keeping the third-body in the simulation instead of directly removing it as worn volume should greatly reduce the simulated wear rate, potentially bringing it closer to the experimentally measured values.

CONCLUSION

The main objective of this thesis was to obtain a physical understanding of unlubricated adhesive wear across scales. The first sub-objective was the study and formalization of interactions between multiple micro-contacts. Following the approach of Rabinowicz (1958) based on competing energies, we first studied the interactions of nanoscale junctions in two dimensions. Fundamental contact mechanics solutions were used to evaluate the elastic energy stored by shearing the micro-contacts, and the stored energy was compared to the energy needed to detach a single joined wear particle or multiple wear particles under the micro-contacts. The model provides simple criteria to evaluate the energetic feasibility of the different wear formation scenarios. The sheared system is either in a plastic regime, a "separated wear particles formation" regime, or a "combined wear particle formation" regime. The predicted behavior depends on material properties (all grouped into a single quantity, the material's critical length scale d^*) and geometrical parameters (the apparent contact area and the real contact area). MD simulations were used to test the predictions of the outcome for various sets of parameters. Each asperity-scale regime can be associated with a macroscopically observed wear regime. The plastic regime, where surfaces only deform without creating wear debris, corresponds to low wear; the separated regime relates to mild wear, with the wear volume being proportional to the real contact area; and the existence and predictability of the combined regime formalize the transition toward severe wear, with much larger wear volumes.

Working in two dimensions came with some flaws. For example, the elastic energies evaluated in the theoretical model are infinite. This issue was resolved when moving toward three-dimensional systems. Using the same energetic approach, a "wear map" was derived to predict the wear behavior of two nearby circular micro-contacts. The predicted nanoscale wear regimes remain unchanged and still depend on the material critical length scale d^* and the geometrical parameters (size of junctions and distance between them). The 3D analytical model was easily adapted to the case of rough contact. In such contact, the application of a normal load makes more and more micro-contacts appear, grow, and cluster together, all being events favoring elastic interactions. The wear map devised for rough contacts now expresses the wear behavior as a function of d^* and the real contact area (function of the normal load and surface roughness). Three regions are clearly identifiable in the wear map. The first region is a "plasticity" region, with zero wear volume. The second is a "separated" region, where both the wear volume and the number of generated particles increase with the normal load. The last region is a "combined" region, existing thanks to the presence of elastic interactions. In this regime, under normal loading, the number of wear particles decreases and their volume increases drastically with the formation of wear particles encompassing several micro-contact zones (contrasting with the "separated" regime). One drawback of the model is that it only predicts an instantaneous wear volume, with no notion of sliding distance, like Brink *et al.* (2021) is including. Our model is limited by its computational cost, making the implementation of sliding not straightforward. Since the model was implemented in serial, a parallel approach could be used instead.

The second sub-objective of the thesis was the development and usage of upscaling techniques. The study of elastic interactions at the scale of rough surfaces was already a form of upscaling the asperity-scale model, but the resulting model is static. The wear behavior is predicted, but not realized nor verified. To serve as a tool to model adhesive wear dynamically at scales larger than MD, a coarse-grained DE model was developed, with particles having contact and reversible cohesive forces in order to model fracture and reattachment of matter. The pairwise forces are tuned to obtain a solid with reasonably approximated elastic and fracture properties. The nanoscale ductile-brittle transition, observed with MD, is reproducible with the DEM simulations using particles having a diameter at least 10 times larger than atoms, and therefore for a fraction of the computational cost. The model is also able to replicate macroscopic experimental tests realized with a cohesive material mimicking wet sand. The newly developed model helped us establish a link between a material's ideal strength (measured at small scale) and the macroscopic strength of a tribological interface featuring this material, showing that the tangential strength of an interface depends on the real contact area, the material ideal shear strength, and its compressive strength.

Other preliminary numerical studies were conducted using the coarse-grained model, demonstrating that its usage is suitable for the study of dynamical adhesive wear mechanisms at a scale larger than reachable by MD. Looking at dynamical effects was part of the third sub-objective of the thesis. The model is capable of simulating the creation, growth, and interaction of wear particles originating from rubbed rough surfaces. To keep the details of the nanoscale, the size of the discrete particles must not exceed d^*. In accordance with a previous work conducted with MD (Brink *et al.* 2022), two frictional regimes were uncovered: one has rolling and growing wear particles, with low sliding resistance, and the other one features a shear band, with a higher tangential resistance.

Still, in the assessment of dynamical behaviors, the evolution of surface topography due to wear was observed experimentally on SiO_2 samples using a *pin-on-disc* tribological setup. We showed that roughness is created from flat surfaces with the building up of a TBL, aggregated from nanoscale wear particles whose size is related to d^*. The small wear particles grow into rolling cylinders, and then accumulate into a TBL, taking the form of flakes, and crating the macroscopic roughness. The history of the creation of the TBL is backed up by experimental observations and numerical simulations. Conversely, initially rougher surfaces are smoothed. In all cases, the surface converges toward obtaining a self-affine surface roughness independent of the initial surface state, and persistent over time. Since friction and wear are shown to be primarily dependent on the real contact area, it is sensible to assert that reaching a steady state of surface roughness means also keeping a controlled friction coefficient and constant wear rate.

Finally, similar experiments were run on Si samples to investigate the effect of an oxide layer on tribological properties, which was the last and more applied objective of this thesis. The experiments showed that the presence of an oxide layer increases the friction coefficient while protecting against wear. MD simulations of Si and SiO_2 were performed to find the physical origins of this macroscopic tribological behavior, revealing that crystalline Si, while having a higher static strength than SiO_2, becomes amorphous under stress and loses its strength, thus explaining its lower frictional resistance. Macroscopic BEM simulations were used to input the MD computed material properties into a model reproducing the experimental setup. The friction and wear trends were successively recovered. The numerical simulations also uncovered the high sensibility of the tribological system to small disturbances, with for example a non-planarity of 2% in the setup leading to friction coefficients twice as large. Ultimately, we found no optimal oxide layer thickness leading to the best tribological behavior (lowest friction and wear), so engineers working with such material must engage in a trade-off. In any case, the presence of the oxide layer is known to enhance other mechanical properties.

Outlook

A phenomenon that is inherently present in MD/DEM simulations but lacking in our BEM simulations is *plasticity*, which plays a big role in rough contacts. Weber *et al.* (2018) compares an experimental method and a FE-based method to get the contact area of a rough sphere pressed against a flat surface as a function of the normal load. It shows that the FE model considering only elastic deformations is not sufficient to reproduce the experimental results, as the contact area is significantly underestimated. A model considering plastic effects must be used to match the experimental data. Simplified plasticity models, like saturation models, can be used with BEM to better predict the contact area. However, this is not sufficient in the context of wear, as it was shown that saturation plasticity models underestimate the number of crack nucleation sites, compared to "real" plasticity models (Frérot *et al.* 2020a). Von Mises plasticity was implemented in our BEM software Tamaas to meet this need (Frérot *et al.* 2019). In principle, plasticity is also inherently present in coarse-grained DEM simulations. The effect of plasticity on the prediction of wear on rough surfaces may be an object of future analysis.

The study of tribology should not be limited to unlubricated and adhesive wear. When two materials with different hardnesses are put in contact, mostly the softest body will wear out, enabling a regime of *abrasive* wear. This phenomenon has been studied using AFM scratching experiments (Gnecco *et al.* 2002) and MD simulations (Kato 2003), showing that a work similar to the one carried out during this thesis can be conducted for abrasive wear. The outcomes could be adapted to more practical matters, such as the process of material removal (Molinari & Pham-Ba 2022). The other tribological phenomenon that can be studied with our tools is lubrication, which can be modeled at the nanoscale with MD simulations (Eder *et al.* 2011), or at the mesoscale with an appropriate BEM formulation (Akchurin *et al.* 2017). The DEM model we developed can model materials with contrasting properties, and being a discrete method, it can by nature represent flows. Therefore, it could be used to upscale the works on abrasive wear and lubrication performed with MD.

Even though we were able to prove that elastic interactions are of crucial importance for the emergence of macroscopic wear regimes, we were not able to validate our model dynamically. With the rise of experimental methods capable of *in situ* measurements during sliding of rough surfaces (Petrova *et al.* 2018; Sahli *et al.* 2018; Weber *et al.* 2018; Garabedian *et al.* 2019), one could imagine verifying experimentally the effects of micro-contacts' interaction on the creation of wear particles. While the newly developed coarse-grained DE model could be used to verify the analytical theory of wear for several micro-contacts, simulating 3D rough surfaces in dynamical sliding motion would not be computationally manageable. To model rough surfaces with the same resolution as in the BEM model of Chapter 5, one would need at least $500 \times 500 \times 100$ particles per body, for a total of 25 million particles. This is where the *coupling* methods can shine. The computational cost can be reduced by modeling the continuum domain beneath the rough surfaces using the finite element method (FEM) instead of using discrete particles everywhere. The coupling happens in a region between the DEM domain and the FEM domain. Coupling is already well developed for linking MD with FEM. The two main families of coupling methods are the *edge-to-edge* methods, where boundary conditions are applied to the atomic and the continuum domains at their interface (Broughton *et al.* 1999), and the *overlapping* methods, in which, as the name suggests, the two domains overlap. A classical example of overlapping method is the *bridging* method (Belytschko &

Xiao 2003). The coupling method is also applicable to coarse-grained MD (Rudd & Broughton 1998), as well as DEM (Wellmann & Wriggers 2012). Correctly matching the material properties of an amorphous DEM domain, a FEM domain, and their interface is a current topic of research in our group (Voisin–Leprince *et al.* 2022). With such coupling methods, it would be manageable to simulate the formation and evolution of a TBL in three dimensions, from the creation of the very first wear particles of size d^*. As the material properties of a numerical simulation can be tuned at one's liking (unlike in physical experiments), it would be possible to tackle the following question: Does the actual value of d^* influence the macroscopic tribological properties of an interface, or is it buried inside the nanoscale, having no more effect than the size of atoms on our seemingly continuous macroscopic world?

APPENDICES

APPENDIX A

FRICTIONAL CONTACT WITH THE BOUNDARY ELEMENT METHOD

A boundary element code based is available at our laboratory: Tamaas (Frérot *et al.* 2020b). The BE formulation used in the code allows to solve normal contact problems with normal adhesion between the surfaces. For use in problems involving sliding, we implemented frictional contact with tangential forces.

Bugnicourt *et al.* (2018) shows a way to implement a BE solver able to solve contact problems with a tangential load and Coulomb friction at the interface between the surfaces. Since both a normal contact problem and a tangential contact problem have to be solved at the same time, the Poisson's ratio ν has to be set at $\nu = 0.5$ in order to decouple the normal and tangential components, meaning that a normal pressure applied on a point of the surface will not induce any tangential displacement around this point, and the same will be true between a tangential pressure and normal displacements. Khajeh Salehani *et al.* (2018) shows that they can solve a coupled problem while having normal and tangential adhesive forces instead of Coulomb friction. Unlike Coulomb friction, these adhesion forces are not directly dependent on the normal load. Such formulations are more suited for a nanoscale point of view of friction, where the strength of an interface is directly linked to the strength of bonds between atoms. Conversely, Coulomb friction is more suitable at mesoscale or macroscale.

Despite the problem of contact with friction being known for not having unique solutions even in the simplest cases (Hild 2003), we attempt to formulate a method to solve it in the general uncoupled case (ν not necessarily equal to 0.5). The method was implemented in Tamaas and validated against analytical solutions of frictional contact.

A.1 FORMULATION

Since the contact between a rigid rough surface and an elastic flat surface is equivalent to the contact between two elastic rough surfaces with different material properties, the former case is considered, as shown in Figure A.1. The elastic material is given an *effective Young's modulus* E^* defined as

$$\frac{1}{E^*} = \frac{1-\nu_1^2}{E_1} + \frac{1-\nu_2^2}{E_2} \tag{A.1}$$

where E_1, ν_1, E_2 and ν_2 are the Young's moduli and the Poisson's ratios of the materials of the two surfaces initially considered. The height profile $h(x_i, y_j)$ of the new surface is taken simply as the difference of the heights of the initial surfaces. Our solver can handle problems where the normal and tangential quantities (loads and displacement) are decoupled ($\nu = 0.5$) or coupled ($\nu < 0.5$).

At each contacting point, the rigid surface is applying a normal pressure p_N on the elastic surface. One contacting point can support a tangential pressure $||\boldsymbol{p}_\mathrm{T}||$ up to $p_{\mathrm{T,max}}$. If $||\boldsymbol{p}_\mathrm{T}|| < p_{\mathrm{T,max}}$, the point of the elastic surface in contact with the rough surface sticks to it, and if $||\boldsymbol{p}_\mathrm{T}|| = p_{\mathrm{T,max}}$, sliding can occur by having a relative tangential displacement of the point of the elastic surface. Two friction laws have been implemented: the Coulomb's friction law

$$p_{\mathrm{T,max}} = \mu\, p_\mathrm{N} \tag{A.2}$$

where μ is the friction coefficient of the interface, and the Tresca's friction law

$$p_{\mathrm{T,max}} = \sigma_{\mathrm{m,T}} \tag{A.3}$$

where $\sigma_{\mathrm{m,T}}$ is the *shear strength* of the interface. Coulomb friction is more suited to represent a macroscale or mesoscale contact, while Tresca friction portrays more properly nanoscale (asperity level) phenomena.

A.1.1 *Continuous formulation*

BEM is based on a *fundamental solution* linking the displacement field to the pressure field:

$$\boldsymbol{u}(\boldsymbol{x}) = \int_\Gamma \boldsymbol{F}(\boldsymbol{x} - \boldsymbol{x}')\boldsymbol{p}(\boldsymbol{x}')\,d\boldsymbol{x}', \qquad \forall \boldsymbol{x} \in \Gamma, \tag{A.4}$$

where $\boldsymbol{F}$ is the elastic surface deflection caused by a concentrated load applied at the origin.

Frictionless case

Solving the contact problem amounts to solve an optimization problem (Rey *et al.* 2017). Given the rough surface shape $h(\boldsymbol{x})$ and the target mean pressure $\boldsymbol{p}_0$, the following functional must be minimized:

$$\mathcal{J}(\boldsymbol{p}) = \underbrace{\frac{1}{2}\int_\Gamma \boldsymbol{p}\cdot\boldsymbol{u}\,d\boldsymbol{x} - \int_\Gamma \boldsymbol{p}\cdot\boldsymbol{h}\,d\boldsymbol{x}}_{-E_\mathrm{c}(\boldsymbol{p})}, \tag{A.5}$$

under the constraints

$$p_\mathrm{N} \geqslant 0, \quad \forall \boldsymbol{x} \in \Gamma, \tag{A.6a}$$

$$\boldsymbol{p}_\mathrm{T} = \boldsymbol{0}, \quad \forall \boldsymbol{x} \in \Gamma, \tag{A.6b}$$

$$\frac{1}{\mathrm{mes}(\Gamma)}\int_\Gamma \boldsymbol{p}\,d\boldsymbol{x} = \boldsymbol{p}_0, \tag{A.6c}$$

where E_c is called the complementary energy.

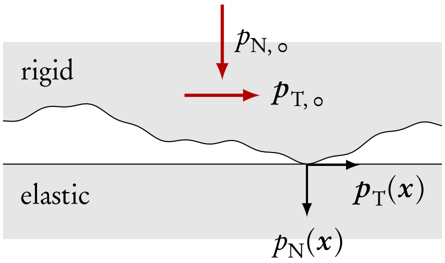
$p_{\mathrm{N},\circ}$
rigid
$\boldsymbol{p}_{\mathrm{T},\circ}$
elastic
$\boldsymbol{p}_\mathrm{T}(\boldsymbol{x})$
$p_\mathrm{N}(\boldsymbol{x})$

Figure A.1 – Tangential contact setup

Coulomb friction

In the formulation with Coulomb friction, a term is added in the minimized functional and one of the constraints is modified. The following functional must be minimized:

$$\mathcal{J}(\boldsymbol{p}) = \frac{1}{2}\int_\Gamma \boldsymbol{p}\cdot\boldsymbol{u}\,dx - \int_\Gamma \boldsymbol{p}\cdot\boldsymbol{h}\,dx + \underbrace{\int_\Gamma \mu p_\mathrm{N}\|\boldsymbol{g}_\mathrm{T}\|dx}_{j(\boldsymbol{p})}, \tag{A.7}$$

under the constraints

$$p_\mathrm{N} \geqslant 0, \quad \forall x \in \Gamma, \tag{A.8a}$$

$$\mu p_\mathrm{N} - \|\boldsymbol{p}_\mathrm{T}\| \geqslant 0, \quad \forall x \in \Gamma, \tag{A.8b}$$

$$\frac{1}{\mathrm{mes}(\Gamma)}\int_\Gamma \boldsymbol{p}\,dx = \boldsymbol{p}_0, \tag{A.8c}$$

where j is the frictional work, and $\boldsymbol{g} = \boldsymbol{u} - \boldsymbol{h}$ is the gap between the surfaces.

Tresca friction

In the case of Tresca friction, the frictional work and the constraints are appropriately modified. Minimize

$$\mathcal{J}(\boldsymbol{p}) = \frac{1}{2}\int_\Gamma \boldsymbol{p}\cdot\boldsymbol{u}\,dx - \int_\Gamma \boldsymbol{p}\cdot\boldsymbol{h}\,dx + \underbrace{\int_\Gamma \sigma_\mathrm{m,T}\|\boldsymbol{g}_\mathrm{T}\|dx}_{j(\boldsymbol{p})}, \tag{A.9}$$

under the constraints

$$p_\mathrm{N} \geqslant 0, \quad \forall x \in \Gamma, \tag{A.10a}$$

$$\sigma_\mathrm{m,T} - \|\boldsymbol{p}_\mathrm{T}\| \geqslant 0, \quad \forall x \in \Gamma, \tag{A.10b}$$

$$\frac{1}{\mathrm{mes}(\Gamma)}\int_\Gamma \boldsymbol{p}\,dx = \boldsymbol{p}_0. \tag{A.10c}$$

A.1.2 *Discrete formulation*

In the following text, we only present the algorithm for Coulomb friction. The derivation for Tresca friction is very similar. Every instance of μp_N would be replaced by $\sigma_\mathrm{m,T}$.

The surface Γ is discretized as a grid I of $N \times N$ points. The continuous problem is sampled. The fundamental solution (A.4) becomes discretized:

$$\boldsymbol{u}(\boldsymbol{x}) = \sum_{x'\in I} \boldsymbol{F}(\boldsymbol{x}-\boldsymbol{x}')\boldsymbol{p}(\boldsymbol{x}')\Delta x', \qquad \forall x \in I. \tag{A.11}$$

The functional to minimize (A.7) is also discretized:

$$\mathcal{J}(\boldsymbol{p}) = \frac{1}{2}\sum_{x\in I} \boldsymbol{p}\cdot\boldsymbol{u} - \sum_{x\in I} \boldsymbol{p}\cdot\boldsymbol{h} + \sum_{x\in I} \mu p_\mathrm{N}\|\boldsymbol{g}_\mathrm{T}\|, \tag{A.12}$$

and the constraints remain identical to those in the continuous formulation (A.8).

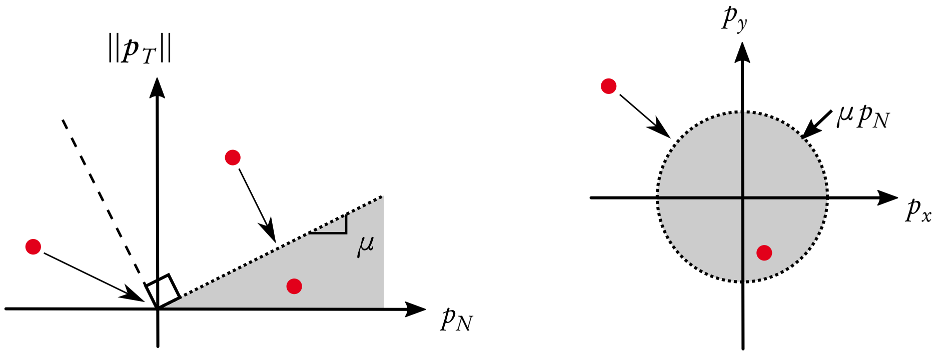

(a) Side view

(b) Front view

Figure A.2 – Friction cone for constraints enforcement. The red dots show the initial value of p, and the arrows (if present) indicate how the inequality constraints are solved. Points lying outside of the cylinder are brought to the closest point on its surface.

A.1.3 *Minimization*

The solving of the discretized problem is based on the conjugate gradient algorithm (Polonsky & Keer 1999). During solving, the functional does not need to be explicitly computed, as only its gradient is used:

$$\frac{\partial \mathcal{J}(p)}{\partial p}(x) = \tilde{g}(x) + \mu||\tilde{g}_\mathrm{T}(x)||e_\mathrm{N}, \qquad \forall x \in I, \tag{A.13}$$

where $\tilde{g}(x) = g(x) - g_s$ is the gap shifted to be zero in the region of sticking contact $I_s = \{x \in I \mid p_\mathrm{N} > 0 \text{ and } ||p_\mathrm{T}|| < \mu p_\mathrm{N}\}$, with g_s being the mean value of the gap g in I_s. Note that in the case of Tresca friction, the derivative of the functional would only be equal to $\tilde{g}(x)$.

The inequality constraints (A.8A) and (A.8B) are enforced by projecting the pressure p on a *friction cone* (see Figure A.2). The equality to target mean pressure p_0 (A.8C) is ensured by rescaling p_N and shifting p_T.

Monitoring the convergence of the minimization is done by evaluating a cost function

$$\mathcal{G}_\mathrm{T}(p, g) = \sum_{x \in I} p_\mathrm{N} g_\mathrm{N} + \sum_{x \in I} (\mu p_\mathrm{N} - ||p_\mathrm{T}||)||g_\mathrm{T}||. \tag{A.14}$$

The full procedure is given in Algorithm 1.

Algorithm 1: Computation of $\boldsymbol{p}(\boldsymbol{x})$ minimizing $\mathcal{J}(\boldsymbol{p})$

```
Input: $h(x), \boldsymbol{p}_0, \varepsilon$ and $n_{\max}$
Output: $\boldsymbol{p}(\boldsymbol{x})$ and $\boldsymbol{u}(\boldsymbol{x})$
$R_{\text{old}} \leftarrow 1$ ;   $\boldsymbol{t}(\boldsymbol{x}) \leftarrow \boldsymbol{0}$ ;   $n \leftarrow 0$ ;                          // initialization
do
    $\bar{\boldsymbol{p}} \leftarrow \frac{1}{N} \sum_{\boldsymbol{x}\in I} \boldsymbol{p}(\boldsymbol{x})$ ;
    $p_{\text{N}}(\boldsymbol{x}) \leftarrow \frac{p_{N,0}}{\bar{p}_{\text{N}}} p_{\text{N}}(\boldsymbol{x})$ ;   $\boldsymbol{p}_{\text{T}}(\boldsymbol{x}) \leftarrow \boldsymbol{p}_{\text{T}}(\boldsymbol{x}) - \bar{\boldsymbol{p}}_{\text{T}} + \boldsymbol{p}_{T,0}$ ;   // enforce mean
    $\boldsymbol{g}(\boldsymbol{x}) \leftarrow \sum_{\boldsymbol{x}'\in I} \boldsymbol{F}(\boldsymbol{x}-\boldsymbol{x}')\boldsymbol{p}(\boldsymbol{x}')\Delta \boldsymbol{x}' - \boldsymbol{h}(\boldsymbol{x})$ ;
    $\Delta \boldsymbol{p}(\boldsymbol{x}) \leftarrow \frac{\partial \mathcal{J}(\boldsymbol{p})}{\partial \boldsymbol{p}}(\boldsymbol{x})$ ;          // compute gradient using shifted gap
    $R \leftarrow \sum_{\boldsymbol{x}\in I} \Delta \boldsymbol{p}^2(\boldsymbol{x})$ ;
    $\boldsymbol{t}(\boldsymbol{x}) \leftarrow \Delta \boldsymbol{p}(\boldsymbol{x}) + \frac{R}{R_{\text{old}}} \boldsymbol{t}(\boldsymbol{x})$ ;                 // update search direction
    $R_{\text{old}} \leftarrow R$ ;
    $\boldsymbol{r}(\boldsymbol{x}) \leftarrow \sum_{\boldsymbol{x}'\in I} \boldsymbol{F}(\boldsymbol{x}-\boldsymbol{x}')\boldsymbol{t}(\boldsymbol{x}')\Delta \boldsymbol{x}'$ ;         // projected search direction
    $\bar{\boldsymbol{r}} \leftarrow \frac{1}{N} \sum_{\boldsymbol{x}\in I} \boldsymbol{r}(\boldsymbol{x})$ ;
    $\boldsymbol{r}'(\boldsymbol{x}) \leftarrow \boldsymbol{r}(\boldsymbol{x}) - \bar{\boldsymbol{r}}$ ;
    $\tau \leftarrow (\sum_{\boldsymbol{x}\in I} \Delta \boldsymbol{p}(\boldsymbol{x})\boldsymbol{t}(\boldsymbol{x}))/(\sum_{\boldsymbol{x}\in I} \boldsymbol{r}'(\boldsymbol{x})\boldsymbol{t}(\boldsymbol{x}))$ ;   // compute step size
    $\boldsymbol{p}(\boldsymbol{x}) \leftarrow \boldsymbol{p}(\boldsymbol{x}) - \tau \boldsymbol{t}$ ;                        // update pressure
    project $\boldsymbol{p}(\boldsymbol{x})$ on friction cone ;            // enforce inequality constraints
    $f \leftarrow \mathcal{G}_{\text{T}}(\boldsymbol{p}, \boldsymbol{g})$ ;
    $n \leftarrow n+1$ ;
while $f > \varepsilon$ and $n < n_{\max}$ ;
$\boldsymbol{u}(\boldsymbol{x}) \leftarrow \sum_{\boldsymbol{x}'\in I} \boldsymbol{F}(\boldsymbol{x}-\boldsymbol{x}')\boldsymbol{p}(\boldsymbol{x}')\Delta \boldsymbol{x}'$ ;
```

A.2 VALIDATION

Our solver has been validated with analytical contact solutions, valid in the uncoupled case $\nu = 0.5$. The contact with a rigid spherical indenter of radius R (Figure A.3) was validated with the Hertz solution in the frictionless case and with the Mindlin solution (Johnson 1985) in the case with Coulomb friction (Figure A.4A). Denoting by $2a$ the diameter of the contact zone, $L = L_x = L_y$ the size of the simulation and $n = n_x = n_y$ the number of discretization points (see Figure A.3B), we find that the numerical solution only matches the analytical solution if the contact diameter is small enough compared to the simulation size ($2a < L/10$), because the solver accounts for periodic boundary conditions which is not the case for Hertz and Mindlin theories, and the grid size must also be small compared to the contact diameter ($L/n < 2a/10$). The solver was also validated for the contact of a 2D sinusoidal (therefore periodic) line of wavelength L and amplitude D with the solutions presented in Block & Keer (2008) at different levels of friction (frictionless, partial slip and sliding) (Figure A.4B). In this case, there is no limitation on the maximal contact size compared to the simulation size.

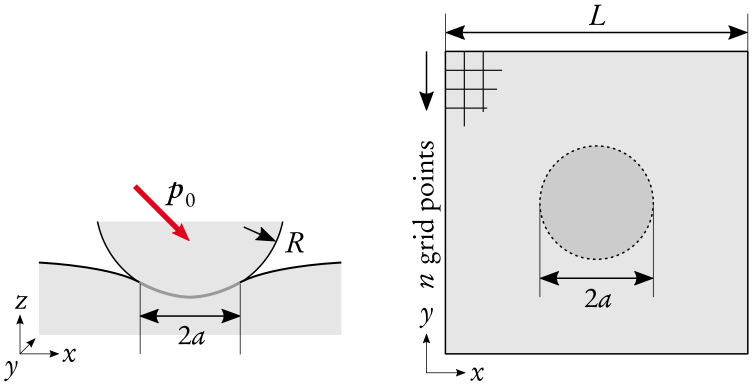

(a) Spherical contact

(b) Top view

Figure A.3 – Spherical tangential contact. (b) The darker area is the contact zone.

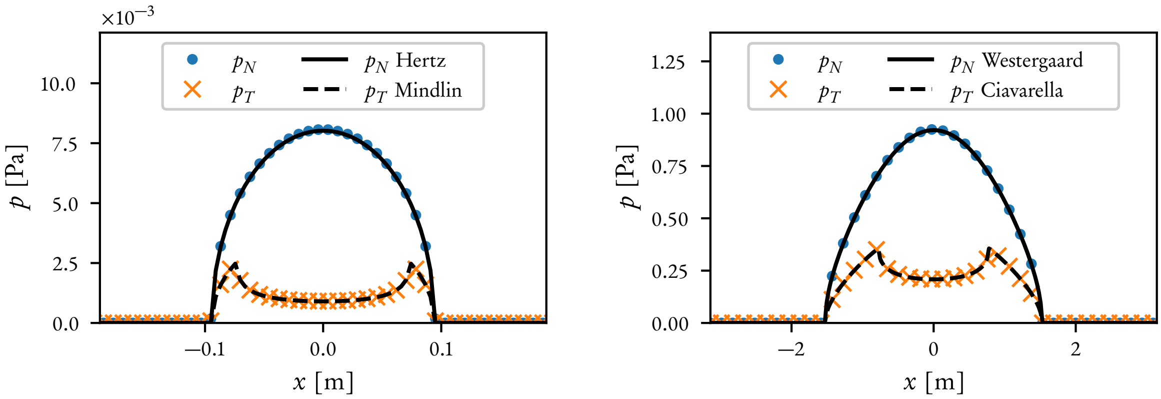

(a) 2D spherical contact

(b) 1D sinusoidal contact

Figure A.4 – Validation of the BE solver at partial friction in the uncoupled case. (a)-(b) $n = 243$, $E = 1\,\mathrm{Pa}$, $\nu = 0.5$, $\mu = 0.5$. (a) $L = 1\,\mathrm{m}$, $R = 10\,\mathrm{m}$, $p_{N,0} = 1.5 \times 10^{-4}\,\mathrm{Pa}$, $p_{x,0} = 4 \times 10^{-5}\,\mathrm{Pa}$. The slice $y = 0$ is plotted for a limited range of x, and only one of every two points of the simulated output pressures is shown for clarity. The analytical solutions are from (Johnson 1985). (b) $L = 2\pi\mathrm{m}$, $D = 1\,\mathrm{m}$, $p_{N,0} = 2\,\mathrm{Pa}$, $p_{T,0} = 0.7\,\mathrm{Pa}$. The full range of x is plotted. Only one of every six points of the simulated output pressures is shown for clarity. The analytical solutions are from (Block & Keer 2008).

A.3 COMPUTED QUANTITIES

For a given shape of rigid indenter $h(\boldsymbol{x})$ and a targeted mean pressure $\boldsymbol{p}_0$, the BE solver outputs a distribution of pressures $\boldsymbol{p}(\boldsymbol{x}) = \boldsymbol{p}(x_i, y_j)$ applied onto the elastic surface. From these pressures, it is possible to compute the displacements $\boldsymbol{u}(x_i, y_j, z)$ and the stresses $\boldsymbol{\sigma}(x_i, y_j, z)$, at the surface and in the elastic bulk. We define the *gap* $\boldsymbol{g}(x_i, y_j)$ between the two surfaces as $g_\mathrm{N} = u_\mathrm{N} - h$ and $\boldsymbol{g}_\mathrm{T} = \boldsymbol{u}_\mathrm{T}$. The pressures also tell us for each point of the surface if it is in contact with the indenter ($p_\mathrm{N} > 0 \Leftrightarrow g_\mathrm{N} = 0$) and if it is sticking ($||\boldsymbol{p}_\mathrm{T}|| < p_{\mathrm{T,max}} \Leftrightarrow ||\boldsymbol{g}_\mathrm{T}|| = 0$) or sliding ($\boldsymbol{p}_\mathrm{T} = p_{\mathrm{T,max}} \Leftrightarrow ||\boldsymbol{g}_\mathrm{T}|| > 0$). An example is shown in Figure A.5A.

From the stress tensor $\boldsymbol{\sigma}(x_i, y_j, z)$, it is possible to compute the three principal stresses σ_I, σ_II and σ_III, as well as their directions, for each point of the elastic bulk. The value of σ_I at a given point is the *maximum tensile stress* at this point, and the *maximum shear stress* is given by $\tau_\mathrm{m} = (\sigma_\mathrm{I} - \sigma_\mathrm{III})/2$. The maximum tensile stresses on the surface are of prime interest, because they tell if a crack can be initiated, which is the case if $\sigma_\mathrm{I} \geqslant \sigma_\mathrm{m}$, where σ_m is the *tensile strength* of the material. The values of σ_I in the bulk are also interesting because they can give the SIF K_I of mode I fracture at a point of concentrated stress. Examples of plots of σ_I and τ_M are given in Figures A.5B and A.5C.

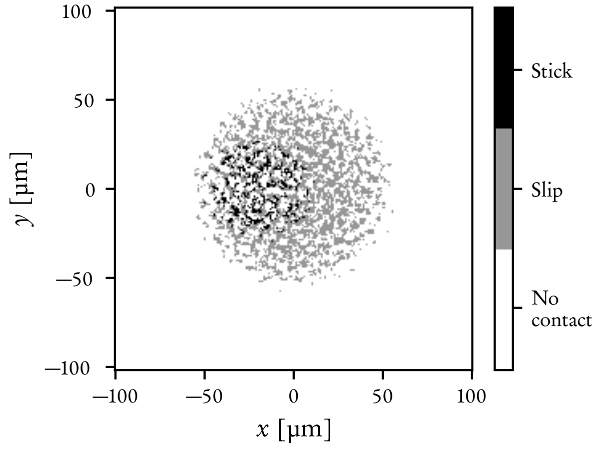

(a) Stick and slip

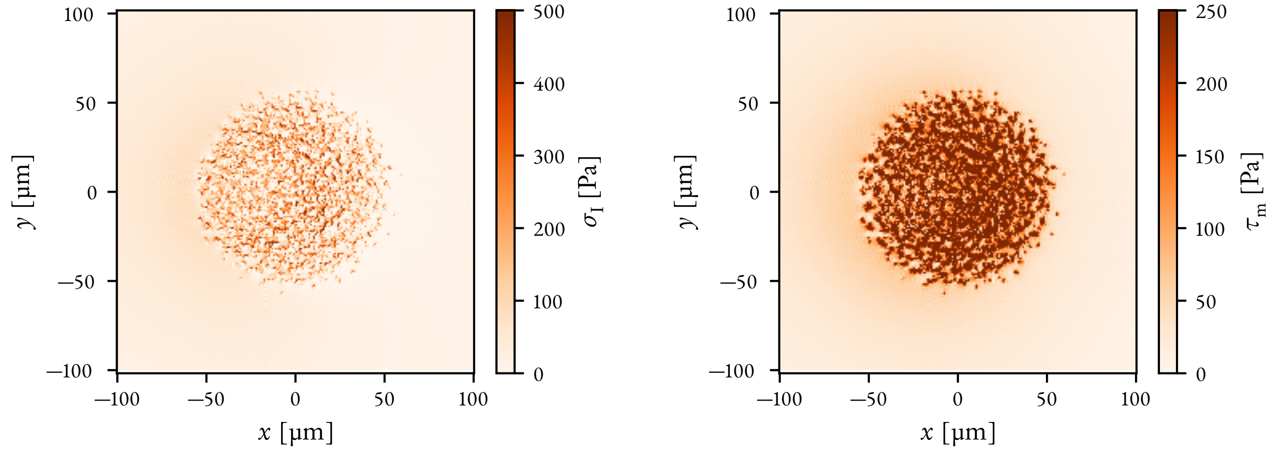

(b) 1st principal stress

(c) Maximum shear stress

Figure A.5 – Elastic tangential contact of a rough sphere. The parameters of the simulation are $n = 729$, $L = 500\,\mu\mathrm{m}$, $E = 70\,\mathrm{GPa}$, $\nu = 0.17$, $\sigma_\mathrm{m} = 500\,\mathrm{MPa}$, $\sigma_\mathrm{m,T} = 250\,\mathrm{MPa}$ (using Tresca friction), $p_{N,0} = 10\,\mathrm{MPa}$ and $p_{x,0} = 2\,\mathrm{MPa}$. The sphere has a radius $R = 6\,\mathrm{mm}$. The rough surface has the parameters $Sa = 0.01\,\mu\mathrm{m}$, $\lambda_l = \lambda_r = 10\,\mu\mathrm{m}$, $\lambda_s = 1.37\,\mu\mathrm{m}$ and $H = 0.8$.

BIBLIOGRAPHY

Aghababaei, R., T. Brink, and J.-F. Molinari (2018), “Asperity-level origins of transition from mild to severe wear”, *Physical review letters* 120.18.

Aghababaei, R., D. H. Warner, and J.-F. Molinari (2016), “Critical length scale controls adhesive wear mechanisms”, *Nature communications* 7.

Aghababaei, R., D. H. Warner, and J.-F. Molinari (2017), “On the debris-level origins of adhesive wear”, *Proceedings of the national academy of sciences* 114.30.

Aghababaei, R. and K. Zhao (2021), “Micromechanics of material detachment during adhesive wear: A numerical assessment of Archard’s wear model”, *Wear* 476.

Ajayi, O. O. and K. C. Ludema (1990), “Mechanism of transfer film formation during repeat pass sliding of ceramic materials”, *Wear* 140.2.

Akchurin, A., R. Bosman, and P. M. Lugt (2017), “Generation of wear particles and running-in in mixed lubricated sliding contacts”, *Tribology international* 110.

Amontons, G. (1699), “De la résistance causée dans les machines, tant par les frottemens des parties qui les composent, que par la roideur des cordes qu’on y emploie, et la manière de calculer l’un et l’autre”, *Mémoires de l’académie royale des sciences*.

André, D., J. Girardot, and C. Hubert (2019), “A novel DEM approach for modeling brittle elastic media based on distinct lattice spring model”, *Computer methods in applied mechanics and engineering* 350.

Archard, J. F. (1953), “Contact and Rubbing of Flat Surfaces”, *Journal of applied physics* 24.8.

Archard, J. F. and T. E. Allibone (1957), “Elastic deformation and the laws of friction”, *Proceedings of the royal society of london. series a. mathematical and physical sciences* 243.1233.

Belytschko, T and S. P. Xiao (2003), “Coupling Methods for Continuum Model with Molecular Model”, *International journal for multiscale computational engineering* 1.

Biegel, R. L., C. G. Sammis, and J. H. Dieterich (1989), “The frictional properties of a simulated gouge having a fractal particle distribution”, *Journal of structural geology* 11.7.

Block, J. and L. Keer (2008), “Periodic contact problems in plane elasticity”, *Journal of mechanics of materials and structures* 3.7.

Bongiorno, A. and A. Pasquarello (2002), “Oxygen Diffusion through the Disordered Oxide Network during Silicon Oxidation”, *Physical review letters* 88.12.

Bowden, F. P. and D. Tabor (1966), “Friction, lubrication and wear: a survey of work during the last decade”, *British journal of applied physics* 17.12.

Brink, T., L. Frérot, and J.-F. Molinari (2021), “A parameter-free mechanistic model of the adhesive wear process of rough surfaces in sliding contact”, *Journal of the mechanics and physics of solids* 147.

Brink, T., E. Milanese, and J.-F. Molinari (2022), “Effect of wear particles and roughness on nanoscale friction”, *Physical review materials* 6.1.

Brink, T. and J.-F. Molinari (2019), “Adhesive wear mechanisms in the presence of weak interfaces: Insights from an amorphous model system”, *Physical review materials* 3.5.

Brodsky, E. E., J. J. Gilchrist, A. Sagy, and C. Collettini (2011), “Faults smooth gradually as a function of slip”, *Earth and planetary science letters* 302.1.

Broughton, J. Q., F. F. Abraham, N. Bernstein, and E. Kaxiras (1999), “Concurrent coupling of length scales: Methodology and application”, *Physical review b* 60.4.

Bugnicourt, R., P. Sainsot, D. Dureisseix, C. Gauthier, and A. A. Lubrecht (2018), “FFT-Based Methods for Solving a Rough Adhesive Contact: Description and Convergence Study”, *Tribology letters* 66.1.

Burns, S. J., P. T. Piiroinen, and K. J. Hanley (2019), "Critical time step for DEM simulations of dynamic systems using a Hertzian contact model", *International journal for numerical methods in engineering* 119.5.

Bush, A., R. Gibson, and T. Thomas (1975), "The elastic contact of a rough surface", *Wear* 35.1.

Candela, T. and E. E. Brodsky (2016), "The minimum scale of grooving on faults", *Geology* 44.8.

Celigueta, M. A., S. Latorre, F. Arrufat, and E. Oñate (2017), "Accurate modelling of the elastic behavior of a continuum with the Discrete Element Method", *Computational mechanics* 60.6.

Chen, X., A. S. E. Madden, and Z. Reches (2017), "Powder Rolling as a Mechanism of Dynamic Fault Weakening", *Geophysical Monograph Series*, ed. by M. Y. Thomas, T. M. Mitchell, and H. S. Bhat, Hoboken, NJ, USA: John Wiley & Sons, Inc.

Cheng, H., S. Luding, K. Saitoh, and V. Magnanimo (2020), "Elastic wave propagation in dry granular media: Effects of probing characteristics and stress history", *International journal of solids and structures* 187.

Ciavarella, M. (2016), "Rough contacts near full contact with a very simple asperity model", *Tribology international* 93.

Collet, S., J.-F. Molinari, and S. Brach (2020), "Variational phase-field continuum model uncovers adhesive wear mechanisms in asperity junctions", *Journal of the mechanics and physics of solids*.

Coulomb, C.-A. (1785), "Théorie des machines simples, en ayant égard de leurs parties et de la roideur des cordages", *Mémoires de Mathématique et de Physique de l'Académie Royale des Sciences*, First, vol. 10, Paris.

Crouch, S. L. and A. M. Starfield (1983), *Boundary Element Methods in Solid Mechanics*, London: George Allen & Unwin.

Cundall, P. A. (1971), "A Computer Model for Simulating Progressive, Large-scale Movement in Blocky Rock System", *Proceedings of the international symposium on rock mechanics, 1971*.

Cundall, P. A. and O. D. L. Strack (1979), "A discrete numerical model for granular assemblies", *Géotechnique* 29.1.

De, T., J. Chakraborty, J. Kumar, A. Tripathi, M. Sen, and W. Ketterhagen (2022), "A particle location based multi-level coarse-graining technique for Discrete Element Method (DEM) simulation", *Powder technology* 398.

Dubois, S. M.-M., G.-M. Rignanese, T. Pardoen, and J.-C. Charlier (2006), "Ideal strength of silicon: An *ab initio* study", *Physical review b* 74.23.

Eder, S., A. Vernes, G. Vorlaufer, and G. Betz (2011), "Molecular dynamics simulations of mixed lubrication with smooth particle post-processing", *Journal of physics: condensed matter* 23.17.

Fillot, N., I. Iordanoff, and Y. Berthier (2007), "Modelling third body flows with a discrete element method—a tool for understanding wear with adhesive particles", *Tribology international* 40.6.

Fillot, N., I. Iordanoff, and Y. Berthier (2005), "Simulation of Wear Through Mass Balance in a Dry Contact", *Journal of tribology* 127.1.

Fleitout, L. and C. Froidevaux (1980), "Thermal and mechanical evolution of shear zones", *Journal of structural geology* 2.1.

Frérot, L., R. Aghababaei, and J.-F. Molinari (2018), "A mechanistic understanding of the wear coefficient: From single to multiple asperities contact", *Journal of the mechanics and physics of solids* 114.

Frérot, L., G. Anciaux, and J.-F. Molinari (2020a), "Crack nucleation in the adhesive wear of an elastic-plastic half-space", *Journal of the mechanics and physics of solids* 145.

Frérot, L., G. Anciaux, V. Rey, S. Pham-Ba, and J.-F. Molinari (2020b), "Tamaas: a library for elastic-plastic contact of periodic rough surfaces", *Journal of open source software* 5.51.

Frérot, L., M. Bonnet, J.-F. Molinari, and G. Anciaux (2019), "A Fourier-accelerated volume integral method for elastoplastic contact", *Computer methods in applied mechanics and engineering* 351.

Garabedian, N. T., A. Bhattacharjee, M. N. Webster, G. L. Hunter, P. W. Jacobs, A. R. Konicek, and D. L. Burris (2019), "Quantifying, Locating, and Following Asperity-Scale Wear Processes Within Multiasperity Contacts", *Tribology letters* 67.3.

Ghesquière, T., S. Pham-Ba, and J.-F. Molinari (2022), *Optimal material removal process*, EPFL.

Gnecco, E., R. Bennewitz, and E. Meyer (2002), "Abrasive Wear on the Atomic Scale", *Physical review letters* 88.21.

González-Cataldo, F., S. Davis, and G. Gutiérrez (2016), “Melting curve of SiO2 at multimegabar pressures: implications for gas giants and super-Earths”, *Scientific reports* 6.1.

Gosvami, N. N., J. A. Bares, F. Mangolini, A. R. Konicek, D. G. Yablon, and R. W. Carpick (2015), “Mechanisms of antiwear tribofilm growth revealed in situ by single-asperity sliding contacts”, *Science* 348.6230.

Greenwood, J. A. and J. B. P. Williamson (1966), “Contact of Nominally Flat Surfaces”, *Proceedings of the royal society of london. series a, mathematical and physical sciences* 295.1442.

Greenwood, J. and J. Wu (2001), “Surface Roughness and Contact: An Apology”, *Meccanica* 36.6.

Griffiths, D. V. and G. G. W. Mustoe (2001), “Modelling of elastic continua using a grillage of structural elements based on discrete element concepts”, *International journal for numerical methods in engineering* 50.7.

Grigoratos, T. and G. Martini (2015), “Brake wear particle emissions: a review”, *Environmental science and pollution research* 22.4.

Guo, Y. and J. K. Morgan (2007), “Fault gouge evolution and its dependence on normal stress and rock strength - Results of discrete element simulations: Gouge zone properties”, *Journal of geophysical research: solid earth* 112.B10.

Hentz, S., L. Daudeville, and F. V. Donzé (2004), “Identification and Validation of a Discrete Element Model for Concrete”, *Journal of engineering mechanics* 130.6.

Hild, P. (2003), “An example of nonuniqueness for the continuous static unilateral contact model with Coulomb friction”, *Comptes rendus mathematique* 337.10.

Holmberg, K. and A. Erdemir (2017), “Influence of tribology on global energy consumption, costs and emissions”, *Friction* 5.3.

Hopcroft, M. A., W. D. Nix, and T. W. Kenny (2010), “What is the Young’s Modulus of Silicon?”, *Journal of microelectromechanical systems* 19.2.

Hutchings, I. M. (2016), “Leonardo da Vinci’s studies of friction”, *Wear* 360–361.

Hyun, S., L. Pei, J.-F. Molinari, and M. O. Robbins (2004), “Finite-element analysis of contact between elastic self-affine surfaces”, *Physical review e* 70.2.

Jaccodine, R. J. (1963), “Surface Energy of Germanium and Silicon”, *Journal of the electrochemical society* 110.6.

Jacobs, T. D. B., T. Junge, and L. Pastewka (2017), “Quantitative characterization of surface topography using spectral analysis”, *Surface topography: metrology and properties* 5.1.

Jerier, J. F. and J. F. Molinari (2012), “Normal contact between rough surfaces by the Discrete Element Method”, *Tribology international* 47.

Jiang, Z., T. Tsuji, K. Washino, and T. Tanaka (2021), “Influence of model particle size and spatial resolution in coarse-graining DEM-CFD simulation”, *Advanced powder technology* 32.10.

Johnson, K. L. (1985), *Contact Mechanics*, Cambridge: Cambridge University Press.

Johnson, K. L., K. Kendall, A. D. Roberts, and D. Tabor (1971), “Surface energy and the contact of elastic solids”, *Proceedings of the royal society of london. a. mathematical and physical sciences* 324.1558.

Kanjilal, S. and S. Schneiderbauer (2021), “A revised coarse-graining approach for simulation of highly poly-disperse granular flows”, *Powder technology* 385.

Kato, H. and K. Komai (2007), “Tribofilm formation and mild wear by tribo-sintering of nanometer-sized oxide particles on rubbing steel surfaces”, *Wear* 262.1.

Kato, K. (2003), “Nanoscale Analyses of Wear Mechanisms”, *Nanotribology: Critical Assessment and Research Needs*, ed. by S. M. Hsu and Z. C. Ying, Boston, MA: Springer US.

Khajeh Salehani, M., N. Irani, M. Müser, and L. Nicola (2018), “Modelling coupled normal and tangential tractions in adhesive contacts”, *Tribology international* 124.

Kirk, A. M., P. H. Shipway, W. Sun, and C. J. Bennett (2019), “The effect of frequency on both the debris and the development of the tribologically transformed structure during fretting wear of a high strength steel”, *Wear* 426–427.

— (2020), “Debris development in fretting contacts – Debris particles and debris beds”, *Tribology international* 149.

Kole, P. J., A. J. Löhr, F. G. A. J. Van Belleghem, and A. M. J. Ragas (2017), "Wear and Tear of Tyres: A Stealthy Source of Microplastics in the Environment", *International journal of environmental research and public health* 14.10.

Komvopoulos, K. and D.-H. Choi (1992), "Elastic Finite Element Analysis of Multi-Asperity Contacts", *Journal of tribology* 114.4.

Kubiak, K. J., T. W. Liskiewicz, and T. G. Mathia (2011), "Surface morphology in engineering applications: Influence of roughness on sliding and wear in dry fretting", *Tribology international* 44.11.

Lai, K., M.-Y. Hao, W.-M. Chen, and J. C. Lee (1994), "Effects of surface preparation on the electrical and reliability properties of ultrathin thermal oxide", *Ieee electron device letters* 15.11.

Leclerc, W., H. Haddad, and M. Guessasma (2017), "On the suitability of a Discrete Element Method to simulate cracks initiation and propagation in heterogeneous media", *International journal of solids and structures* 108.

Lehuen, J., J.-Y. Delenne, A. Duri, and T. Ruiz (2020), "Forces and flow induced by a moving intruder in a granular packing: coarse-graining and DEM simulations versus experiments", *Granular matter* 22.4.

Lewandowski, J. J. and A. L. Greer (2006), "Temperature rise at shear bands in metallic glasses", *Nature materials* 5.1.

Luo, J., J. Wang, E. Bitzek, J. Y. Huang, H. Zheng, L. Tong, Q. Yang, J. Li, and S. X. Mao (2016), "Size-Dependent Brittle-to-Ductile Transition in Silica Glass Nanofibers", *Nano letters* 16.1.

Mair, K., K. M. Frye, and C. Marone (2002), "Influence of grain characteristics on the friction of granular shear zones", *Journal of geophysical research: solid earth* 107.B10.

Majumdar, A. and C. L. Tien (1990), "Fractal characterization and simulation of rough surfaces", *Wear* 136.2.

Mandelbrot, B. B., D. E. Passoja, and A. J. Paullay (1984), "Fractal character of fracture surfaces of metals", *Nature* 308.5961.

Meierhofer, A., C. Hardwick, R. Lewis, K. Six, and P. Dietmaier (2014), "Third body layer—experimental results and a model describing its influence on the traction coefficient", *Wear* 314.1.

Meng, H. C. and K. C. Ludema (1995), "Wear models and predictive equations: their form and content", *Wear* 181–183.443-457.

Meurer, A., C. P. Smith, M. Paprocki, O. Čertík, S. B. Kirpichev, M. Rocklin, A. Kumar, S. Ivanov, J. K. Moore, S. Singh, T. Rathnayake, S. Vig, B. E. Granger, R. P. Muller, F. Bonazzi, H. Gupta, S. Vats, F. Johansson, F. Pedregosa, M. J. Curry, A. R. Terrel, Š. Roučka, A. Saboo, I. Fernando, S. Kulal, R. Cimrman, and A. Scopatz (2017), "SymPy: symbolic computing in Python", *Peerj computer science* 3.

Mikelis, A. and J.-F. Molinari (2021), *Optimized shovelling tool*, EPFL.

Milanese, E., T. Brink, R. Aghababaei, and J.-F. Molinari (2019), "Emergence of self-affine surfaces during adhesive wear", *Nature communications* 10.1.

— (2020), "Role of interfacial adhesion on minimum wear particle size and roughness evolution", *Physical review e* 102.4.

Milanese, E. and J.-F. Molinari (2020), "A mechanistic model for the growth of cylindrical debris particles in the presence of adhesion", *International journal of solids and structures* 203.

Mizoguchi, K., T. Hirose, T. Shimamoto, and E. Fukuyama (2007), "Reconstruction of seismic faulting by high-velocity friction experiments: An example of the 1995 Kobe earthquake", *Geophysical research letters* 34.1.

Molinari, J.-F. and S. Pham-Ba (2022), "An optimized material removal process", *Current Trends and Open Problems in Computational Mechanics*, Springer International Publishing.

Morante, S., G. C. Rossi, and M. Testa (2006), "The stress tensor of a molecular system: An exercise in statistical mechanics", *The journal of chemical physics* 125.3.

Morgan, J. K. (1999), "Numerical simulations of granular shear zones using the distinct element method: 2. Effects of particle size distribution and interparticle friction on mechanical behavior", *Journal of geophysical research: solid earth* 104.B2.

Müser, M. H., W. B. Dapp, R. Bugnicourt, P. Sainsot, N. Lesaffre, T. A. Lubrecht, B. N. J. Persson, K. Harris, A. Bennett, K. Schulze, S. Rohde, P. Ifju, W. G. Sawyer, T. Angelini, H. Ashtari Esfahani, M. Kadkhodaei, S. Akbarzadeh, J.-J. Wu, G. Vorlaufer, A. Vernes, S. Solhjoo, A. I. Vakis, R. L. Jackson, Y. Xu, J. Streator, A. Rostami, D. Dini, S. Medina, G. Carbone, F. Bottiglione, L. Afferrante, J. Monti,

L. Pastewka, M. O. Robbins, and J. A. Greenwood (2017), "Meeting the Contact-Mechanics Challenge", *Tribology letters* 65.4.

Nguyen, N. H. T., H. H. Bui, J. Kodikara, S. Arooran, and F. Darve (2019), "A discrete element modelling approach for fatigue damage growth in cemented materials", *International journal of plasticity* 112.

Nguyen, N. H. T., H. H. Bui, G. D. Nguyen, and J. Kodikara (2017), "A cohesive damage-plasticity model for DEM and its application for numerical investigation of soft rock fracture properties", *International journal of plasticity* 98.

O'Sullivan, C. and J. D. Bray (2004), "Selecting a suitable time step for discrete element simulations that use the central difference time integration scheme", *Engineering computations* 21.2/3/4.

Pande, G., G. Beer, and J. Williams (1990), "Numerical methods in rock mechanics".

Persson, B. N. J. (2006), "Contact mechanics for randomly rough surfaces", *Surface science reports* 61.4.

Petrova, D., B. Weber, C. Allain, P. Audebert, D. Bonn, and A. M. Brouwer (2018), "Fast 3D Microscopy Imaging of Contacts Between Surfaces Using a Fluorescent Liquid", *Acs applied materials & interfaces* 10.48.

Pham-Ba, S., T. Brink, and J.-F. Molinari (2020), "Adhesive wear and interaction of tangentially loaded micro-contacts", *International journal of solids and structures* 188–189.

Pham-Ba, S. and J.-F. Molinari (2021a), "Adhesive wear regimes on rough surfaces and Interaction of micro-contacts", *Tribology letters* 69.3.

— (2021b), "Creation and evolution of roughness on silica under unlubricated wear", *Wear* 472–473.

— (2022), "Adhesive wear with a coarse-grained discrete element model", *Computer methods in applied mechanics and engineering* 397.

Plimpton, S. (1995), "Fast Parallel Algorithms for Short-Range Molecular Dynamics", *Journal of computational physics* 117.1.

Polonsky, I. and L. Keer (1999), "A numerical method for solving rough contact problems based on the multi-level multi-summation and conjugate gradient techniques", *Wear* 231.2.

Popov, V. L. and R. Pohrt (2018), "Adhesive wear and particle emission: Numerical approach based on asperity-free formulation of Rabinowicz criterion", *Friction* 6.3.

Power, W. L., T. E. Tullis, and J. D. Weeks (1988), "Roughness and wear during brittle faulting", *Journal of geophysical research: solid earth* 93.B12.

Queteschiner, D., T. Lichtenegger, S. Pirker, and S. Schneiderbauer (2018), "Multi-level coarse-grain model of the DEM", *Powder technology* 338.

Rabinowicz, E. (1958), "The effect of size on the looseness of wear fragments", *Wear* 2.1.

— (1984), "The least wear", *Wear* 100.1.

Rapaport, D. C. (2004), *The Art of Molecular Dynamics Simulation*, Second, Cambridge: Cambridge University Press.

Reches, Z. and T. A. Dewers (2005), "Gouge formation by dynamic pulverization during earthquake rupture", *Earth and planetary science letters* 235.1.

Renouf, M., F. Massi, N. Fillot, and A. Saulot (2011), "Numerical tribology of a dry contact", *Tribology international* 44.7.

Rey, V., G. Anciaux, and J.-F. Molinari (2017), "Normal adhesive contact on rough surfaces: efficient algorithm for FFT-based BEM resolution", *Computational mechanics* 60.1.

Riahi, A. R and A. T Alpas (2001), "The role of tribo-layers on the sliding wear behavior of graphitic aluminum matrix composites", *Wear* 251.1.

Rudd, R. E. and J. Q. Broughton (1998), "Coarse-grained molecular dynamics and the atomic limit of finite elements", *Physical review b* 58.10.

Sahli, R., G. Pallares, C. Ducottet, I. E. Ben Ali, S. Al Akhrass, M. Guibert, and J. Scheibert (2018), "Evolution of real contact area under shear and the value of static friction of soft materials", *Proceedings of the national academy of sciences* 115.3.

Sarnthein, J., A. Pasquarello, and R. Car (1995), "Structural and Electronic Properties of Liquid and Amorphous SiO2 : An *Ab Initio* Molecular Dynamics Study", *Physical review letters* 74.23.

Schneider, T. and E. Stoll (1978), "Molecular-dynamics study of a three-dimensional one-component model for distortive phase transitions", *Physical review b* 17.3.

Scholz, C. H. (1987), "Wear and gouge formation in brittle faulting", *Geology* 15.6.

Starfield, A. M. and P. A. Cundall (1988), “Towards a methodology for rock mechanics modelling”, *International journal of rock mechanics and mining sciences & geomechanics abstracts* 25.3.

Stillinger, F. H. and T. A. Weber (1985), “Computer simulation of local order in condensed phases of silicon”, *Physical review b* 31.8.

— (1986), “Erratum: Computer simulation of local order in condensed phases of silicon [Phys. Rev. B 31, 5262 (1985)]”, *Physical review b* 33.2.

Stukowski, A. (2009), “Visualization and analysis of atomistic simulation data with OVITO–the Open Visualization Tool”, *Modelling and simulation in materials science and engineering* 18.1.

Thom, C. A., E. E. Brodsky, R. W. Carpick, G. M. Pharr, W. C. Oliver, and D. L. Goldsby (2017), “Nanoscale Roughness of Natural Fault Surfaces Controlled by Scale-Dependent Yield Strength”, *Geophysical research letters* 44.18.

Towle, L. C. (1967), “Empirial relationship between shear strength, pressure and temperature”, *Applied physics letters* 10.11.

Trageser, J. and P. Seleson (2020), “Bond-Based Peridynamics: a Tale of Two Poisson’s Ratios”, *Journal of peridynamics and nonlocal modeling* 2.3.

Varga, Z., V. Grenard, S. Pecorario, N. Taberlet, V. Dolique, S. Manneville, T. Divoux, G. H. McKinley, and J. W. Swan (2019), “Hydrodynamics control shear-induced pattern formation in attractive suspensions”, *Proceedings of the national academy of sciences* 116.25.

Vashishta, P., R. K. Kalia, J. P. Rino, and I. Ebbsjö (1990), “Interaction potential for SiO2: A molecular-dynamics study of structural correlations”, *Physical review b* 41.17.

Vink, R., G. Barkema, W. van der Weg, and N. Mousseau (2001), “Fitting the Stillinger–Weber potential to amorphous silicon”, *Journal of non-crystalline solids* 282.2-3.

Voisin–Leprince, M., G. Anciaux, J. Garcia-Suarez, and J.-F. Molinari (2022), “An energy-based coupling approach to FEM-DEM simulations with application to gouge modeling”, *Arxiv*.

Wang, Y., F. Alonso-Marroquin, and W. W. Guo (2015), “Rolling and sliding in 3-D discrete element models”, *Particuology* 23.

Weber, B., T. Suhina, T. Junge, L. Pastewka, A. M. Brouwer, and D. Bonn (2018), “Molecular probes reveal deviations from Amontons’ law in multi-asperity frictional contacts”, *Nature communications* 9.1.

Wellmann, C. and P. Wriggers (2012), “A two-scale model of granular materials”, *Computer methods in applied mechanics and engineering* 205–208.

Wilson, B., T. Dewers, Z. Reches, and J. Brune (2005), “Particle size and energetics of gouge from earthquake rupture zones”, *Nature* 434.7034.

Wirth, A., D. Eggleston, and R. Whitaker (1994), “A fundamental tribochemical study of the third body layer formed during automotive friction braking”, *Wear* 179.1.

Yang, C. C., G Li, and Q Jiang (2003), “Effect of pressure on melting temperature of silicon”, *Journal of physics: condensed matter* 15.29.

Yastrebov, V. A., G. Anciaux, and J.-F. Molinari (2015), “From infinitesimal to full contact between rough surfaces: Evolution of the contact area”, *International journal of solids and structures* 52.

Yuan, C. Q., Z. Peng, X. P. Yan, and X. C. Zhou (2008), “Surface roughness evolutions in sliding wear process”, *Wear* 265.3.

Zanoria, E. and S. Danyluk (1993), “Ball-on-flat reciprocating sliding wear of single-crystal, semiconductor silicon at room temperature”, *Wear* 162–164.

Zanoria, E. S., S. Danyluk, and M. J. Mcnallan (1995), “Formation of Cylindrical Sliding-Wear Debris on Silicon in Humid Conditions and Elevated Temperatures”, *Tribology transactions* 38.3.

Zhang, J. and A. T. Alpas (1997), “Transition between mild and severe wear in aluminium alloys”, *Acta materialia* 45.2.

Zhao, K. and R. Aghababaei (2020), “Adhesive wear law at the single asperity level”, *Journal of the mechanics and physics of solids* 143.

Son Pham-Ba

Curriculum Vitae

Avenue de Cour 81
1007 Lausanne
+41 79 246 80 65
son.j.phamba@gmail.com

EDUCATION

2018 – 2022 **Docteur ès Sciences**
École Polytechnique Fédérale de Lausanne
Supervisor: Prof. Jean-François Molinari
Thesis: Modeling the origins of adhesive wear across scales

2015 – 2017 **Master of Science in Mechanical Engineering**
École Polytechnique Fédérale de Lausanne
Minor in Biocomputing

2012 – 2015 **Bachelor of Science in Mechanical Engineering**
École Polytechnique Fédérale de Lausanne

EXPERIENCE

2018 – 2022 **Doctoral Assistant**
École Polytechnique Fédérale de Lausanne
PhD thesis at the Computational Solid Mechanics Laboratory
(head: Prof. Jean-François Molinari)

2017 **Project manager**
ROLEX
Master project in industry

PEER-REVIEWED PUBLICATIONS

2022 **Adhesive wear with a coarse-grained discrete element model**
Son Pham-Ba & Jean-François Molinari, *Computer Methods in Applied Mechanics and Engineering*

2021 **Adhesive wear regimes on rough surfaces and interaction of micro-contacts**
Son Pham-Ba & Jean-François Molinari, *Tribology Letters*
Selected as Best from STLE's Research Community (*Tribology & Lubrication Technology* magazine, November 2021)

2021 **Creation and evolution of roughness on silica under unlubricated wear**
Son Pham-Ba & Jean-François Molinari, *Wear*

2020 **Tamaas: a library for elastic-plastic contact of periodic rough surfaces**
Lucas Frérot, Guillaume Anciaux, Valentine Rey, Son Pham-Ba & Jean-François Molinari, *Journal of Open Source Software*

2020 **Adhesive wear and interaction of tangentially loaded micro-contacts**
Son Pham-Ba, Tobias Brink & Jean-François Molinari, *International Journal of Solids and Structures*

BOOK CHAPTERS

2022 **An optimized material removal process**
Jean-François Molinari & Son Pham-Ba, *Current Trends and Open Problems in Computational Mechanics*, Springer International Publishing

ONGOING WORKS

2022 **Role of material characteristic size in third body layer properties**
Son Pham-Ba & Jean-François Molinari, in preparation

2022 **Tribological effect of an oxide layer on silicon**
Son Pham-Ba & Jean-François Molinari, in preparation

Presentations, Conferences, Seminars

2022 **CMIS Symposium**
Chexbres
Attending

2021 **ECCOMAS Thematic Conference**
"VII International Conference on Particle-based Methods", Hamburg
Son Pham-Ba & Jean-François Molinari, Adhesive wear with a coarse-grained discrete element model

2020 **SWICCOMAS General Assembly**
ETH Zurich
Poster: Son Pham-Ba & Jean-François Molinari, Adhesive wear of rough surfaces and interaction of micro-contacts

2019 **ECCOMAS Thematic Conference**
"Computational Modeling of Complex Materials across the Scales", Glasgow
Poster: Son Pham-Ba, Tobias Brink & Jean-François Molinari, Adhesive wear and interaction of tangentially loaded micro-contacts

2018 **45th Leeds-Lyon Symposium on Tribology**
"Smart Tribology Systems", Leeds
Poster: Son Pham-Ba, Lucas Frérot, Tobias Brink & Jean-François Molinari, Boundary element formulation of normal and tangential contact with Coulomb friction

2018 **CECAM Workshop**
"Surface and Interface Structure", Lausanne
Attending

Teaching assistantship

2019 – 2021 **Numerical modeling of solids and structures**
by Prof. Jean-François Molinari & Dr Guillaume Anciaux
3 semesters of 14 weeks, responsible for 2 hours/week of exercise sessions and class projects supervision, grading

2018 – 2020 **Continuum mechanics**
by Prof. Jean-François Molinari
3 semesters of 14 weeks, responsible for 2 hours/week of exercise sessions, grading

Supervised projects

Fall 2021 **Optimal material removal process**
Master intern: Thibault Ghesquière

Fall 2021 **Discrete element simulation of indented soil**
Master student: Vibhu Baibhav
Co-supervied with Dr Joaquin Garcia

Spring 2021 **Optimized shoveling tool**
Engineering intern: Angelos Mikelis

Fall 2020 **Numerical simulation of a two layered elastic system using the Boundary Element Method**
Bachelor student: Jeremy Bussat

Spring 2020 **Numerical simulation of a layered elastic system using the boundary element method**
Master student: Ariele Forni

Spring 2019	**Introduction à la dynamique en éléments finis : Modélisation d’une corde tendue** Bachelor student: Stefan Marceta
Fall 2018	**Griffith’s Theory Validation using Finite Element Method** Bachelor student: Máximo Jara
Spring 2018	**1D dynamical model of frictional stick-slip motion** Bachelor student: Nicolas Woerle